Advances in Understanding Graphene Hybrids and MXenes

by

Fatima Hamade

A dissertation submitted to the Graduate Faculty of
Auburn University
in partial fulfillment of the
requirements for the Degree of
Doctor of Philosophy

Auburn, Alabama
May 6, 2023

Keywords: nanomaterials, microstructure, rheology, electrodes, graphene, MXene

Approved by

Virginia A. Davis, Chair, Daniel F. and Josephine Breeden Professor, Chemical Engineering
Bryan S. Beckingham, Assistant Professor of Chemical Engineering
Tae-Sik Oh, Assistant Professor of Chemical Engineering
Majid Beidaghi, Associate Professor of Materials Engineering
Kyle Schulze, Assistant Professor of Mechanical Engineering

Abstract

The overall goal of this research was to contribute to understanding the effects of additional components on the microstructures and properties of two-dimensional (2D) systems, namely graphene hybrids and MXenes. The first part of this research involved synthesizing, characterizing, and electrochemical testing of graphene/manganese oxide hybrids. Combining 2D ultra-large reduced graphene oxide (RGO) sheets with an aspect, or length to diameter, ratio of ~40,000 with 1D manganese oxide (MnO_2) nanowires consisting of an aspect ratio of ~50 produced a hybrid (MnO_2/RGO) material. Testing two different compositions of hybrids were studied to understand the effects of combining different geometries and orders of magnitude different aspect ratios on the electrochemical properties. The individual components provided insights into the microstructures and electrochemical behavior of the hybrids. The 3:1 ratio of MnO_2/RGO (75/25 wt%) showed a more uniform distribution of nanowires along the sheets and outstanding electrochemical performance compared to the 10:1 ratio of MnO_2/RGO (90/10 wt%). The very large specific surface area of the RGO sheets in this research enabled faster ion and electron diffusion compared to smaller sheets used in the prior literature. Also, combining 2D/1D geometries with very different aspect ratios in the hybrid showed enhanced electrochemical performance than either component alone. This highlights the potential advantages of multicomponent systems that can be extended to other applications, such as fibers and sensors.

The second part of this dissertation was performed in collaboration with Dr. Majid Beidaghi in Materials Engineering at Auburn University. It involved understanding the rheological properties of aqueous $Ti_3C_2T_x$ MXene dispersions with two different objectives. The first objective was to provide insights into direct ink writing design parameters for a highly concentrated unfractionated MXene dispersion. Since MXenes are a recently developed class of 2D materials, particle interactions for processing are not well understood. The rheological behavior provided insights into viscoelastic properties and flow behavior necessary for determining optimal printability. The second objective was to investigate the effects of varying ionic strength, through sodium chloride (NaCl) addition, on the phase behavior and dispersion microstructures of large MXene flake dispersions. Polarized optical microscopy was performed to investigate different structures and phases with varying flake and salt concentrations. Rheology experiments were performed to better understand the thermodynamic interactions and augment the microscopy results. A simplified theoretical approach based on DLVO theory was also performed to provide insights into the phase behavior. A phase diagram was proposed that consists of liquid crystalline phases, gel, and flocculation.

Graphene and MXenes are charged systems, similar to nanoclays, that exhibit unique optical, mechanical, and electrical properties. Understanding the fundamental particle and solvent interactions provided a basis for fluid-phase processing and fabrication into electrochemical devices. Dispersion properties such as Debye screening length, aspect ratio, viscosity, and the presence of additional components were studied to increase understanding of the graphene hybrids and MXenes. In summary, results from this research contribute to bridging the gap in understanding the effects of tuning 2D

nanomaterial dispersions on processing and final properties for improving microscale and macroscale applications.

Acknowledgments

This work could not have been achieved without the help of many contributions. I would like to appreciate my advisor, Dr. Virginia Davis, for the guidance and providing interesting projects that enabled me to expand my interests and expertise. I would like to thank my former research advisor, Dr. Emmy Radich, for the support earlier in my graduate career. Thank you to the university reader for reviewing my dissertation. Furthermore, I would like to thank my committee members for their feedback throughout the process. This work was completed with collaborations from Dr. Majid Beidaghi in Materials Engineering for the MXene projects.

The graphene/manganese oxide research project was financially supported by the U.S. Department of Education Graduate Assistance in Areas of National Need Award Number P200A180002. Furthermore, the MXene/NaCl system work was financially supported by the National Science Foundation Award Number 2005413.

Thank you to Dr. Partha Saha, Dr. Matthew Noor, Dr. Rohit Kanungo, and Dr. Animesh Mondal for their trainings, knowledge, and advice throughout graduate school. Thank you to Dr. Jafar Oranji for synthesizing MXene dispersions in collaboration to understand how ink properties are related to 3D printing and electrode properties. Thank you to Elnaz Jamshidi for synthesizing size-fractionated MXenes in collaboration to understand the effects of sheet size and salt content on phase behavior. Thank you to Mackenzie Woods for wonderful work on the phase behavior of MXenes. Thank you to undergraduate researcher Lindsey Parsons for great work on the manganese oxide project.

To all of my colleagues, Dr. Zahra Karimi, Dr. Partha Saha, Dr. Matthew Noor, Mackenzie Woods, Sadat Amit, Delaney Clouse, Daniel Meadows, Tanmay Rahman, Dr. Rohit Kanungo, Dr. Animesh Mondal, and Dr. Rong Zhao, I appreciate all of the philosophical conversations, engineering challenges, support, and good times in the labs and group gatherings outside the labs.

A special appreciation to my family that has supported me throughout graduate school. To my mom, Zeinab Hamade, thank you for being encouraging and helping me along the way. To my sisters, Mariam and Noura, thank you for being the best and looking forward to all my visits back home. To my friends, thank you for all the wonderful times exploring, tailgating, playing soccer, and celebrating. Finally, I would like to thank my managers at Evonik for providing me the opportunity to begin my career as a process engineer while revising my dissertation and guidance with the final presentation.

Table of Contents

Abstract ii

Acknowledgments v

List of Tables xi

List of Figures xii

List of Abbreviations xviii

Chapter 1 Introduction 1

Chapter 2 Background 6

2.1 Carbon Structures 6

2.2 Manganese Oxide 9

2.3 GO/MnO_2 Systems 11

2.4 Liquid Crystal Phase Behavior 13

2.4.1 Overview 13

2.4.2 Types of Liquid Crystals 14

2.4.3 Fundamental Theory 15

2.4.4 Liquid Crystal Signatures 18

2.5 Ultra-large GO 25

2.6 Fundamentals of Charged Materials 29

2.6.1 Electric Double Layer (EDL) 29
2.6.2 Electroviscous Effect 31
2.6.3 Derjaguin-Landau-Verwey-Overbeek (DLVO) Theory 33
2.7 MXenes 35
2.8 Nanoclays 40
2.8.1 Nanoclay Structures 40
2.8.2 Nanoclay Phase Behavior 44
Chapter 3 Materials & Methods 48
3.1 Syntheses 48
3.1.1 Ultra-Large Graphene Oxide (GO) 48
3.1.2 Reduced Graphene Oxide (RGO) Preparation 50
3.1.3 Manganese Dioxide Nanowires (MnO_2 NWs) 50
3.1.4 Hybrid (RGO/MnO_2) 53
3.1.5 MXene Inks 54
3.1.5.1 Unfractionated MXenes 55
3.1.5.2 Large MXene Flake Dispersions 56
3.2 Characterization 57
3.2.1 Ultraviolet-Visible Spectroscopy (UV-vis) 57
3.2.2 Fourier-Transform Infrared Spectroscopy (FTIR) 58

3.2.3 Raman Spectroscopy....58
3.2.4 X-Ray Diffraction (XRD)....59
3.2.5 Atomic Force Microscopy (AFM)....59
3.2.6 Scanning Electron Microscopy (SEM)....59
3.2.7 Thermogravimetric Analysis (TGA)....60
3.3 Electrodes....60
3.4 Dispersion Microstructure....61
3.4.1 Optical Microscopy....61
3.4.2 Rheology....61
Chapter 4 Microstructure and Electrochemical Properties of Graphene/Manganese Oxide Hybrid Electrodes....63
4.1 Motivation....63
4.2 Results....64
4.2.1 Material Sizes – AFM analysis....64
4.2.2 Thermal Analysis....67
4.2.3 Spectroscopy Study....69
4.2.3.1 UV-vis & FTIR Spectroscopy analysis....69
4.2.3.2 XRD analysis....73
4.2.3.3 Raman analysis....75
4.2.4 Electrochemical Capacitive Behavior....78

4.3 Conclusions 85

Chapter 5 Phase Behavior & Rheological Properties of MXene Dispersions 86

5.1 Rheological Behavior of MXene Dispersions 86

5.1.1 Motivation 86

5.1.2 Results 87

5.1.3 Conclusions 91

5.2 Salt Effects on the Phase Behavior and Rheology of Large Flake MXene Dispersions 91

5.2.1 Motivation 91

5.2.2 Results 93

5.2.2.1 Material Characterization 93

5.2.2.2 Dispersion Behavior with Polarized Optical Microscopy 95

5.2.2.3 Steady Shear Rheology 119

5.2.2.4 Oscillatory Dynamic Rheology 134

5.2.3 Conclusions 153

Chapter 6 Conclusions 155

References 158

Appendix 174

List of Tables

Table 1. GO and MnO_2 Material Sizes from AFM Measurements 67

Table 2. Electroviscous Effects.....126

Table 3. Scaling Relationships with Flake Concentration 132

Table 4. Viscoelastic model for oscillatory data.....140

Table 5. Scaling Relationships with Flake Concentration 141

Table 6. Total Interaction Energies Based on DLVO Theory for Varying Ionic Strengths 150

Table 7. Experimental evidence of phase assignments.....152

Table A.1. Herschel-Bulkley Model Parameters for MXene/NaCl Dispersions for All Concentrations 178

Table A.2. Steady Shear Viscosities at Different Shear Rates 179

Table A.3. Storage and Loss Moduli at Different Angular Frequencies 180

List of Figures

Figure 2.3. Shape-controlled synthesis of MnO_2 to yield the shapes at the right of the schematic spindle- (top), rod- (middle), and needle-like (bottom) morphologies.[18] 10

Figure 2.4. Schematic of the interactions between GO sheets and nanowires, including hydrogen bonding and ion-dipole interactions.[55].....11

Figure 2.5. Variation of nanowire length on morphology by SEM of GO/MnO_2 system (a) large and (c) small nanowires with (b) and (d) higher magnifications of (a) and (c), respectively.[19].....12

Figure 2.6. (a) CV and (b) EIS Nyquist plots of a GO dispersion freeze-dried into an aerogel or sponge (GS) and then thermally annealed compared with pristine graphene (PG), both in 1M NaCl electrolyte.[62].....13

Figure 2.7. Classes of Friedelian liquid crystals a) nematic, b) cholesteric, and c) smectic.[64] 14

Figure 2.8. Phase behavior of rigid rods with increasing concentration.[70] 16

Figure 2.9. Birefringence of liquid crystals.[75].....19

Figure 2.10. Michel-Levy birefringence chart displaying the relationship between liquid crystalline film thickness, birefringence, and interference order.[77] 20

Figure 2.11. Three-region flow behavior from shear thinning (region I) to Newtonian plateau (region II) to shear thinning (region III).[79] 21

Figure 2.12. Viscosity as a function of volume fraction for graphene oxide.[87] 22

Figure 2.13. Oscillatory transients and first normal stress difference as a function of shear units (shear rate multiplied by time). Solid diamonds show shear stress and open triangles show N1.[2].....23

Figure 2.14. N1 as a function of shear rate for plate-like dispersions: organically-modified montmorillonite (OMMT), GO, and Kaolin, all in silicon oil (SO) with optical microscopy images on the right.[92] 24

Figure 2.15. Comparison of complex viscosity (η^*) and steady shear viscosity (η) of two different GO dispersion concentrations not obeying the Cox-Merz rule.[93] 25

Figure 2.16. Proposed model for fluid-phase ordering of ultra-large GO sheets compared with small GO sheets.[94].....26

Figure 2.17. Oscillatory dynamics of storage modulus (G') and loss modulus (G") with optical microscopy images of ultra-large GO dispersions.[95] 28

Figure 2.18. Illustration of the electrical double layer (EDL) for charged surface with Stern layer closest to the surface and diffuse layer, or outer Helmholtz plane (OHP), further away from the surface. For a negatively charged surface, the cations decrease with increasing distance away from the surface. The Debye length is calculated as the total length of the electrical double layer.[96] 30

Figure 2.21. Schematic representation of MXenes.[114] 36

Figure 2.26. Schematic representation of particle association in clay dispersions showing dispersed, flocculated, and aggregated phases.[122].....42

Figure 2.27. Schematic representation of nanoclays when dispersed in water forming the proposed house-of-cards structure.[137] 43

Figure 2.28. Gibbsite phase separation observed between crossed polarizers with ionic strength of 10^{-3} M and (left to right) 300, 400, and 500 g/L gibbsite concentration. I – isotropic, Col – columnar, and G – gel phases.[155] 45

Figure 3.1. Schematic of the synthesis of ultra-large GO via modified Hummer's method. 49

Figure 3.2. Synthesis scheme of MnO_2 via double-solvent system to yield long NWs. ...51

Figure 4.1 AFM images of a) GO with an average sheet size of 40 μm long and ~ 1nm thick, b) MnO_2 nanowires indicating network formation, and hybrids c) 3H that represents uniform distribution of nanowires along the GO sheets and d) 10H that represents clusters of MnO_2 attached to RGO sheets.[166].....66

Figure 4.2. TGA performed under argon atmosphere at a rate of 5 °C/min. a) GO exhibits two thermal transitions upon decomposition – loss of oxygen functionality and break carbon backbone. b) MnO_2 is much more thermally stable than GO and is converted to Mn_2O_3 and then Mn_3O_4. The hybrid exhibits transitions consisting of both individual components.[166] 69

Figure 4.3. a) UV-vis spectra indicating electronic transitions of ultra-large GO, MnO_2, and both hybrids 3H and 10H. Presence of oxygen functional groups in GO occurs at the shoulder of 300 nm. The 3H hybrid spectrum consists of the conjugated carbon peak blue-shifted to 215 nm ascribed to GO exfoliation and indication of the Mn-O transition with a broad peak at 410 nm. The higher MnO_2 content of 10H primarily indicates the Mn-O transition. b) FTIR spectra of expandable graphite, GO, RGO, and hybrids reveal presence of hydroxyl, carboxyl, carbonyl, and epoxy groups for GO, 3H, and 10H with 10H exhibiting the least intensities. FTIR spectra of MnO_2 indicates hydroxyl functionality in its crystal lattice and contributes to both hybrid spectra. RGO demonstrates no evident oxygen functionality similar to the expandable graphite (precursor) indicating successful reduction.[166] 71

Figure 4.4. To analyze if the graphene oxide is reduced through the hybrid synthesis, GO was subject to the same conditions in the synthesis without addition of the reacting agent.

a) UV-vis and b) FTIR spectroscopy were performed and demonstrate a partially reduced graphene oxide (P-RGO).[166] 72

Figure 4.5. XRD patterns of the materials at slow scan rate of 0.01 °/s. a) The expandable graphite exhibits two characteristic peaks that correspond to a d-spacing of 0.342 nm and GO exhibits an intense peak at $2\theta = 9.9°$ with calculated d-spacing of 0.892 nm indicating oxidation of the sheets. b) RGO spectrum exhibits a (002) peak at $2\theta = 22.7°$ with calculated d-spacing of 0.391 nm, conveying successful reduction of GO. c) The spectrum of MnO_2 confirms formation of the α-phase crystal structure and both hybrids display a similar pattern. d) magnification of low 2θ angles.[166] 74

Figure 4.6. Raman spectra performed using a 514 nm laser. a) Expandable graphite, ultra-large GO, and RGO result in D/G ratios of 0.22, 1.46 and 1.72, respectively. b) The 3H and 10H hybrid materials exhibit D/G ratios of 1.65 and 2.20, respectively. The ratio of Mn-O to G-peak is higher for 10H than 3H, further supporting the presence of more MnO_2 content. c) Magnification of the spectrum of MnO_2 confirms α-phase morphology produced from potassium-based reactive species.[166] 77

Figure 4.7. Cyclic voltammetry curves at different scan rates of a) GO, b) RGO, c) MnO_2, d) 3H, and e) 10H. f) An overlay of the CV curves of all materials at 5 mV/s scan rate.[166] 80

Figure 4.8. Electrochemical behavior with cyclability and EIS. a) Comparison of specific capacitance as a function of scan rate for all materials. b) Cycling behavior over a range of 1000 CV cycles performed at 20 mV/s scan rate. After 1000 cycles, the materials exhibit >95% capacitance retention. c) Nyquist plot overlay of electrodes in 1 M Na_2SO_4 aqueous solution with inset showing high frequency region.[166] 82

Figure 5.1. Schematic of MXene ink preparation and ~7 vol % MXene ink rheology. a) AFM of MXene dispersion confirming single-layer flakes. b) Adding SAP beads to a low concentration resulted in a uniform concentrated MXene dispersion. c) Steady shear viscosity rheology data (blue diamonds) and Herschel−Bulkley (line) model fit, and d) showing the dramatic viscosity drop at the yield stress. Small amplitude oscillatory shear (SAOS) data show e) G′ (blue diamonds) > G″ (red diamonds) and G′ nearly constant over the measured frequency range, and f) ratio of G′ to G′′ over the measured frequency range. Note: error bars represent standard error (n = 10 for SAOS data and n = 5 for steady shear data).[13] 90

Figure 5.2. SEM showing a) flake morphology and b) size distribution. c) AFM analysis with height profile in the inset and d) DLS of average hydrodynamic diameter versus [NaCl]. Error bars are standard deviation with four measurements at each ionic strength. 95

Figure 5.3. Bar graphs comparing 0 and 0.1 M NaCl with varying flake concentrations from a) oscillatory storage modulus G' and b) yield stress. 96

Figure 5.4. Microcentrifuge tubes inverted of MXene dispersion concentrations (left to right) 0.050, 0.10, 0.25, 0.50, 0.70, and 0.80 vol% all with 0.1 M NaCl. 98

Figure 5.5. Polarized optical microscopy images with the analyzer in crossed (top) and uncrossed (bottom) configurations for a) 0.050 vol%/0 M, b) 0.050 vol%/0.1 M, c) 0.10 vol%/0 M, and d) 0.10 vol%/0.1 M NaCl. Scale bar is 5 μm. The arrows indicate the solvent rich regions (white regions of uncrossed images).....100

Figure 5.6. Partially crossed optical microscopy of 0.10 vol% with magnified images and stage rotations for a) 0 M, b) 0.01 M, c) 0.05 M, d) 0.1 M NaCl. Scale bar is 5 μm. 101

Figure 5.7. Uncrossed images of 0.15 vol% for a) 0 M, b) 0.01 M, c) 0.05 M, d) 0.1 M NaCl. Scale bar is 5 μm. 102

Figure 5.8. Partially crossed images of 0.15 vol% for a) 0 M, b) 0.01 M, c) 0.05 M, d) 0.1 M NaCl. Scale bar is 5 μm.....103

Figure 5.9. Crossed (a) and uncrossed (b) optical microscopy images of 0.15 vol%/0.1 M at lower magnification of 40X. Scale bar is 10 μm. 103

Figure 5.10. Uncrossed images of 0.20 vol% for a) 0 M, b) 0.01 M, c) 0.05 M, d) 0.1 M NaCl. Scale bar is 5 μm. 104

Figure 5.11. Partially crossed images of 0.20 vol% for a) 0 M, b) 0.01 M, c) 0.05 M, d) 0.1 M NaCl. Scale bar is 5 μm.....104

Figure 5.12. MXene dispersions of a) 0.20 vol% and b) 0.40 vol% both with 0.01 (left), 0.05 M (middle), and 0.1 M (right) NaCl. 105

Figure 5.13. Uncrossed optical microscopy images of 0.25 vol% MXene dispersions with a) 0 M, b) 0.01 M, c) 0.05 M, d) 0.1 M, e) 0.5 M NaCl. Scale bar represents 20 μm. 109

Figure 5.14. Optical microscopy for 0.25 vol% at a) 0 M, b) 0.01 M, c) 0.05 M, d) 0.1 M, and e) 0.5 M NaCl. All images are with 60X/1.40 NA with 2x magnification under partially crossed configurations with 0° and 90° stage rotations. Scale bar is 5 μm. 110

Figure 5.15. SEM of 0.25 vol%/0.5 M at a) low and b,c) high magnifications. Images indicate presence of both b) small and c) large structures form in the dispersion at high salt content.....111

Figure 5.16. Polarized optical microscopy images of MXene dispersion concentration of 0.40 vol% with a) 0 M, b) 0.05 M, and c) 0.1 M under crossed (top) and uncrossed (bottom) configurations. 112

Figure 5.17. Polarized optical microscopy images of MXene dispersion concentration of 0.40 vol% with a) 0 M, b) 0.01 M, c) 0.05 M, and d) 0.1 M NaCl under partially crossed configurations with 0° and 90° stage rotations. Scale bar is 5 μm. 112

Figure 5.18. Optical microscopy under uncrossed configuration for 0.50 vol% at a) 0 M, b) 0.1 M, and c) 0.5 M consisting of areas with dense (left) and loosely connected (right) particles. Scale bar is 10 μm. 114

Figure 5.19. Optical microscopy under partially crossed configuration for 0.50 vol% at a) 0 M, b) 0.1 M, and c) 0.5 M consisting of areas with dense (left) and loosely connected (right) particles. Scale bar is 10 μm. 115

Figure 5.20. Optical microscopy for 0.50 vol% at a) 0 M, b) 0.1 M, and c) 0.5 M. All images are with 60X/1.40 NA with 2x magnification under partially crossed configurations with 0° and 90° stage rotations. Scale bar is 10 μm. 116

Figure 5.21. Optical microscopy at low magnification of 40X with partially crossed (left) and uncrossed (right) images for a) 0.25 vol%/0 M, b) 0.50 vol%/0 M, c) 0.25 vol%/0.1 M and d) 0.50 vol%/0.1 M. Scale bar is 10 μm. 117

Figure 5.22. Uncrossed (left) and partially crossed (middle and right) polarized optical microscopy images with stage rotations for 1.0 vol% with a) 0 M and b) 0.1 M NaCl. .118

Figure 5.23. Viscosity versus shear rate of flake concentrations 0.050, 0.10, 0.25, and 0.40 vol% with a) 0 M, b) 0.05 M, and 0.10 M NaCl. Error bars are from at least three measurements showing minimum and maximum values. 123

Figure 5.24. Viscosity versus stress of MXene flake concentrations 0.05, 0.10, and 0.25 vol% with 0, 0.05, and 0.1 M NaCl. 124

Figure 5.25. Steady shear viscosity measurements of 0.15 vol%/0.1 M dispersion with a) flow curve with Herschel-Bulkley models and b) yield stress. 125

Figure 5.26. Flow behavior of MXene flake concentration 0.25 vol% with 0, 0.01, 0.05, 0.1, and 0.3 M NaCl. Viscosity as a function of a) shear rate with Herschel-Bulkley models (curves) and b) shear stress. 127

Figure 5.27. Oscillatory transients at constant shear rate of 0.01 s^{-1}. 128

Figure 5.28. Overlay of flow curves comparing 0.40, 0.50, and 1.0 vol% with varying salt concentrations. 130

Figure 5.29. Yield stresses of a) 0.40 vol% and b) 0.50 and 1.0 vol% with varying salt concentrations. 131

Figure 5.30. Plots of a) viscosity and b) yield stress versus MXene concentration comparing 0 and 0.1 M results. Note: Lines are drawn between symbols for ease of visualizing. ...133

Figure 5.31. Oscillatory sweep for 0.25 vol%/0.1 M as a function of a) strain and b) stress. 135

Figure 5.32. Frequency sweep with storage modulus G’ and loss modulus G” of 0.15 vol%/0.1 M dispersion. 136

Figure 5.33. SAOS rheology with a) storage modulus G', b) loss modulus G", and c) tan δ versus angular frequency for 0.25 vol% with 0 M (black diamonds), 0.01 M (gray circles), 0.05 M (blue squares), 0.1 M (red triangles), and 0.3 M (green left-pointing triangles).138

Figure 5.34. Examples of the Cox-Merz rule not obeyed for a) 0.25 vol% with 0 M (black) and b) 0.25 vol% with 0.01 M (black) and 0.1 M (blue). Solid symbols are steady shear viscosity η and open symbols are complex viscosity η*.....140

Figure 5.35. Oscillatory rheology with a) G', b) G", and c) tan δ for flake concentration of 0.40 vol% with 0 M (black squares), 0.05 M (red circles), 0.1 M (blue triangles). 143

Figure 5.36. Storage G' (closed symbols) and loss G" (open symbols) moduli of 0.50 vol% with 0, 0.1, and 0.5 M NaCl.....145

Figure 5.37. a) Oscillatory response of tan δ for 0.50 vol% with 0, 0.1, and 0.5 M NaCl. b) Comparison of steady shear η (solid symbols) and complex viscosities η* (open symbols) for 0.50 vol% with 0 and 0.1 M. 145

Figure 5.38. Oscillatory response showing storage and loss moduli with 0.1 M NaCl of a) 0.50, 0.70, and 0.80 vol% flake concentration. b) Comparison of 1.0 vol% with 0 and 0.1 M NaCl.....147

Figure 5.39. Edge fracture of a 1.0 vol%/0.1 M dispersion (left) and large-sized clumps of particles (right). Arrows indicate the MXene/NaCl dispersion. 148

Figure 5.40. a) Total interaction energy as a function of interparticle distance for the ionic strengths 0.01, 0.05, 0.1, and 0.5 M NaCl (legend applies to entire figure). b-d) Closer look at the secondary minima. The dashed line is drawn for reference at net zero interaction energy.....150

Figure 5.41. Proposed phase diagram of MXene/NaCl system. I – isotropic, N – nematic, I + N – biphasic, G – gel, F – flocculation. 153

Figure A.1. EIS after 1 (closed squares) and 1000 (open squares) CV cycles performed at 20 mV/s. 174

Figure A.2. Cross polarized optical microscopy of 0.15 vol%/0.1 M with stage rotations of the magnified portion of the box. The representative uncrossed image is also shown (bottom left). Scale bar is 5 μm. 175

Figure A.3. MXene dispersions of crossed (top) and uncrossed (bottom) polarized optical microscopy images comparing 0.50 vol%/0.1 M, 0.70 vol%/0.1 M, and 0.80 vol%/0.1 NaCl. Scale bars represent 5 μm. 176

Figure A.4. Sample rotations of 0.80 vol%/0.1 M NaCl dispersion of the square region in top left. Bottom left image indicates the same area with uncrossed configuration. 177

List of Abbreviations

0D	Zero-dimensional
1D	One-dimensional
2D	Two-dimensional
3D	Three-dimensional
AFM	Atomic Force Microscopy
AM	Additive Manufacturing
ATR	Attenuated Total Reflection
B	Biphasic
C	Columnar
CB	Carbon Black
CNF	Cellulose Nanofibers
CNT	Carbon nanotubes
CV	Cyclic Voltammetry
DI	Deionized Water
DIW	Direct Ink Writing

DLS Dynamic Light Scattering

DLVO Derjaguin Landau Verwey Overbeek

EDL Electrical Double Layer

EDLC Electrochemical Double Layer Capacitance

EIS Electrochemical Impedance Spectroscopy

F Flocculation

FE-SEM Field Emission-Scanning Electron Microscope

FTIR Fourier Transform Infrared Spectroscopy

G Gel

GO Graphene Oxide

GS Graphene Sponge

I Isotropic

IG Isotropic Gel

IL Isotropic Liquid

IPA Isopropyl Alcohol

LC Liquid Crystal

MILD Mild Intensive Layer Delamination

MMT Montmorillonite

MSC Micro-supercapacitor

MWNT Multiwalled nanotubes

N Nematic

NL Nematic Liquid

NG Nematic Gel

NW Nanowire

OHP Outer Helmholtz Plane

OMMT Organically modified montmorillonite

PG Pristine Graphene

PPTA P-Polyphenylene Terephthalamide

P-RGO Partially Reduced Graphene Oxide

PTFE Polytetrafluoroethylene

RGO Reduced Graphene Oxide

SAOS Small Amplitude Oscillatory Shear

SAP Superabsorbent Polymer

SEM Scanning Electron Microscopy

SO Silicon Oxide

SWNT Single Walled Carbon Nanotubes

SAXS Small Angle X-ray Scattering

TA Thermal Analysis

TEM Transmission Electron Microscopy

TGA Thermogravimetric Analysis

UV-vis Ultraviolet-Visible

vdW van der Waals

XRD X-ray Diffraction

Chapter 1 Introduction

The objective of this research was to understand the effects of additional components on the microstructures of dispersions and electrochemical properties of two-dimensional (2D) nanomaterials. In this work, two separate systems were explored: 1) graphene/manganese oxide hybrid electrodes and 2) aqueous MXene/sodium chloride dispersions.

Exploring the fundamentals of nanomaterial behavior enables development of systems and devices with new properties for novel applications. The synthesis controls the nanoscale structures which has led to many advances in the fields of colloid science, medicine, transportation, agriculture, and energy storage.[1] Many efforts have focused on minimizing costs and resources as well as finding new methods for efficient energy conversion, energy storage, filtration, and computing.[1] However, the drive to overcome key challenges between materials and dispersions is necessary for nanotechnology to fulfill its potential for economical and sustainable production. To date, a diverse range of inorganic, organic, and hybrid (multicomponent) nanomaterials are available and being developed for commercial applications such as insulation, microelectronics, coatings, inks, and packaging. When nanomaterials are dispersed in solvents, characteristics such as size, shape, and specific surface area significantly affect interactions at, or near, their interfaces and produce different dispersion microstructures. Many nanomaterials tend to aggregate into larger, often disordered, structures; therefore, understanding dispersion state at every step is critical for nanomaterial processing to achieve desired properties. Colloid science provides a framework for these understanding structure-processing-property relationships

but cannot yet fully predict the properties of dispersions or the solid assemblies they are used to produce. The approach in this dissertation was to increase the understanding of two fascinating 2D systems: ultra-large reduced graphene oxide/manganese oxide hybrids and MXenes by viewing their behavior in terms of a colloidal framework.

Among the advances in nanotechnology, low dimensional materials, such as 2D nanomaterials, have attracted attention in the past decade for development of energy storage devices with higher charge storage capabilities. Carbon-based nanomaterials, including single-walled carbon nanotubes (SWNTs),[2-4] activated carbon,[5, 6] reduced graphene oxide (RGO),[7-11] and titanium carbide ($Ti_3C_2T_x$),[12-15] possess exceptional electrical, mechanical, thermal, and optical properties enabling their applications in flexible electronics, catalysts, actuators, deionization, and capacitors. Supercapacitors offer advantages over traditional electrical double-layer capacitors (EDLCs) and batteries due to their higher power densities. 2D materials have high surface area-to-volume ratio enabling more surface interactions with active sites. The exfoliation or synthesis of 2D materials can involve intercalation and exfoliation, among other processes, producing structures that can be easily functionalized and enhance ion and electron diffusion. However, fundamental understanding of the thermodynamic interactions governing the dispersion phase behavior is lacking. For dispersions of charged nanomaterials, such as graphene and MXenes, the surface potential, Debye screening length, polydispersity, aspect ratio (length/diameter), and viscosity influence or characterize the thermodynamic interactions in the dispersions. Therefore, understanding these interactions provides a basis for fluid-phase processing and fabrication into electrochemical devices. In this research, investigating these effects made advances in developing the framework for graphene and MXenes.

Graphene is a single-layer sheet of graphite with a honeycomb carbon lattice structure that exhibits unique electrical, optical, and mechanical properties. These properties have led to its use in applications such as transparent conductive films, sensors, rechargeable lithium ion batteries, and electrochemical double layer capacitors.[16,17] Its high accessible surface area allows graphene to be modified or functionalized in many ways. Graphene oxide (GO) is produced by exfoliation and oxidation of graphite to separate the graphene layers and introduce oxygen functional groups results in GO with monolayer to few-layer sheets. In the first part of this research, ultra-large GO sheets, an order of magnitude larger in aspect ratio than smaller GO sheets (approximately 40,000 compared to 2,000), was of interest due to their large accessible surface area and ease of ordering in the fluid phase. Larger sheets are more prone to wrinkling, crumpling, and restacking. To reduce these effects, additional components can be added to 2D materials, such as metal oxides, polymers, or other carbon materials. The inclusion of 1D transition metal oxides, particularly manganese dioxide (MnO_2) nanowires, as guest materials to form a sandwich structure with 2D ultra-large RGO sheets called hybrids was explored. MnO_2 nanowires were chosen due to the low cost of reagents and abundance of manganese in earth's crust, ease of synthesis in a double-solvent system without use of any acids, and short synthesis time. The MnO_2 crystal structure consists of MnO_6 octahedron units that connect to produce different crystallographic forms resulting in distinctive morphologies. α-MnO_2 with wire-like morphology was favored for this work due to its unidirectional growth and demonstrating the highest aspect ratio of approximately 50 as opposed to needle-, rod-, or spindle-like forms[18] with aspect ratios of 2-10. Coupling small GO sheets with MnO_2 nanowires had previously shown enhanced cycling behavior and capacity as electrodes

tested in lithium ion cells.[19] Therefore, the aim of this part of the research was to understand the effects of combining different geometries with orders of magnitude different aspect ratios on the electrochemical properties.

MXenes are an emerging class of 2D transition metal carbides and nitrides with a general formula of $M_{n+1}X_nT_X$ (n = 1, 2, or 3), where M is a transition metal (Ti, Cr, V, etc.), X is carbon and/or nitrogen, and T_X is surface functional groups (O, OH, and F) randomly distributed on the surface of the 2D flakes.[20-23] For example, titanium carbide $Ti_3C_2T_x$ is produced from Ti_3AlC_2 and is most commonly studied due to its promising properties that have found applications in catalysis, coatings, energy storage, and thin films.[24-26] The combination of high electrical conductivity, outstanding electrochemical properties, and hydrophilicity makes $Ti_3C_2T_x$ an attractive material for 3D printing of micro-supercapacitors (MSCs).[20] Direct ink writing (DIW) is an extrusion-based additive manufacturing method that has been extensively used for the fabrication of complex structures used in various fields, including energy storage.[27-30] In this research, rheology, or the study of dispersion flow behavior, was used to gain insights into dispersion microstructure. Several rheological properties are desired to achieve 3D printed hierarchical architectures. These include larger elastic modulus G' than viscous modulus G" for shape retention and interlayer adhesion and G' independent of frequency for percolated network formation.[31] In addition, yield stress and shear thinning behavior are necessary to retain print resolution and facilitate flow through a nozzle.[29, 31, 32] While few reports explored the dispersion microstructure of MXene dispersions, little is known about the complex interactions. Therefore, the goal of the second part of this research was to understand the rheological properties of MXene dispersions with 1) a high concentration

of unfractionated flakes which enabled choosing design parameters for printability and 2) varying concentrations of large flakes in sodium chloride (NaCl) solutions which provided insights into the dispersion phase behavior also studied.

In summary, results from this dissertation contribute to understanding the effects of flake size, concentration, and component addition on phase behavior, rheology, and electrochemical properties of graphene and MXene dispersions that provide insight into structure-processing-property relationships. Chapter 2 discusses a literature review consisting of 1D and 2D nanomaterials, fundamentals of self-assembly and charged systems, phase behavior and rheology. Chapter 3 provides detailed information regarding syntheses, characterization, electrodes, and dispersion microstructure methods. Chapter 4 explores the RGO/MnO_2 hybrid electrodes research with insights into microstructure effects of combining 2D/1D geometries. Chapter 5 explores the phase behavior and rheology of MXene dispersions, where the first section investigates the rheology behavior of a highly concentrated MXene ink composed of small flakes (~0.3 μm) to understand dispersion quality for printing hierarchical structures followed by a second section that investigates tuning the MXene dispersion behavior by varying size to produce large flakes (~3 μm) and adding NaCl as a rheological modifier. Finally, conclusions from this research are summarized in Chapter 6.

Chapter 2 Background

2.1 Carbon Structures

The versatility of carbon structures results from the common sp^2 and sp^3 bonding configurations producing structures such as fullerenes, carbon nanotubes, graphene, and graphite as shown in Figure 2.1a.[33] In the sp^3 configuration, such as diamond, carbon atoms are covalently bonded to four neighboring carbon atoms forming a tetrahedral structure (Figure 2.1b).[34, 35] Graphite consists of a three-dimensional (3D) structure with nanoscale layers composed of intact aromatic carbons that form the two-dimensional (2D) structure called graphene. Graphite consists of sp^2 hybridized carbons, where three of the four valence electrons are covalently bonded with neighboring carbon atoms and the fourth electron forms a π bond perpendicular to each plane (Figure 2.1b). The graphene layers are attracted to each other by weak van der Waals forces. The graphene structure consists of single-layer atoms arranged in hexagonal honeycomb lattices. Rolling the sheets of graphene into cylinders forms carbon nanotubes (CNTs), a one-dimensional (1D) structure. The chirality of CNTs depends on the atomic arrangement in graphene and has a significant effect on the electronic properties. Nanotubes exist as single-walled carbon nanotubes (SWNT) or multi-walled carbon nanotubes (MWNT) composed of concentric SWNT. Fullerenes, or buckyballs, consist of carbon atoms linked to three other carbon atoms by covalent bonds. The carbon atoms are connected in a pattern of hexagons and pentagons forming a zero-dimensional (0D), or spherical structure. One of the most common buckyballs is C60, which contains 60 carbon atoms.

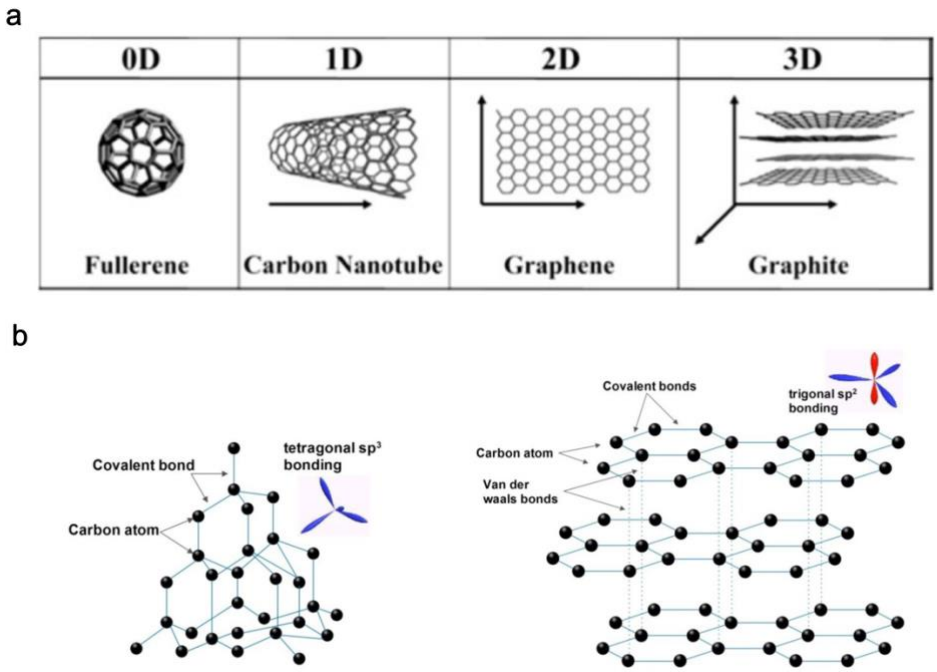

Figure 2.1. a) Illustration of carbon structures[33] and b) bond configurations of diamond (left) and graphite (right).[34, 35]

Graphene's exceptional properties as a carbon-based nanomaterial include high theoretical specific surface area (2630 m^2/g), Young's modulus (1 TPa), electrical conductivity (10^4–10^5 S/m), thermal conductivity (~3000 W/(m K)), intrinsic phonon mobility, and up to 98% optical transmittance.[36, 37] These properties have led to the use of graphene in applications such as transparent conductive films, sensors, rechargeable lithium ion batteries, and electrochemical double layer capacitors (EDLCs).[38-40] The robust and flexible nature of graphene enable it to be modified or functionalized in many ways to change its electronic structure and yield different surface properties.[41, 42] The intercalation of acids through the graphite structure followed by exfoliation with sonication produces solution-based graphene oxide (GO).[43] GO results in predominantly monolayer nanosheets

with oxygen functionality including carboxylic acid groups primarily around the edges and hydroxyl and epoxy groups along the basal planes as shown in Figure 2.2.[44] The surface groups of GO enable its solubility in water and polar solvents that provide advantages in producing multicomponent functional materials.

These groups can be removed by chemical, electrochemical, or thermal reduction methods that form reduced graphene oxide (RGO). The carbon skeleton of RGO becomes disrupted with defects introduced and some restoration of the sp^2 hybridized structure of graphite. The defects may occur due to the GO sheets restacking, or aggregating, from strong π –π interactions which leads to variable pore size distributions. In addition, the sheets are susceptible to wrinkling, rippling, and crumpling and produce low accessible surface areas that limit their practical usage.[41] Therefore, the structure of RGO is not pristine like graphite. However, producing graphene with fewer corrugations and preventing sheet aggregation is required to achieve control of the structure patterns, sizes, and shapes for improving applications in electronics, composites, microelectromechanical systems, and device fabrication.[45, 46] Commonly used methods to suppress sheet restacking include introducing spacers between the graphene sheets, such as carbon materials, metal oxides, or conductive polymers as well as constructing a macroporous 3D structure.[10, 47-52] For example, inserting CNT between graphene sheets through a modified exfoliation approach resulted in improved electrical conductivity and higher accessible surface area enabling higher electrosorption of ions onto the electrodes for capacitive deionization than graphene alone. In another report, addition of polystyrene to graphene produced similar conductivities to SWNT-filled polystyrene composites; however, the higher surface-to-

volume ratio of graphene makes it more favorable for surface modifications and resulting properties.[48]

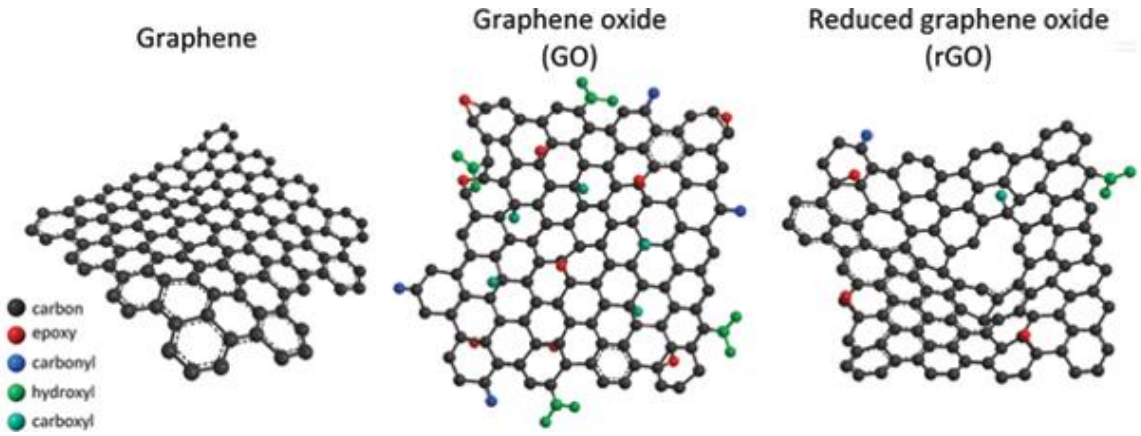

Figure 2.2. Chemical structures of graphene, graphene oxide, and reduced graphene oxide.[44]

2.2 Manganese Oxide

Manganese oxide (MnO_2) is a transition metal oxide that demonstrates an octahedron crystal structure connected to form a tunneled configuration. The synthesis of MnO_2 can be controlled to achieve nanostructures with desired properties. Nucleation and then crystal growth of the 1D morphology 1) along only the (001) direction (unidirectional growth) produces rod- and needle-like morphologies and 2) along the (001) direction and other directions in the octahedral plane produce spindle-like morphologies as shown in Figure 2.3.[18] The presence of more water for the potassium permanganate ($KMnO_4$) solution in the synthesis (higher than 1:10 ratio of water/isopropanol) results in the spindle-like shapes due to the lack of coordination between solvents that hinders crystal growth of the intermediate species. In contrast, adjusting the injection time to drop-wise instead of

very fast results in rod-like shapes due to the stacking behavior of nuclei during the growth process.[18, 53]

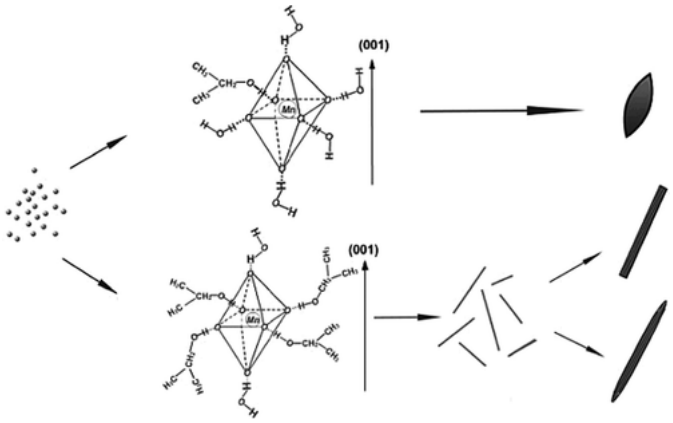

Figure 2.3. Shape-controlled synthesis of MnO_2 to yield the shapes at the right of the schematic spindle- (top), rod- (middle), and needle-like (bottom) morphologies.[18]

Manganese oxide has been studied for various applications including catalysts, absorbents, biosensors, and cathodes for alkaline batteries.[49] MnO_2 exhibits a pseudocapacitive behavior, in contrast to graphene, which exhibits EDLC. Pseudocapacitance is defined as a charge storage mechanism where Faradaic redox reactions with charge-transfer occur on the surface or by intercalation to store charge electrochemically. A significant advantage of MnO_2-based electrodes is their ability to operate in neutral electrolytes, which is a promising characteristic for large-scale applications.[54] In addition, transition metal oxides are useful for preventing re-stacking of multi-layer materials as well as allowing for intercalation of ionic species.

2.3 GO/MnO_2 Systems

GO has been explored in several multicomponent systems including various polymer composites, metal oxides, and other 1D materials.[10, 11, 32] Mixed nanostructures with different sizes and shapes have been the topic of several studies.[55-61] The self-assembly of GO/MnO_2 has been studied with droplet drying and observing nanowire alignment near the surface with optical microscopy imaging at different drying times.[55] Increasing GO concentration in GO/MnO_2 dispersions resulted in orientational ordering to form a continuous film with self-aligned nanowires. Figure 2.4 also shows the interactions between the GO sheets and MnO_2 nanowires indicative of how the sheets adsorb onto the nanowires and alter the surface properties.[55]

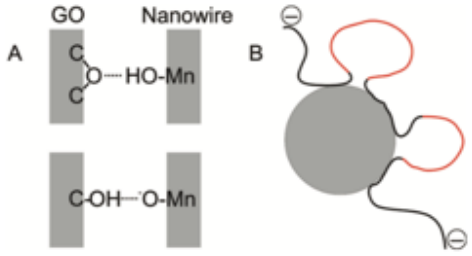

Figure 2.4. Schematic of the interactions between GO sheets and nanowires, including hydrogen bonding and ion-dipole interactions.[55]

Another study of a reduced graphene oxide and manganese oxide (RGO/MnO_2) system tested the influence of nanowire length on the resulting electrode morphology and electrochemical behavior as shown in Figure 2.5.[19] The short nanowires (<500 nm) were at least an order of magnitude smaller than the longer nanowires (>5 μm); both structures maintained a 3D network with channels allowing intercalation of electrolyte species.

RGO/MnO_2 with long nanowires resulted in formation of a continuous path throughout the structure and conformed onto the sheets, whereas the shorter nanowires had needle-like morphology.[19]

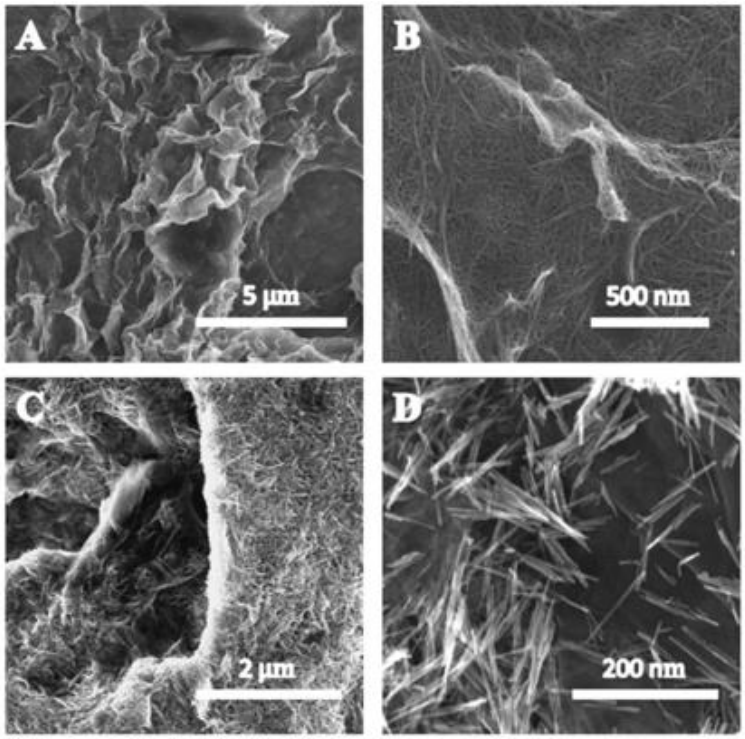

Figure 2.5. Variation of nanowire length on morphology by SEM of GO/MnO_2 system (a) large and (c) small nanowires with (b) and (d) higher magnifications of (a) and (c), respectively.[19]

Xu *et al* reported a novel synthesis of a graphene sponge (GS) for capacitive deionization by freeze-drying a 4 mg/mL dispersion and then thermally annealing to remove oxygen functionality.[62] Figure 2.6 shows corresponding cyclic voltammetry (CV) and electrochemical impedance spectroscopy (EIS) Nyquist plots for comparing GS with a pristine graphene (PG) sample. The specific capacitance of the GS was 205.20 F/g, which

was higher than that of PG (117.31 F/g), and the charge-transfer resistance found from the diameter of the semi-circle at high frequencies is 0.27 Ω for GS and 1.12 Ω for PG which is indicative of the GS having a higher electrical conductivity.

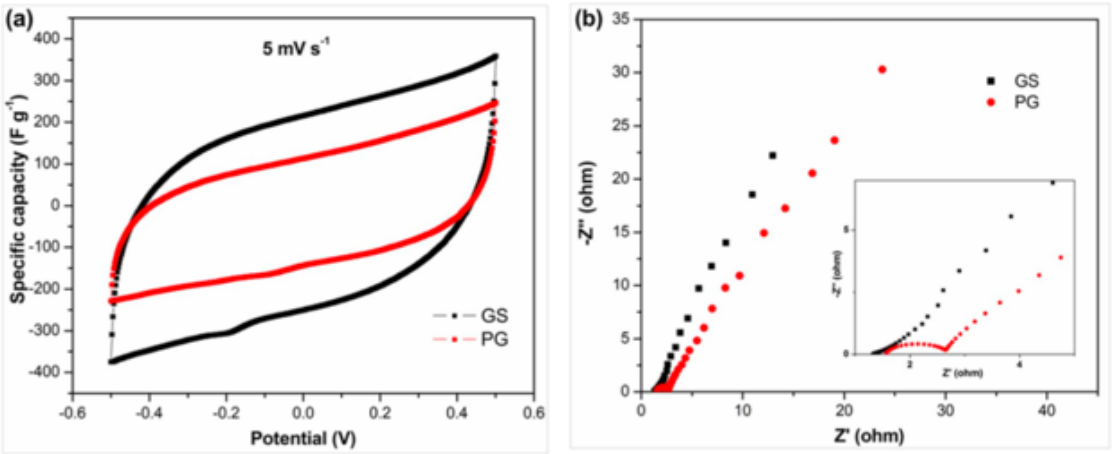

Figure 2.6. (a) CV and (b) EIS Nyquist plots of a GO dispersion freeze-dried into an aerogel or sponge (GS) and then thermally annealed compared with pristine graphene (PG), both in 1M NaCl electrolyte.[62]

2.4 Liquid Crystal Phase Behavior

2.4.1 Overview

Liquid crystals (LCs) are mesophases that exhibit the fluidity of a liquid and order of a solid. These phases consist of mesogens, molecules or particles that possess rigidity and shape anisotropy. From their discovery in 1888 through the mid 1950's, advancements in liquid crystals and colloid science were made through optical microscopy investigations and theoretical approaches. LCs consist of ordered structures and preserving the anisotropic character through processing can be used to produce macroscale aligned structures. Additional advantages of liquid crystals include their viscoelastic properties,

and tunability which enable their processing into coatings, fibers, medical imaging devices, and electronic displays.[63]

2.4.2 Types of Liquid Crystals

Two types of liquid crystals exist: thermotropic that exhibit phase transitions with changes in temperature and lyotropic that exhibit phase transition with changes in dispersion concentration. In 1920, Friedel categorized liquid crystals based on molecular arrangements of rod-like molecules that can form nematic, cholesteric, and smectic phases with anisotropic character of optical, mechanical, and magnetic properties as shown in Figure 2.7.[64]

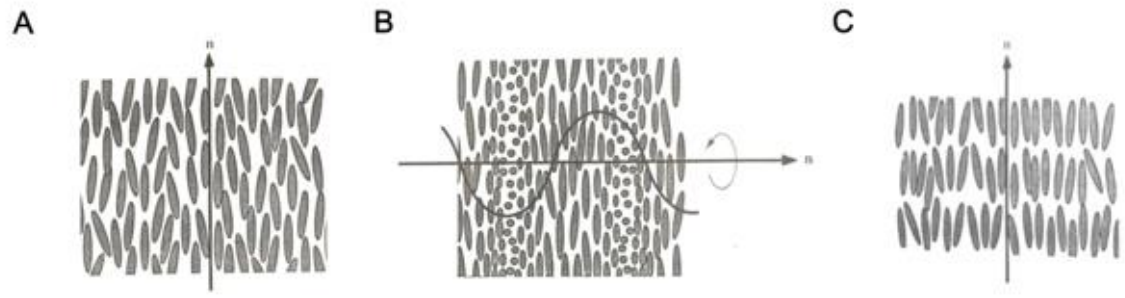

Figure 2.7. Classes of Friedelian liquid crystals a) nematic, b) cholesteric, and c) smectic.[64]

In a liquid crystal, the preferred direction, a vector, towards which the mesogens locally orient is called the director, *n*. In the nematic mesophase, no long-range ordering of the positions of the mesogens exists but they have a preferred orientation. In the cholesteric mesophase, also known as chiral nematic, no long-range positional ordering is present, but they have a preferred direction that is oriented perpendicular to the director plane and varies along a helical axis. Smectic mesophases are the most ordered liquid crystals that are

arranged in well-defined layers. The degree of alignment is quantified by the order parameter *S:*[64]

$$S = \left\langle \frac{3\cos^2\theta - 1}{2} \right\rangle \quad (1)$$

where θ is the angle between the rod-like molecule with respect to the director and the brackets identify the spatial average of molecules. The order parameter for completely isotropic or random molecules is $S = 0$ and for perfectly aligned molecules, $S = 1$. Both smectic and columnar phases demonstrate long-range orientational ordering; however, their positional ordering differs. The smectic phase consists of layers of particles arranged in a one-dimensional array, while the columnar phase consists of stacks of particles arranged in a two-dimensional lattice of columns. For example, the fairly monodisperse system of semiflexible, charged *fd* virus exhibits a cholesteric phase at low rod concentration in Tris buffer solution and smectic phase at higher rod concentrations, while similarly DNA can form columnar and cholesteric phases.[65, 66]

2.4.3 Fundamental Theory

To date, two widely used theories have been used to describe the phase behavior, or thermodynamics of rodlike liquid crystals: Onsager[67] and Flory.[68] In 1949, Onsager's theory predicted that the phase behavior is entropy-driven. Phase behavior of dispersions of rodlike 1D and 2D mesogens is based on excluded volume interactions. The phase changes occur due to the balance of rotational and translational entropy. The rods can arrange in the fluid to maximize excluded volume when they are oriented at 90° and minimize them at 0°. Therefore, the rods have minimum excluded volume with a parallel

arrangement resulting in a gain in translational entropy compensated by the loss in rotational entropy.[64, 69]

Concentration ν (rod fraction) for phase transitions is a function of the aspect ratio *L*/*D*, where *L* is the length and *d* is the diameter of the rod. Dilute concentrations exhibit Brownian, or thermally induced, motion and results in their random movement by rotation and translation. The maximum dilute concentration can be approximated as $\nu < 1/L^3$. Increasing concentration to a semi-dilute regime, rotation becomes inhibited for concentrations from $1/DL^3 < \nu < 1/DL^2$.[70] At higher concentrations, rods are then prohibited from rotating and translating in the isotropic concentrated phase. Further increasing concentration above the percolation threshold where network formation occurs results in a biphasic region at a critical concentration ϕ_I. The biphasic region consists of an isotropic concentrated phase and a LC phase at equilibrium. Then the system becomes fully liquid crystalline when the concentration is further raised to a critical concentration denoted as ϕ_{LC}. Figure 2.8 illustrates these phase transitions.

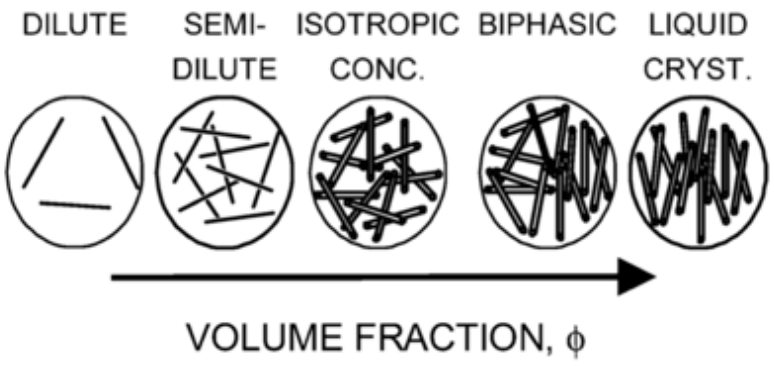

Figure 2.8. Phase behavior of rigid rods with increasing concentration.[70]

Onsager's theory predicts phase transitions with statistical thermodynamics where a virial expansion is truncated to the second term virial coefficient.[67] According to Onsager's theory for dispersions of monodisperse rods that are long and rigid (L>>D) and interact only through hard-rod interactions, the volume fractions ϕ of the phase transitions are

$$\phi_I = \frac{3.34}{L/D} \tag{2}$$

$$\phi_{LC} = \frac{4.49}{L/D} \tag{3}$$

where ϕ_I is the isotropic-biphasic transition, ϕ_{LC} is the biphasic to liquid crystal ϕ_{LC}, L is the length, and D is diameter.

The assumptions of Onsager's original theory exclude the effects of electrostatic interactions, steric hindrance, solute-solvent interactions, sedimentation, and polydispersity. This causes a discrepancy between experimental results and theoretical transition calculations. Khokhlov and Semenov extended Onsager's theory to include the effects of finite rod flexibility, which shifts the isotropic–nematic phase transition to higher densities, reduces the width of the isotropic–nematic coexistence, and lowers the order parameter of the coexisting nematic phase.[71] The concentration window between the critical concentrations ϕ_I and ϕ_{LC} depends on both the aspect ratio as well as solvent quality.[3] In addition, many advancements have been made since Onsager's seminal work to include attractive interactions as well as account for polydispersity. An example is the works of Green *et al* for carbon nanotubes.[72]

The other foundational theory is Flory's 1956 theory. This theory was based on a lattice model to describe rod location.[73] Flory's theory results in different quantitative values for phase transitions from the less to more ordered states and is compatible with lower aspect ratio systems. Then, from 1960's to 1970's, progress in nanotechnology led to forming lyotropic liquid crystalline polymers such as p-polyphenylene terephthalamide (PPTA) in sulfuric acid with applications in aligned fibers. Flory's theory was most compatible for semiflexible liquid crystalline polymers and widely used for almost 50 years.[74]

Since the 1990's, advancements in synthesizing new anisotropic nanomaterials produced a wide range of nanomesogen material sizes, densities, and surface chemistries. The liquid crystalline phase behavior is generally viewed in terms of modifications to Onsager theory. In turn, characterization of these materials' properties provides new opportunities for advancing knowledge of the effects of size, shape, sedimentation, and thermodynamic interactions on phase behavior.

2.4.4 Liquid Crystal Signatures

Optical and rheological characteristics are used to identify liquid crystalline phase behavior. Optical anisotropy is one of the fundamental properties of liquid crystals. Birefringence is an optical signature where the propagation of light as it travels through a medium depends on its orientation. Polarized optical microscopy is used to detect birefringence of anisotropic materials when light passes through crossed polarizers, or optical filters, as shown in Figure 2.9.[75] Linearly polarized light becomes elliptically polarized after passing through the material. Once the light ray reaches the analyzer, it has

a component that can pass through it depending on the phase shift. Ordinary and extraordinary rays are defined as light rays that pass along the optical axis (director) or deviate from the optical axis, respectively. The intensity of transmitted light passing through the material appears light or dark depending on the orientation (angle) of the analyzer with respect to the polarizer. Upon stage rotation, birefringence of the LC is determined as

$$\Delta n = n_e - n_o \tag{4}$$

where n_e and n_o are the refractive indices of the extraordinary and ordinary axes refractive indices of rodlike polymers.[76] The thickness of the material also affects the color patterns of liquid crystal textures observed with optical microscopy as shown in the Michel-Levy birefringence chart (Figure 2.10).[77]

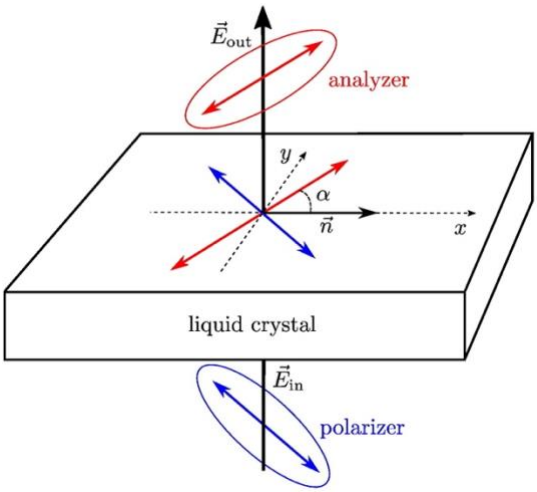

Figure 2.9. Birefringence of liquid crystals.[75]

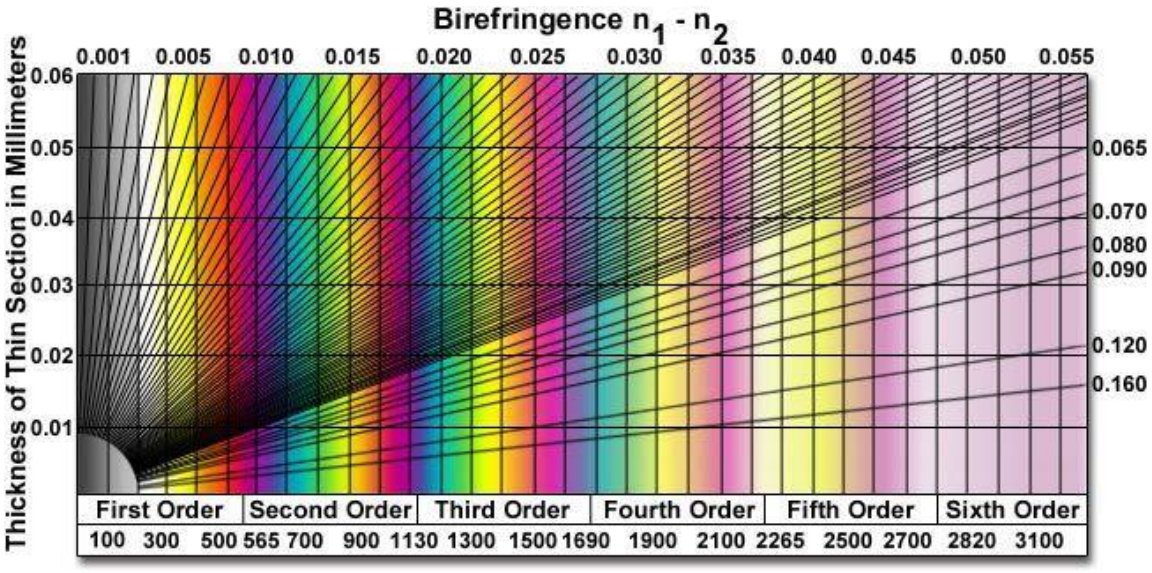

Figure 2.10. Michel-Levy birefringence chart displaying the relationship between liquid crystalline film thickness, birefringence, and interference order.[77]

Rheology is a powerful tool for detecting liquid crystalline phase behavior. The rheological signatures of lyotropic liquid crystals were mainly studied in rodlike polymers and are not found in all systems. The rheological signatures are summarized as follows:[78, 79]

◊ Three-region flow behavior from steady-shear viscosity curves

◊ Maximum and minimum on viscosity versus concentration curves

◊ Transient shearing tests result in shear stress and first normal stress difference (N_1) oscillating over ~100 shear units to reach steady-state

◊ Change in sign of N_1 from positive to negative and back to positive with increasing shear rate

◊ Cox-Merz rule is not obeyed

Three-region flow behavior was initially observed for liquid crystalline polymers and has been observed for many lyotropic LC dispersions.[79-82] Regions I and III indicate shear thinning behavior and region II indicates a Newtonian plateau as shown in the flow curve in Figure 2.11.[79] These regions are the result of changes in dispersion microstructure with shear. The competing interactions of molecular orientation at the boundary and shear field,[83] plastic deformations of piled domains,[84] and phase separation and shear history[85] affect the microstructure. Region I is typically attributed to tumbling behavior. The Newtonian plateau, or hesitation, is attributed to the log-rolling or wagging of the rodlike molecules in thermotropic LCs[86] and has been observed for SWNTs in superacids[2] as well as other systems.[79, 81] Shear thinning occurs at higher shear rates resulting in alignment of the director with the flow direction.[69]

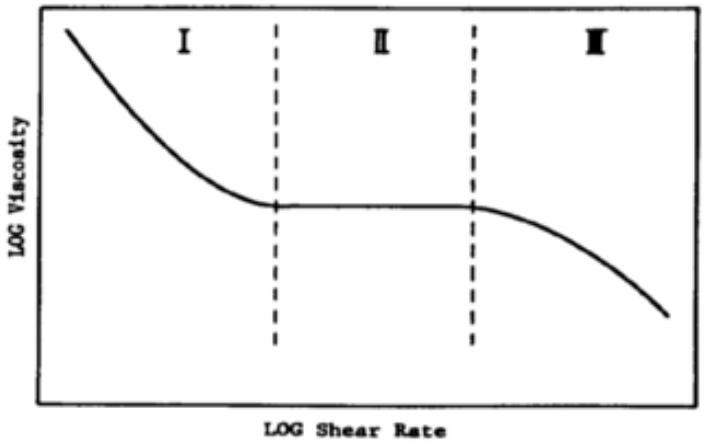

Figure 2.11. Three-region flow behavior from shear thinning (region I) to Newtonian plateau (region II) to shear thinning (region III).[79]

A minimum and maximum on the viscosity as a function of concentration plot have been observed for graphene oxide dispersions as shown in Figure 2.12 among other

dispersions.[87] The viscosity values are reported at three different shear rates illustrating a non-monotonic trend in behavior. Initially, viscosity increases with concentration due to the limited rotational and translational motion of the particles. At the onset of the biphasic regime, the majority of the system is still isotropic so viscosity still increases with concentration. However, once the fraction of liquid crystal phase exceeds that of the isotropic phase, viscosity decreases with concentration because the aligned phase provides less resistance to flow. A local minimum occurs as the transition to a fully liquid crystalline phase, owing to the gain in translational entropy compensated by the loss in rotational entropy. However, not all LC dispersions exhibit all of the signatures for LC behavior. Sulfated cellulose nanocrystals dispersed in water are charged 1D materials that do not exhibit the non-monotonic trend which was attributed to the electroviscous effect.[88]

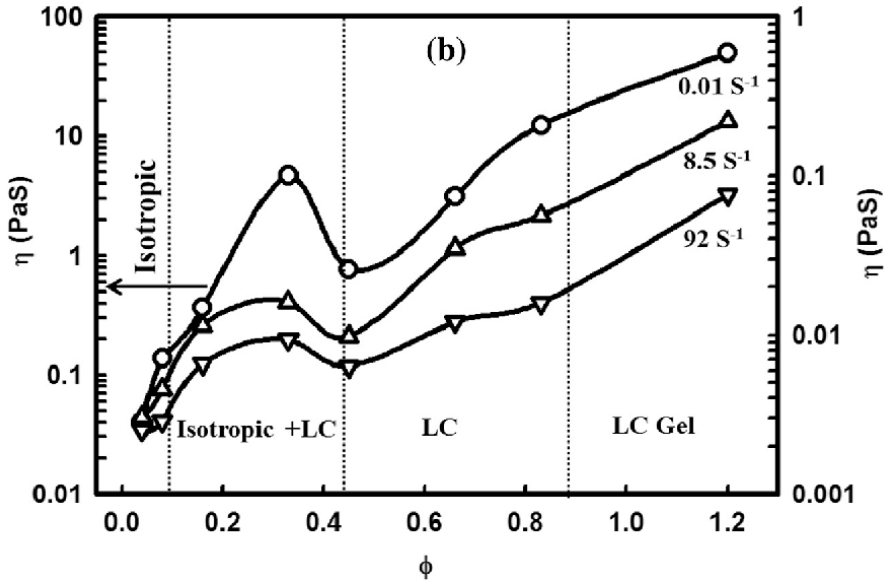

Figure 2.12. Viscosity as a function of volume fraction for graphene oxide.[87]

Normal stress differences are used to characterize the viscoelastic behavior of dispersions. The oscillating behavior of shear stress and first normal stress difference N1 dampen and reach steady state.[89, 90] This was illustrated with SWNTs in superacids (Figure 2.13).[2] The change of N1 from positive to negative and back to positive is typically found in lyotropic nematic liquid crystalline polymers. While the presence of negative N1 values is not well understood, it is believed to be the transition from tumbling to wagging of the particles.[91] In plate-like dispersions (Figure 2.14), LC ordering was found for organically-modified montmorillonite (OMMT) and GO both in silicon oil (SO) and not in Kaolin/SO. Montmorillonite and Kaolin are types of nanoclays. Interestingly, negative N1 values are shown for all three dispersions and is explained as the tumbling and rotating motions of the OMMT sheet. However, for GO/SO and Kaolin/SO dispersions exhibit aggregation and the negative N1 is attributed to the vorticity alignment of large GO clusters and Kaolin aggregates.[92]

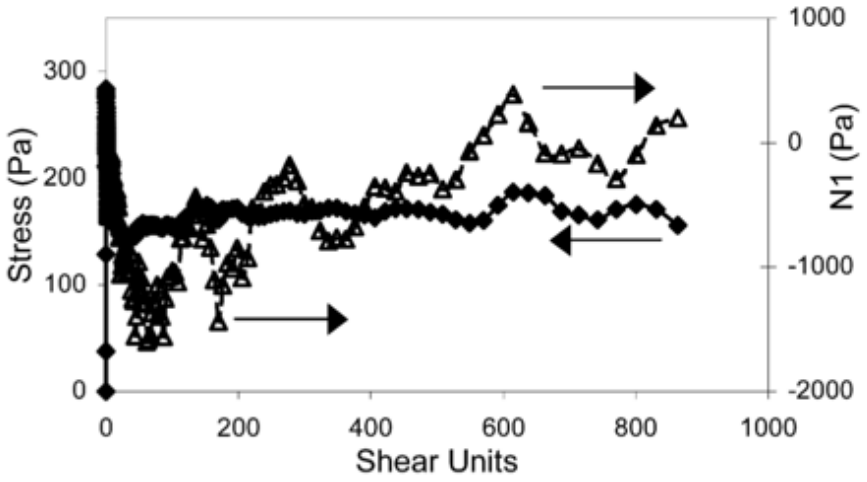

Figure 2.13. Oscillatory transients and first normal stress difference as a function of shear units (shear rate multiplied by time). Solid diamonds show shear stress and open triangles show N1.[2]

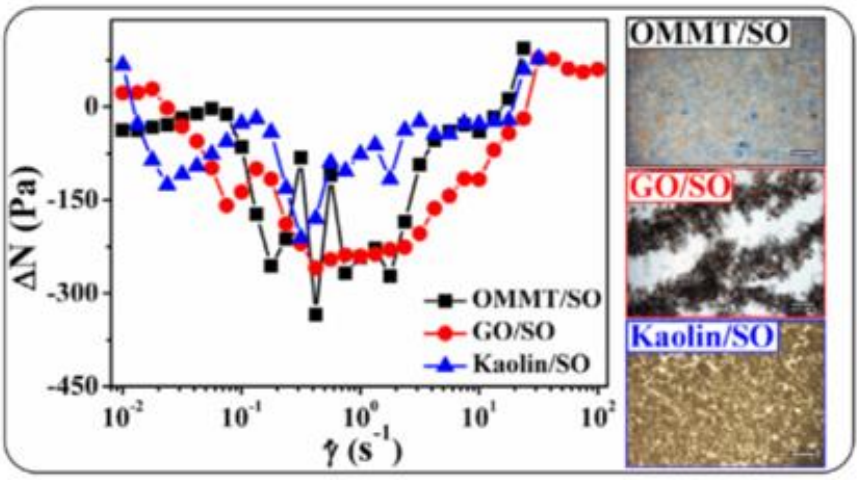

Figure 2.14. N1 as a function of shear rate for plate-like dispersions: organically-modified montmorillonite (OMMT), GO, and Kaolin, all in silicon oil (SO) with optical microscopy images on the right.[92]

The Cox-Merz rule states that the complex, or dynamic, viscosity (η*) and steady shear viscosity (η) are closely superimposable for equivalent values of shear and frequency.[90] This rule holds true for isotropic polymeric solutions and polymer melts, but not for liquid crystals or flocculated dispersions. An example of the application of the Cox-Merz rule not being obeyed is shown in Figure 2.15 for two graphene oxide dispersion concentrations.[93] This indicates that the GO sheets are interacting and the dynamic behavior cannot be interpreted from the steady shear behavior.[93]

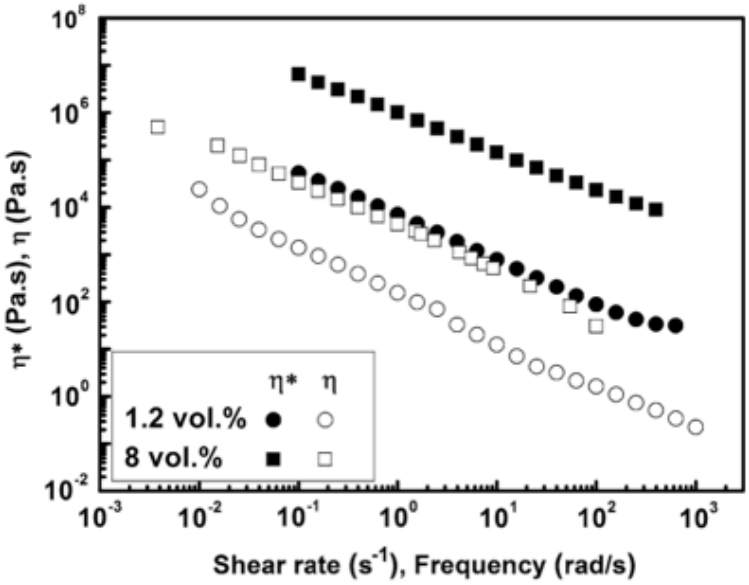

Figure 2.15. Comparison of complex viscosity (η*) and steady shear viscosity (η) of two different GO dispersion concentrations not obeying the Cox-Merz rule.[93]

2.5 Ultra-large GO

The structure and properties of GO dispersions depend on the interactions between the sheets. Excluded volume plays a role in entropy-driven alignment with increasing concentration (volume fraction). The excluded volume is the volume inaccessible to other particles as a result of repulsive forces between the particles. The repulsive forces of long-range interactions among the sheets that exhibit highly polar surfaces allows them to approach each other to a certain distance.[94] Larger GO sheets have about an order of magnitude higher aspect ratio than the smaller sheets. The larger sheet size consists of higher excluded volume than smaller sheets. As the concentration of sheets increases, the ultra-large sheets approach each other and orient in a parallel configuration due to

minimizing the Gibbs free energy of the system. This results in an increase in the translational, or positional, entropy and decrease of orientational, or rotational, entropy favoring nematic ordering. In contrast, increasing the concentration of small sheets does not result in packing of the nematic phase; rather the sheets remain in the isotropic phase. Jalili *et. al* proposed a model for liquid crystalline evolution in ultra-large and smaller GO sheets as shown in Figure 2.16.[94]

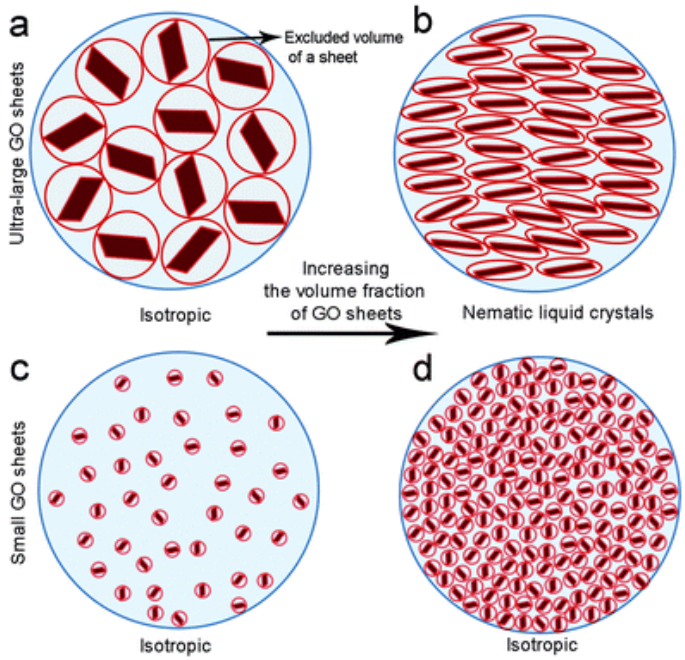

Figure 2.16. Proposed model for fluid-phase ordering of ultra-large GO sheets compared with small GO sheets.[94]

In addition, studies on varying ultra-large GO concentration by Naficy *et. al* provided insight into initial dispersion microstructure and rheological properties of the material. At a very low concentration of 0.05 mg/mL, GO sheets are free to rotate and translate in a random manner and exhibit a liquid-like response (G" dominant).[95] Increasing

concentration to 0.25 – 0.50 mg/mL (Figure 2.17b,c) results in nematic ordering with G' exceeding G" in the biphasic regime. This behavior was suggestive crowding of the sheets due to their extremely high aspect ratios and wrinkling behavior, which may indicate gelation of the system.[95] Figure 2.17d at 0.75 mg/mL concentration shows a fully nematic liquid crystalline phase with G'-G" crossover points at which solid-like behavior is shown at lower frequencies, liquid-like at intermediate, and solid-like at higher frequencies. In Figure 2.17e, G' remains constant at large time-scales (low frequencies). This is indicative of a jammed system as the curves also represent similar behavior in weak polymer gels or biological cells. Further increasing the concentrations results in more ordered packing of the sheets and distinct separation of G' and G" with G' having much higher values (Figure 2.17f-h).[95] These responses allow understanding of what concentrations are desirable for inkjet printing and suitable for various applications due to their ease of self-assembly.

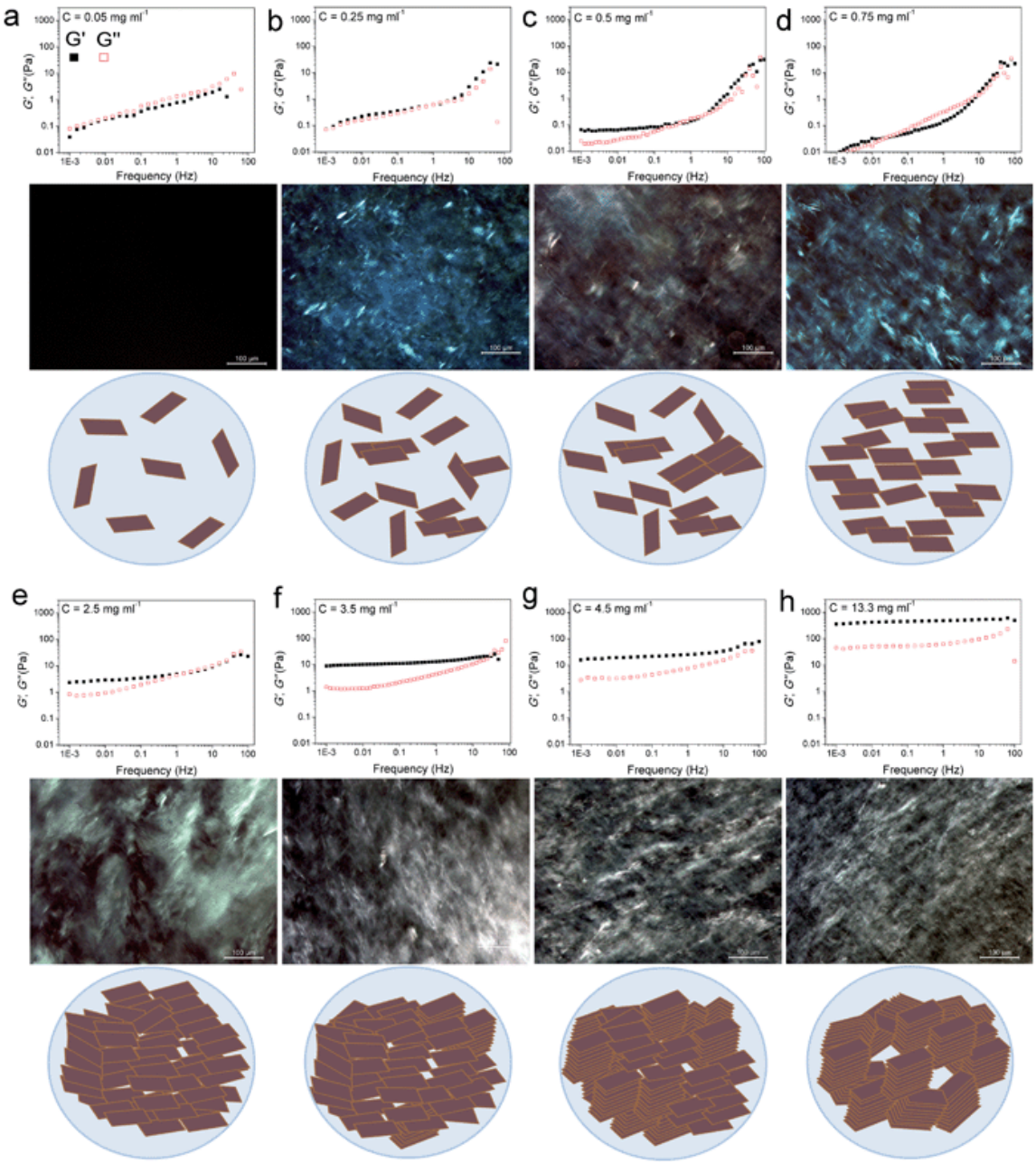

Figure 2.17. Oscillatory dynamics of storage modulus (G') and loss modulus (G") with optical microscopy images of ultra-large GO dispersions.[95]

2.6 Fundamentals of Charged Materials

2.6.1 Electric Double Layer (EDL)

When charged particles are placed in solutions, they can acquire a strong electric charge with the ions in solution arranging around the particles.[96] For a negatively charged surface, the surrounding counterions are positively charged (cations). The inner layer closest to the surface is called the Stern layer. The oppositely charged ions are the co-ions (anions). Adjacent to the Stern layer is the diffuse layer, or outer Helmholtz plane (OHP), that consists of less concentrated counterions and co-ions. These two layers form the electrical double layer (EDL) found in charged systems. Figure 2.18 shows an illustration of the EDL.[96] The distribution of charges neutralizes the charged surface. As a result, the charged potential can be measured from the surface to any point in the dispersion and can be approximated with the zeta potential which is measured from the outer plane of the Stern layer. For oxide-based materials, zeta potential is determined as a function of pH, or OH^- and H^+ ions. Beyond the diffuse layer is the bulk solution. In addition, the thickness of the EDL is the Debye screening length and is proportional to the reciprocal of ionic strength. The Debye length only depends on properties of the solution, not the charged surface and increases with decreasing counterion concentration. The Debye length (κ^{-1}) is calculated according to the following equation:

$$\kappa^{-1} = \sqrt{\frac{\varepsilon_r \varepsilon_0 k_B T}{\sum_i \rho_{\infty i} e^2 z_i^2}} \tag{5}$$

where ε_r is dielectric constant (78.4 for NaCl), ε_0 is permittivity of free space, k_B is Boltzmann constant, T is temperature, e is electric charge, z_i is ion valency, and $\rho_{\infty i}$ is

number density of ion i.[96] The ionic strength (I) of the salt solution is calculated by the following equation:

$$I = \sum_{i=1}^{n} \frac{1}{2} c_i z_i^2 \quad (6)$$

where c_i is the concentration of ion i. For monovalent ions, Na^+ and Cl^-, z_i is 1. Therefore, the ionic strengths are equivalent to the molarity of the solutions. For example, an NaCl solution at 25 °C has a Debye length 1/κ of 30.4 nm at 10^{-4} M and 0.96 nm at 0.1 M.[96] In comparison, pure water has a Debye length of 960 nm. The potential gradient is also a function of Debye length, where 1/κ is the exponential decay length of the potential.

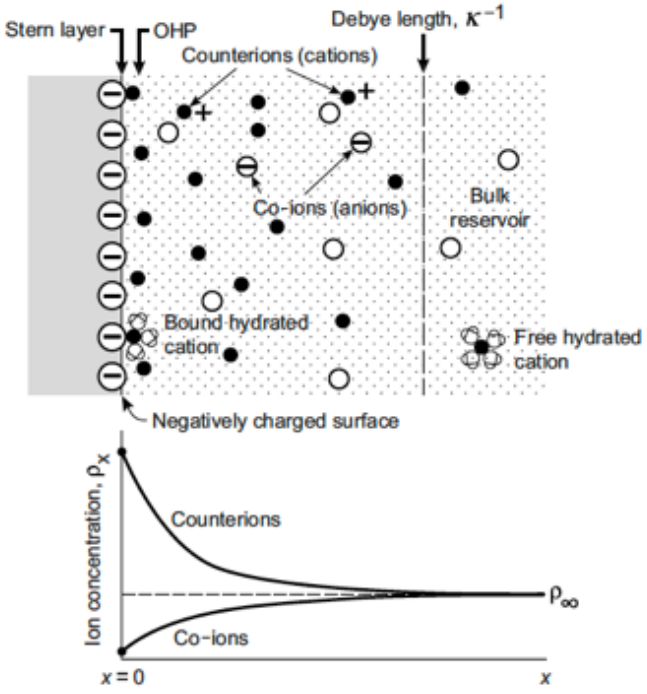

Figure 2.18. Illustration of the electrical double layer (EDL) for charged surface with Stern layer closest to the surface and diffuse layer, or outer Helmholtz plane (OHP), further away from the surface. For a negatively charged surface, the cations decrease with increasing distance away from the surface. The Debye length is calculated as the total length of the electrical double layer.[96]

Increasing the ionic strength, or electrolyte concentration, results in decreasing the Debye length. The ion valency also plays a role in the Debye length. The variation of Debye length with electrolyte concentration is shown for different valency salts 1:1 such as NaCl, 2:1 such as $CaCl_2$, or 3:1 such as $AlCl_3$ in Figure 2.19. At a negatively charged surface, the ions at the surface are mainly the counter ions. From the Debye length equation, z_i would be 2 for Ca^{2+} and 3 for Al^{3+}. The larger the valence, the screening length becomes smaller due to the higher efficiency of ions at screening electrostatic forces.

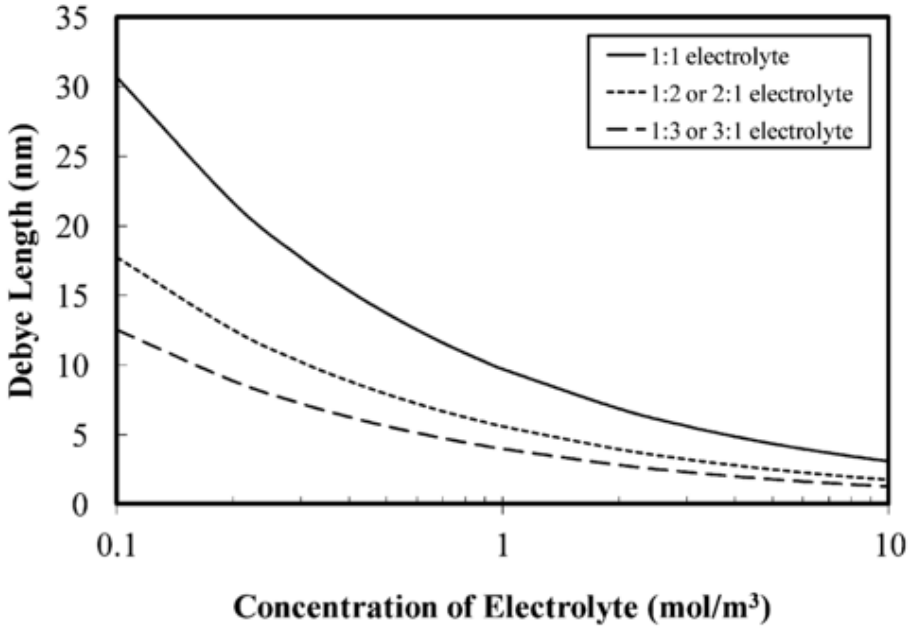

Figure 2.19. Debye length as a function of electrolyte concentration.

2.6.2 Electroviscous Effect

The effective viscosity η of a dispersion of uncharged spherical particles is higher than that of the pure liquid medium η_0. For low volume fraction of particles ϕ, the effective viscosity of the dispersion can be calculated from the Einstein equation,[97]

$$\eta = \eta_0(1 + 2.5\phi) \quad (7)$$

When particles are charged and dispersed in an aqueous electrolyte solution, such as salt solutions, the particles acquire electric charge on their surface. This results in electric double layers (EDLs) that form around the particles to neutralize the surface charge. The general theory for viscosity of electrolyte solutions was developed by Onsager and the concept of ion atmospheres was proposed.[98] Each ion in the electrolyte solution is surrounded by an atmosphere of ions having a net charge of opposite sign to that of central ion. Overlapping between ion atmospheres may generate more drag force in a shear field. The electrostatic force exerted by the particle on the fluid within the EDL changes the flow fields near the particles, thus distorting the EDL. Distorting the EDL from equilibrium leads to increasing both energy dissipation and viscosity. This effect is called the primary electroviscous effect and was first considered by Smoluchowski[99] and can be written as,

$$\eta = \eta_0[1 + 2.5\phi(1 + p)] \quad (8)$$

where p is the primary electroviscous coefficient and is a function of the zeta potential ζ and ratio of the particle radius a to EDL thickness κ^{-1}. The primary electroviscous coefficient approaches zero when κa is very large due to the hydrodynamic disturbance confined to a thin EDL around the particle. This does not affect the bulk fluid field. However, when κa is small, the particle size is comparable to the EDL thickness causing hydrodynamic disturbances with large values of p. In addition, a secondary electroviscous effect can occur if the EDLs of neighboring particles overlap ($\kappa a \sim 1$) at high particle concentrations. This causes significant contributions from both EDL repulsive forces and van der Waals attractive forces. A tertiary electroviscous effect occurs from a change in size and/or shape of soft particles, such as polymers or biomolecules.

Several authors have proposed theoretical treatments of the primary electroviscous effect. Initial theories for the primary electroviscous coefficient only considered $\kappa a > 10$, while later Booth derived an expression to include all κa values.[100] Booth's theory only accounted for small values of zeta potential and Peclet numbers. The Peclet number measures the ratio of diffusion time to convective time, or the extent of movement of fluid with respect to the particle disturbing the surrounding ions. At small Peclet numbers, ion diffusion is sufficiently strong compared to convection such that the EDL is only slightly distorted from equilibrium. In theory, large Peclet numbers mean the hydrodynamic forces become strong enough to deform the EDL in the plane of constant velocity. This results in increases in the viscosity. The viscosity increment due to electroviscous effects usually is limited to a factor of 2 orders of magnitude. More recent theories incorporate all values of κa and zeta potential.[101-103]

2.6.3 Derjaguin-Landau-Verwey-Overbeek (DLVO) Theory

The classical DLVO theory for colloidal interactions was developed by Derjaguin and Landau (1941) and Verwey and Overbeek (1948). The theory states that the overall force between particles is the sum of the attractive van der Waals (vdW) and repulsive EDL interactions.

$$W_{total}(D) = W_{vdW}(D) + W_{EDL}(D) \quad (9)$$

The range of electrostatic repulsions in salt solutions is determined by the ionic concentration of electrolyte. As two similarly charged particles approach each other, their electric double layers overlap resulting in repulsive forces. The repulsive interactions occur

from the decrease in entropy and range of repulsion can vary with the electrolyte concentration. For two planar surfaces, the electric double layer interaction energy (W_{EDL}) can be calculated as follows:

$$W_{EDL}(D) = \frac{\kappa}{2\pi} Z e^{-\kappa D} \approx 2\varepsilon_0 \varepsilon \kappa {\psi_0}^2 e^{-\kappa D} \quad (10)$$

where ψ_0 is the surface potential, κ is the inverse of Debye length determined from Equation 7, and *D* is the distance between the surfaces.[96] As ionic strength increases, Debye length decreases and the repulsive interactions decrease. The attractive van der Waals forces are short-ranged and arise from the interaction of polarizable molecules and surfaces. The planar surface-surface interaction for van der Waals attraction energy (W_{vdW}) can also be approximated by the following equation:

$$W_{vdW}(D) = \frac{-\pi C \rho^2}{12D^2} = \frac{-A}{12\pi D^2} \quad (11)$$

where *A* is the Hamaker constant and *D* is the distance between the plates.[96] An example of the interaction energy plot based on DLVO theory is shown in Figure 2.20.[104] At short interparticle distances, a deep primary minimum occurs due to the increased van der Waals attraction forming irreversible aggregation. At intermediate interparticle distances, a positive energy barrier occurs due to dominating electrostatic repulsion. At large interparticle distances, a shallow secondary minimum occurs that can be attributed to reversible aggregation, or flocculation. However, a deep secondary minimum can occur with micron-sized particles than with smaller ones.[105] The secondary minimum has been reported as the main mechanism for aggregation for systems with large potential barriers

or where a primary minimum does not exist.[105-107] For particles dispersed in salt solutions, decreasing ionic strength can reduce the depth of the secondary minimum.[108, 109]

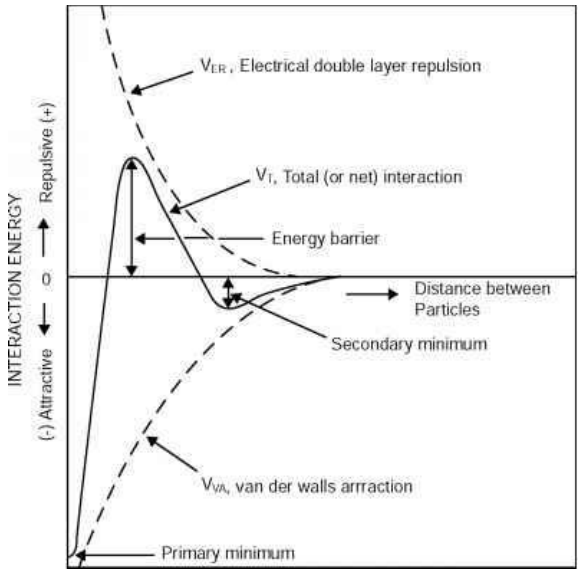

Figure 2.20. Interaction energy curve as a function of interparticle distance.[104]

2.7 MXenes

MXenes are a recently developed class of inorganic 2D materials that have sparked attention in the scientific community due to their exceptional electrical, mechanical, and electrochemical properties.[24, 110, 111] The MXene structure consists of transition metal oxides and hydroxyl functional groups along the basal planes, which impart the MXene flakes to be dispersible in aqueous solvents.[21] MXenes have the formula of $M_{n+1}X_nT_x$, where M is an early transition metal, such as Ti, V, or Mo, n is 1-4, X is C and/or N, and T_x is the surface termination groups (such as −O, −OH, or −F). The structure of MXenes is given in Figure 2.21. For example, titanium carbide $Ti_3C_2T_x$ is most studied due to its

unique properties that have found applications in catalysis, coatings, energy storage, fibers and thin films.[12, 13, 24-26, 112, 113]

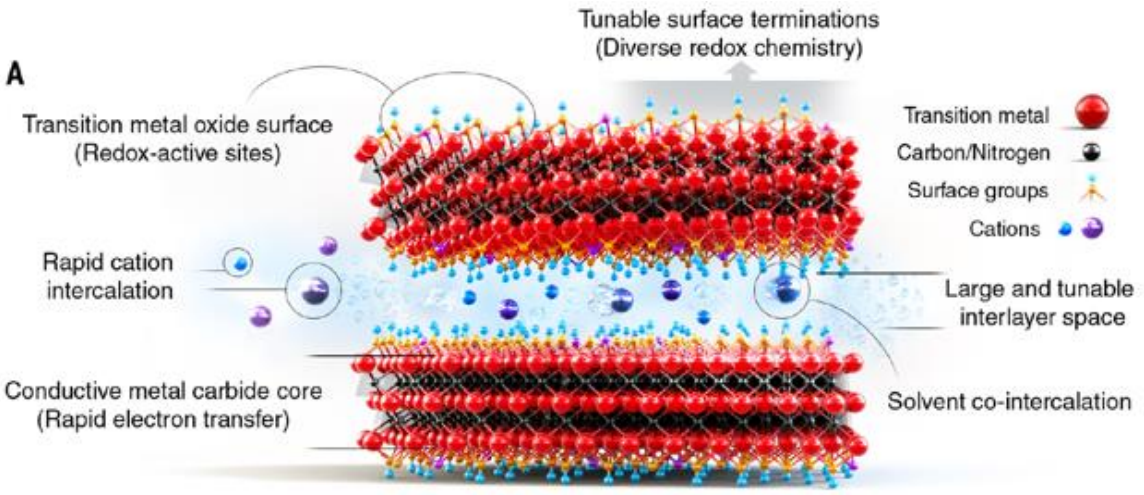

Figure 2.21. Schematic representation of MXenes.[114]

The structure and behavior of MXenes has analogies to other colloidal particles. The faces of MXene flakes are negatively charged while the edges are positively charged providing face and edge interactions that can result in network formation similar to the mechanisms for nanoclays.[21, 115] Complex interactions due to the high aspect ratio and negatively charged surfaces significantly impacts the rheological properties of dispersions. Understanding the rheological behavior provides insights into the effects of binder addition, solvent, and composition on the electrochemical behavior. Particle size, shape, and whether the flakes are individual or multi-layer play a critical role in the ordering of dispersions. MXenes are similar to the graphene family, such as GO, where exfoliation during the complex synthesis forms irregular shapes.[22, 43] Tuning the sonication conditions

through the synthesis produces MXene flakes of varying thicknesses, lateral sizes, and polydispersity.[116] A recent report explored the rheological response MXene dispersions with single and multi-layer flakes as shown in Figure 2.22.[117] Newtonian behavior was observed at very low concentrations where no changes in viscosity were observed with increasing shear rate. At higher concentrations, shear thinning behavior where viscosity decreases as shear increases, with higher viscosities was achieved with single-layer flakes. In addition, the single-layer flakes exhibit an elastic response at much lower concentrations than multi-layer flakes enabling ordering and percolation in the dispersions (Figure 2.23). This was attributed to the strong surface charge and lower packing density and enabled their use for spin or spray coating. The higher particle mass and packing density of the multi-layer flakes enabled their higher concentrations to be used for inkjet or extrusion printing that require thicker materials.[117]

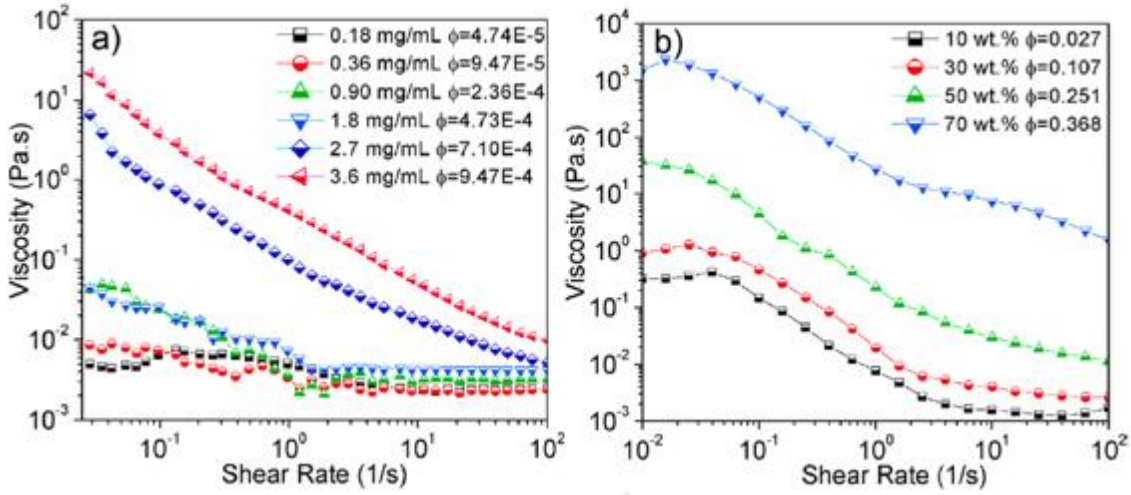

Figure 2.22. Viscosity versus shear rate of a) single and b) multi-layer MXene dispersions at varying concentrations.[117]

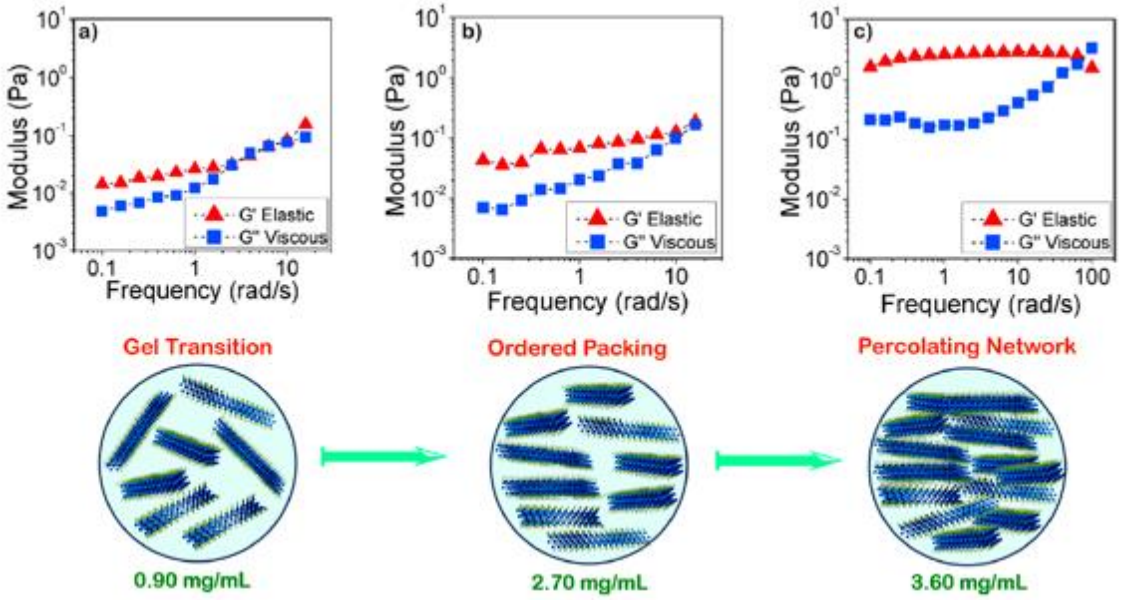

Figure 2.23. Viscoelastic properties of single-layer MXene dispersions at various concentrations: (a) 0.90, (b) 2.70, and (c) 3.60 mg/mL. A schematic representation of the dispersion states is shown under each plot.[117]

Like nanoclays and GO, MXenes can self-assemble into ordered structures and have rich phase behavior.[25] The remarkable phase behavior of MXenes was recently studied in a report without addition of binders or stabilizing agents showing the formation of nematic liquid crystalline phase with increasing concentration.[25] The effect of aspect ratio was also explored, where achieving the nematic liquid crystalline (LC) phase in both small (~0.3 μm) and large (~3 μm) flakes at different concentrations as shown in Figure 2.24. The formation of nematic LC phases enabled wet-spinning the MXenes into aligned fibers with volumetric capacitance of 1265 F/cm^3 that can also be used as heaters.[25] While this new family of materials exhibits excellent capabilities, some challenges remain in understanding the dispersion phase behavior and rheological properties of these systems.

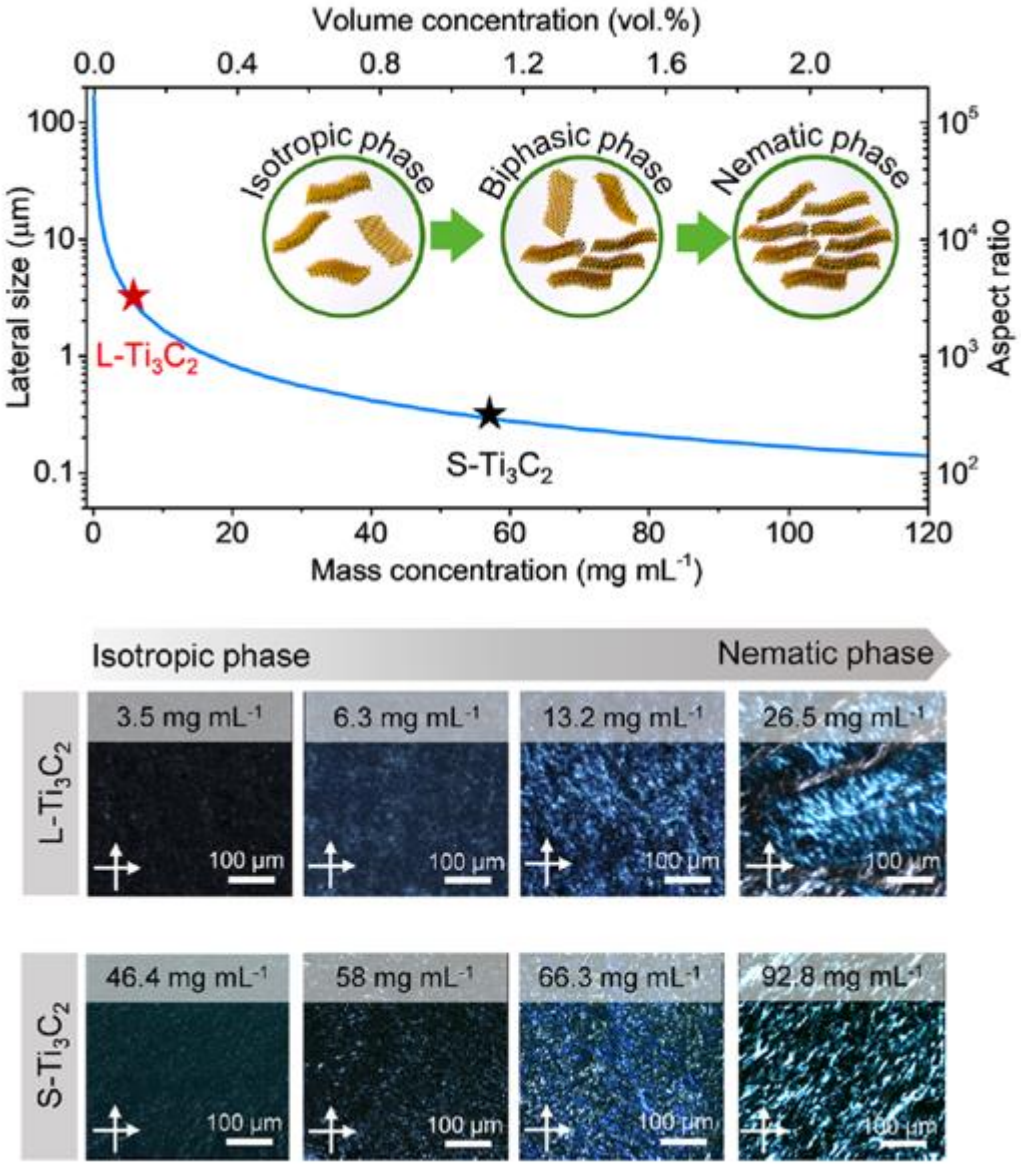

Figure 2.24. a) Relationship between MXene concentration and flake size (lateral size and aspect ratio) for isotropic to nematic (I−N) phase transformation based on theoretical calculations. The stars represent the theoretical LC transition concentrations for large flakes (L-Ti_3C_2, 3.1 μm) and small flakes (S-Ti_3C_2, 310 nm). b) Polarized optical microscopy images of the dispersions.[25]

2.8 Nanoclays

Nanoclays are layered silicates such as bentonite, gibbsite, beidellite, and laponite that have been studied for over a century. Nanoclays are commercially used in applications such as food packaging, cosmetics, thermal insulation coatings, paints, nanocomposites, and rheology modifiers.[118] Many nanoclays are plate-like, also referred to as disks or sheets in the literature for 2D materials, that have been studied to provide theoretical insight into their dispersion microstructures and rheological properties. Clay particles are charged species with negatively charged planes and edges that are positive in acidic solutions and negative in basic solutions.[115] Clay sediments, or minerals, dispersed in water exhibit strong intermolecular forces due to their charged surfaces.

2.8.1 Nanoclay Structures

To date, aqueous clay dispersions have been studied extensively to provide a framework for understanding the phase behavior of liquid crystalline and arrested states of inorganic 2D materials.[119] The structure of the nanoclay smectite group is shown in Figure 2.25 where a single octahedral sheet is surrounded by two tetrahedral sheets and held together with van der Waals attraction. The combination of the sheets is a unit layer.[120] Most nanoclay layers consist of parallel stacked sheets. For example, the composition of sodium montmorillonite (Na^+MMT) is $Na_{1/3}\left[\left(Al_{5/3}Mg_{1/3}\right)Si_4O_{10}(OH)_2\right]$ consisting of Si^{4+} tetrahedral and Al^{3+} octahedral cations. The cations can be substituted by different valence ions when dispersing nanoclays in different solvents or electrolyte solutions.

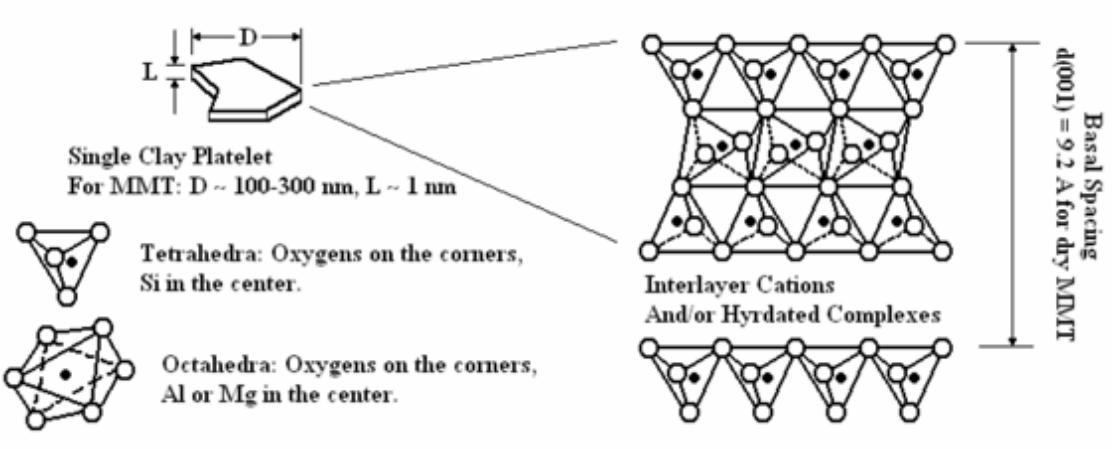

Figure 2.25. Schematic of the layered silicate montmorillonite (MMT), also referred to as bentonite.[121]

Particles in dispersions can associate due to their thermal motion and charge distribution to form dispersed (exfoliated), aggregated by face-face association, flocculated but dispersed, and flocculated and aggregated structures as shown in Figure 2.26.[120, 122] Flocs are large clusters of particles that are loosely bound and can be broken up more readily than aggregates.[123] Aggregates are multiple layers of particles that are strongly attached in a dispersion and are shown as the primary minimum on the potential energy curve (Figure 2.19). Aggregation has been studied extensively in the literature with experimental, simulation, and theoretical approaches.[124-127] Tuning the dispersion by changes in pH or addition of a salt or polymer can induce flocculation. Floc structures were observed in dispersions of minerals (such as nanoclays)[128, 129] biological materials,[130, 131] and polymer modified systems.[132, 133] Floc behavior is colloidally unstable and is characterized in terms of factors such as floc size, shape, density, and porosity. The sizes of flocs range from colloidal particles consisting of several nanometers to larger aggregates consisting of

thousands of microns.[131, 134] The extent to which the particles flocculate depends on the double layer which is governed by the concentration and valence of the ions with opposite charge than the particle charge.[120] Flocculation is found at larger interparticle distances as the secondary minimum and can be the preferred mechanism for aggregation for large particle sizes (Figure 2.20).[106, 135, 136] Low electrolyte concentrations can produce small flocs, which interact by a long-range repulsion. In high electrolyte concentrations, attraction forces dominate at any particle distance except at very close approach and rapidly cause particle agglomeration. For example, denser and larger flocs can form when face-edge and edge-edge interactions lead to the three-dimensional voluminous "house-of-cards" structure (Figure 2.27).[122]

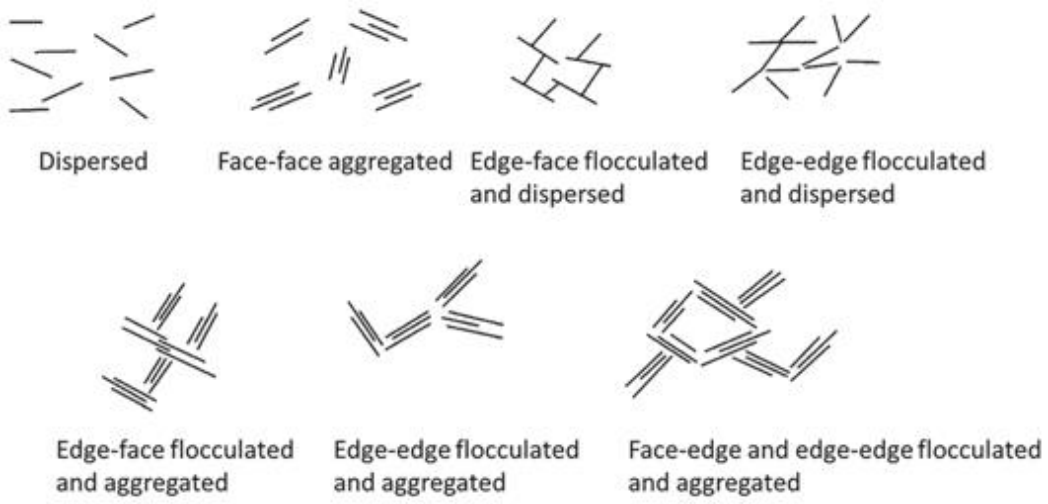

Figure 2.26. Schematic representation of particle association in clay dispersions showing dispersed, flocculated, and aggregated phases.[122]

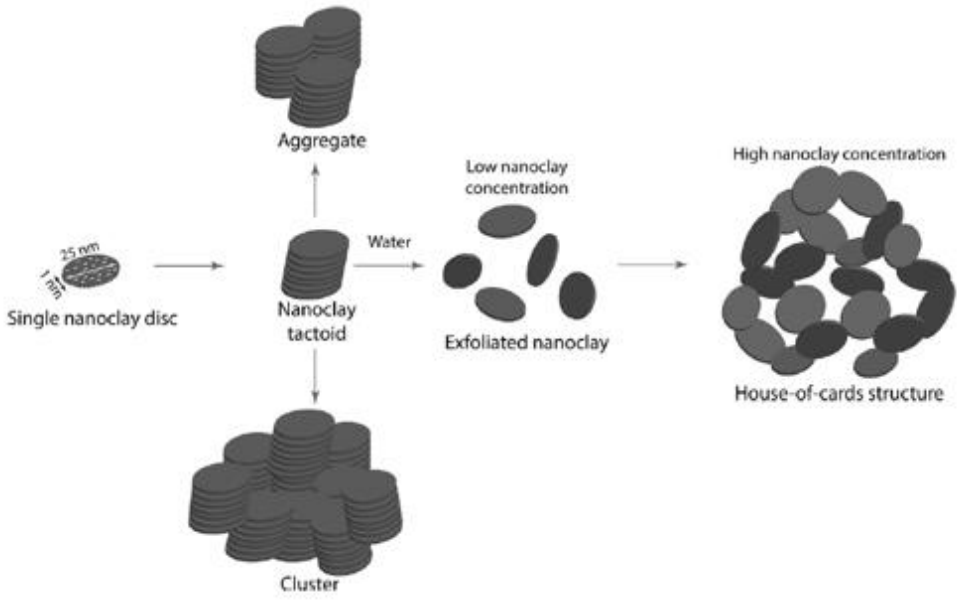

Figure 2.27. Schematic representation of nanoclays when dispersed in water forming the proposed house-of-cards structure.[137]

Pignon *et al.* studied the particle arrangements of laponite in weak electrolytes with rheology and light scattering where the percolation of platelet clusters can form a gel at rest.[138] The gel state is an arrested state defined as the semi-rigid network of associated particles which holds a liquid.[139] When aggregating, low volume fraction dispersions can form a gel if aggregates or clusters of sufficient strength associate to form space filling networks through intercluster bonds.[140, 141] Small deformations to the gel structure at low shear can form rodlike aggregates along the shear direction, while above a critical shear rate the aggregates break up into smaller ones.[121, 138] Several mechanisms have been proposed for the formation of colloidal gelation including diffusion-limited aggregation, kinetic or dynamic arrest, percolation, phase separation, or jamming.[125, 142-146]

2.8.2 Nanoclay Phase Behavior

Nanoclays can exhibit self-assembled structures including liquid crystalline phase behavior. For example, a polydisperse system of gibbsite particles can exhibit a combination of nematic and columnar phases due to sedimentation induced size fractionation.[147] Some examples of nanoclays consisting of charged platelets that form liquid crystal phases include bentonite, gibbsite, laponite, and beidellite. Bentonite and laponite dispersions form gel-like arrested states with increasing relaxation time at low densities;[148, 149] whereas, gibbsite and beidellite exhibit isotropic-nematic (I-N) transitions at moderate densities.[150, 151]

The inclusion of salts can impact the phase behavior of dispersions and resulting properties. Sodium chloride has been most commonly studied due to it being cost-effective, environmentally benign, and easily dissociating in water to form an aqueous solution. Adding the electrolyte at varying ionic strengths to colloidal dispersions can result in liquid crystalline phase behavior. For example, at intermediate ionic strength of 10^{-3} M NaCl phase separation into isotropic and columnar phases forms for gibbsite concentration of 300 and 400 g/L and a birefringent gel forms at 500 g/L (Figure 2.28).[152] At a higher ionic strength of 10^{-2} M NaCl, the volume of columnar phase, compared to isotropic phase, increases with gibbsite concentration. The inclusion of NaCl provides a route to enabling dispersions to potentially achieve liquid crystallinity over a wider concentration range by delaying gelation.[153, 154]

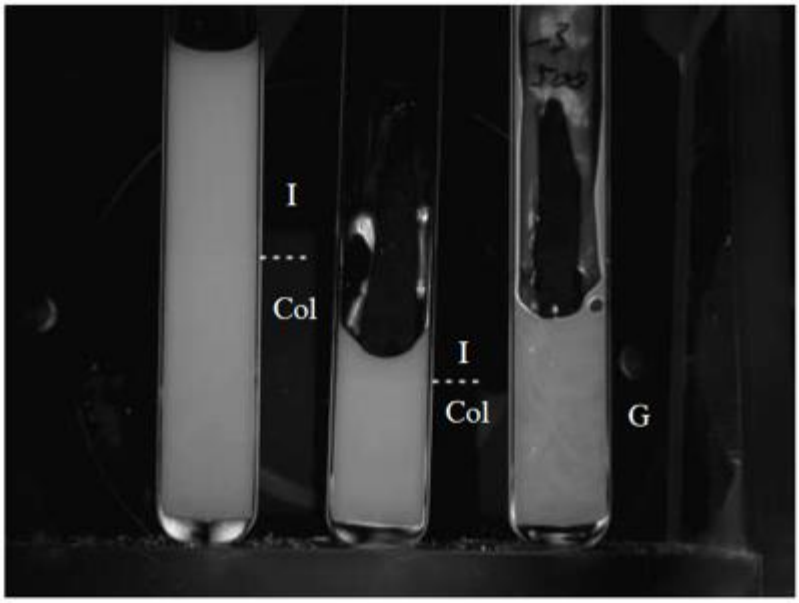

Figure 2.28. Gibbsite phase separation observed between crossed polarizers with ionic strength of 10^{-3} M and (left to right) 300, 400, and 500 g/L gibbsite concentration. I – isotropic, Col – columnar, and G – gel phases.[155]

Laponite dispersions exhibit a rich phase diagram including flocculation (F), isotropic liquid (IL), isotropic gel (IG), and nematic gel (NG) as shown in Figure 2.29a.[156] A sol-gel transition without macroscopic phase separation can occur. Steady shear viscosity rheological measurements have been performed to further investigate these phases. Increasing the ionic strength with NaCl shifts the sol-gel transition to a lower concentration that reduces the swelling pressure as also indicated from osmotic pressure measurements that is due to reduced interparticle repulsions.[156] A pseudoplateau in the phase diagram separates the liquid and gel phases, which was also found in montmorillonite dispersions.[154] For high salt concentrations, phase separation results in flocculation or sedimentation with aggregates increasing in size over time.[129] In addition,

the shear rheology results indicated formation of a gel at a higher concentration. It followed a power-law model above its yield stress and the storage modulus G' is much greater than the loss modulus G". As ionic strength increased, the yield stress increased and the dispersion exhibited more elastic behavior. Laponite gels do not exhibit the isotropic-nematic phase transition governed by translational and rotational entropy as has been observed with beidellite dispersions.[156] Paineau *et al* found that the isotropic-nematic transition occurred in a small concentration range before the gel phase as shown in the phase diagram of Figure 2.28b.[156] This was designated as the fluid nematic phase, or nematic liquid (NL). Formation of the nematic phase occurs with dominating hard rod repulsion forces according to Onsager's theory or numerical simulations for disk particles.[157, 158]

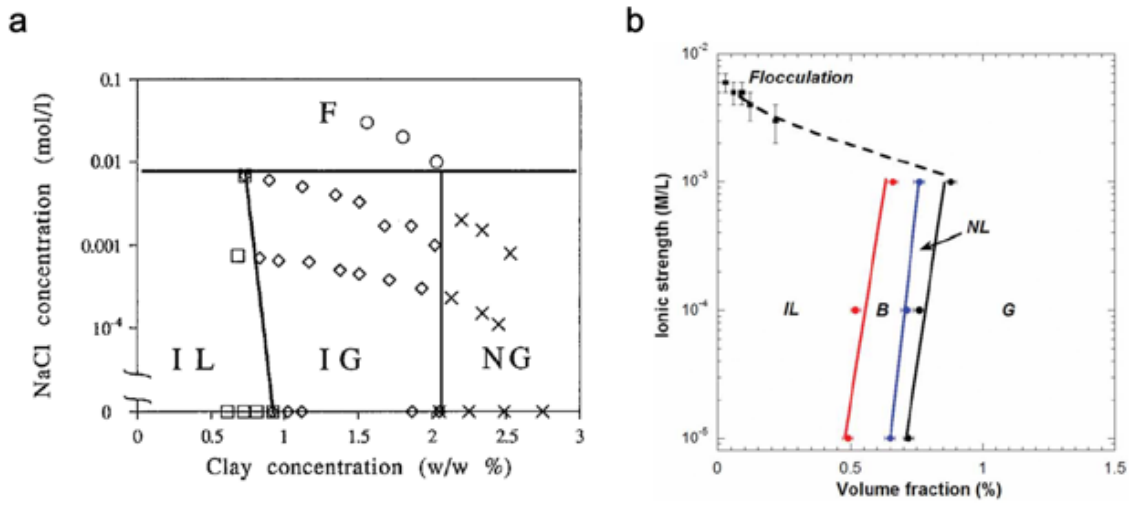

Figure 2.29. Phase diagrams for a) laponite and b) beidellite. IL – isotropic liquid, IG – isotropic gel, NG – nematic gel, F – flocculation, B – biphasic, NL – nematic liquid, G – gel.[156]

The addition of polymers to clay/salt systems has been investigated in several studies. The effects of salts on gelation of laponite hydrogels with sodium polyacrylate and different inorganic salts was investigated including rheological measurements of viscoelastic properties.[159] Rheological and SAXS measurements showed that the laponite hydrogel behavior results in clusters that form due to attractive forces in the dispersion (laponite/polymer/salt).[159] The rheological behavior of laponite included that the elastic modulus G' was three times higher for the dispersion with NaCl than without it.[159] In addition, the laponite dispersion consisting of the polymer and no NaCl had a lower G' than without the polymer. Therefore, the effect of NaCl addition drastically increased the structure elasticity, even more than the effect of polymer addition. Another study investigated the behavior of laponite/gelatin dispersions with different ionic strengths of NaCl (Figure 2.30).[137] With increasing ionic strength, the dispersion drastically increased in elasticity and the onset of structural breakdown occurs at lower stress observed with the sharp decrease in G' versus stress plot.[137] These results highlight that choosing the type of salt and ionic strength can be used to achieve the desired macroscopic properties.

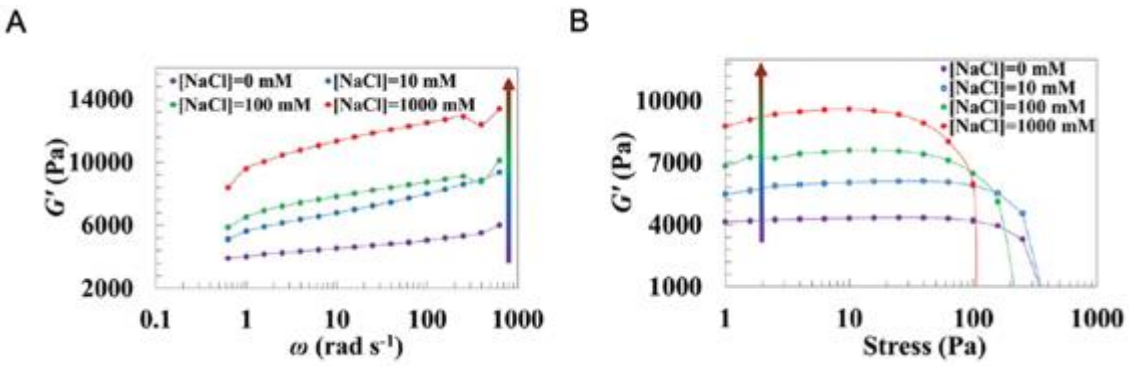

Figure 2.30. Oscillatory dynamic rheology of laponite/gelatin dispersions at different ionic strengths with G' as a function of a) frequency and b) stress.[137]

Chapter 3 Materials & Methods

3.1 Syntheses

3.1.1 Ultra-Large Graphene Oxide (GO)

The synthesis of ultra-large graphene oxide used initial thermal expansion of expandable graphite flakes followed by a modified Hummer's method.[43, 95] Expandable graphite flakes from Asbury Graphite Mills USA (3772 grade) were microwaved for 30 seconds as a thermal treatment to increase the interlayer spacing of the layers within the graphite structure for intercalation and reactivity with the expanded structure. This resulted in very low density expanded graphite that was then transferred to an Erlenmeyer flask. 100 mL of 93-98 wt% sulfuric acid (H_2SO_4) was added to the flask and stirred continuously for three days. This time was chosen to ensure diffusion and intercalation of the H_2SO_4 through the graphite layers. Next, 5 g of crystalline potassium permanganate ($KMnO_4$) was added very slowly while stirring the mixture over the course of 1 hour. This step was performed very slowly and carefully since the addition of $KMnO_4$ to H_2SO_4 results in a highly exothermic reaction and could detonate if added quickly. $KMnO_4$ reacts with H_2SO_4 to form diamanganese heptoxide (Mn_2O_7), which is highly reactive and serves as the oxidant species with the expanded graphite according to the following equations:

$$KMnO_4 + 3H_2SO_4 \rightarrow K^+ + {MnO_3}^+ + H_3O^+ + 3{HSO_4}^- \quad (12)$$

$${MnO_3}^+ + {MnO_4}^- \rightarrow Mn_2O_7 \quad (13)$$

After three days, the mixture became very viscous and dark green, indicating that most of the $KMnO_4$ had reacted. The mixture was then placed in an ice bath with a

thermometer to monitor reaction temperature upon water and hydrogen peroxide additions. 100 mL of deionized water (H_2O) was added using a pipet to the mixture (about 1 mL per minute) in the presence of the sulfuric acid, changing the mixture color to dark red. After water addition, 25 mL of 30 wt% hydrogen peroxide (H_2O_2) solution was added slowly to react the leftover potassium permanganate and manganese oxide complexes that formed throughout the synthesis to produce manganese sulfate. This resulted in a light brown ultra-large GO mixture as illustrated in Figure 3.1.

Removal of residual reagents was performed initially by centrifugation with 36.5 – 38 wt% hydrochloric acid (HCl) and water in a 1:9 ratio by volume of HCl/H_2O. Hydrochloric acid was utilized to react the residual manganese oxides to produce $MnCl_2$ and water, which are inert species. Subsequent washes with water alone were then performed via centrifugation to decrease the acidity of the material, which further exfoliates into ultra-large GO.

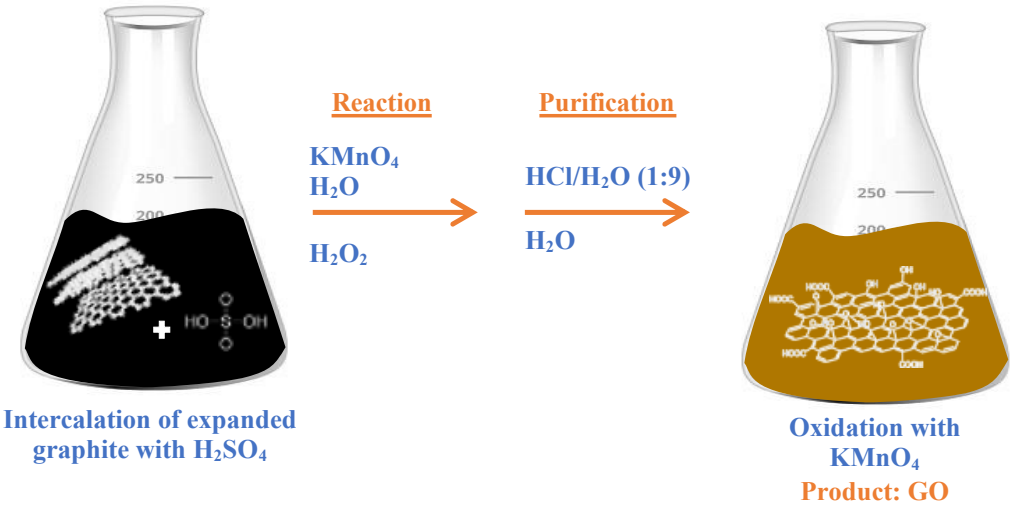

Figure 3.1. Schematic of the synthesis of ultra-large GO via modified Hummer's method.

3.1.2 Reduced Graphene Oxide (RGO) Preparation

Concentrated dispersions (sludges) of ultra-large GO were vacuum dried at ~80 °C overnight. Dried samples were placed in aluminum foil boats. Samples were annealed in a tube furnace under nitrogen flow at a ramp rate of 5 °C/min from 25 °C to 300 °C and then held at 300 °C for 2 hrs. Samples were then cooled before removing them from the tube furnace.

3.1.3 Manganese Dioxide Nanowires (MnO_2 NWs)

The 1D manganese dioxide (MnO_2) nanowires were synthesized via a simple double solvent reacting system as previously reported by Chen *et al.*[18] Initially, 450 mg of $MnCl_2 \bullet 4H_2O$ is added to 80 mL of isopropanol (IPA) in a three-neck round-bottom flask and bath sonicated to dissolve the manganese salt. The mixture is then refluxed at 80 °C while vigorously stirring and monitoring temperature with a thermocouple. 250 mg of crystalline potassium permanganate ($KMnO_4$) is dissolved in 8 mL of deionized water and rapidly injected into the mixture. The reaction was allowed to proceed for 30 min at a temperature not exceeding 83°C to prevent over-reacting the MnO_2. Formation of MnO_2 occurs with the following reaction:

$$2KMnO_4 + 3MnCl_2 + 2H_2O \rightarrow 5MnO_2 + 2KCl + 4HCl \quad (14)$$

A black precipitate of nanowires (NWs) forms as shown in Figure 3.2. Precise control of the shape and size of the MnO_2 strongly depends on the reaction parameters. Previous studies have shown that modifications to this synthesis route such as increasing water

content, dropwise injection of $KMnO_4/H_2O$, or decreasing reaction timing result in spindle-like morphology, rod-like morphology, or short NWs, respectively.

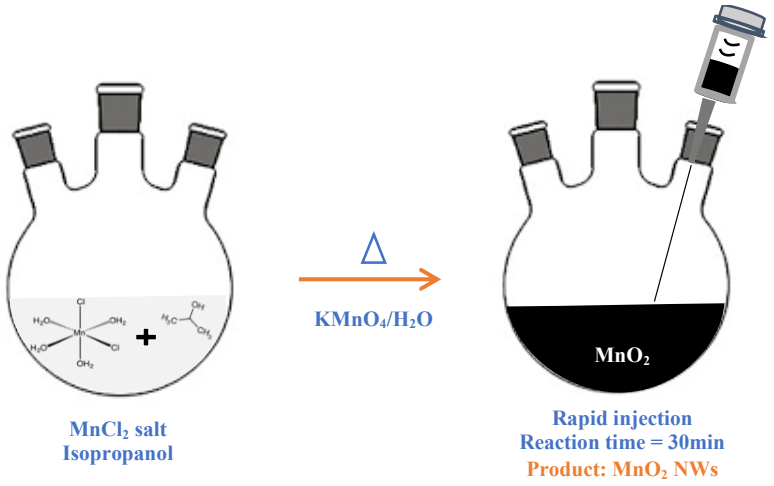

Figure 3.2. Synthesis scheme of MnO_2 via double-solvent system to yield long NWs.

The mechanism for MnO_2 NW formation is simultaneously a dissolution-crystallization and orientated attachment. Initially, the Mn^{2+} ions from the manganese chloride salt dissolve in isopropanol. Nucleation then occurs as the $KMnO_4$ solution is injected rapidly via a redox reaction between Mn^{2+} and Mn^{7+} cations in solution that onsets after a critical minimum concentration of a soluble precursor is reached. This results in abrupt and quick formation of the disordered precursor within a narrow concentration range during phase formation. The crystal growth process of the nuclei occurs as the transformation of the disordered precursor results in the primarily 1D nanowire morphology. As reaction time progresses, more NWs are present and complete NW morphology formation occurs within 5 min.

The ratio of water to isopropanol as well as the manner of injecting $KMnO_4$ solution dictate the crystal growth of the nanowires. Isopropanol is less polar than water due to its alkyl groups that induce higher electron density around the oxygen atom; this results in weaker hydrogen bonding. Therefore, the reaction with water is more favorable where the water molecules bind with the MnO_6 octahedron oxygen atoms along the longitudinal direction, or (001) crystal face. Growth in this direction is preferred due to the (001) face being the most active one and the ratio of water/isopropanol (8 mL/80 mL) hinders lateral growth. Precise control of the MnO_2 synthesis is important to obtain the desired structure. For example, too much water addition can lead to spindle-like NW morphology or aggregation.[18] The $KMnO_4$ solution can be injected dropwise over a longer duration to yield rod-like nanostructure morphology, which results in shorter length and larger diameter MnO_2 than by rapid injection to form nanowire morphology. A synthesis time of 30 min was chosen to form long NWs since it has been previously reported that employing longer NWs on a reduced graphene oxide substrate has shown enhanced cycling and capacity performance than employing shorter NWs for lithium-ion battery application.

A two-stage centrifugation technique was employed to purify the NWs as well as to reduce aggregation in the final product. The precipitate was placed in conical centrifuge tubes and initially centrifuged at $4700 \times g$ for 20 min. The bottoms are then dispersed in ethanol and centrifuged at $47 \times g$ for 3 min. The low centrifugation rate causes the aggregates to settle to the bottom of the tubes, whereas the lighter components remain in the supernatant. Polarized optical microscopy images of samples from the tube were used to qualitatively determine removal of aggregates as previously reported by Murali *et. al* on studies with silver nanowires.[160] The supernatant was decanted into new centrifuge tubes

and then centrifuged at 5000 rpm for 20 min. This completed the first ethanol wash. Ethanol was used as a purification solvent due to ease of NW dispersibility as well as solubilizing the reaction by-product potassium chloride (KCl) and unreacted manganese chloride ($MnCl_2$). The second ethanol wash was performed by dispersing the bottoms of the tubes from the first wash and then centrifuging at 5000 rpm for 20 min. A third ethanol wash was performed in the same manner as the second wash. The bottoms were then dispersed in water and washed three times at $4700 \times g$ for 45 min. The final product was then dispersed at different concentrations in water.

3.1.4 Hybrid (RGO/MnO_2)

A hybrid of RGO/MnO_2 was synthesized by growth of the NWs along the ultra-large GO sheets. The hybrid synthesis method has been previously reported with small-sized GO sheets, but to the authors' knowledge had not previously been performed on ultra large sheets.[19] 100 mg of GO dispersed in 20 mL IPA was added to 450 mg manganese chloride salt dissolved in 60 mL IPA in a three-neck round-bottom flask. The same procedure as synthesizing and purifying the NWs alone as discussed in the previous section was then followed to form the final hybrid product, denoted as 3H for a 3:1 ratio of MnO_2/RGO (75/25 wt%). Another composition of the hybrid was also synthesized for comparison, where the GO mass was reduced to achieve a 10:1 ratio of MnO_2/RGO (90/10 wt%), denoted as 10H. As a control experiment to determine the extent of GO reduction in the hybrid, partially reduced graphene oxide (P-RGO) was also synthesized by taking 100 mg of GO dispersed in IPA and following the MnO_2 synthesis excluding the injection of the $KMnO_4$ solution (reactive species).

The mechanism for the formation of RGO/MnO_2 hybrids occurs via electrostatic binding and growth of nuclei along the ultra-large graphene oxide sheets. Initially, the Mn^{2+} ions from dissolving the manganese chloride salt in isopropanol electrostatically bind with the oxygen atoms of the ultra-large GO sheets. Then rapid injection of the $KMnO_4$ solution at a higher temperature resulted in formation of nuclei along the GO sheets. Nuclei formation is attributed to the redox reaction between the Mn^{2+} and Mn^{7+} ions and the GO sheets act as anchoring sites for crystal growth of MnO_2 NWs.[49] The locations for NW growth on the 2D sheets are along the basal planes and edges of the sheets, where the oxygen functional groups are present. Simultaneously, the GO sheets were reduced via heating to 80 °C for a synthesis time of 30 min. This reduction to form RGO results in deoxygenation of the sheets, which induced defects into the final structure. The complete formation of nanowires along the RGO sheets occurred after 10 min of reaction time as opposed to 5 min for pure NWs. Therefore, the sheets acted as retardants for NW growth due to the additional interactions with the oxygen functional groups on the sheets. The final product RGO/MnO_2 hybrid was purified in the same manner as the pure MnO_2 NWs via a two-stage centrifugation technique.

3.1.5 MXene Inks

This work was performed in collaboration with Dr. Majid Beidaghi's group in Auburn Materials Engineering. The first section includes the synthesis and preparation for a highly concentrated MXene ink (~7 vol%) with flake size of ~0.3 μm performed by Dr. Jafar Oranji.[13] The next section describes the size-fractionation procedure to achieve large (0.3

μm) and small (~0.3 μm) flake MXene dispersions performed by Elnaz Jamshidi in Dr. Beidaghi's Auburn Materials Engineering group.

3.1.5.1 Unfractionated MXenes

The MXene ($Ti_3C_2T_x$) dispersions were initially prepared based on a previously reported method.[161] Briefly, concentrated hydrochloric acid (HCl, ACS grade, BDH) solution was diluted with deionized (DI) water to obtain 40 mL of 6 M HCl solution. A 2 g portion of lithium fluoride (LiF, 98+% purity, Alfa Aesar) was added to the solution and stirred for 10 min using a Teflon coated magnetic stir bar at room temperature. The solution was then moved to an ice bath, and 2 g of Ti_3AlC_2 powder was slowly added to the solution (to prevent overheating). The resulting mixture was transferred to a hot bath (35 °C) and kept for 24 h (stirring at 550 rpm). The mixture was then washed several times with DI water and centrifuged at 3500 rpm until the supernatant pH was ~6. The MXene powder was then collected (filtered using a Celgard porous membrane), redispersed in DI water, and sonicated for 30 min. The resulting suspension was centrifuged at 3500 rpm for 1 hour, and the supernatant was collected and used as the initial dispersion.

The printable MXene ink was produced without any additives or high-temperature drying, which can affect the properties of $Ti_3C_2T_x$. Superabsorbent polymer (SAP) beads were used to increase dispersion concentration by absorbing water similar to a previous report performed with graphene oxide.[162] The dispersion was stirred continuously at 400 rpm to prevent possible concentration gradient and to speed up the absorption process. The SAP beads were easily collected from the dispersion (after saturation) and replaced by new

beads to precisely tune the dispersion concentration. This step was repeated until a homogeneous and highly concentrated dispersion was achieved.

3.1.5.2 Large MXene Flake Dispersions

Preparation of Large MXene ($Ti_3C_2T_x$) Flakes

The $Ti_3C_2T_x$ MXenes were synthesized utilizing the mild intensive layer delamination (MILD) process,[1] which involved selective etching of aluminum from Ti_3AlC_2 using in situ HF-forming etchant. The weight fractions of dispersions were determined from thermogravimetric analysis (TGA) with thermal measurements performed at 10 °C/min to 120 °C and hold for 30 min to remove the water. Weight fraction w was then converted to volume fraction ϕ according to the following equations:

$$\phi = \frac{w\rho_{rel}}{1+(\rho_{rel}-1)w} \tag{15}$$

$$\rho_{rel} = \frac{\rho_s}{\rho_p} \tag{16}$$

where ρ_{rel} is the relative density, ρ_s is the solvent density, and ρ_p is the particle density of MXene flake 5.2 g/mL[163]. The concentration c was also calculated in units of mg/mL as follows:

$$c = \frac{w}{w+(\rho_{solvent}-w\rho_{rel})} \tag{17}$$

Dispersions were kept refrigerated when not in use to reduce the rate of oxidation or hydrolysis,[164] and all dispersions were tested within three weeks of MXene synthesis although the samples qualitatively appeared stable for longer.

Preparation of MXene/NaCl Dispersions

Varying NaCl salt solutions were added to MXene dispersions to achieve desired flake concentrations and ionic strengths. The MXene/NaCl dispersions were allowed to stir for ~1 hr before proceeding with characterization. Since NaCl is a monovalent salt, the ionic strengths of the NaCl solutions are equivalent to the molarity of the solutions. The ionic strengths studied in this work are 0.01, 0.05, 0.1, and 0.5 M NaCl. For 0.01, 0.05, 0.1, and 0.5 M NaCl, the corresponding Debye lengths are 3.04, 1.36, 0.96, and 0.43 nm, respectively.

3.2 Characterization

3.2.1 Ultraviolet-Visible Spectroscopy (UV-vis)

Ultraviolet-visible spectroscopy (UV-vis) was used to detect electronic transitions across the ultraviolet-visible spectral regions for confirming synthesis and measuring concentration. On a Cary 60 (Agilent Technologies) UV-vis Spectrometer, 4 mL of water (or other solvents – ethanol, isopropanol, etc.) was placed in a quartz cuvette and used as baseline correction. Then 10 μL of dispersion was added to the cuvette, shaken to ensure uniformity, and the first absorbance measurement was taken. Subsequent runs were performed on the same sample by addition of 10-20 μL sample to previous run. An overlay of the absorbance versus wavelength data was used to obtain the parameters for the Beer-Lambert law. Beer-Lambert law states that the absorbance is linearly related to the concentration of the dispersion as

$$A = \varepsilon c l \tag{18}$$

where c is concentration, l is the path length, and ε is the absorption coefficient. The absorption coefficients were determined from multiple dilutions and used for determining subsequent batches of unknown dispersion concentrations.

3.2.2 Fourier-Transform Infrared Spectroscopy (FTIR)

Fourier-transform infrared spectroscopy (FTIR) gathers spectroscopic data of functional groups for chemical identification by sending infrared radiation through the sample where it is absorbed or reflected. The detector is initially cooled with liquid nitrogen and then the background data is collected before performing any runs. Samples of either dried dispersions or aerogels were placed on a clean germanium crystal for performing ATR (Attenuated Total Reflectance) FTIR. ATR is a technique that utilizes internal reflection as the incident beam bounces through the crystal from top to bottom and interacts with the sample. The interaction energy of the beam with the sample then gives the spectral response of absorbance (or transmission) as a function of wavenumber (defined as inverse wavelength). Omnic software is used to run the experiments and Omnic Spectra software is used to perform peak data analysis.

3.2.3 Raman Spectroscopy

Raman spectra were collected on a Renishaw inVia Raman microscope using a 514 nm laser. Samples were prepared by drying dispersions and then pressing the solid onto double-sided tape on a microscope slide. At least three different spots were chosen for each sample using a 5% laser power, 45 sec exposure time, and 10 accumulations.

3.2.4 X-Ray Diffraction (XRD)

X-Ray Diffraction was performed on AXRD+ Powder Diffractometer (Proto Manufacturing) with a Cu Kα radiation ($\lambda \approx 1.54$ Å) at a scan rate of 0.01°/s of diffraction angles 2θ from 5 to 70°.

3.2.5 Atomic Force Microscopy (AFM)

Tapping-mode atomic force microscopy (AFM) was performed on an Anton Paar Tosca 400 to acquire sample sizes and morphology. AFM sample preparation was performed by drop-casting a very low of concentration dispersion onto a silicon wafer with 300 nm thermal oxide layer (oxygen plasma cleaned) that is placed onto a hot plate for ~30 sec to quickly remove the solvent (water). High resolution scans were performed and processed with SmartScan Imaging Software. Height profiles were also measured to determine sheet and nanowire sizes.

3.2.6 Scanning Electron Microscopy (SEM)

The morphology and material architecture were investigated by field emission scanning electron microscopy (FE-SEM) using a JEOL JSM-7000F. Dispersions were drop-casted onto silicon wafers at 70 °C, then adhered to cylindrical SEM stubs using carbon tape. All SEM samples were sputtered with gold for 15 sec to increase conductivity for obtaining high resolution images.

3.2.7 Thermogravimetric Analysis (TGA)

Once the materials were synthesized, thermogravimetric analysis (TGA) was performed on a TA Instruments Q5000 to investigate thermal degradation profiles and determine dispersion concentration. TGA monitors mass loss as a function of temperature by utilizing a precise balance and a furnace. The procedure begins with adding a concentrated dispersion to a tared platinum pan, then heating the sample and pan to 120 °C at a rate of 10 °C/min under argon atmosphere and leaving it isothermal for 30 min. This removes the water from the dispersion and concentration of solute is measured as a weight percent using the Thermal Analysis (TA) software. Thermal degradation was performed under air atmosphere by further heating the sample and pan to 800 °C at a rate of 10 °C/min and then leaving it isothermal for 45 min. Pure component degradation runs were analyzed to determine compositions of hybrids.

3.3 Electrodes

Electrochemical measurements were performed for the graphene work on the materials ultra-large GO and RGO, MnO_2, and hybrids. Cyclic voltammetry (CV) and electrochemical impedance spectroscopy (EIS) measurements were carried out using a Gamry Interface 1000 E Potentiostat. The electrochemical experiments were performed in a three-electrode mode, including a silver/silver chloride (Ag/AgCl) reference electrode, platinum (Pt) wire counter electrode, and working electrode. The working electrode was composed of sample, carbon black (CB), and polytetrafluoroethylene (PTFE) with a ratio of sample/CB/PTFE of 80/15/5 wt% dried on nickel foam current collector. The electrolyte tested in this work was 1M Na_2SO_4.

3.4 Dispersion Microstructure

3.4.1 Optical Microscopy

Optical imaging in transmission mode was performed on a Nikon Eclipse 80i microscope with imaging workstation, Nikon DS-Ri2 camera, and Nikon Elements software. Cross-polarized images were captured with 20X/0.45 NA LU Plan Fluor and 60X/1.40 NA oil immersion objectives. Samples were prepared for imaging by placing a drop of sample onto a microscope glass slide. A thin layer (~20 μm) of nail polish was used as a spacer between the glass slide and cover slip. Another layer was applied on top of the cover slip to prevent solvent evaporation during imaging.

3.4.2 Rheology

Rheological properties of MXene inks were studied using a strain-controlled rotational rheometer (Physica MCR301, Anton Paar). The fixture geometries (made of stainless steel) used for testing were parallel-plates (25 mm diameter) and cone and plates (25 mm diameter with cone angle = 0.0345 rad and 50 mm diameter with cone angle = 0.0352) as well as a Couette fixture (cone angle = 0.033 rad). This enabled testing a broad range of viscosities and ensuring that there are no artifacts in the data due to testing geometry. Samples were kept refrigerated to prevent oxidation. After a series of experiments, the following protocol was established that produced consistent results. The dispersions were taken out of the refrigerator and vortex mixed for ~10 sec, then allowed 2 hr to reach thermal equilibrium at 25 °C. The dispersions were loaded onto the rheometer at 25 °C and silicone oil was coated along the edges of the fixture. A solvent trap of deionized water was used to prevent water loss due to extended testing. Samples were

allowed 1 hr to equilibrate on the rheometer to reduce effects of shear history before the investigation of rheological properties. A preliminary shear protocol was then performed at a shear rate of 0.01 s^{-1} prior to measuring oscillatory and steady shear rheology.

Chapter 4 Microstructure and Electrochemical Properties of Graphene/Manganese Oxide Hybrid Electrodes

4.1 Motivation

The need to develop energy storage devices with higher charge storage capabilities has gained attention in the past decade as a result of increased environmental concerns.[165] Supercapacitors offer advantages over traditional electrical double-layer capacitors and batteries due to their higher power densities. Furthermore, advancements in nanomaterial research have revealed unique material properties and behavior that are more desirable for many applications. Fundamental understanding of the effects of tailoring initial dispersion parameters at the nanoscale on its final properties provides a framework for developing structure-processing-property relationships. These relationships provide insight into the material interactions and microstructures that enable fluid-phase processing and fabrication into complex architectures. Carbon-based nanomaterials, including single-walled carbon nanotubes (SWNTs),[2-4] activated carbon,[5, 6] reduced graphene oxide (RGO),[7-11] and titanium carbide ($Ti_3C_2T_x$),[12-15] have been found to possess exceptional electrical, mechanical, thermal, and optical properties enabling their applications in flexible electronics, catalysts, actuators, deionization, and capacitors. They store charge by electric double-layer capacitance (EDLC), which occurs at the interface between the conductive electrode surface and electrolyte.

This research investigated the individual and combined interactions of the ultra-large RGO sheets and MnO_2 nanowires as well as the effects of combining 2D/1D geometries with very different aspect ratios. Two different hybrid compositions were

studied for comparison with MnO_2/GO ratios of 1) 75/25 wt% designated as 3:1 hybrid, or 3H, and 2) 90/10 wt% designated as 10:1 hybrid, or 10H. The RGO sheets serve as anchoring supports for the MnO_2 to reduce the possibility of agglomeration of the sheets, which would affect final material properties. Analysis of the dispersion and post-processing microstructures provides insights into the effects of the inclusion of MnO_2 on resulting electrochemical properties. All the materials were then characterized by multiple spectroscopy techniques, microscopy and thermal analysis to understand the material properties including functionality, sizes, crystal structure, thermal stability and transitions, and graphitic domains. Electrodes of the individual and hybrid materials were fabricated and tested to understand the electrochemical behavior. Initial parts of this research were co-advised with Dr. Emmy Radich, former professor in Chemical Engineering at Auburn University.

4.2 Results

4.2.1 Material Sizes – AFM analysis

Expandable graphite, ultra-large graphene oxide (GO), partially reduced graphene oxide (P-RGO), reduced graphene oxide (RGO), and manganese oxide (MnO_2) were prepared as described in the experimental section in Chapter 3. Furthermore, hybrids (RGO/MnO_2) were synthesized with addition of GO through the MnO_2 synthesis that enables electrostatic binding of the MnO_2 nanowires (NWs) onto the GO sheets. AFM was performed on GO, MnO_2, and hybrid materials for determining aspect ratio. Figure 4.1a,b shows the AFM images of GO and MnO_2, respectively.[166] The GO sheets have an irregular shape and range in length from 10 – 70 μm, consisting of primarily 30 – 50 μm sheets, with evident folding

and wrinkling indicated by the lighter areas along the sheet dimensions (Figure 4.1a). Monolayer and few-layer sheets were observed with an average thickness of ~1 nm, which is in agreement with previous studies on ultra-large GO.[167, 168] Figure 4.1b shows the MnO_2 nanowires (NWs) that tend to form fractal networks during AFM measurements. The measured lengths ranged from 500 – 1000 nm, and diameter (or height) ranges from 5 – 25 nm for an average aspect ratio of 50, which is higher than other morphologies that can be produced by tuning the MnO_2 synthesis. Earlier work showed that the size and morphology of MnO_2 nanostructures was sensitive to the synthesis time. For example, MnO_2 nanoneedles produced during a 10 min reaction time have dimensions of length from 200 – 500 nm and diameter from 20 – 50 nm.[18] The longer synthesis time of 30 min in this work permitted further longitudinal growth of the MnO_2 into nanowires. However, the aspect ratio for the ultra-large GO sheets is three orders of magnitude higher than that of the NWs as shown in Table 1. For comparison, the typical dimensions for small GO sheets ranges from 0.7 – 5 μm in length and thickness (diameter) of ~1 nm that gives an aspect ratio of ~2,000.[48, 169] This is one order of magnitude smaller than the ultra-large GO and still two orders of magnitude higher than that of the NWs studied in this work. High aspect ratio nanomaterials exhibit larger surface areas that enable more access for diffusion and interactions along their surfaces, which are desired for this work to enable better electrochemical properties. AFM results of the 3:1 hybrid (3H) show a uniform distribution of nanowires along the GO sheets and 10:1 hybrid (10H) show regions of more concentrated bundles of MnO_2 that do not exhibit similar 1D structures to that of 3H (Figure 4.1c,d).

Many studies have previously shown advantages of combining 2D and 1D morphologies to achieve better optical, electrical, and mechanical properties;[170-172] however, the challenge remains in developing a comprehensive understanding of the material interactions. In this work, combining very different aspect ratios and content of 2D and 1D components were combined to enable tuning their microstructure to suit many applications.

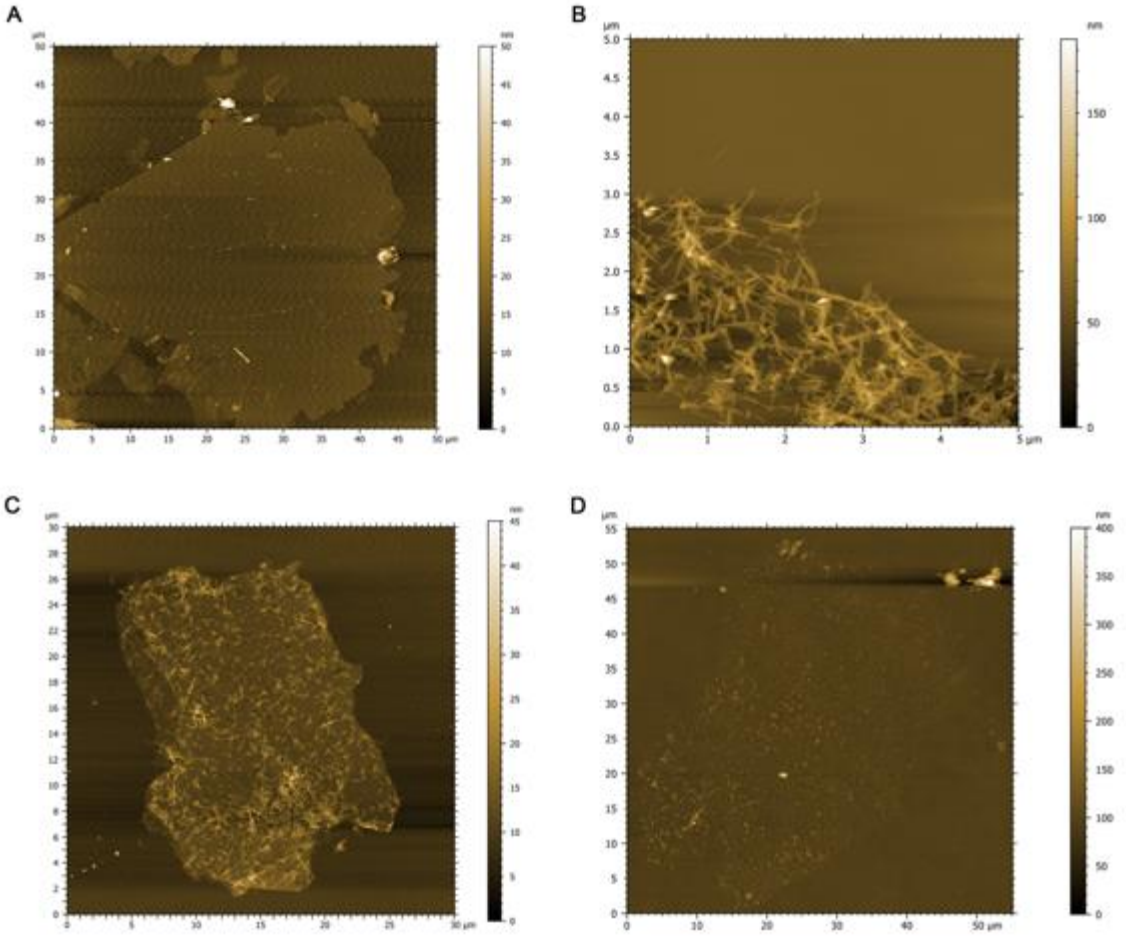

Figure 4.1 AFM images of a) GO with an average sheet size of 40 μm long and ~ 1nm thick, b) MnO_2 nanowires indicating network formation, and hybrids c) 3H that represents uniform distribution of nanowires along the GO sheets and d) 10H that represents clusters of MnO_2 attached to RGO sheets.[166]

Table 1. GO and MnO_2 Material Sizes from AFM Measurements

Material	Length – L (nm)	Diameter – D (nm)	Aspect Ratio (L/D)
GO sheets	10,000 – 70,000	0.8 – 1.2	~40,000
MnO_2 NWs	500 - 1000	5 - 25	~50

4.2.2 Thermal Analysis

Thermal degradation of the materials was investigated by TGA. Figure 4.2a shows the TGA curves for GO, MnO_2, and both hybrids 3H and 10H in argon after a 30 min isothermal hold at 120 °C for water removal from the dispersions.[166] GO exhibits two thermal transitions, one with an onset temperature at 150 °C indicative of the decomposition of the oxygen functional groups and the other at 450 °C indicative of breaking the carbon backbone.[173, 174] Each transition corresponds to approximately half of the initial mass loss. The curve for MnO_2 exhibits three thermal transitions and is more thermally stable than GO as shown in Figure 4.2b. At 200 °C, MnO_2 loses any remaining water adsorbed to the surface ~3 wt%. Next, at 425 °C, MnO_2 is converted into Mn_2O_3 by the reaction $4\ MnO_2 \rightarrow 2\ Mn_2O_3 + O_2$ that contributes to ~5 wt% mass loss. Then at 610 °C, Mn_2O_3 is converted into Mn_3O_4 by the reaction $6\ Mn_2O_3 \rightarrow 4\ Mn_3O_4 + O_2$, which results in ~4 wt% mass loss and is comparative to previous studies of degradation of MnO_2.[49, 175, 176]

Throughout the hybrid syntheses, MnO_2 nanowires are electrostatically bound to the GO sheets. Therefore, the thermal degradation of the hybrids exhibit transitions of both individual components. The 3H and 10H hybrids exhibit a thermal transition starting at 160

°C that results in mass loss of ~10 wt% for 3H and ~5% wt% for 10H indicative of the removal of oxygen functionality from GO and adsorbed water from MnO_2. The next transition occurs from 300 – 600 °C with mass loss of 20 wt% for 3H and ~11 wt% for 10H that is attributed to conversion of $MnO_2 \rightarrow Mn_2O_3$ with possible destruction of the carbon skeleton. The carbon breakdown at a lower temperature in the hybrids than GO (550 – 800 °C) may have occurred because of the MnO_2 phase change that weakens the RGO sheets. However, more fundamental understanding of the sheet and nanowire interactions is necessary to explain this phenomenon. The mass ratio of MnO_2/RGO in the dispersions were then calculated by taking the final mass after complete degradation at 800°C divided by the initial mass at 120°C. The 3H hybrid consists of MnO_2/RGO ratio of 3:1 (75% MnO_2/25% RGO by wt), while 10H consists of 10:1 (90% MnO_2/10% RGO by wt) for this work. Since the hybrids consist of MnO_2, their thermal stability is shown to be much higher than that of GO. These results are in agreement with previous reports.[49, 175] The additional MnO_2 content in 10H shows higher thermal stability than that of 3H.

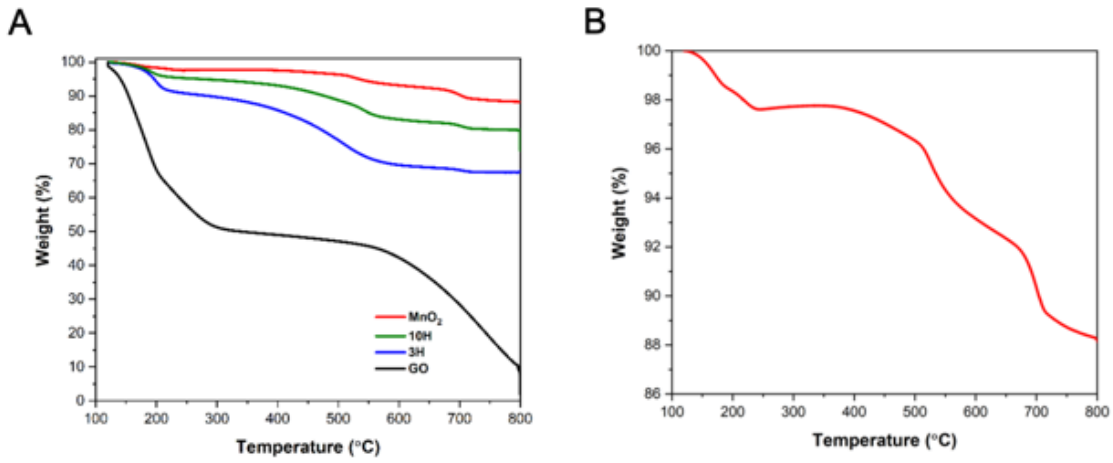

Figure 4.2. TGA performed under argon atmosphere at a rate of 5 °C/min. a) GO exhibits two thermal transitions upon decomposition – loss of oxygen functionality and break carbon backbone. b) MnO_2 is much more thermally stable than GO and is converted to Mn_2O_3 and then Mn_3O_4. The hybrid exhibits transitions consisting of both individual components.[166]

4.2.3 Spectroscopy Study

4.2.3.1 UV-vis & FTIR Spectroscopy analysis

A combination of UV-vis and FTIR spectroscopy methods were used to investigate the electronic transitions and functionality of the materials. Figure 4.3a shows the UV-Vis spectra for ultra-large GO, MnO_2, and the hybrids 3H and 10H.[166] GO exhibits a peak at 230 nm indicative of the $\pi \rightarrow \pi^*$ transition of electrons in conjugated carbon-carbon double bonds (aromatic), or C=C, and a shoulder at 300 nm indicative of the $n \rightarrow \pi^*$ transition of electrons in C=O bonds connected to the C=C bond in the GO plane.[177] The shoulder in GO is a signature of the presence of oxygen functional groups in the material. MnO_2 exhibits a d – d transition at a broad absorption band between 350 – 500 nm with the peak

position at 410 nm of the Mn ions from lower to higher d-orbital energy state in the MnO_2 crystal.[18] The UV-vis spectrum of the 3H hybrid exhibits a blue-shift in the conjugated carbon peak to 215 nm corresponding to GO sheet exfoliation[49] and shows presence of the broad Mn peak at 410 nm. Interestingly, 10H primarily exhibits a sharp Mn-O transition at 410 nm and much higher absorption values for the whole spectrum than GO and 3H demonstrating some restoration of the sp^2 carbon framework.[9, 178] A control experiment was performed with only GO and the manganese salt as precursors (excluding $KMnO_4$ addition) to determine the extent of GO reduction through the hybrid synthesis. However, it is shown that GO is not fully reduced by chemical reduction throughout the hybrid synthesis conditions, indicative of a partially reduced graphene oxide (P-RGO) material (Figure 4.4). The UV-vis spectroscopy analysis confirms the electronic transitions present in the individual materials as well as some reduction of GO in both hybrid materials.

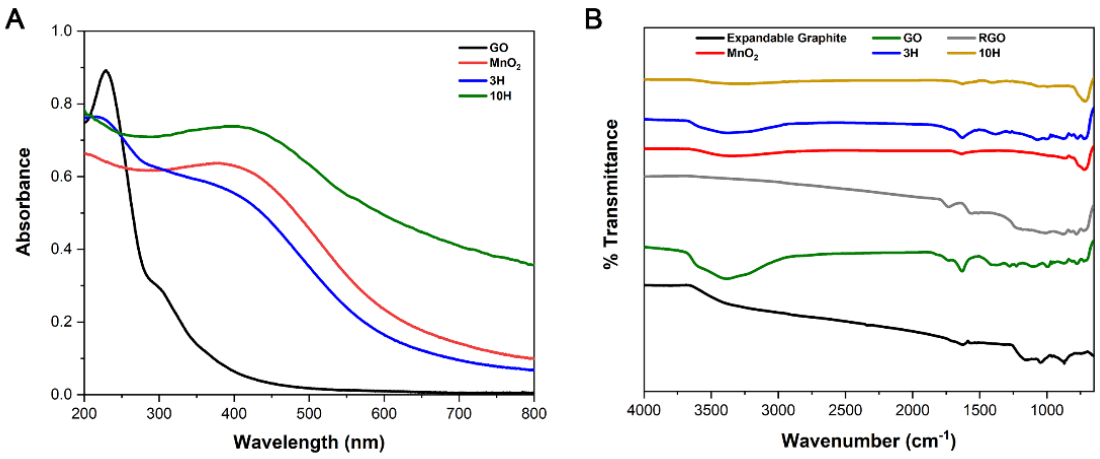

Figure 4.3. a) UV-vis spectra indicating electronic transitions of ultra-large GO, MnO_2, and both hybrids 3H and 10H. Presence of oxygen functional groups in GO occurs at the shoulder of 300 nm. The 3H hybrid spectrum consists of the conjugated carbon peak blue-shifted to 215 nm ascribed to GO exfoliation and indication of the Mn-O transition with a broad peak at 410 nm. The higher MnO_2 content of 10H primarily indicates the Mn-O transition. b) FTIR spectra of expandable graphite, GO, RGO, and hybrids reveal presence of hydroxyl, carboxyl, carbonyl, and epoxy groups for GO, 3H, and 10H with 10H exhibiting the least intensities. FTIR spectra of MnO_2 indicates hydroxyl functionality in its crystal lattice and contributes to both hybrid spectra. RGO demonstrates no evident oxygen functionality similar to the expandable graphite (precursor) indicating successful reduction.[166]

FTIR spectroscopy was performed to determine presence of different functionality within the materials (Figure 4.3b). FTIR spectra of expandable graphite, GO, RGO, MnO_2, and both hybrids (3H and 10H) are shown in Figure 3b. The peak at 1630 cm^{-1} is evident of conjugated, or aromatic, carbons (C=C), which is present in the expandable graphite, GO, RGO, and both hybrids. The oxygen functional groups occur at the following peaks: 3387 cm^{-1} (O–H stretch), 1730 cm^{-1} (C=O, carboxyl), 1374 cm^{-1} (C–O, carbonyl), and 1227 cm^{-1} (C–O–C, epoxy). These peaks are clearly shown in GO and have a low intensity in 3H and much lower intensities in 10H, which is a result of the higher MnO_2/RGO ratio in

10H. The MnO_2 curve indicates presence of O–H groups in the crystal lattice shown as a broad stretching vibration at 3340 cm^{-1} and bending vibration at 1633 cm^{-1} in the FTIR spectrum (Figure 4.3b). The P-RGO (Figure S2b in the SI) also exhibits the conjugated carbon peak at 1630 cm^{-1} as well as low intensities of the oxygen functionalities. This reveals that P-RGO is not fully reduced, which is in agreement with the UV-vis spectroscopy study. The RGO produced in this work was prepared by thermal annealing the ultra-large GO sheets. The extent of its reduction was characterized by spectroscopy techniques, where the FTIR spectrum indicates complete removal of the hydroxyl peak and no other evident functionality. Hence, the FTIR spectroscopy analysis demonstrates reduction of the ultra-large graphene oxide in the RGO and hybrids as confirmed with the functional groups. Further analyses were then investigated for all materials to identify more details regarding their structure.

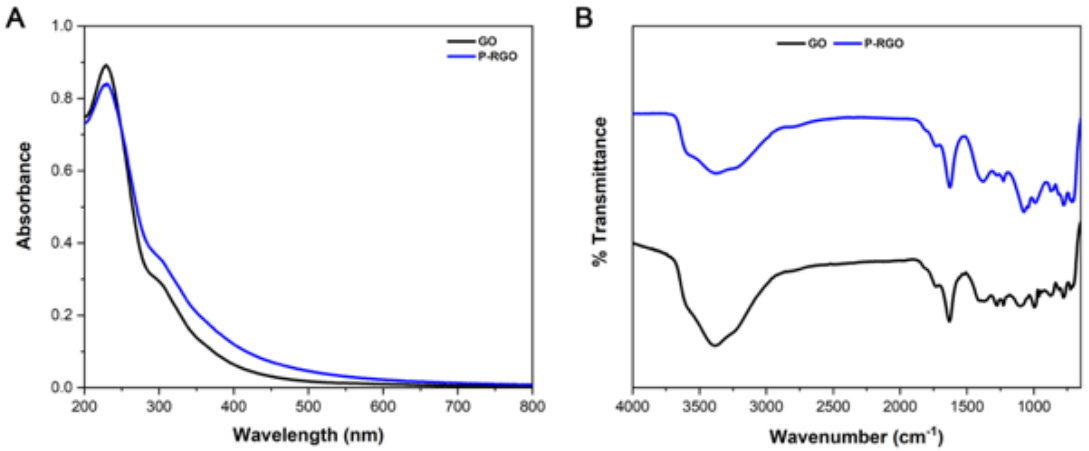

Figure 4.4. To analyze if the graphene oxide is reduced through the hybrid synthesis, GO was subject to the same conditions in the synthesis without addition of the reacting agent. a) UV-vis and b) FTIR spectroscopy were performed and demonstrate a partially reduced graphene oxide (P-RGO).[166]

4.2.3.2 XRD analysis

XRD spectra of the expandable graphite, GO, RGO, MnO_2, and both hybrids were performed to characterize the material crystal structure (Figure 4.5).[166] Figure 4.5a shows a comparison of the expandable graphite and resulting GO. The XRD spectrum of the expandable graphite presents two distinct peaks located at 26° indicative of the (002) reflection and 55° representing the (004) reflection. According to Bragg's law where $n\lambda = 2dsin\theta$ and utilizing a Cu kα source for α = 1.54 Å = 0.154 nm, the d-spacing of expandable graphite was 0.342 nm. GO exhibits an intensive peak at 2θ = 9.9°, which corresponds to the (001) reflection indicative of oxygen functionality. The interlayer spacing of ultra-large GO was 0.892 nm as a result of the formation of functional groups resulting from oxidation. The results from characterizing the expandable graphite and GO synthesized in this work are in agreement with those produced in a previous report.[168] Furthermore, the XRD spectrum of RGO produced in this work is shown in Figure 4.5b, where it exhibits loss of the (001) peak and presence of a (002) peak at 2θ = 22.7°. The interlayer spacing calculated for RGO is 0.391 nm, conveying that the thermal annealing procedure successfully removed the majority of oxygen functionality from the sheets to produce a reduced graphene oxide form.

The diffraction spectrum of MnO_2 in this work illustrates similar peak identifications as those shown in previous reports[18, 179] and corresponds to the powder diffraction file from JCPDS 44-0141 (Figure 4.5c). This validates formation of the tetragonal α-phase structure of MnO_2. Furthermore, diffraction peaks of both hybrids (Figure 4.5c) are almost identical to those of the MnO_2 nanowires where the peak intensity

of the (001) reflection of GO has diminished significantly (Figure 4.5d). This has also been previously observed with synthesizing RGO/MnO_2 with small sheets.[49]

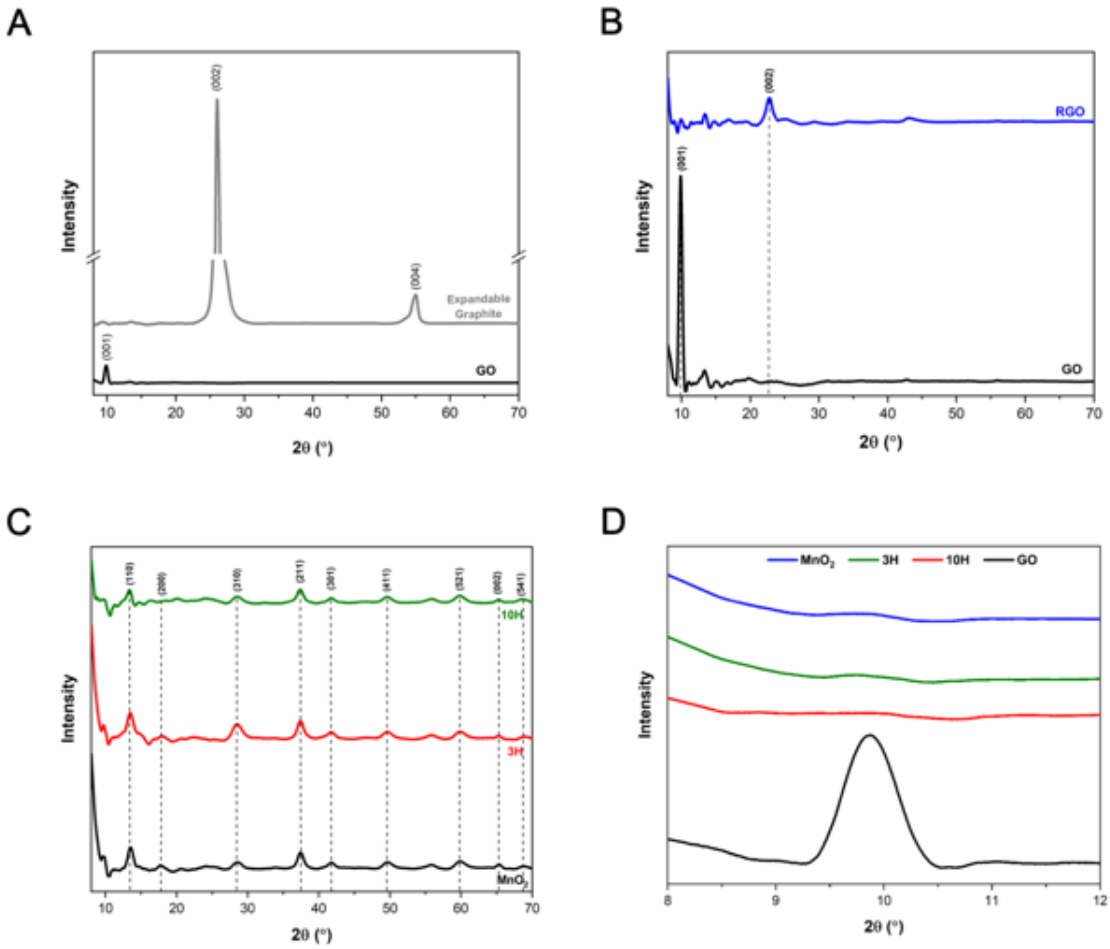

Figure 4.5. XRD patterns of the materials at slow scan rate of 0.01 °/s. a) The expandable graphite exhibits two characteristic peaks that correspond to a d-spacing of 0.342 nm and GO exhibits an intense peak at 2θ = 9.9° with calculated d-spacing of 0.892 nm indicating oxidation of the sheets. b) RGO spectrum exhibits a (002) peak at 2θ = 22.7° with calculated d-spacing of 0.391 nm, conveying successful reduction of GO. c) The spectrum of MnO_2 confirms formation of the α-phase crystal structure and both hybrids display a similar pattern. d) magnification of low 2θ angles.[166]

4.2.3.3 Raman analysis

Raman spectroscopy was performed to further characterize the structures of all the materials. The Raman spectra of expandable graphite, GO, and RGO are presented in Figure 4.6a. The D-band of carbon-based materials is ascribed to the density of disorder sites, or sp^3 characteristic, and the G-band is associated with the sp^2 conjugated structure of the carbon domains.[180] The D and G bands occur around 1355 and 1595 cm^{-1}, respectively. The D/G intensity ratio for expandable graphite (Asbury Carbons) was 0.22. Interestingly, the D/G ratios of GO and RGO are 1.46 and 1.72, respectively. While GO has shown to have multiple oxygen functional groups along the sheet edges and basal planes, RGO has shown to lack some of this functionality as demonstrated from FTIR spectroscopy and XRD results. The higher D/G ratio suggests a higher defect concentration is introduced into the structure as the thermal annealing procedure occurs, which provides support that RGO was successfully obtained. The increased ratio is also attributed to the formation of many smaller graphitic domains as a result of reduction.[180-183] Another procedure for the reduction of GO is by chemical methods (eg. hydrazine, L-ascorbic acid, or sodium borohydride) and has shown D/G ratios of up to 0.90.[9, 43, 178, 184] Thermal annealing studies of graphene-based materials previously reported in the literature have demonstrated effective thermal reduction that results in more conductive graphene materials, typically with values greater than 1.[10, 62, 185-187] In addition, the 2D and G' peaks appear in graphene-based materials that can be used to identify the presence of graphene layers.[186, 188] The 2D band occurs at ~2700 cm^{-1}, while the G' band occurs at ~2930 cm^{-1}. The clear identification of the sharp 2D bands indicate the RGO and hybrids have decreased layers of graphene sheets. The ratio of G to 2D bands was also much greater than

1 for GO, RGO and hybrids compared with the expandable graphite, which shows a few-layered structure.

The Raman spectrum of MnO_2 consists of multiple peaks in the region of 100 – 1000 cm^{-1} (Figure 4.6b). Magnification of this low wavenumber region is presented in Figure 4.6c. The most intense peaks identified in this work occur at the Raman bands of 180, 382, 579, and 629 cm^{-1}, as well as five weak peaks that occur at 281, 322, 463, 504, and 745 cm^{-1}, which are all in agreement with previous studies[175] on MnO_2-type materials that are attributed to the Mn-O lattice vibrations. The external vibrations are due to translational motion of the MnO_6 octahedra framework at 180 cm^{-1}, Mn-O bending vibrations at 380 cm^{-1}, tunneling species at 579 and 629 cm^{-1}, and antisymmetric Mn-O stretching vibrations at 745 cm^{-1}.[189] Comparison of these spectroscopy results with previous reports in the literature that utilize $KMnO_4$ as the reactive species for MnO_2 synthesis reveals successful formation of α-phase MnO_2.

Both hybrid materials consist of RGO; therefore, they have D and G peaks. Peaks for MnO_2 and RGO are evident in the hybrid spectra. The values of D/G for 3H and 10H are 1.65 and 2.20, respectively. The higher D/G ratio of 10H compared with 3H indicates more disorder in the carbon structure which also results in lower electron mobility.[190] The content of MnO_2 can be determined by comparing the ratio of MnO_2/RGO in the hybrid spectra as also examined in previous reports.[49, 191, 192] 10H exhibits a higher ratio of the Mn-O to G-peak than 3H, further confirming that more MnO_2 is bound to the RGO sheets in 10H.

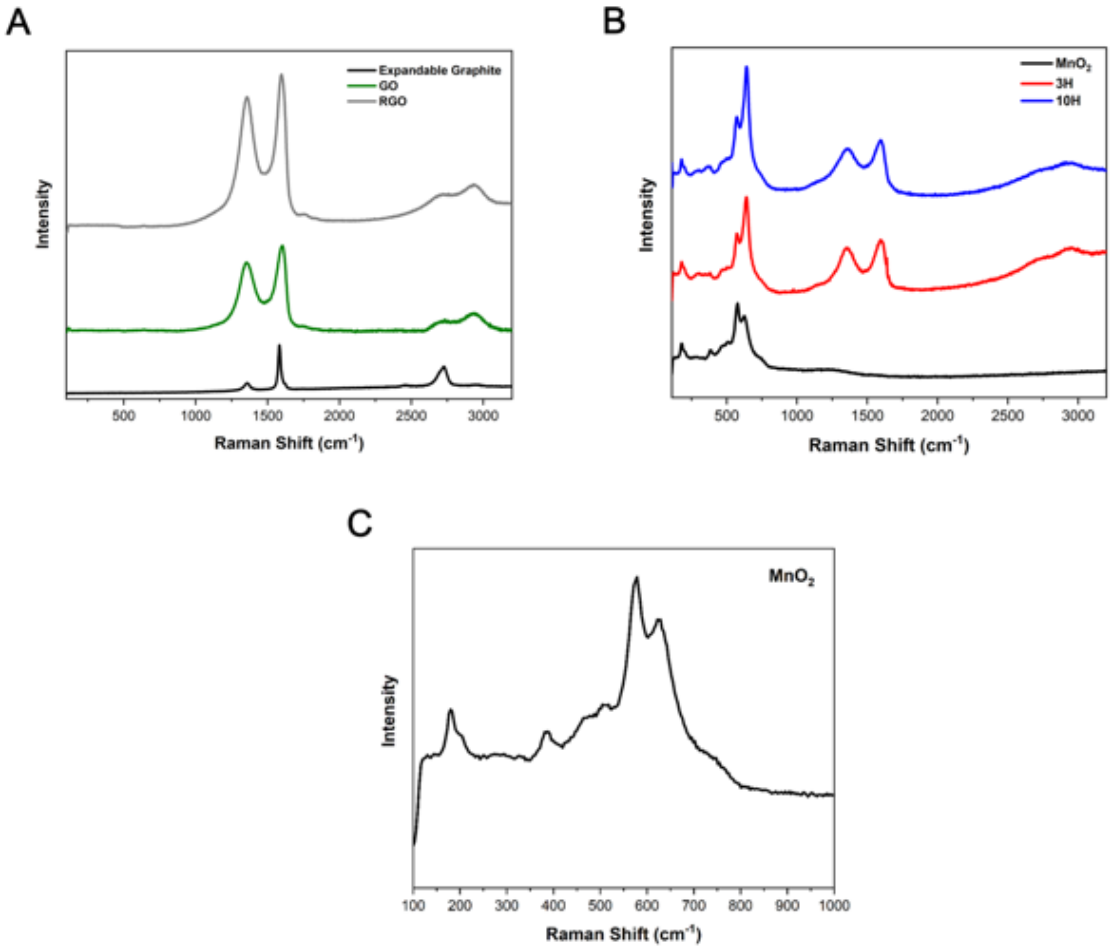

Figure 4.6. Raman spectra performed using a 514 nm laser. a) Expandable graphite, ultra-large GO, and RGO result in D/G ratios of 0.22, 1.46 and 1.72, respectively. b) The 3H and 10H hybrid materials exhibit D/G ratios of 1.65 and 2.20, respectively. The ratio of Mn-O to G-peak is higher for 10H than 3H, further supporting the presence of more MnO_2 content. c) Magnification of the spectrum of MnO_2 confirms α-phase morphology produced from potassium-based reactive species.[166]

In summary, the microscopy, thermal, and spectroscopy analyses performed on the individual (expandable graphite, GO, RGO, P-RGO, and MnO_2) and multi-component materials (3H and 10H) provide a detailed understanding to their microstructure and behavior. For the first time, we reported in this work the successful integration of ultra-

large GO sheets and nanowire-like morphology of α-phase MnO_2 that co-exist in the hybrid materials with two different compositions. In the next section, the electrochemical behavior of the materials is explored.

4.2.4 Electrochemical Capacitive Behavior

The materials GO, RGO, MnO_2 and hybrids 3H and 10H were fabricated into supercapacitor electrodes and characterized by cyclic voltammetry at varying scan rates to determine their electrochemical response and explore potential applications in energy storage. The electrochemical properties were measured using a three-electrode configuration in 1M Na_2SO_4 electrolyte. Cyclic Voltammetry (CV) was performed in the potential range of -0.2 – 0.8 V at scan rates of 5, 10, 20, 50, and 100 mV/s.

The CV curves for all materials at the different scan rates are shown in Figure 4.7.[166] GO is a supercapacitive material that exhibits electrochemical double layer capacitance (EDLC), where non-Faradaic reactions take place at the electrode surface. GO is not conductive; therefore, it has very low specific capacitance. However, RGO has shown some reduction from the characterizations in the previous sections and demonstrates higher capacitance than GO (Figure 4.7b). In contrast to GO, manganese dioxide (MnO_2) is a transition metal oxide that exhibits a Faradaic process along the surface of the electrode material, owing to its pseudocapacitive nature. Figure 6c illustrates the quasi-rectangular shapes of the MnO_2 CV curves, representing pseudocapacitive behavior. The combination of RGO and MnO_2 in the hybrid materials 3H and 10H in this work represents contributions of both pseudocapacitive and EDLC behavior as shown in the CV curves of Figure 4.7d,e. The 10H CV curves look similar to the MnO_2 curves, indicating more pseudocapacitive

effect from the higher MnO_2 content in 10H than 3H. Furthermore, an overlay of all the materials at the lowest scan rate of 5 mV/s is shown in Figure 4.7f. This captures the shapes of the curves together with no obvious oxidation/reduction peaks.

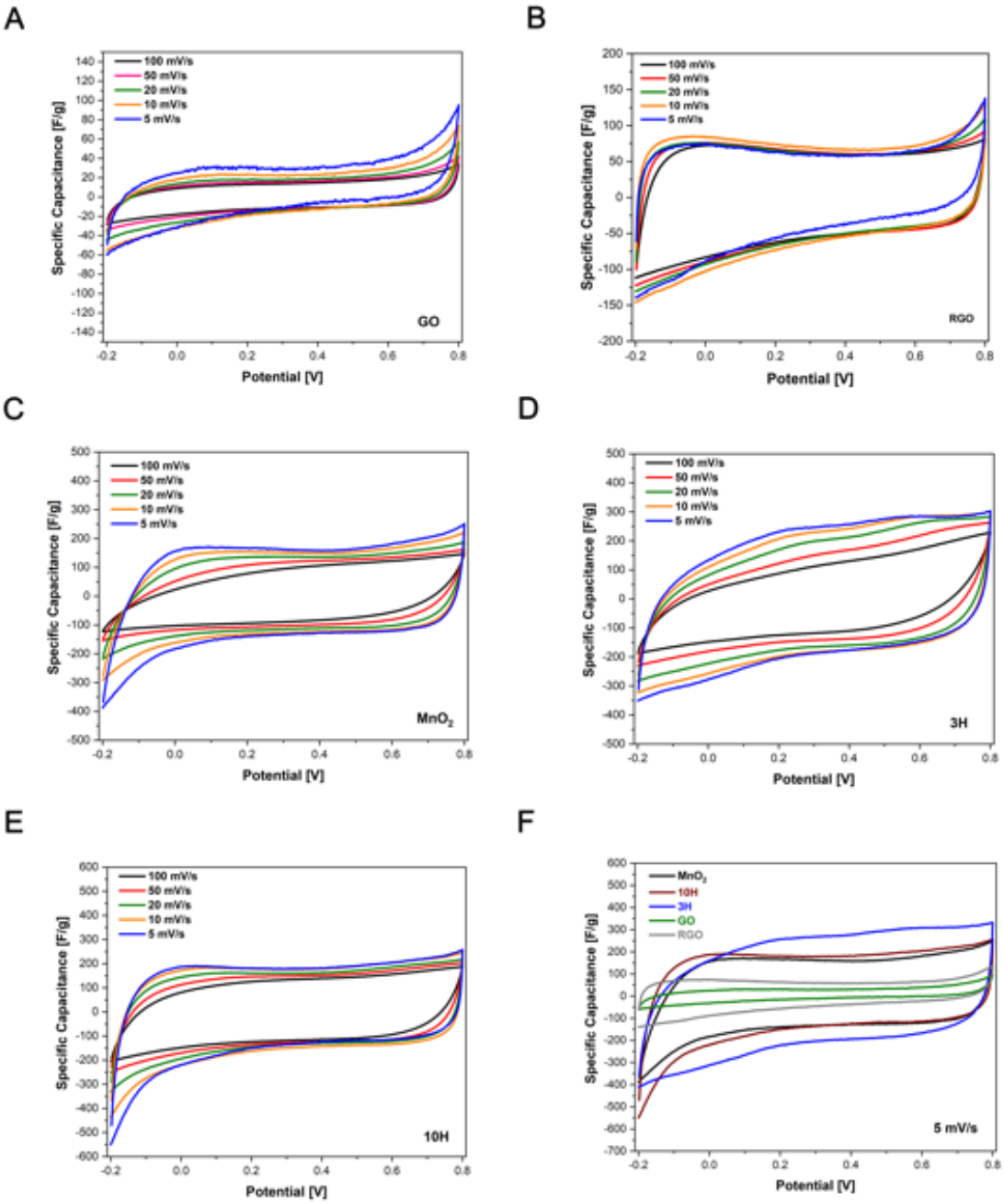

Figure 4.7. Cyclic voltammetry curves at different scan rates of a) GO, b) RGO, c) MnO_2, d) 3H, and e) 10H. f) An overlay of the CV curves of all materials at 5 mV/s scan rate.[166]

The rate capability for the materials is shown in Figure 4.8a. The RGO prepared in this work utilizing ultra-large GO and thermal annealing at 300 °C demonstrates higher specific capacitance than GO. The higher RGO performance confirms the thermal annealing was successful in removing oxygen functional groups as shown by FTIR, XRD, and Raman techniques producing a more conductive material. These results suggest that increasing the annealing temperatures up to 1000 °C may result in enhanced electrical conductivity as previous reports have shown for small sheets of GO.[9, 185, 186] Furthermore, the capacitive performance of MnO_2 exceeds that of RGO. MnO_2 consists of an octahedron configuration and is well-known for its exceptional performance due to its intricate tunnelling structure that enables more efficient ion transfer.

Interestingly, the hybrids exhibit higher capacitance than MnO_2 alone, which can be attributed to more effective ion and electron diffusion in the complex structure that enables faster charge transfer. At the lowest scan rate studied, MnO_2 exhibits a specific capacitance of 145 F/g. Furthermore, 3H exhibits a specific capacitance of ~225 F/g, while that of 10H is 170 F/g. The lower capacitance of the 10H is attributed to a larger fraction of sp^3 hybridized carbon as indicated by its higher D/G ratio.

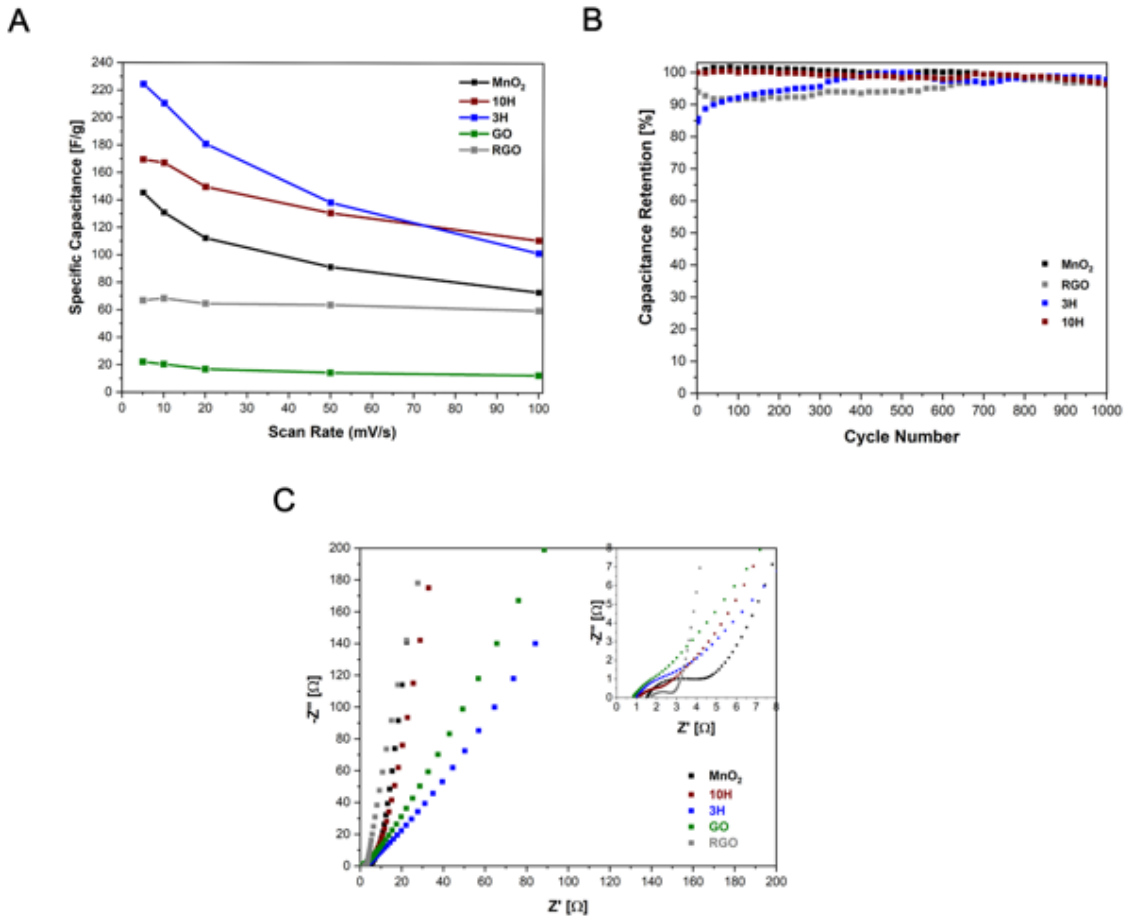

Figure 4.8. Electrochemical behavior with cyclability and EIS. a) Comparison of specific capacitance as a function of scan rate for all materials. b) Cycling behavior over a range of 1000 CV cycles performed at 20 mV/s scan rate. After 1000 cycles, the materials exhibit >95% capacitance retention. c) Nyquist plot overlay of electrodes in 1 M Na_2SO_4 aqueous solution with inset showing high frequency region.[166]

The cycling behavior for the individual and hybrid electrodes was investigated to understand the electrochemical stability of the materials. Repeated CV cycles at a 20 mV/s scan rate were performed for the conductive materials MnO_2, RGO, 3H and 10H. The capacitance retention over the course of 1000 cycles is shown in Figure 4.8b. The results from the cycling studies show that MnO_2 retains 96.5 % capacitance, while RGO retains

96.0%, 3H retains 97.8 %, and 10H retains 96.4 %. This work is inspired in part by few other studies that have investigated the electrochemical behavior of a hybrid of graphene oxide and manganese oxide materials. However, our work is unique by incorporating ultra-large graphene oxide sheets (~40 μm long) which produce larger active surface areas for ion and electron diffusion compared to the smaller graphene oxide sheets (~2 μm long). Previously reported by Chen et al, a graphene-MnO_2 supercapacitor exhibits 197 F/g specific capacitance and after 1000 cycles, the hybrid in their work retained 84 % capacitance.[49] An MnO_2/RGO electrode produced via a hydrothermal method decorating MnO_2 onto the graphene indicates pseudocapacitive and double-layer contributions with the nearly ideal rectangular CV shapes and 205 F/g specific capacitance at 5 mV/s scan rate.[193] However, their work demonstrated ~85% capacitance retention after 1000 charge/discharge cycles. Furthermore, the cycling stability of an asymmetric supercapacitor of MnO_2/rGO hybrid after 1000 cycles remains near 80%.[194] Interestingly, the hybrid electrodes from this research demonstrate higher cycling stability which conveys longer lifetime with the 3H MnO_2/RGO hybrid electrode also demonstrating a high specific capacitance of 225 F/g.

The electrochemical performance of the MnO_2 and hybrid electrodes was further investigated with an electrochemical impedance spectroscopy (EIS) study (Figure 4.8c). The Nyquist profiles in the high frequency region indicate the solution resistance R_s as shown by the intercept of the real axis, which is related to the ionic resistance from the salt solution, contact resistance at the solution/electrode interface, and intrinsic resistance. Furthermore, the high frequency region illustrates a small quasi- semicircle, representing

the charge-transfer resistance R_{ct}. For GO, RGO, MnO_2, 3H, and 10H, the values for R_s are 0.846, 1.75, 1.53, 1.01, and 1.15 Ω, respectively. The values for R_{ct} can be observed from the inset in Figure 4.8c where the straight line intersects the real axis. For all the materials studied, $R_{ct} < 3$ Ω, which demonstrates their excellent charge-transfer resistance. R_{ct} for the hybrids is ~1 Ω, illustrating higher electrical conductivity that enables faster ion and electron diffusion than the individual components which serves as an advantage of combining different morphologies. The Nyquist plots in the low-frequency region represents the diffusion resistance, which shows linear characteristics for the materials. The more vertical the diffusing line is along the imaginary axis, the more representative of ideal capacitive behavior. Comparing the GO and RGO results, it is evident that RGO demonstrates electrochemical behavior closer to that of an ideal capacitor. The lower charge-transfer resistance and combination of pseudocapacitive and EDLC behavior of the hybrids provide advantages as electrode materials than their individual components.

Furthermore, EIS was performed after the 1000 CV cyclability study to determine the changes in resistivity (Figure A.1). There is not a significant change in charge-transfer resistance for the hybrids. Interestingly, in the low-frequency region of the Nyquist profile, the linear characteristics of MnO_2 and 10H exhibit shift to a lower phase angle indicating a deviation from ideal capacitive performance. However, 3H exhibits a shift to a higher phase angle, closer to the imaginary axis, which can be attributed to the higher capacitance retention achieved than the other electrodes studied. The electrochemical behavior studies have shown superior performance for the 3H hybrid electrode, conveying 225 F/g specific

capacitance, 97.8 % capacitance retention after 1000 cycles, very low charge-transfer resistance, and contributions of pseudocapacitive and EDLC components.

4.3 Conclusions

A novel hybrid material consisting of α-type manganese oxide (MnO_2) nanowires anchored along ultra-large reduced graphene oxide (RGO) sheets, comprising of ~40 μm long sheet size and higher specific surface areas than traditional RGO sheets, has been successfully fabricated. Microscopy, spectroscopy, and thermal analysis characterizations of the individual components have contributed to understanding the microstructural development and behavior of the hybrids. The electrochemical results show that in this work the 3H hybrid electrode consisting of MnO_2/RGO (75/25 wt%) exhibits both electrochemical double-layer capacitance and pseudocapacitive contributions as well as low internal resistance (R_{ct} ~ 1 Ω). Furthermore, 3H demonstrates excellent specific capacitance of up to 225 F/g with 97.8 % cycling stability after 1000 cycles. The outstanding electrochemical performance can be attributed to the uniform distribution of the nanowires along the sheets, which suppresses the restacking of the GO sheets, as well as the ultra-large active surface area that reduces ion and electron diffusion lengths and improves charge transfer. The combination of 2D and 1D nanomaterials from this work make them promising candidates for potential applications in electronic devices, catalysts, and sensors.

Chapter 5 Phase Behavior & Rheological Properties of MXene Dispersions

The following chapter is separated into two sections that describe the rheological behavior of a high concentration of an aqueous MXene dispersion and the effects of salt on phase behavior and rheological properties of large flake MXene dispersions. Both projects were collaborative with Dr. Beidaghi's group (Auburn University). Their group synthesized and provided the MXene dispersions for the contributions shown in this work. In addition, Mackenzie B. Woods from the Davis research group led the phase behavior and rheology of the aqueous MXene dispersions with no salt described in Section 5.2. The focus for my part of this research was contributing to the effects of ionic strength by investigating adding salt to various MXene dispersions with different ionic strengths.

5.1 Rheological Behavior of MXene Dispersions

5.1.1 Motivation

Direct ink writing (DIW) is an extrusion-based additive manufacturing (AM) method that has been used for fabricating complex structures for energy storage applications.[27-29, 195] In this printing method, a colloidal or gel-type ink (filament) is extruded through a nozzle and deposited on a substrate in a layer-by-layer fashion to fabricate 3D structures. This direct printing method is more efficient and less complex compared to lithography and deposition methods that have been previously used for the fabrication of 3D energy storage devices.[195] However, fabrication of 3D micro-supercapacitors (MSCs) using extrusion-based 3D printing depends on the availability of printable inks that are based on highly conductive and electrochemically active electrode materials. To be printable, the ink should have a

yield stress, exhibit shear thinning behavior, as well as be viscoelastic to enable each layer to retain its shape while still providing enough fluidity for substrate and interlayer adhesion.[29, 196] Although significant progress has been made in the direct ink writing of electrochemical devices and electrodes based on the materials such as carbon nanotubes (CNTs), graphene, molybdenum disulfide, and a few other materials, most printable inks have been prepared by using additives such as secondary solvents or surfactants to adjust their rheological properties.[32, 197-199] These additives can affect the electrical and electrochemical properties of the printed electrodes and may require removal after printing.[200] In this section, the rheological properties of an additive-free concentrated MXene ($Ti_3C_2T_x$) dispersion are explored that resulted in low-cost and scalable fabrication of high-performance 3D MSCs.

5.1.2 Results

AFM was performed to measure the size and thickness of the MXene flakes as illustrated in Figure 5.1a. The average flake length, or lateral dimension, was ~ 0.3 μm with layer thicknesses of 1.6 nm confirming mostly single-layer MXene flakes, which is in agreement with previous reports.[201, 202] However, the concentration of the prepared dispersions (~0.2 vol%) was too low to achieve the rheological properties required for extrusion printing.[117, 199] Increasing the concentration of MXene dispersions by solvent evaporation is not straightforward. Evaporation of excess water under vacuum at room temperature is time-consuming and may result in agglomeration of $Ti_3C_2T_x$ flakes. In addition, increasing the temperature to accelerate water evaporation rate may result in the oxidation of $Ti_3C_2T_x$ flakes.[203] Therefore, the method reported for concentrating graphene oxide dispersions by

using superabsorbent polymer (SAP) beads[162] was adopted in this work for concentrating MXene dispersions as shown in Figure 5.1b.

Achieving good dispersion quality, including homogeneity, and controlled rheological properties, plays a critical role in the line width and uniformity of 3D printed structures.[117, 199, 204] Figure 5.1c shows that the viscosity versus shear rate behavior of the 28.9 wt % (ϕ = ~7 vol%) $Ti_3C_2T_x$ ink could be fitted to Herschel−Bulkley model. The Herschel-Bulkley model is a type of power-law model with a yield stress as follows,

$$\tau = \tau_0 + K\dot{\gamma}^n \quad (19)$$

where τ is shear stress, τ_0 is yield stress, K is flow consistency index, $\dot{\gamma}$ is shear rate, and n is flow behavior index. Yield stress is defined as the amount of stress required for the fluid to flow and is a fluid-phase property. For concentrated dispersions, the development of a yield stress typically occurs due to the particles linked together to build a network. Once the yield stress is overcome, the shear stress increases with shear rate. For values of the power law exponent $0<n<1$, the fluid is shear thinning, where viscosity decreases with shear rate. The model viscosities were calculated from $\eta = \tau/\dot{\gamma}$, which is the ratio of shear stress to shear rate, and overlayed as curves on the steady shear plots with the data represented by symbols. The model was fit to the data with parameter values τ_0 = 24, K = 1.07, and n = 0.73, where the model maintains <10% error with the data. Shear thinning behavior (Figure 5.1c) above a yield stress that can be overcome in the print head is essential for a uniform flow out of a narrow orifice. Figure 5.1d highlights the dramatic decrease in viscosity that occurs at the yield stress of 24 Pa.

The structure of the printed layers, including shape retention and interlayer adhesion, is largely determined by ink viscoelastic properties. An elastic modulus G′ greater than the viscous modulus G″ enables the printed tracks to retain their shape while still having enough viscous character to enable interlayer coalescence. The ratio of G" to G', called tan δ, describes how viscous or elastic the dispersion behaves. Values of tan $\delta < 1$ indicate more elastic behavior that is desirable to achieve hierarchical architectures by printing. Figure 5.1e shows that for the prepared MXene ink G′ is greater than G″ throughout the measured frequency range; the lower frequencies probe the long-time scale dynamics of the microstructural rearrangement prior to solidification while the higher frequencies probe shorter time scales. Figure 5.1e also shows that G′ is nearly independent of frequency indicating a percolated (continuous) network of sheets even prior to the concentration increase accompanying solvent evaporation. The inverse of tan δ or G′/G″ versus frequency ω is increasingly being used to establish whether an ink has suitable viscoelastic behavior for specific processes including electrospraying, inkjet printing, fiber spinning, and extrusion printing.[117, 205, 206] Akuzum et al.[117] predicted that, for single-layer MXene, $2 < G'/G'' < 20$ in the frequency range $0.01 < \omega < 10$ Hz would be appropriate for the 3D printing process. A similar range was found for the printing ink used in this work (Figure 5.1f).

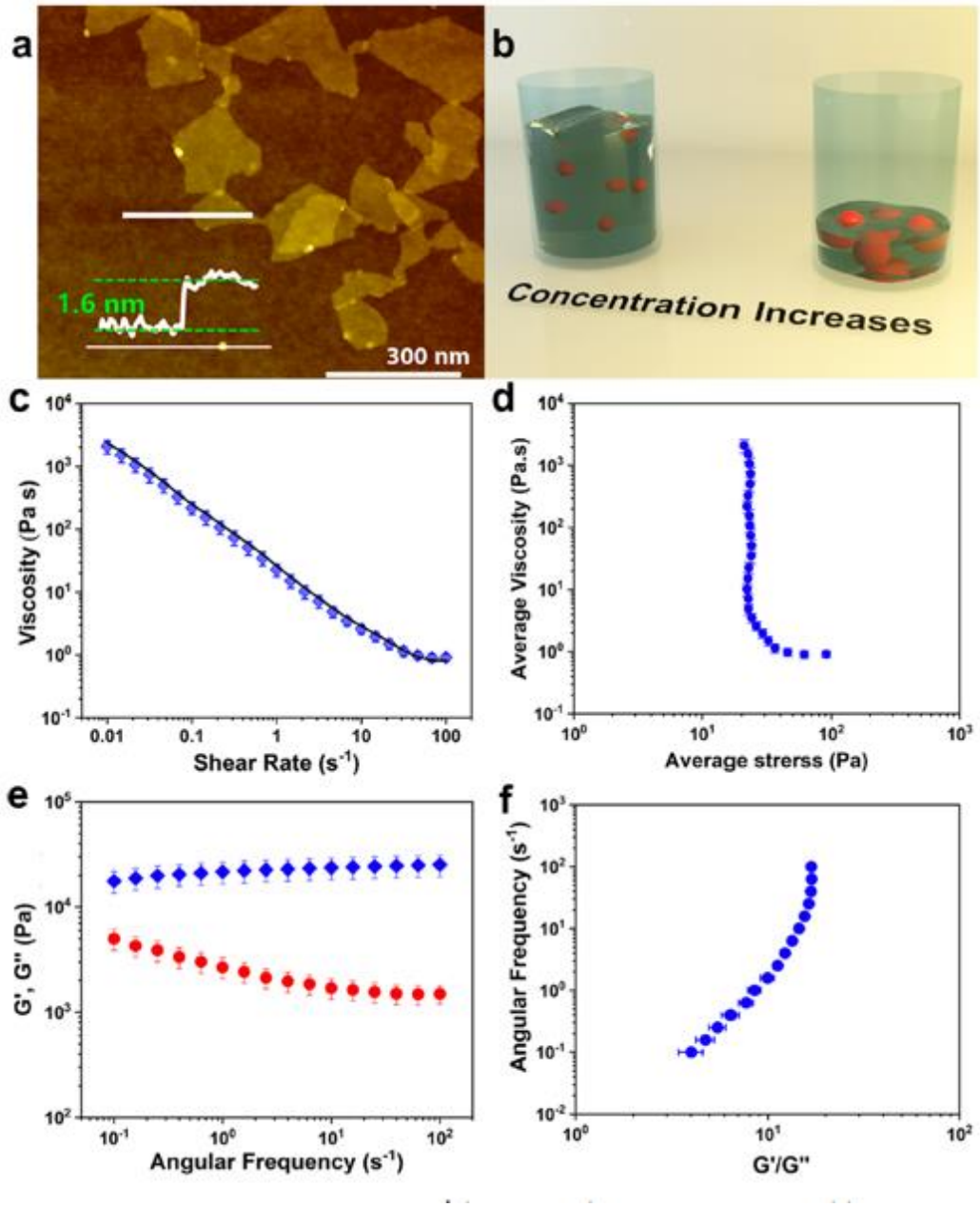

Figure 5.1. Schematic of MXene ink preparation and ~7 vol % MXene ink rheology. a) AFM of MXene dispersion confirming single-layer flakes. b) Adding SAP beads to a low concentration resulted in a uniform concentrated MXene dispersion. c) Steady shear viscosity rheology data (blue diamonds) and Herschel−Bulkley (line) model fit, and d) showing the dramatic viscosity drop at the yield stress. Small amplitude oscillatory shear (SAOS) data show e) G′ (blue diamonds) > G″ (red diamonds) and G′ nearly constant over the measured frequency range, and f) ratio of G′ to G′′ over the measured frequency range. Note: error bars represent standard error (n = 10 for SAOS data and n = 5 for steady shear data).[13]

5.1.3 Conclusions

In this section, the steady shear viscosity and small amplitude oscillatory rheology behavior for a ~29 wt% MXene dispersion were discussed. The rheological properties of the MXene ink, including low yield stress, shear thinning behavior, and higher elastic modulus than viscous modulus allowed room temperature printing of devices that could be fabricated on a variety of substrates including flexible polymer and paper. The prepared ink was used for printing of 3D MSCs with interdigital electrode architectures. Results from this work provided insights into tailoring dispersion concentration of a recently developed 2D material to achieve properties for producing a layered structure. Understanding the flow behavior of an additive-free MXene dispersion enables a foundation for further tuning the dispersion properties.

5.2 Salt Effects on the Phase Behavior and Rheology of Large Flake MXene Dispersions

5.2.1 Motivation

The transition metals and hydroxides of MXenes enable them to exhibit similar behavior to graphenes and nanoclays.[22, 43] MXenes are a recently developed family of 2D inorganic nanomaterials so there is little insight into their dispersion microstructures and rheological responses. Understanding the dispersion phase behavior and rheological properties provides insights into the thermodynamic interactions. The effects of size, shape, and Debye length affect the self-assembly in dispersions, which further affect shear behavior

for processing and final performance. The extensive studies in the literature on GO, nanoclays, and nanoclay/salt systems can be used as a foundation for further developing structure-processing-property relationships of MXenes. For example, increasing the volume fraction of GO with lateral dimension of 0.2 μm resulted in no change in the isotropic phase and no spinnability; however, increasing the volume fraction with 3 μm flakes resulted in formation of a fully nematic liquid crystal that was successfully spinnable.[94, 95] In addition, a previous study investigated the phase behavior of liquid crystalline MXene dispersions where the flakes self-assembled into nematic LC phases at ~13 mg/mL for large (~3 μm) and ~66 mg/mL for small (~0.3 μm) flakes.[25] The formation of nematic LC phases enabled the dispersions to produce fibers by wet-spinning with different morphologies.[25] Viscoelastic and steady shear properties of single and multi-layer MXene dispersions showed ordering and percolation occurring at about three orders of magnitude lower volume fractions for single than multi-layer flakes.[117] This was attributed to the strong surface charge and hydrophilicity of the flakes, which enables their processability at lower concentrations into applications such as thin films, supercapacitors, and 3D printing.[117, 207]

Since MXenes are a new family of materials, there is less understanding of the behavior of the large flakes and role of salt addition on the dispersion microstructure. The focus of this research is to illustrate the effects of NaCl salt on phase behavior and rheological properties with the goal of extending the colloidal framework established for other 2D materials.

5.2.2 Results

5.2.2.1 Material Characterization

Similar to most other nanomaterials, MXenes are polydisperse. Moreover, similar to exfoliated graphene sheets they are irregularly shaped. As for many other nanomaterials, centrifugation has been shown as an effective way to fractionate bulk samples into sample with different average dimensions.[160, 208] Since both phase behavior and rheological properties are largely driven by the ratio of the lateral flake size L to the flake thickness D, SEM, AFM, and DLS were used to evaluate multiple average dimensions in the sample of large flakes by the centrifugation method used in this work. Errors in all the measurements are reported as standard deviation. The representative SEM images in Figure 5.2a show that the flakes are irregularly shaped. Since the longest axis determines the maximum volume swept by the particle, the longest axis of each flake was taken as the lateral dimension L. SEM measurements on 177 MXene flakes resulted in $\langle L \rangle = 2.86 \pm 1.16$ μm as shown in the size distribution plot in Figure 5.2b. The large sheet size made it more challenging to image numerous whole sheets by AFM, but AFM had the advantage of being able to measure thickness. The size and thickness of 50 MXene flakes measured with AFM resulted in $\langle L \rangle = 2.47 \pm 0.99$ μm and thickness $\langle D \rangle = 2.09 \pm 0.39$ nm as illustrated in Figure 5.2c. The size range is in good agreement with previous literature values for a similar MXene synthesis method to obtain large flakes.[13, 25] Hence, the length from SEM and thickness from AFM were used to calculate the aspect ratio (L/D) of ~1400, which is an order of magnitude higher than that of small flake sizes shown in previous reports.[13, 25] Dynamic light scattering (DLS) which measures the hydrodynamic size of the particle, or

lateral dimension based on the volume swept, was used to provide insights into the effects of increasing ionic strength on the effective flake size. For samples prepared from dispersions without NaCl addition, SEM and AFM resulted in similar values, but the measurements by DLS were markedly lower at 1.28 ± 0.097 μm (Figure 5.2d). These results are similar to those of a previous report that shows DLS measurements of ~1 μm compared to ~3 μm size flakes found with SEM, TEM, and AFM.[9] This discrepancy is partially due to the DLS measurements assuming spherical particles and being less sensitive to size differences for particles larger than 1 μm and that sizes are more influenced by the tail of the size distribution. For rods or disks the discrepancies are often minor but the elongated, irregular shapes of MXene sheets along with sheet wrinkling create additional discrepancies. Therefore, while DLS has the advantage of probing a bulk sample of dispersed sheets, DLS measurements need to be interpreted with caution. A key advantage of DLS is that it can be used to probe changes in effective size resulting from varying ionic strength. Salt addition increases the hydrodynamic size measured by DLS from 1.3 μm at 0 M to 5.5 μm at 0.1 M NaCl. In contrast, Natu *et al.* found that for 500 nm MXene flakes increasing NaCl concentration from 0 to 0.01 M results in only slightly increasing size from ~450 to 500 nm.[209]

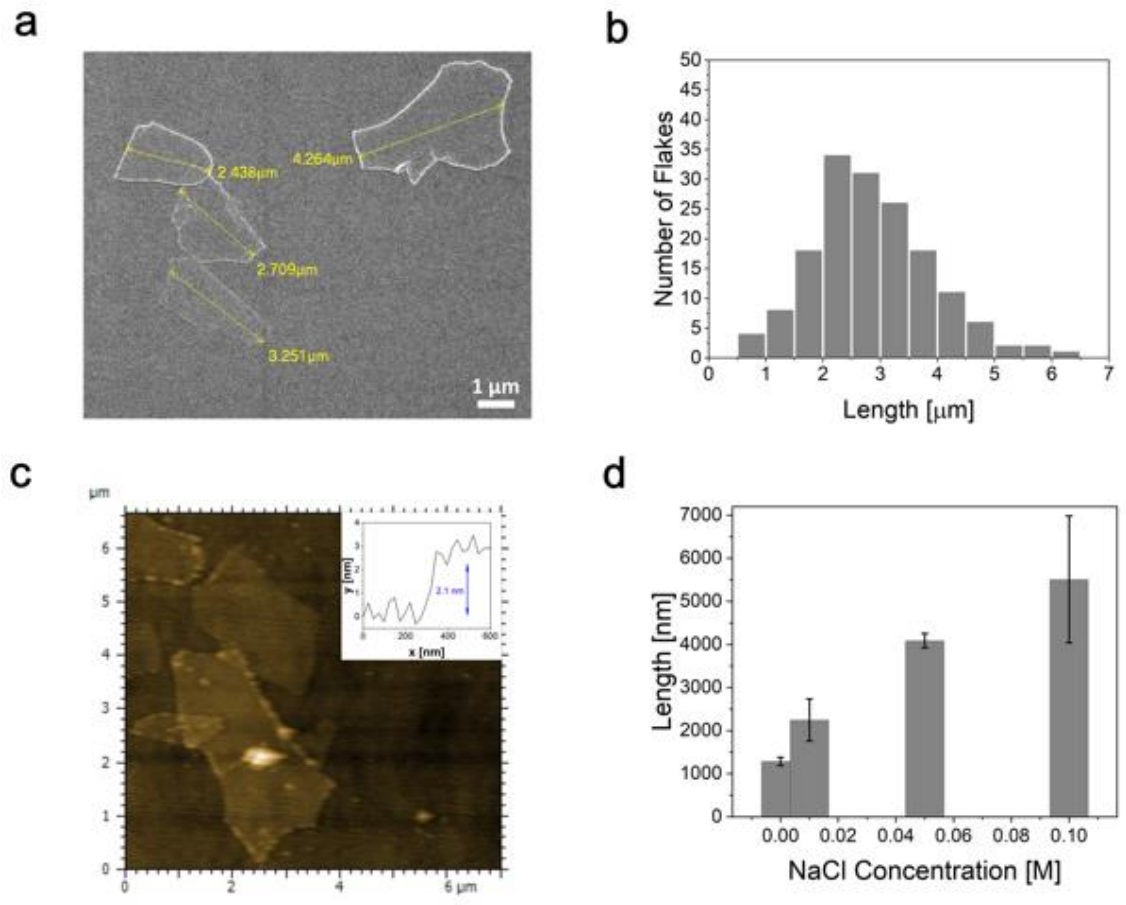

Figure 5.2. SEM showing a) flake morphology and b) size distribution. c) AFM analysis with height profile in the inset and d) DLS of average hydrodynamic diameter versus [NaCl]. Error bars are standard deviation with four measurements at each ionic strength.

5.2.2.2 Dispersion Behavior with Polarized Optical Microscopy

In this study, the phase behavior and rheological properties of large flake $Ti_3C_2T_x$ dispersions were investigated with various concentrations. The range of MXene flake concentrations were from 0.05 – 1.0 vol% with salt concentrations from 0 – 0.5 M NaCl. Specifically of interest is capturing the phase transitions that might occur in the dispersions with increasing flake and salt concentrations. Microscopy and rheology were used to develop a phase diagram was summarized. Since MXenes are a new family of materials,

only very few studies have been performed and characterized the rheological behavior of MXene dispersions.

Briefly, the results in this work provide an understanding of the effects of salt addition on phase behavior and rheology of MXene dispersions. Figure 5.3 shows a comparison of properties with 0 and 0.1 M NaCl with varying flake concentrations. It is observed that drastic increases in the storage modulus G' and yield stresses occur with addition of 0.1 M NaCl.

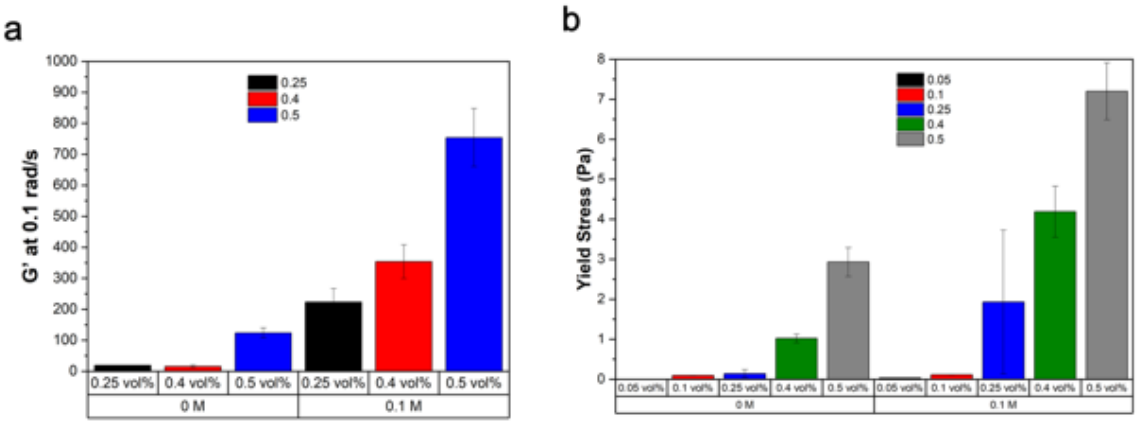

Figure 5.3. Bar graphs comparing 0 and 0.1 M NaCl with varying flake concentrations from a) oscillatory storage modulus G' and b) yield stress.

To understand the phase behavior of MXene dispersions, a series of dispersions were prepared with flake concentrations in the range of 0.05 – 1.0 vol% (2.5 to 55 mg/mL) MXene and 0 – 0.5 M NaCl. In accordance with DLVO theory, increasing MXene concentration decreases the distance between flakes increasing the effects of attractive van der Waals interactions while changing the salt concentration affects the electrostatic interactions. The dispersion behavior is enriched by the flake anisotropy. In 1949,

Onsager's seminal theory of monodisperse spherocylinders with hard-rod interactions showed that the isotropic-nematic (ϕ_I) transition occurs as a result of the loss in orientational entropy being compensated by the gain in translational entropy.[70] As rod concentration is increased, the fraction of the ordered phase becomes more dominant until a fully liquid crystalline (ϕ_{LC}) phase is achieved. Numerical solutions to Onsager's theory for calculating critical volume fractions of the isotropic-nematic transition for colloidal platelets is as follows:[139]

$$\Phi = \frac{\pi}{4}\frac{D}{L}\frac{(1+\sigma^2)}{(1+3\sigma^2)}\rho L^3 \quad (20)$$

where D is thickness, L is length, σ is the polydispersity of L calculated as the ratio of standard deviation to the mean, and ρL^3 = N/V is the dimensionless number density, where N is the number density of MXene flake per unit area and V is the volume of MXene flake. While this simple model assumes rigid circular disks and the absence of attractive or repulsive forces it provides a benchmark for understanding the phase behavior of the more complex MXene flake dispersions. Using the same L and D as aspect ratio determination, the above equation yields a theoretical isotropic transition Φ_I = 0.192 vol% (10.0 mg/mL) and liquid crystalline transition Φ_{LC} = 0.196 vol% (10.2 mg/mL) using values of $\rho_I L^3$ = 4.04 and $\rho_{LC} L^3$ = 4.12, respectively, for infinitely thin disks[25, 157, 210].

In this research, birefringence was examined with polarized optical microscopy and considered as indicative of MXene self-assembly into aligned phases. The interparticle distance between the flakes is influenced by the MXene dispersion concentration and is an important parameter to determine stability. Birefringence was detected at a very low flake

concentration of 0.050 vol% (2.7 mg/mL), where the MXene flakes self-assemble into liquid crystalline domains that occurs at about four times lower than that of the theoretical value (0.192 vol%). In addition, the experimental value of Φ_{LC} was found to be 0.25 vol% (13.2 mg/mL), resulting in a wider biphasic region than theoretical calculations. Using the experimentally found phase transitions, the dimensionless number densities were calculated to be $\rho_I L^3$ = 2.22 and $\rho_{LC} L^3$ = 5.56 for isotropic and nematic transition concentrations, respectively. The discrepancies between theoretical and experimental transitions can arise from flake wrinkling behavior and thermodynamic interactions. Also, shifting of the biphasic transition to a lower density and broadening of the biphasic region are well known features of rod-like liquid crystals that result from polydispersity.[139, 211, 212]

Initial visual observations of the MXene dispersions in 0.1 M NaCl are shown in Figure 5.4 where the tubes with the dispersions are turned upside down. The 0.050 vol%/0.1 M and 0.10 vol%/0.1 M dispersions show more liquid-like character compared to 0.25 vol%/0.1 M that holds the dispersion in the bottom of the tube, suggestive of having more solid-like character.

Figure 5.4. Microcentrifuge tubes inverted of MXene dispersion concentrations (left to right) 0.050, 0.10, 0.25, 0.50, 0.70, and 0.80 vol% all with 0.1 M NaCl.

At the lowest studied flake concentration of 0.050 vol%, the polarized optical microscopy images indicate formation of birefringent domains as shown in Figure 5.5a. The addition of salt in the 0.050 vol%/0.1 M dispersion shows non-uniformity as observed in the uncrossed image of Figure 5.5b. Increasing the flake concentration to 0.10 vol%, the long thread like domains weave in and out of the focal plane often extending across the entire field of view (Figure 5.5c). Imaging with the polarizers partially crossed at 85° enabled simultaneous visualization of domains with perpendicular orientations; each domain changed from bright to dark as the circular stage was rotated between the polarizers (Figure 5.6a). The addition of only 0.01 M NaCl at the low flake concentration of 0.10 vol% results in similar behavior with orientational alignment of the domains in the dispersion (Figure 5.6b). However, addition of 0.05 and 0.1 M NaCl disrupted the structure as shown in Figure 5.6c,d and resulted in sedimentation overnight. The uncrossed images of 0.10 vol% in Figure 5.5c,d also clearly show the changes in structures with salt addition.

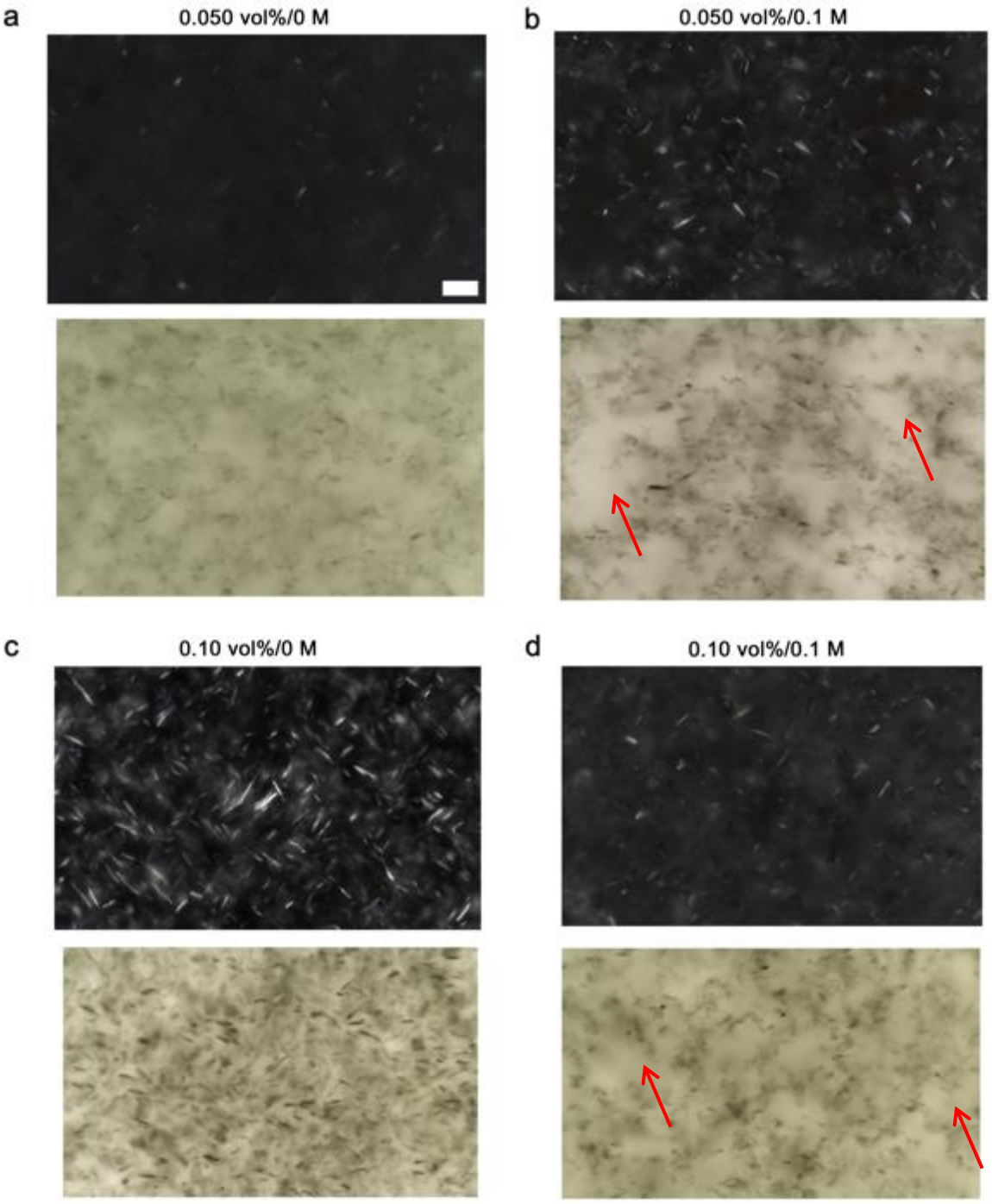

Figure 5.5. Polarized optical microscopy images with the analyzer in crossed (top) and uncrossed (bottom) configurations for a) 0.050 vol%/0 M, b) 0.050 vol%/0.1 M, c) 0.10 vol%/0 M, and d) 0.10 vol%/0.1 M NaCl. Scale bar is 5 μm. The arrows indicate the solvent rich regions (white regions of uncrossed images).

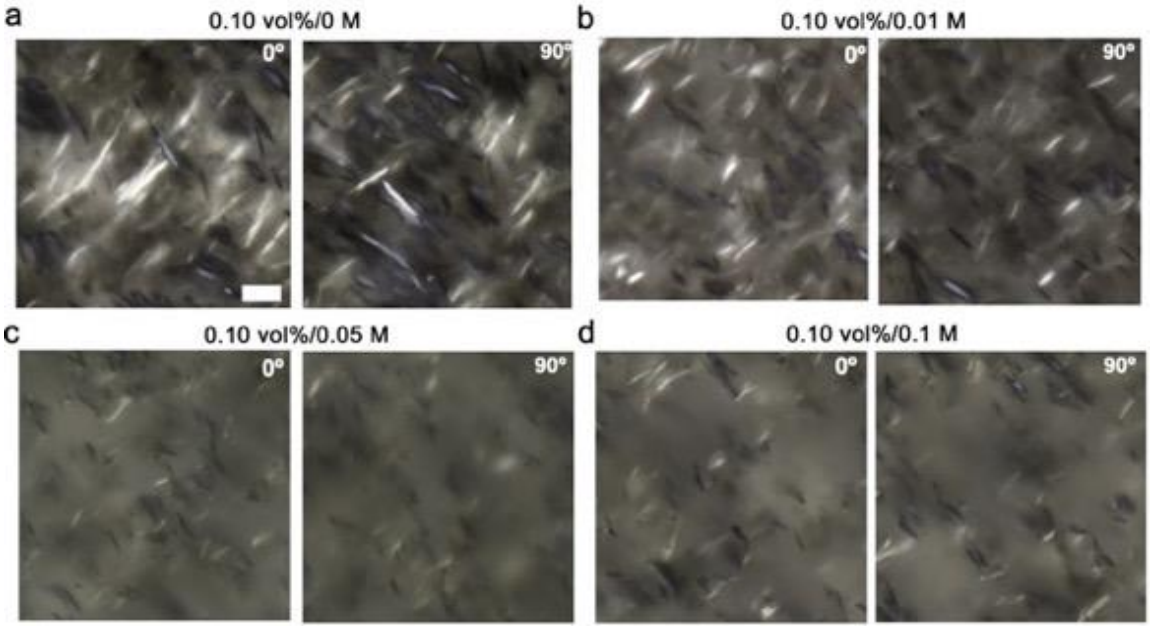

Figure 5.6. Partially crossed optical microscopy of 0.10 vol% with magnified images and stage rotations for a) 0 M, b) 0.01 M, c) 0.05 M, d) 0.1 M NaCl. Scale bar is 5 μm.

The dispersions in the inverted vials from Figure 5.4 showed an interesting change in behavior between 0.10 and 0.25 vol%. Therefore, additional flake concentrations of 0.15 and 0.20 vol% with salt addition from 0 – 0.1 M NaCl were also explored with microscopy. A drastic change in microstructure at 0.15 vol%/0.1 M NaCl was observed as illustrated in Figure 5.7 (uncrossed) and Figure 5.8 (partially crossed) polarized images. The addition of 0.1 M NaCl shows more crowdedness of the flakes and cluster formation compared to the more uniformity in the dispersions with 0 and 0.01 M NaCl (Figure 5.9). Rotation images for 0.15 vol%/0.1 M are illustrated in Figure A.2 indicating some presence of birefringence. Further increasing the flake concentration to 0.20 vol% results in increased particle and solvent interactions and similar large clusters on the order of hundreds of microns spanning the dispersions with 0.05 and 0.1 M NaCl (Figure 5.10 and 5.11). The clusters were easily

phase separated in the vials at these low flake concentrations with salt (Figure 5.12). Together with the presence of birefringence and clusters, the dispersions with 0.05 and 0.1 M NaCl are biphasic and flocculated. However, the 0.20 vol% with 0 and 0.01 M NaCl exhibit birefringence, dispersion uniformity, and alignment similar to the 0.10 and 0.15 vol% both with 0 and 0.01 M NaCl, suggesting they are all in the biphasic region.

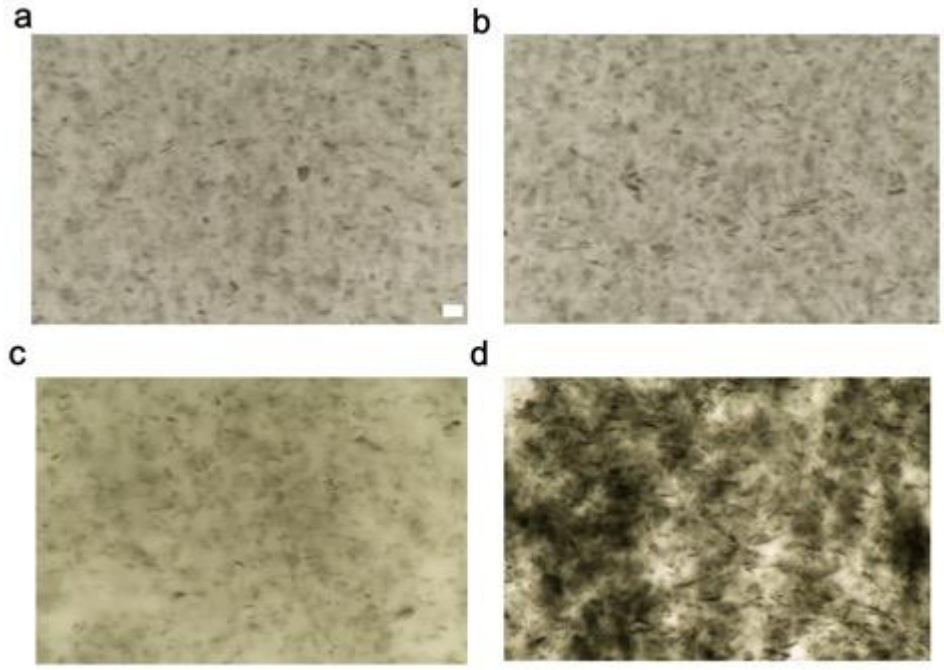

Figure 5.7. Uncrossed images of 0.15 vol% for a) 0 M, b) 0.01 M, c) 0.05 M, d) 0.1 M NaCl. Scale bar is 5 μm.

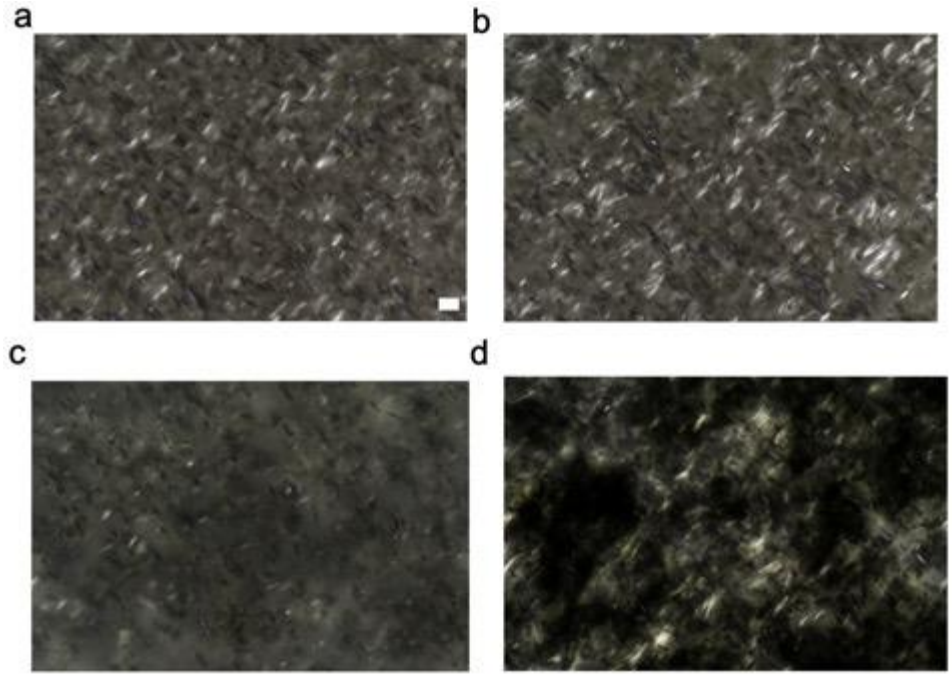

Figure 5.8. Partially crossed images of 0.15 vol% for a) 0 M, b) 0.01 M, c) 0.05 M, d) 0.1 M NaCl. Scale bar is 5 μm.

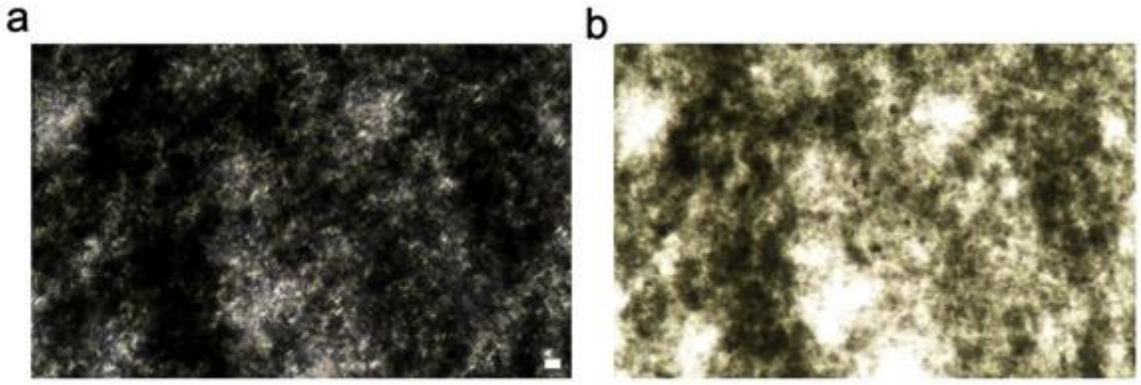

Figure 5.9. Crossed (a) and uncrossed (b) optical microscopy images of 0.15 vol%/0.1 M at lower magnification of 40X. Scale bar is 10 μm.

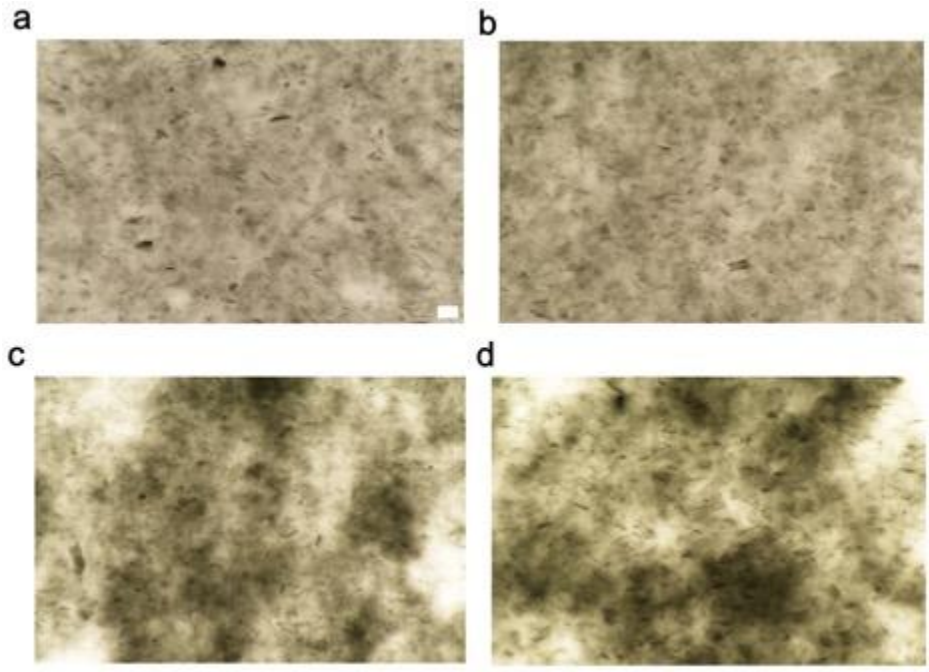

Figure 5.10. Uncrossed images of 0.20 vol% for a) 0 M, b) 0.01 M, c) 0.05 M, d) 0.1 M NaCl. Scale bar is 5 μm.

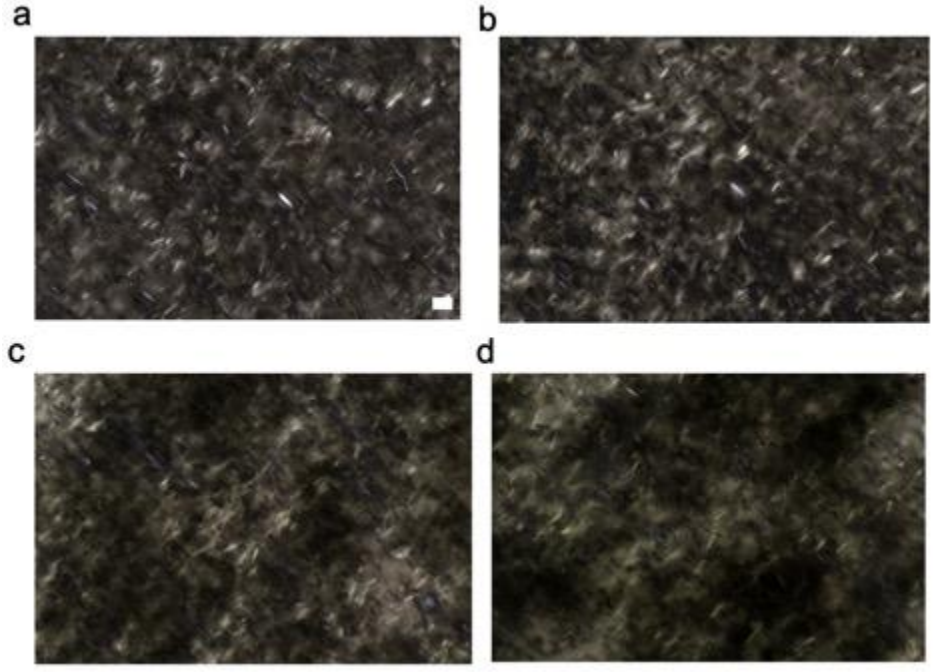

Figure 5.11. Partially crossed images of 0.20 vol% for a) 0 M, b) 0.01 M, c) 0.05 M, d) 0.1 M NaCl. Scale bar is 5 μm.

Additional observations of low 0.20 vol% and 0.40 vol% both with salt concentrations of 0.01, 0.05, and 0.1 M NaCl are shown in Figure 5.12. All of the vials consisted of ~5 mL of MXene/NaCl dispersion and were vortex mixed for ~30 sec and allowed to rest for ~10 min before taking the images. It is evident from the sides of the vials the breakage of the structures at 0.05 and 0.1 M NaCl for 0.20 vol% compared to the more viscous and uniform dispersion with 0.01 M. For 0.40 vol% with salt, more solid-like behavior was observed for all dispersions.

Figure 5.12. MXene dispersions of a) 0.20 vol% and b) 0.40 vol% both with 0.01 (left), 0.05 M (middle), and 0.1 M (right) NaCl.

Increasing the MXene concentration increased the density of the birefringent regions and decreased the isotropic regions (which remained dark regardless of rotation). The uncrossed polarized optical microscopy images for MXene flake concentration of 0.25 vol% at varying ionic strengths are presented in Figure 5.13 and partially crossed images with sample rotations are shown in Figure 5.14. At 0.25 vol% with 0 and 0.01 M NaCl, the entire dispersions appeared birefringent at different stage rotations forming a single-phase nematic liquid crystal (Figure 5.14a,b). In a recent report on the phase behavior of large

(~3 μm) and small (0.3 μm) MXene dispersions, Schlieren texture with defects characteristic of the nematic liquid crystalline phase were found.[25] In this work, at 0 and 0.01 M NaCl up to 0.40 vol%, no obvious aggregation of the MXene flakes was observed. Hence, due to the large size of the flakes, the nematic phase forms large domains with orientational ordering and topological defects present, where the polydomain structure exhibits larger areas than the nematic LCs formed with small MXene flake dispersions[25]. Presence of LC alignment in dispersions is known to provide better properties due to the formation of macroscopic materials with high order.[213] This was observed with a recent study of GO dispersions consisting of sheet sizes larger than 10 μm forming a defect-free nematic liquid crystalline gel-like phase.[214] The nematic LC phase characterized in this work also exhibits alignment over a range of hundreds of microns. Another interesting study with GO sheet sizes of ~37 μm in the gel-like nematic LC region produced robust fibers from wet-spinning that preserved the high order of the sheets as indicated by the birefringent texture.[215]

Addition of 0.05 and 0.1 M causes more crowding of the MXene flakes as shown in Figure 5.13c,d. This is evident of aggregation in the dispersion with darker areas in the images displaying stronger attractive particle-particle interactions, which can be more clearly seen in Figure 5.13 with uncrossed polarized optical microscopy images. The crossed polarized images show a decrease in dispersion birefringence with increasing salt concentration. The aggregation behavior with salt addition is caused by the charge distribution of Na^+ and Cl^- ions interacting with the functional groups along the MXene flakes. As ionic strength increases to 0.05 and 0.1 M NaCl, the Debye screening lengths are 1.36 and 0.96, respectively, which result in higher concentration of charges near the

flake surface. This can impair the self-assembly of the flakes into different structures and rheological properties. The lack of dispersion uniformity was observed at 0.05 and 0.1 M NaCl with the appearance of chain-like or linear aggregates spanning the dispersion. Shielding of the ions on the MXene flakes with increased ionic strength make it difficult to form a homogenous structure; rather, connectivity of the flakes with increased attractive interactions may occur between the faces and edges to produce a linked structure. The larger aggregates of particles sizes observed with optical microscopy are supported with the DLS results in this work. A previous study shows that increasing NaCl ionic strength from 0 to 0.04 M results in increasing zeta potential and decreased light scattering intensities from DLS for the ratio of 500 to 8000 nm, indicating formation of larger structures.[209] In addition, the study also reported the appearance of another peak at 100 nm with salt addition that had much stronger intensities in the size distribution curves than with a high pH, which was attributed to a higher degree of stacking in the lateral direction caused by face-face interactions.[209] Hence, the aggregation mechanism in this work may also be attributed to increased van der Waals attraction, suggesting a lower stability of the higher salt concentration dispersions. The formation of linked structures, or clusters, with varying shapes and sizes of aggregates was studied with light scattering, confocal and optical microscopy, and simulations to understand the gel structure.[127, 216, 217] Cluster morphologies may be driven by the kinetic process of diffusion-limited cluster aggregation, where clusters merge until they connect and span the system.[218] The morphologies of the dispersions with increased salt addition in this work indicate percolated network formation with interconnected aggregates as a result of dominating attractive interactions. This was also observed with their macroscopic grain-like texture compared to the smooth texture of

the uniform dispersion without salt. A clear indication of flocculation occurs with increasing salt concentration as seen with 0.25 vol% with 0.05 M, 0.1, and 0.5 M NaCl.

The critical ionic concentration for flocculation was found to occur at 0.05 M NaCl, representing a Debye length of 1.36 nm on the order of the thickness of the MXene flakes. The 0.25 vol% flake concentration with ionic strengths of 0.05-0.5 M results in insufficient electrostatic interactions to overcome the attractive interactions at small flake distances. The SEM images in Figure 5.15 provide more insights into the structures, although additional association can happen during drying. The dispersion with 0.5 M NaCl exhibits both small flocs few microns long and much larger flocs with evident flake wrinkling and aggregation, supporting the optical microscopy images. The optical microscopy images also show the difference in dispersed (0 and 0.01 M), aggregated and phase separated (0.05 and 0.1 M), and more flocculated (0.5 M) structures. Similarly for high salt concentrations of laponite dispersions, phase separation results in flocculation or sedimentation with aggregates increasing in size over time.[129]

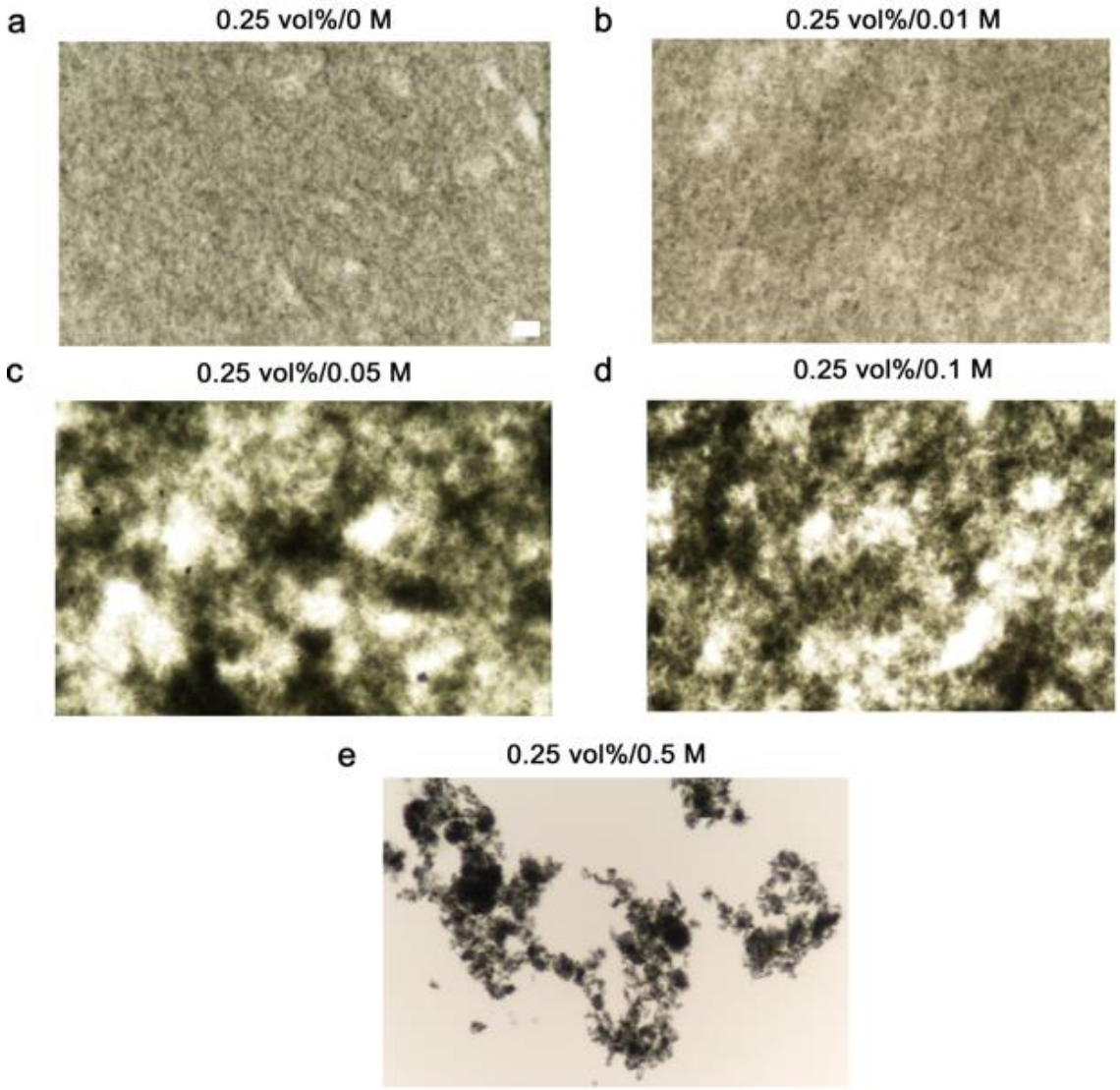

Figure 5.13. Uncrossed optical microscopy images of 0.25 vol% MXene dispersions with a) 0 M, b) 0.01 M, c) 0.05 M, d) 0.1 M, e) 0.5 M NaCl. Scale bar represents 20 μm.

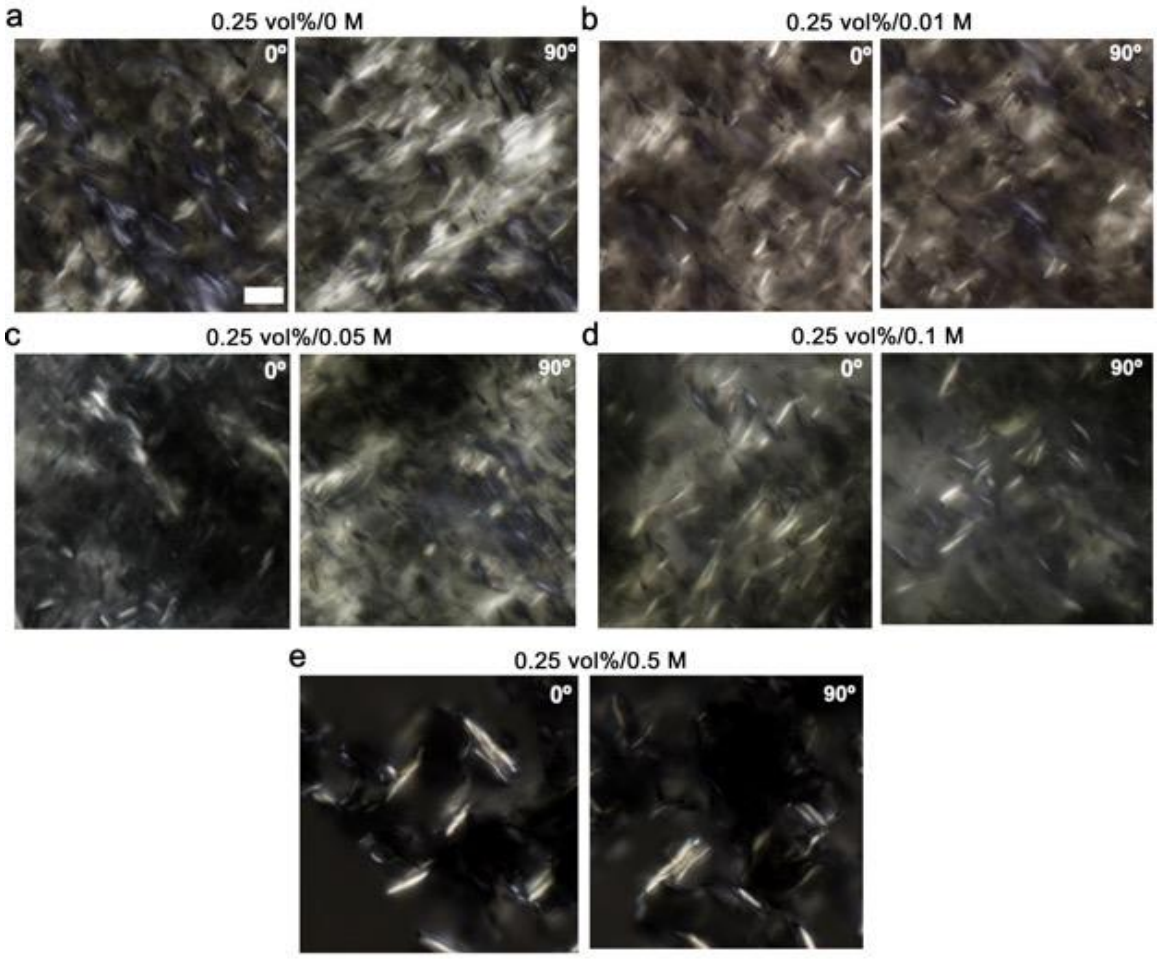

Figure 5.14. Optical microscopy for 0.25 vol% at a) 0 M, b) 0.01 M, c) 0.05 M, d) 0.1 M, and e) 0.5 M NaCl. All images are with 60X/1.40 NA with 2x magnification under partially crossed configurations with 0° and 90° stage rotations. Scale bar is 5 μm.

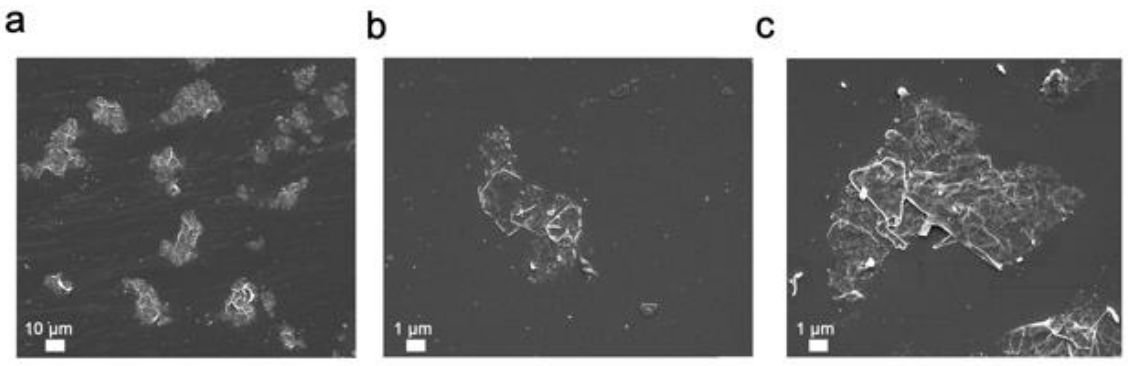

Figure 5.15. SEM of 0.25 vol%/0.5 M at a) low and b,c) high magnifications. Images indicate presence of both b) small and c) large structures form in the dispersion at high salt content.

Increasing the flake concentration to 0.40 vol% (20 mg/mL) maintains the nematic phase for 0 and 0.01 M NaCl with closer packing of the structure (Figure 5.16). Stage rotations indicate full birefringence of the liquid crystalline phase are illustrated for 0 and 0.01 M NaCl in Figures 5.17a and 5.17b, respectively. Comparatively, 0.40 vol% with ionic strengths of 0.05 and 0.1 M NaCl show a decrease in birefringence and increase in aggregation (Figure 5.16). The connected structures of the aggregates suggest the formation of a stronger connected network than 0.40 vol% without salt. LC ordering with presence of aggregates has been shown with GO dispersions in silicon oil and was suggested to form due to van der Waals attractive forces between the sheets.[92] In addition, the optical microscopy with a shear cell showed vorticity alignment of large GO clusters with increasing shear rate.[92]

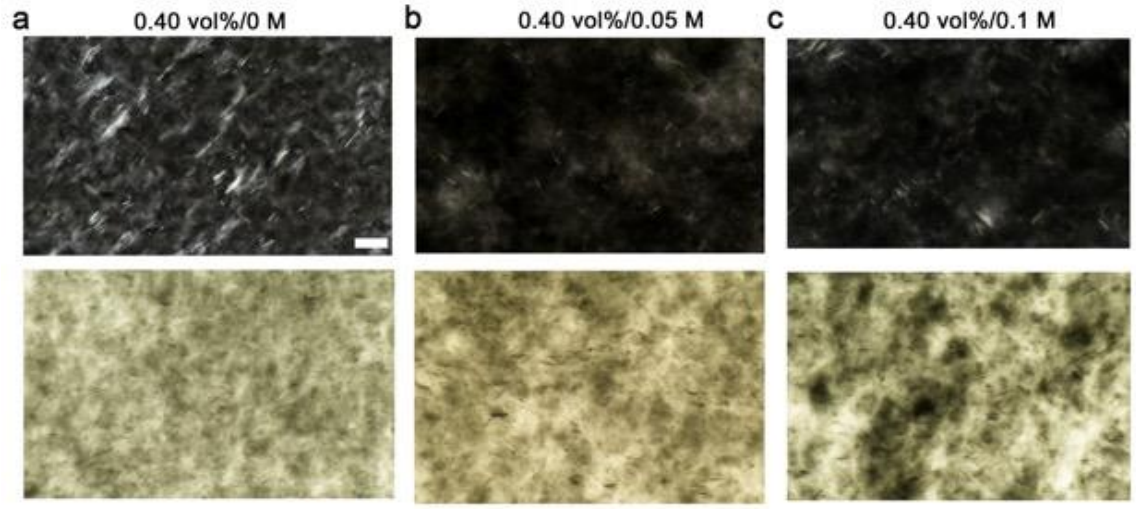

Figure 5.16. Polarized optical microscopy images of MXene dispersion concentration of 0.40 vol% with a) 0 M, b) 0.05 M, and c) 0.1 M under crossed (top) and uncrossed (bottom) configurations.

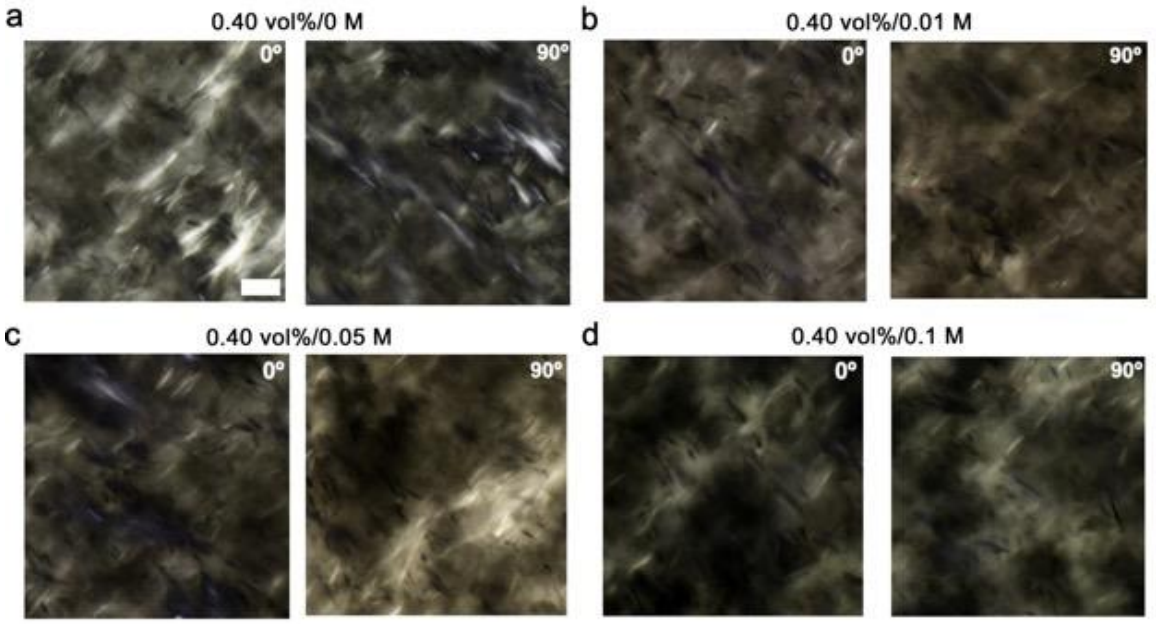

Figure 5.17. Polarized optical microscopy images of MXene dispersion concentration of 0.40 vol% with a) 0 M, b) 0.01 M, c) 0.05 M, and d) 0.1 M NaCl under partially crossed configurations with 0° and 90° stage rotations. Scale bar is 5 μm.

Increasing MXene flake volume fraction to 0.50 vol% transitions the phase behavior to exhibit a gel phase for 0 and 0.1 M NaCl as shown in Figures 5.18a,b, respectively. Interestingly, the optical microscopy images for both dispersions appear to have comparable microstructures. Cluster sizes of ~2-7 μm form throughout the dispersions as shown with the uncrossed images in Figure 5.19 that are on the scale of the contour length of the flakes described previously with the SEM size distribution results. The particles are spatially connected spanning the dispersion and the rotation images illustrate some birefringence (Figure 5.20). Comparing this behavior to that of 0.25 vol% for 0 and 0.1 M NaCl shows very different dispersion microstructures as shown in Figure 5.21. At 0.50 vol% with both salt concentrations, smaller and more circular aggregates form a gel-like network compared to the uniform dispersion at 0.25 vol%/0 M and large clusters of aggregates as flocs at 0.25 vol%/0.1 M.

It has been shown in the literature that aggregates begin to form in GO dispersions above a critical concentration due to their large aspect ratio, wrinkling, and swelling behavior.[219, 220] In a previous report, the network formation in GO was attributed to the percolation of aggregates,[92] which was also reported for a laponite dispersion in poly(ethylene oxide).[221, 222] The breakdown of aggregates with less entanglements that results in shear thinning behavior has also been shown in GO/PDMS systems.[223] The 0.50 vol%/0.5 M dispersion results in flocculation as shown in Figure 5.18c and Figure 5.19c with areas consisting of larger and more dense clusters and smaller flocs similar to those in 0.25 vol%/0.5 M. Scattering experiments, such as SAXS, were used in the literature as fingerprints identifying the gel state where a peak for larger q value shows the short

interparticle distance between aggregates and surplus scattering at low q shows the concentration variations associated with the network structure.[129, 224] Results from this work are promising for exploring scattering techniques as a future study to provide additional insights into the dispersion states of these recently developed materials.

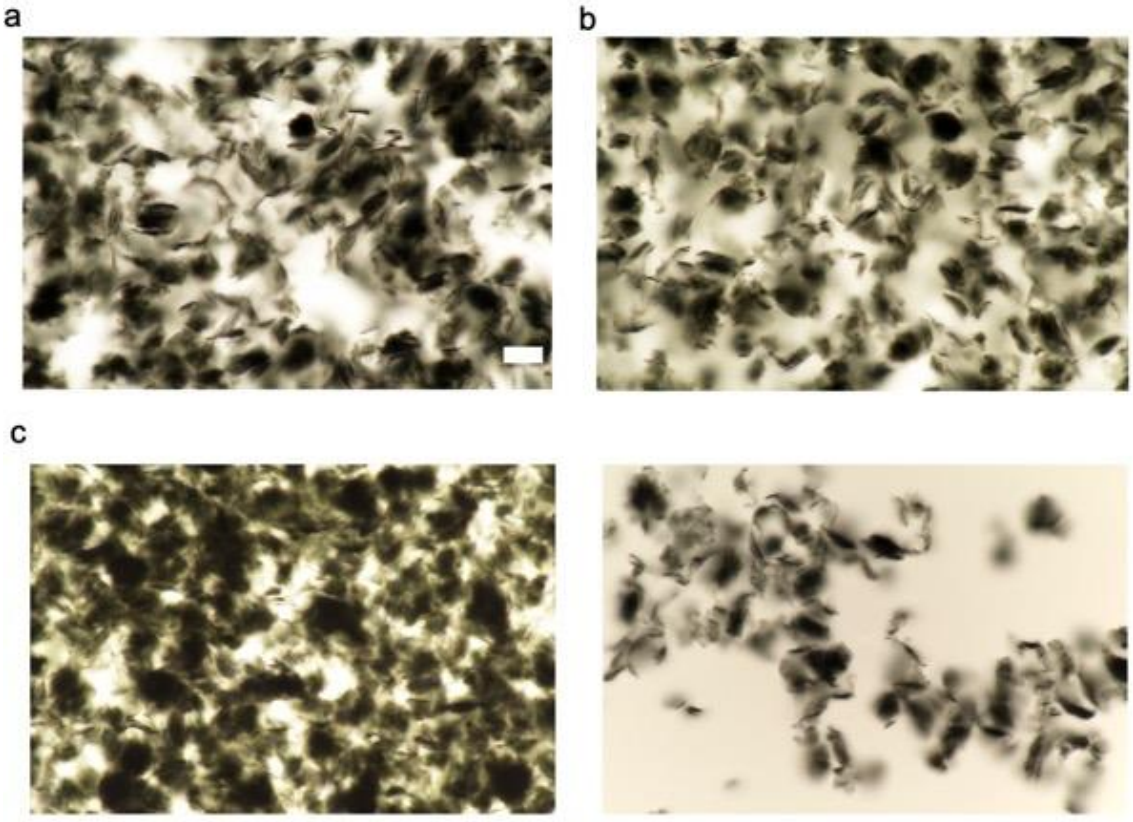

Figure 5.18. Optical microscopy under uncrossed configuration for 0.50 vol% at a) 0 M, b) 0.1 M, and c) 0.5 M consisting of areas with dense (left) and loosely connected (right) particles. Scale bar is 10 μm.

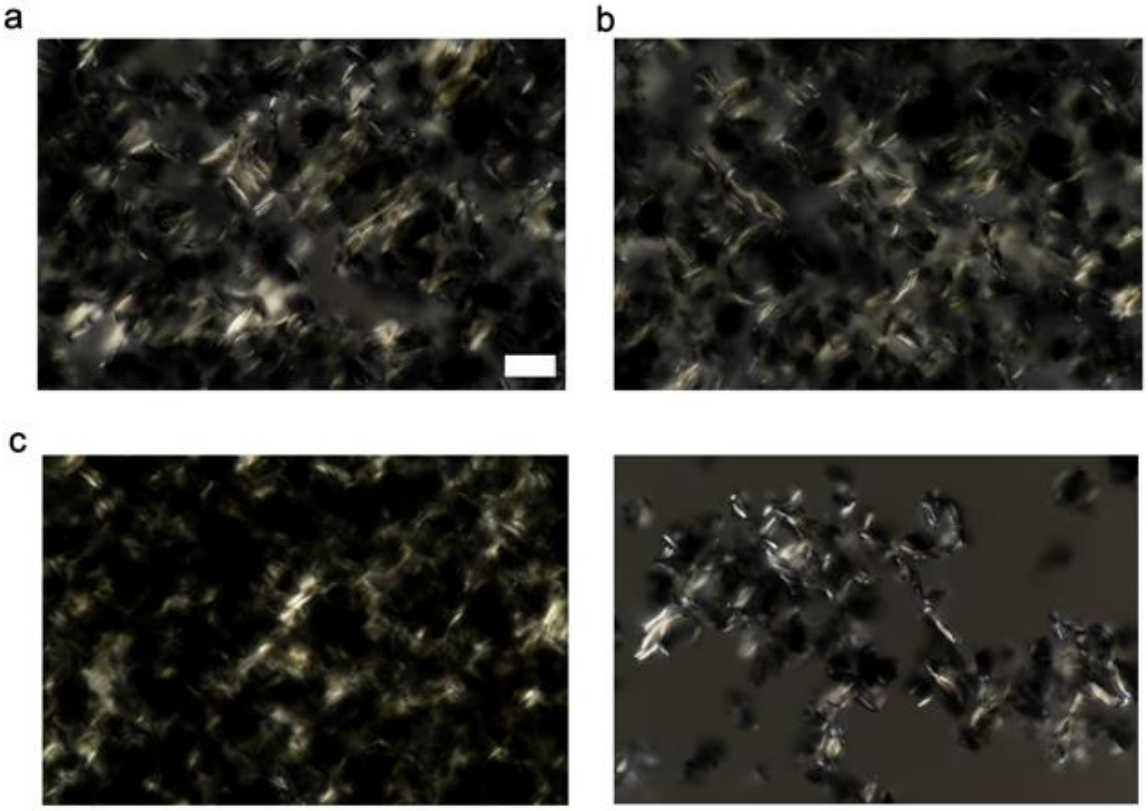

Figure 5.19. Optical microscopy under partially crossed configuration for 0.50 vol% at a) 0 M, b) 0.1 M, and c) 0.5 M consisting of areas with dense (left) and loosely connected (right) particles. Scale bar is 10 μm.

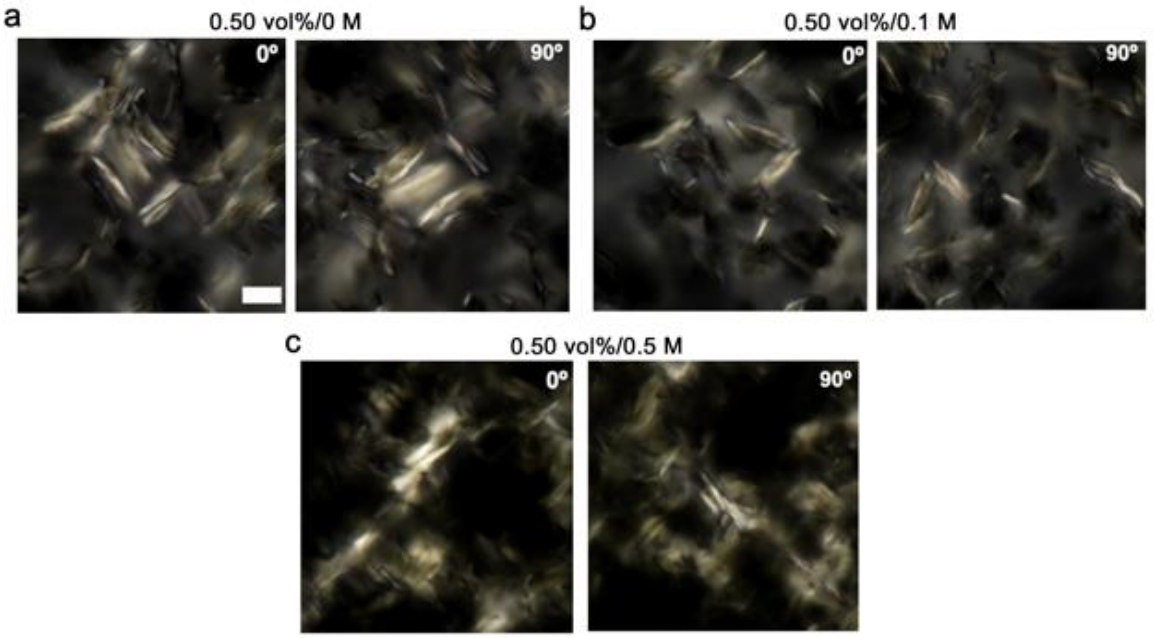

Figure 5.20. Optical microscopy for 0.50 vol% at a) 0 M, b) 0.1 M, and c) 0.5 M. All images are with 60X/1.40 NA with 2x magnification under partially crossed configurations with 0° and 90° stage rotations. Scale bar is 10 μm.

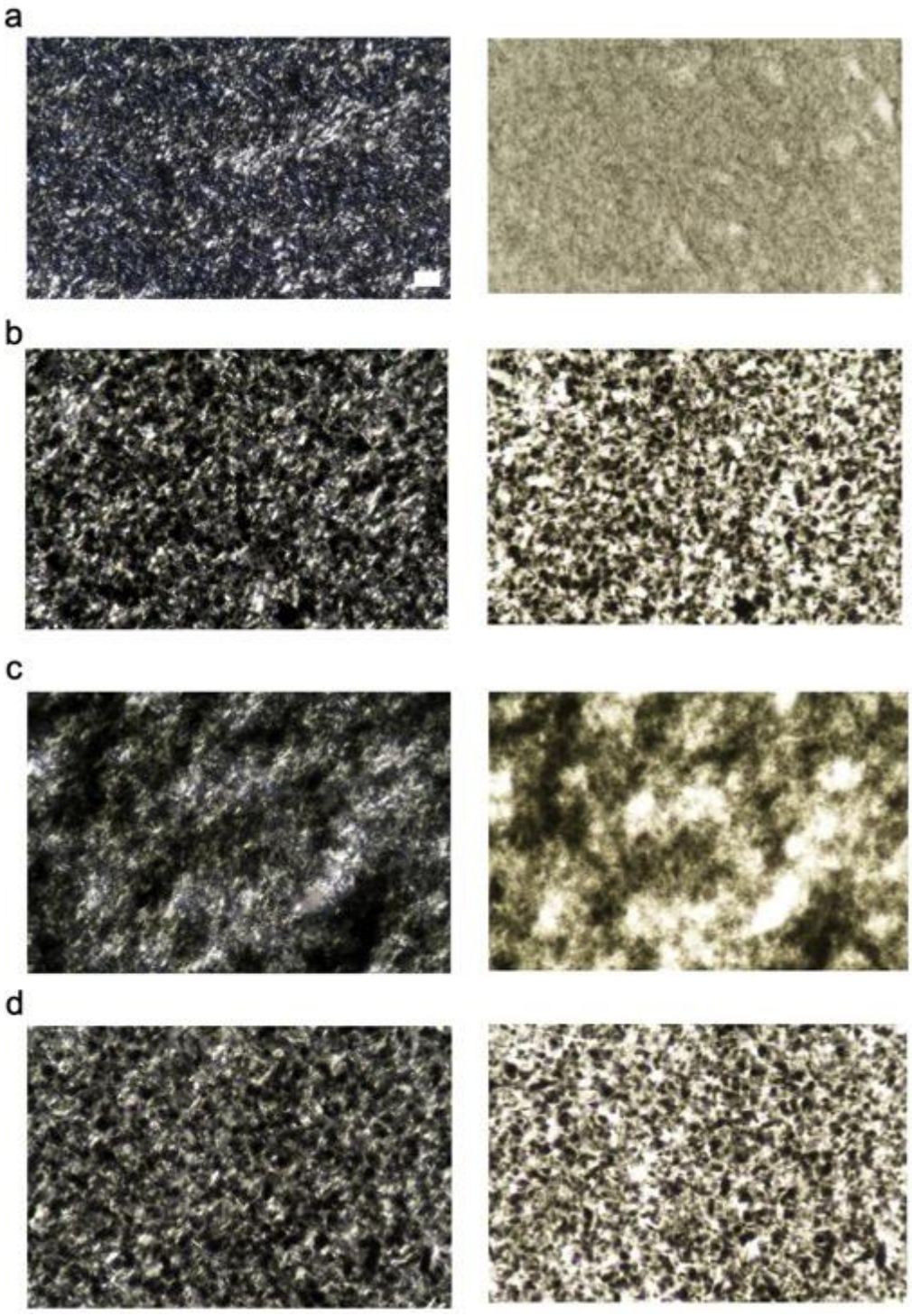

Figure 5.21. Optical microscopy at low magnification of 40X with partially crossed (left) and uncrossed (right) images for a) 0.25 vol%/0 M, b) 0.50 vol%/0 M, c) 0.25 vol%/0.1 M and d) 0.50 vol%/0.1 M. Scale bar is 10 μm.

Additional optical microscopy images were taken of 0.70 vol%/0.1 M and 0.80 vol%/0.1 M as shown in Figure A.3. At 0.1 M NaCl, increasing flake concentration from 0.50 – 0.80 vol% shows increased packing of the network of flakes spanning the dispersion. The rotation images of 0.80 vol%/0.1 M dispersion in Figure A.4 also show regions of clusters of flakes and some domains present in the dispersion. Since MXenes are anisotropic colloids, they show rich phase behavior due to the additional orientational degree of freedom. Further increasing concentration to 1.0 vol% with NaCl results in a grain-like texture in the dispersion that appears mostly aggregated under polarized optical microscopy as shown in Figure 5.22.

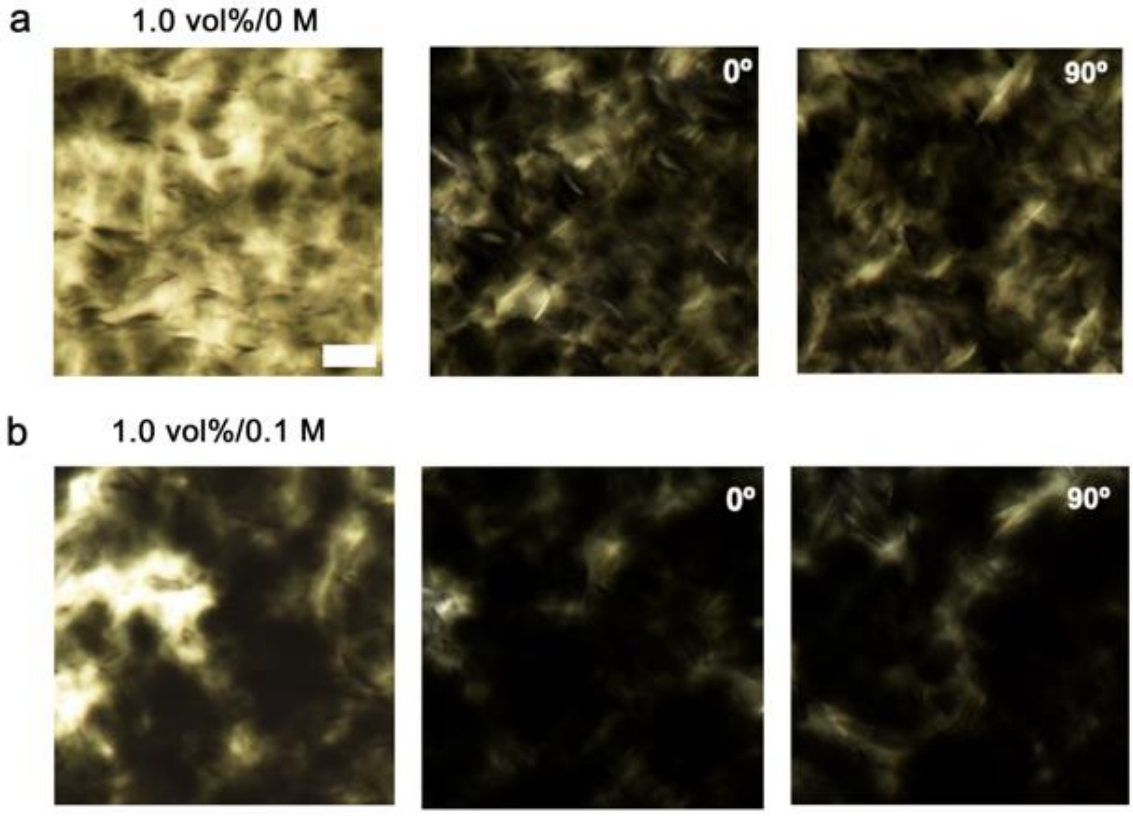

Figure 5.22. Uncrossed (left) and partially crossed (middle and right) polarized optical microscopy images with stage rotations for 1.0 vol% with a) 0 M and b) 0.1 M NaCl.

5.2.2.3 Steady Shear Rheology

In steady shear rheology, a shear stress is applied to the fluid and this external force allows the shear flow to take place. Flow is possible when the applied stress causes the layers of the fluid to move relative to one another creating a velocity gradient, or shear rate. The ratio of shear stress to shear rate is defined as the shear viscosity, $\eta = \tau/\dot{\gamma}$. Newtonian fluids are fluids with shear stress linearly related to the shear rate, hence, invariable viscosity with shear rate. Examples of Newtonian fluids include water, organic solvents, honey, and dilute colloidal dispersions. Non-Newtonian fluids are fluids where the viscosity varies with shear rate. The most common type of non-Newtonian behavior is shear thinning where the fluid viscosity decreases with increasing shear. Some shear thinning fluids show a constant viscosity known as the zero-shear viscosity at very low shear rates. The shear thinning region is identified with a large drop in viscosity and can be fit to a power-law model. It has a linear relationship on a log-log plot of the flow curve, or viscosity versus shear rate plot. In addition, some shear thinning fluids appear to have a yield stress characterized with an increasing viscosity by at least one order of magnitude as shear rate approaches zero. The yield stress is caused by particle interactions resulting in network formation or jamming of dispersed particles that must be broken for the material to flow. When this occurs at higher shear rates, the shear thinning region is the result of the particles rearranging into string-like layers or aligning with the flow. Also, aggregated structures can be broken down. The shear-induced orientation results in decreasing particle interactions as the free space between particles increases, resulting in the large viscosity drop. The infinite-shear viscosity observed at very high shear rates largely depends on the

solvent viscosity and hydrodynamic forces in the dispersion. Typically, the highest degree of orientation achievable at the lowest attainable viscosity.

Many shear thinning fluids possess viscoelastic properties that can be characterized with dynamic oscillatory rheology. At rest, they can form intermolecular or interparticle networks such as by polymer entanglement or particle association. The presence of a network structure identified with a yield stress gives the material predominantly solid-like characteristics. Elasticity is the strength related to the binding, or interparticle forces holding the network together. Prior to the yield stress, the material typically undergoes elastic deformation or simply stretching. The yield stress then indicates when the elastic structure breaks down. When the shear stress applied exceeds the yield stress, the network structure will collapse and the material will begin to flow as if it is a liquid.

Rheological properties are very sensitive to changes in interactions and dispersion state and provide information on fluid flow relevant for fluid phase processing methods such as fiber spinning and direct ink writing. Low flake concentrations were initially investigated with varying salt concentrations as shown in Figure 5.23. The lowest tested concentration was 0.050 vol% (2.6 mg/mL) shows a low viscosity of 0.20 Pa s at the lowest shear rate 0.01 s^{-1}. The viscosity decreases sharply indicating shear thinning behavior from 0.20 to 0.002 Pa s from shear rates 0.01 to 2 s^{-1}, respectively, then shows Newtonian plateau-like behavior between 2 – 100 s^{-1}. At 100 s^{-1}, the viscosity is 0.0013 Pa s which is close to that of the solvent water (0.001 Pa s). Adding 0.05 and 0.10 M NaCl to the 0.050 vol% results in similar shear thinning behavior with steeper slopes at low and intermediate shear rates up to 2 s^{-1} followed by smaller slopes at higher shear rates up to 100 s^{-1}.

However, with increasing salt addition, the viscosities also increase. For example, the viscosity values at a shear rate of 0.2 s^{-1} are 0.015, 0.036, and 0.12 Pa s for 0, 0.05, and 0.1 M NaCl, respectively. The viscosities are about twice as high with addition of 0.05 M NaCl and about an order of magnitude higher compared to no salt. The data was also modeled with a power-law model with the scaling exponent $n = 0.91$ for 0.050 vol%/0 M and no yield stress as also shown in Figure 5.24. Low values of yield stresses were found with the Herschel-Bulkley models fit to the 0.05 and 0.1 M NaCl data and decreasing scaling exponents with increasing salt content. With the polarized optical microscopy results, the 0.050 vol% showed the coexistence of isotropic and nematic phases as the onset of the biphasic region. These findings contradict a recent report in the literature that the MXene dispersion showed only isotropic phase exists below 0.10 vol%.[25]

Increasing the concentration to 0.10 vol% (5.2 mg/mL) shows over one order of magnitude viscosity increase throughout most of the shear rates from 0.01 to 16 s^{-1} compared to the 0.050 vol% dispersion. Between 16 – 100 s^{-1}, the viscosities are about five times higher than the 0.050 vol% dispersion. In addition, the 0.10 vol% dispersion shows a low value of a yield stress of 0.093 Pa with shear-thinning behavior as modeled with Herschel-Bulkley. Together with the optical microscopy results showing some birefringence and some alignment in the dispersion, the rheology supports the transition to a biphasic region where a portion of the flakes remain in the isotropic phase and a portion form liquid crystalline domains. In contrast, the addition of 0.05 and 0.1 M NaCl to the 0.10 vol% dispersion indicate similar trends in behavior to 0.050 vol% without salt where the transition from shear thinning to Newtonian plateau-like behavior occurs at a shear rate of 10 s^{-1}. The power law exponent for both 0.10 vol%/0.05 M and 0.10 vol%/0.1 M is 0.97

which is very close to ideal Newtonian behavior (n=1). This supports the optical microscopy results showing some structure alignment for 0.10 vol%/0 M and structure breaking with more solvent rich regions for 0.10 vol%/0.05 M and 0.10 vol%/0.1 M. Further increasing the flake concentrations to 0.25 vol% and 0.40 vol% show significant changes in steady shear behavior (Figure 5.23 and 5.24).

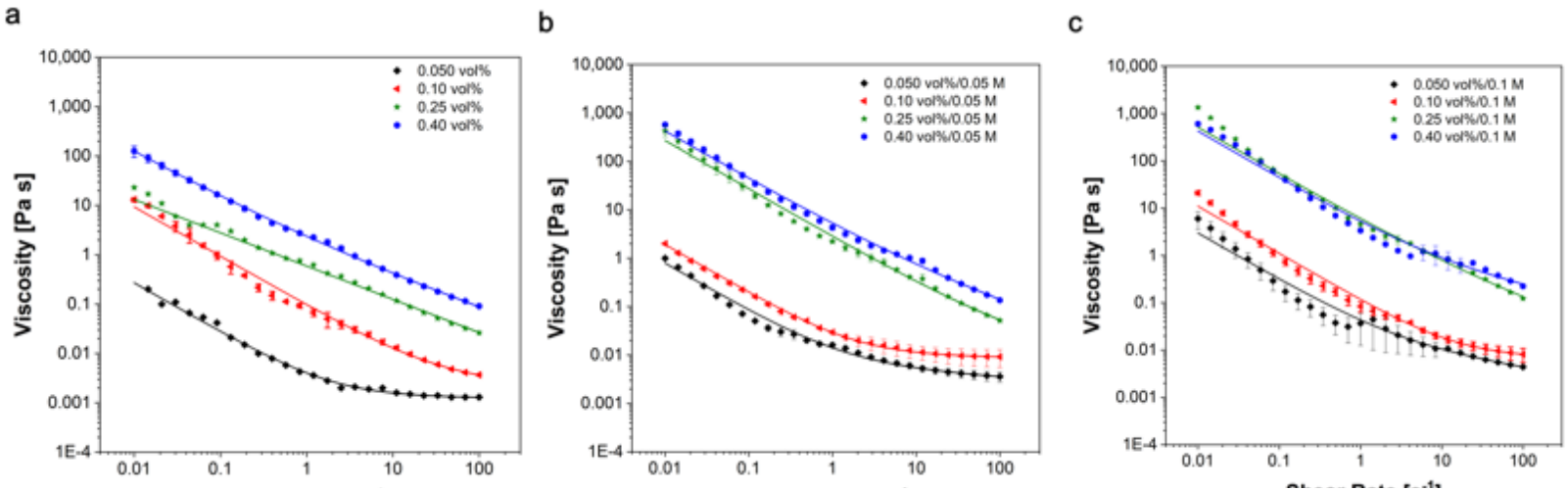

Figure 5.23. Viscosity versus shear rate of flake concentrations 0.050, 0.10, 0.25, and 0.40 vol% with a) 0 M, b) 0.05 M, and 0.10 M NaCl. Error bars are from at least three measurements showing minimum and maximum values.

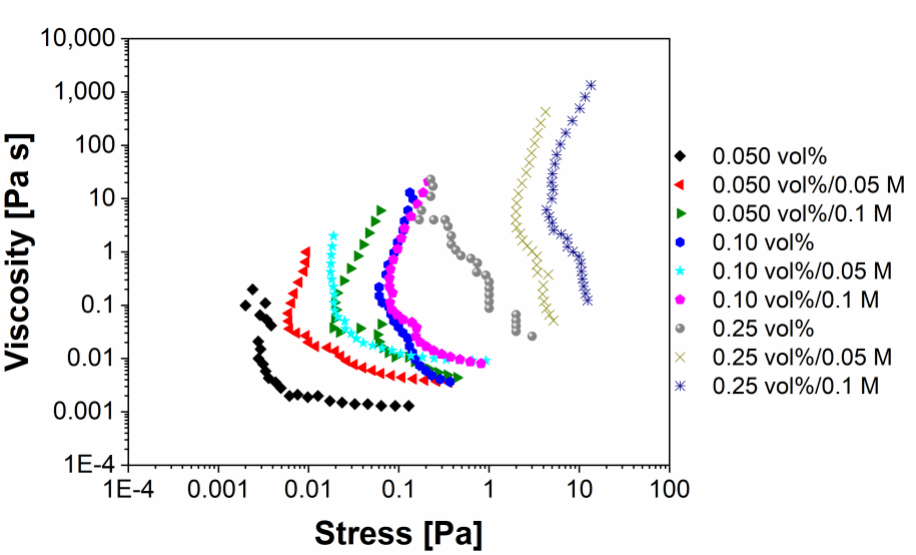

Figure 5.24. Viscosity versus stress of MXene flake concentrations 0.05, 0.10, and 0.25 vol% with 0, 0.05, and 0.1 M NaCl.

Screening was initially performed with many dispersion concentrations and rheology was performed on select concentrations. Rheology was also performed on the 0.15 vol%/0.1 M dispersion which showed a change in phase behavior from the optical microscopy images. Interestingly, the onset of three-region behavior characterized with regions of tumbling, wagging, and flow alignment was observed for 0.15 vol%/0.1 M, which is a signature of lyotropic liquid crystalline phase behavior (Figure 5.25a). A yield stress of 0.71 Pa occurs over about two orders of magnitude of the lower shear rates followed by a plateau region at a viscosity of ~0.1 Pa s, which can also be seen from the yield stress plot (Figure 5.25b). The presence of a yield stress imparts elasticity to the system and indicates network formation, which is supported with the optical microscopy images.

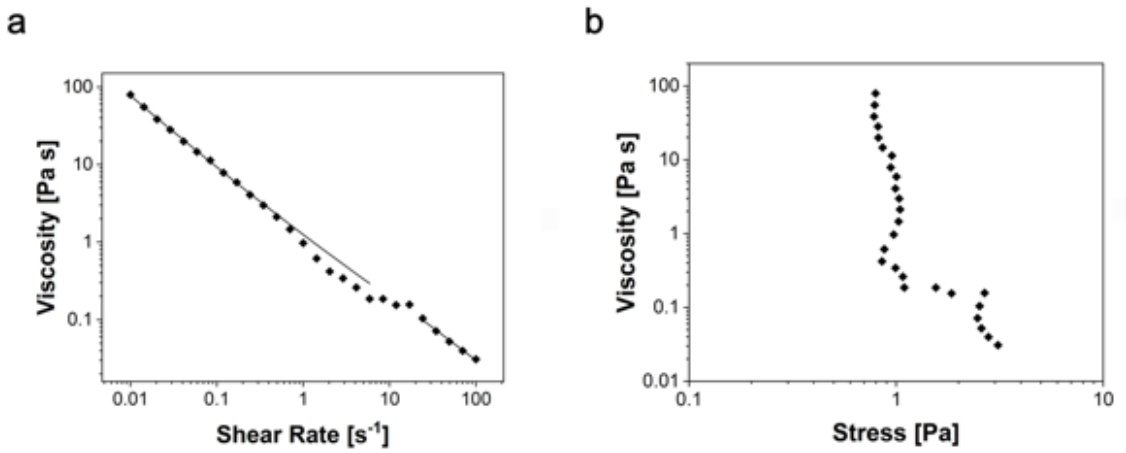

Figure 5.25. Steady shear viscosity measurements of 0.15 vol%/0.1 M dispersion with a) flow curve with Herschel-Bulkley models and b) yield stress.

Rheological properties of 0.25 vol% dispersion were explored in more detail with 0, 0.01, 0.05, 0.1, and 0.3 M NaCl as shown in Figure 5.26. Three-region behavior and yield stress were also observed with the 0.25 vol% dispersion. The presence of a yield stress, complete birefringence and extended alignment of the dispersion from optical microscopy, and three-region behavior support the transition to a fully nematic liquid crystalline phase. Increasing salt concentration from 0 – 0.3 M drastically increases the viscosity and data was modeled with the Herschel-Bulkley model (Equation 19). The data was fit to the model to estimate the yield stress and flow index values. For 0.25 vol%, an order of magnitude increase in the yield stresses was found from 0 to 0.1 M NaCl from 0.14 to 1.9 Pa (Table A.1). In addition, the flow index *n* decreases from 0.88 at 0.10 vol% to 0.38 for 0.25 vol%, supporting its non-Newtonian behavior. Similar decreases in exponent values are observed with salt addition. A more drastic change was also observed at the lowest shear rate of 0.01 s^{-1} with the viscosity values 23, 81, 425, 1,346, 2,190 Pa s for 0, 0.01, 0.05, 0.1, and 0.3 M NaCl (Table A.2).

With increasing salt concentration, the electroviscous effect plays a critical role in regulating the behavior of the charged flakes. For the ionic strengths in this study, the Debye lengths and the term κa where a is the thickness of MXene flake are shown in Table 2. It was suggested that the electrical double layers around particles overlap when $\kappa a \sim 1$ at high concentrations.[225] This occurs for the ionic strengths from 0.1 – 0.5 M NaCl. In this case, the EDL repulsion and van der Waals attraction forces are significant and the secondary electroviscous effect emerges. The remarkable changes in viscosities and viscoelastic properties were also observed in recent reports for laponite composites with NaCl and $CaCl_2$.[137, 226] Cluster formation and subsequent agglomeration of the MXene flakes could contribute to the observation of high yield behavior upon applied stress. The edges of the MXene flakes are positively charged while the planar surfaces are negatively charged, which can lead to face and edge interactions. The attraction between these bonds can also link the flakes and create a network structure.

Table 2. Electroviscous Effects

Ionic Strength (M)	Debye Length κ^{-1} (nm)	κa
0.01	3.04	0.34
0.05	1.36	0.76
0.1	0.96	1.1
0.3	0.55	1.9
0.5	0.43	2.4

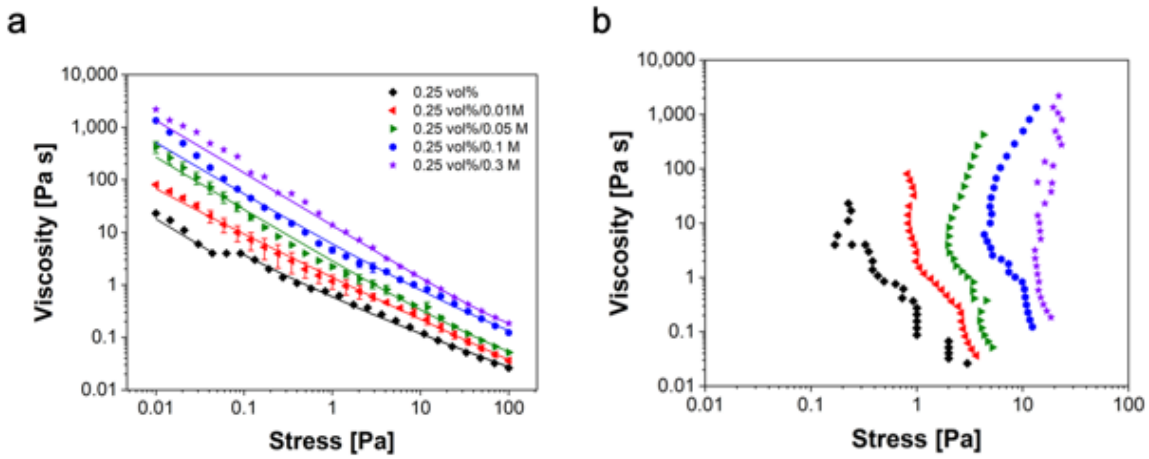

Figure 5.26. Flow behavior of MXene flake concentration 0.25 vol% with 0, 0.01, 0.05, 0.1, and 0.3 M NaCl. Viscosity as a function of a) shear rate with Herschel-Bulkley models (curves) and b) shear stress.

The response to start-up of flow at a constant shear rate for 0.25 vol%/0.01 M dispersion is shown in Figure 5.27. The start-up of shear behavior typically results in an overshoot in viscosity followed by steady state with very short times (less than 100 shear units = shear rate × time) for isotropic phase. Presence of long oscillatory transients after the overshoot is one of the signatures of lyotropic rodlike polymer dispersions and means that the sample is stable for the rheological measurements.[227] The regular oscillations in the start-up curve are suggestive of a tumbling nematic structure.[69] This feature was observed with SWNT-102% H_2SO_4 dispersions and Ag-H_2O dispersions.[2, 160] In this example, the presence of several oscillations was observed over a short time period and not observed with higher salt concentrations.

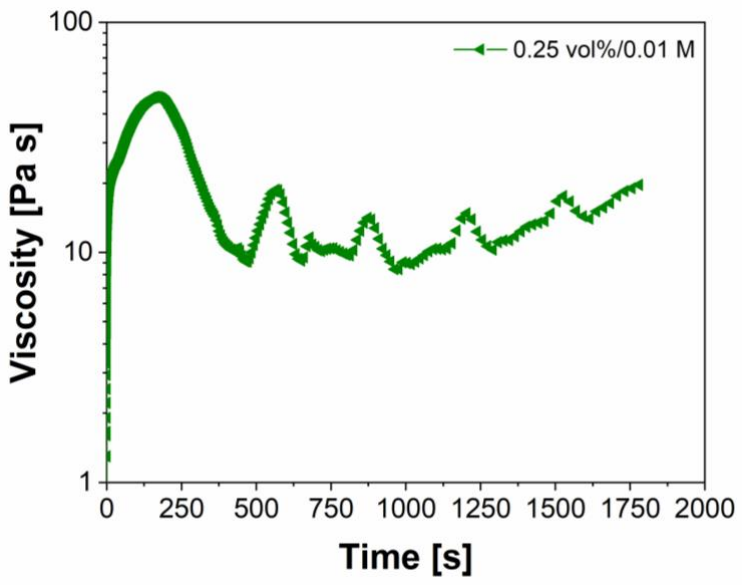

Figure 5.27. Oscillatory transients at constant shear rate of 0.01 s^{-1}.

As flake concentration increases to 0.40 vol%, the steady shear viscosities increase as shown in Figure 5.28. In addition, the Herschel-Bulkley model fits to the flow curve data give an increase in yield stresses τ_0 from 1.02 to 4.19 Pa and power-law exponents *n* from 0.38 to 0.63 for 0 and 0.1 M NaCl, respectively. The MXene flakes in salt solutions for all flake concentrations studied exhibit higher yield stress and viscosity values than dispersions without salt. The relationship of a colloidal gel yield stress to colloidal properties for spherical particles has been derived from particle-particle interaction potentials.[69] The interparticle distance is a critical parameter that plays a role in attractive and repulsive forces with formation of primary and secondary minima in the attractive region and energy barrier in the repulsive region. Herein, flake concentration and ionic strength (Debye length) are the factors changing the interparticle distances and resulting interactions. In another report, the yield stress was related to the colloidal parameters van

der Waals attractions plus the squared zeta potential for clay colloids described by DLVO theory.[228] Therefore, increases in the yield stress values with increasing salt content provide additional support that the interactions between MXene and salt allow the formation of a colloidal network.

The 0.50 vol% MXene dispersions exhibit power law behavior and yield stress values increasing from ~3 to 7 Pa for 0 and 0.1 M, respectively (Figure 5.28 and Figure 5.29). However, the 0.50 vol%/0.5 M dispersion only exhibits a yield stress of ~500 Pa in the flow regime (up to 100 s^{-1}) resulting in the power law exponent of the Herschel-Bulkley model, $n = 0$. The very high yield stress is suggestive of the flakes jamming in the dispersion. The jammed state occurs when reorganization of the structure is very difficult to achieve and the system is not in equilibrium and may be ordered or disordered.[229] Jamming is ultimately the result of insufficient excluded volume available for particles to rearrange. This volume must exceed that of random loose packing for the particles to be able to form a new structure. In this case, overcome the yield stress to break the network and flow. Increasing the bonding force or decreasing repulsion between the MXene flakes in the dispersions reinforces the colloidal network. At high flake concentrations, the strength of attractive forces may dominate due to the decreased separation between the flakes, or increased packing. This results in strong interlinked flakes forming the gel phase.

Increasing flake concentration to 1 vol% results in a very dense system with higher interparticle interactions at 0 and 0.1 M NaCl as shown in Figure 5.28. At 1 vol%, the model fits to the steady shear data have yield stresses of ~30 and ~200 Pa for 0 and 0.1 M, respectively (Figure 5.29). Similar to the 0.50 vol%/0.5 M dispersion, the 1.0 vol%/0.1 M

dispersion only exhibits a yield stress across the shear rates studied. In the literature, the full jamming regime shows the material jammed into a solid even with increasing stress.[229, 230] Our previous report on a highly concentrated Ti_3C_2 MXene dispersion (~29 wt%, ~7 vol%) with flake lateral sizes of ~0.3 μm showed rheological behavior characteristic of a gel with a yield stress followed by shear thinning.[13] Additionally, the viscoelastic properties showed near constant elastic modulus at ~20,000 Pa with dominating elastic behavior that enabled the dispersion to 3D print layered structures with exceptional electrochemical performance.[13] Hence, tuning the dispersion microstructure with increasing flake size and salt addition with results from this work may also be suitable for printing hierarchical structures.

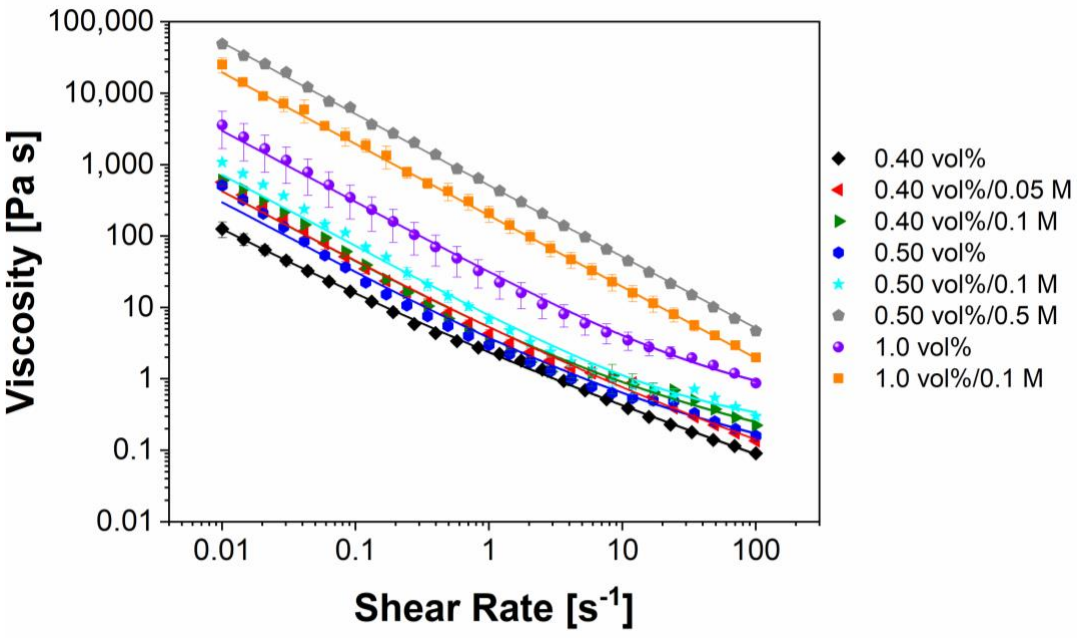

Figure 5.28. Overlay of flow curves comparing 0.40, 0.50, and 1.0 vol% with varying salt concentrations.

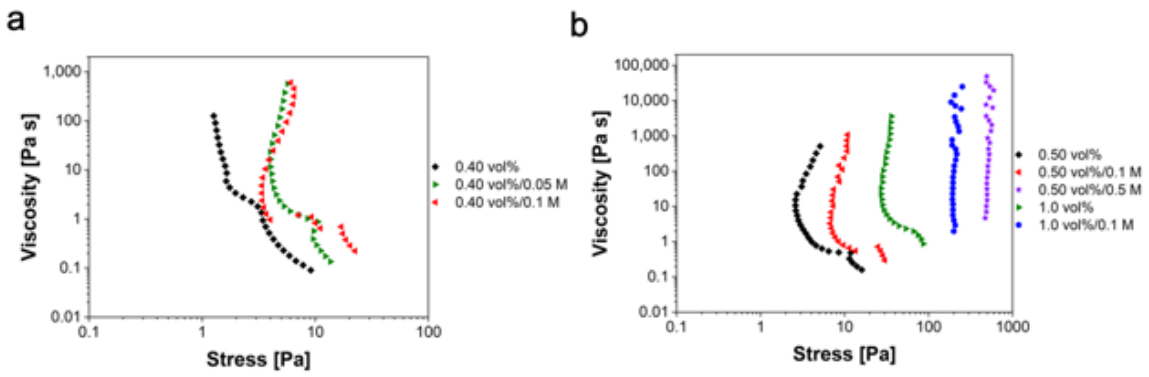

Figure 5.29. Yield stresses of a) 0.40 vol% and b) 0.50 and 1.0 vol% with varying salt concentrations.

Overlays of the viscosity and yield stress as a function of flake concentration are given shown in Figure 5.30. The behavior of viscosity or yield stress as a function of flake concentration for the 0 M NaCl dispersions is monotonic and does not show a decrease in viscosity throughout. The presence of the minima in viscosity is caused by the formation of low-viscosity liquid crystalline phase and is a signature feature of identifying the transition from biphasic to fully liquid crystalline. The lack of exhibiting a non-monotonic trend observed with MXene dispersions could be attributed to the high surface charges along the 2D flakes and electrostatic interactions caused by the electroviscous effect. Simple scaling arguments for the yield stress and viscosity as functions of the flake volume fraction are given in Table 3. At 0 M NaCl, flake concentration ϕ dependence can be quantitatively linked to yield stress as $\tau_0 \sim \phi^{3.4}$ and viscosity as $\eta \sim \phi^{3.0}$. The exponents are similar indicating close scaling for the flow behavior properties. Similar scaling exponents have been shown for graphene oxide, laponite gels, and concentrated yield stress fluids.[87, 231] However, at 0.1 M NaCl, the scaling exponent for viscosity is about two times higher than that of the yield

stress. This can be attributed to the electroviscous effect, where more drastic increases in viscosity occur as a result of screening of electrostatic forces.

Table 3. Scaling Relationships with Flake Concentration

NaCl Concentration (M)	$\tau_0 \sim \phi^a$ a	R^2	$\eta \sim \phi^b$ b	R^2
0	3.4	0.99	3.0	0.99
0.1	3.1	0.99	5.9	0.98

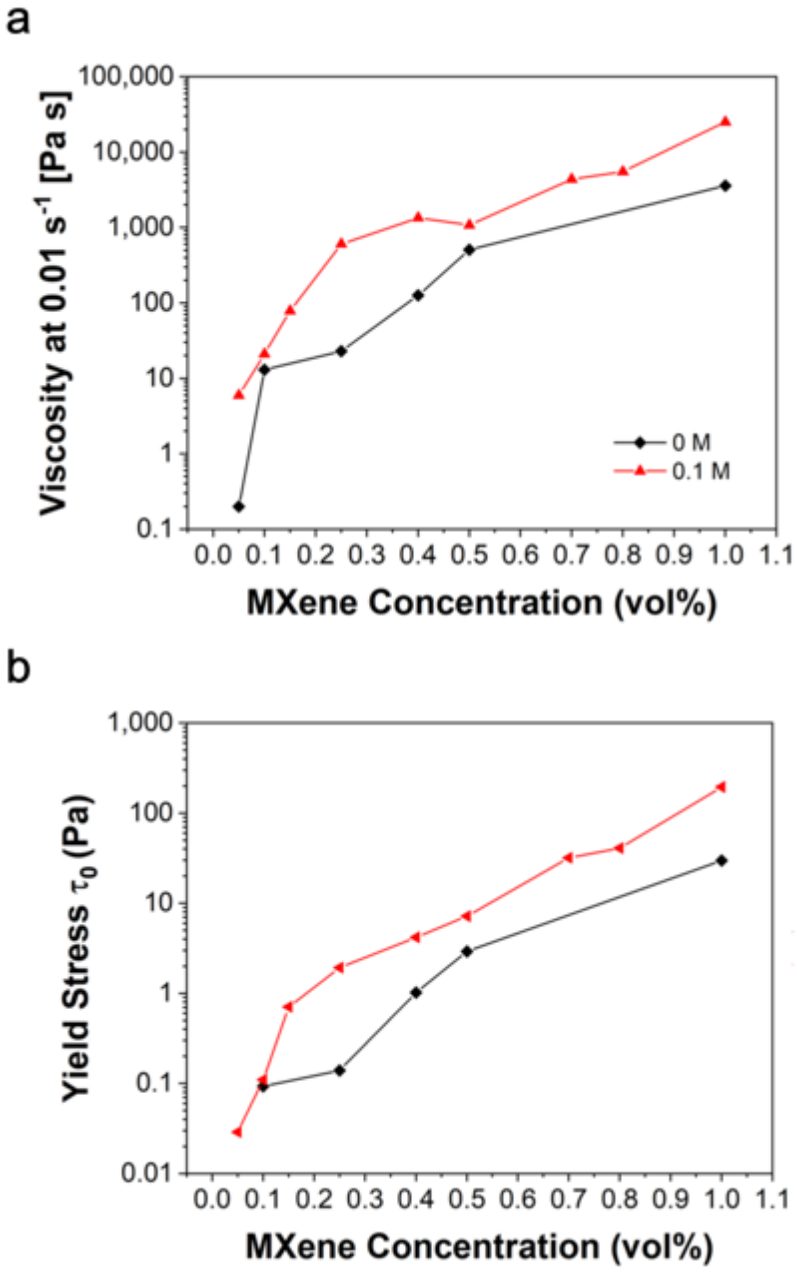

Figure 5.30. Plots of a) viscosity and b) yield stress versus MXene concentration comparing 0 and 0.1 M results. Note: Lines are drawn between symbols for ease of visualizing.

5.2.2.4 Oscillatory Dynamic Rheology

Viscoelastic materials show behavior somewhere between an ideal liquid (viscous) and ideal solid (elastic). The viscoelastic behavior can be measured with dynamic oscillatory rheology. structured fluids have a minimum or equilibrium energy state associated with their microstructure at rest. This microstructure may relate to randomly oriented particles, entangled chains in polymers, or jammed droplets in emulsions. When a force or deformation is applied to the fluid, the minimum energy state is shifted away from equilibrium creating an elastic force that tries to restore the initial microstructure. The elastic, or storage, modulus G' is a measure of stiffness or resistance to deformation. The viscous, or loss, modulus G" is a measure of the deformation energy lost due to internal friction of the molecules or particles in the flowing fluid. Small amplitude oscillatory shear (SAOS) rheology is performed where the sample is oscillated about its equilibrium state at rest in a continuous cycle with a full oscillation considered equivalent to a 360° evolution. The amplitude of oscillation is equal to the maximum applied strain (strain-controlled rheology) or stress (stress-controlled rheology). The angular frequency is the number of oscillations per second.

During oscillatory testing, the top fixture is oscillated back and forth at a strain amplitude and frequency range. For controlled strain measurements, the angular displacement is controlled and torque required for displacement is measured. The resulting storage and loss moduli are measured and shear stress can be calculated. An important characteristic of oscillatory rheology for probing dispersion microstructure and properties (SAOS) is performing the tests in the linear viscoelastic regime (LVR), where the applied

stresses are insufficient to cause structural breakdown or yielding. When the applied stresses exceed the yield stress, a non-linear viscoelastic region appears in the large amplitude oscillatory shear (LAOS) where the properties no longer represent the microstructure at rest. An example of both regions with applying strains from 0.01 – 100% is shown in Figure 5.31 for 0.25 vol%/0.1 M. The strain sweep shows the LVR with a relatively constant plateau of G' at low strains followed by a sharp decrease in G' at higher strains in the LAOS region when G' becomes strain or stress dependent. The cross-over of G' and G" is commonly referred to as the point at which the structure begins to yield. For 0.25 vol%/0.1 M NaCl, the cross-over occurs at 32% strain where G' and G" are equal to 18 Pa. The loss factor, or tan δ, describes the two portions of the viscoelastic behavior and is defined as the ratio of G" to G'. When G' = G", tan δ = 1. The shear stress is calculated and shown in Figure 5.31b, where the cross-over stress occurs at 8.4 Pa. The following oscillatory tests and frequency sweeps in this chapter were performed in the LVR region to describe the sample microstructures.

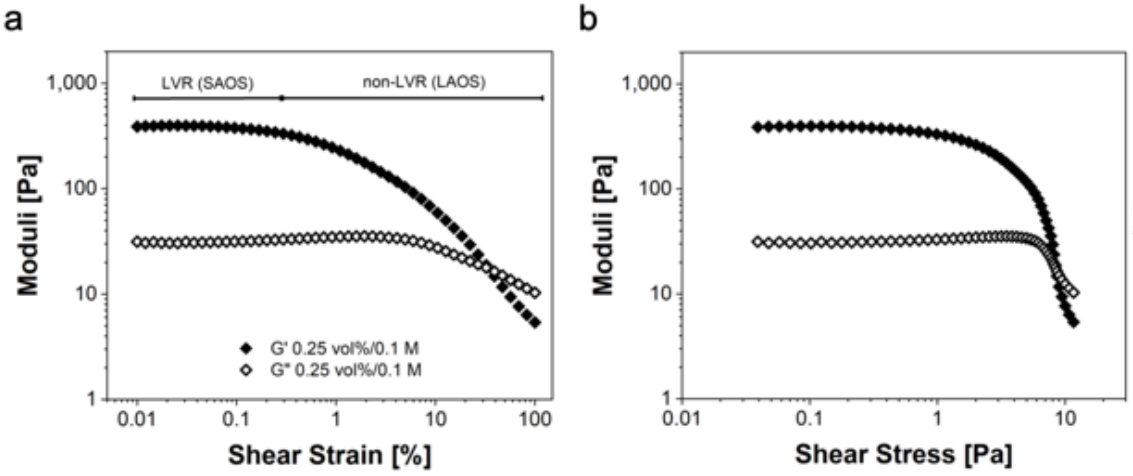

Figure 5.31. Oscillatory sweep for 0.25 vol%/0.1 M as a function of a) strain and b) stress.

In addition to the steady shear rheology, oscillatory rheology was performed on the 0.15 vol%/0.1 M dispersion, which was the lowest achievable concentration with salt within torque limitations. Figure 5.32 shows the oscillatory frequency sweep where the storage modulus G' and loss modulus G" are clearly well separated from each other. G' is relatively constant at ~33 Pa up to about 40 rad/s, then decreases. The loss modulus G" is about an order of magnitude lower than G' and increases approaching G' between 10 -100 rad/s. The dominant elastic behavior indicates more solid-like behavior and network formation.

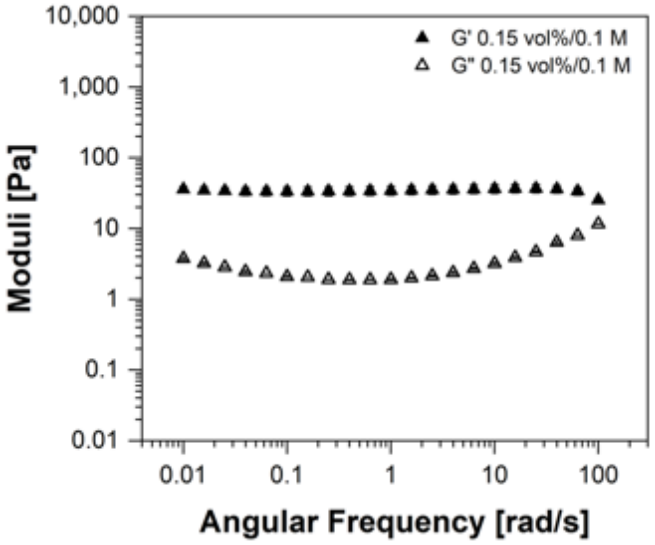

Figure 5.32. Frequency sweep with storage modulus G' and loss modulus G" of 0.15 vol%/0.1 M dispersion.

The lowest achievable concentration for collecting dynamic oscillatory tests within the torque limitations is 0.25 vol% with 0 M NaCl. The oscillatory sweep of 0.25 vol% with varying salt concentrations 0, 0.01, 0.05, 0.1, and 0.3 M are shown in Figure 5.33. The high frequency region corresponds to short time scales while the low frequency region

corresponds to long time scales. For all of the dispersions, G' > G" representing dominant solid-like behavior. The low frequency data between 0.01 and 0.05 rad/s for 0 M (black diamonds) were out of torque and not included in the plots. It is shown that the dispersion with 0 M exhibits higher G' modulus than the 0.01 M NaCl (grey circles) dispersion. However, above 0.01 M NaCl, both G' and G" drastically increase with increasing salt concentration from 0.01 – 0.3 M. The values for shear moduli are included in Table A.3. For example, G' at 0.1 rad/s increases from 2.55 to 233 Pa from 0.01 to 0.1 M NaCl and further increases to 1490 Pa at 0.3 Pa. For all of the dispersions, G' is relatively constant which indicates percolation, or network formation. It is observed for 0 and 0.01 M NaCl that at frequencies >50 rad/s, the storage modulus is frequency dependent and increases with frequency. The changes in elastic modulus (G') with the effects of salt concentration suggest a gelation transition state near 0.05 M NaCl, where the rheological gelation is similar to that of traditional colloidal gels.[141]

The behavior of loss modulus G" is shown in Figure 5.33b, where G" varies slightly in the low frequency region. However, from 1 – 100 rad/s, the behavior is frequency dependent. With 0.01, 0.05, and 0.1 M NaCl, G" increases with increasing frequency in the shorter time scales compared to 0.3 M NaCl that exhibits G" decreasing with increasing frequency. When G'>G", the behavior of G" can be characterized as rubbery plateau region with increasing G" (approaching G') or glassy region with decreasing or relatively constant G". This behavior can also be observed with the loss factor, or tan δ = G"/G'. A value of tan δ = 0.1 means that G' is 10 times larger than G". When tan δ is less than 0.1, G' becomes much higher than G" indicating more glassy or gel-like behavior. When tan δ approaches

1, G” is increasing to approach G’ indicating rubbery behavior, which is also observed in cross-linked polymers where polymer chains are entangled with insufficient time to free themselves imparting an elastically dominant system.[232] Therefore, the rubbery behavior for this work can be ascribed to the limited mobility of the MXene flakes especially at higher frequencies (shorter timescales).

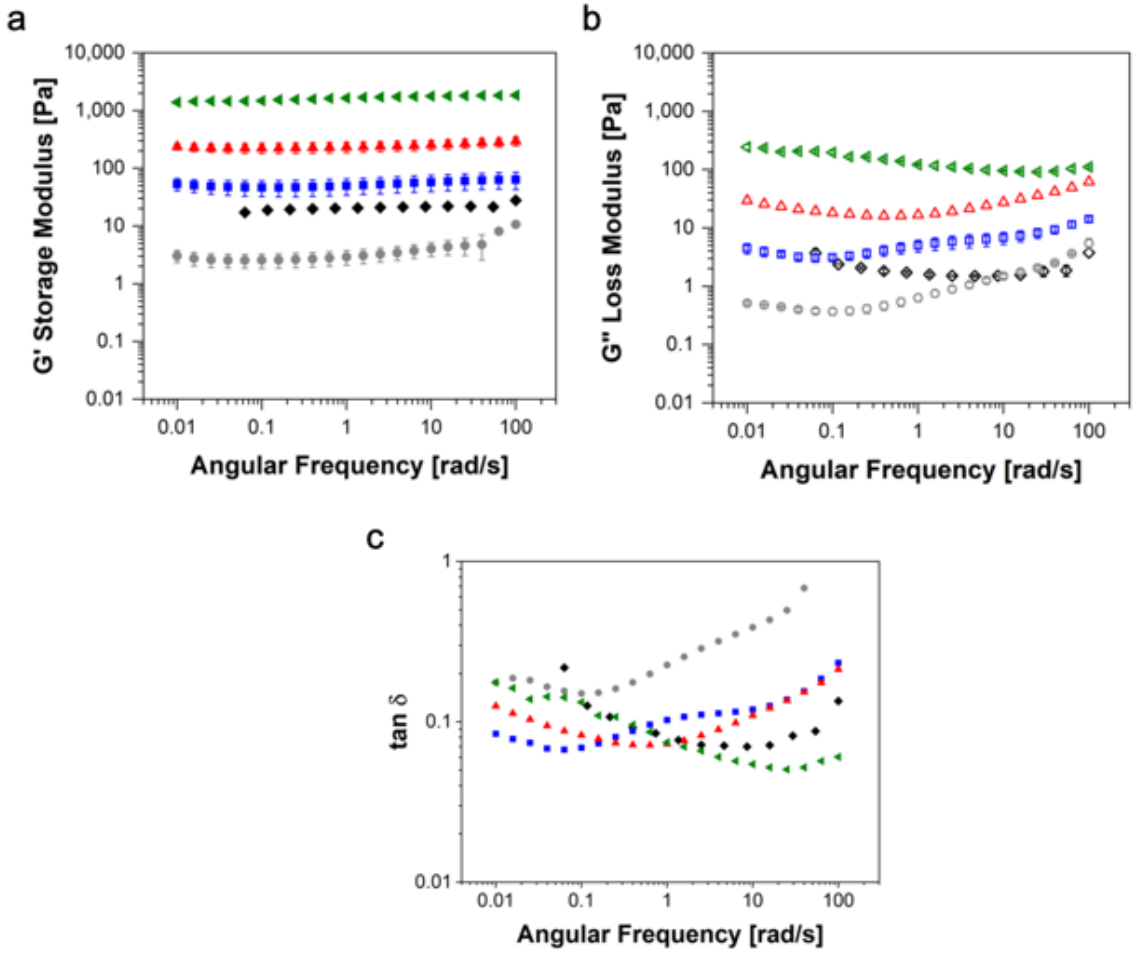

Figure 5.33. SAOS rheology with a) storage modulus G’, b) loss modulus G”, and c) tan δ versus angular frequency for 0.25 vol% with 0 M (black diamonds), 0.01 M (gray circles), 0.05 M (blue squares), 0.1 M (red triangles), and 0.3 M (green left-pointing triangles).

The complex shear modulus G* is the ratio of applied stress to measured strain and defined as the quantitative measure of material stiffness or resistance to deformation. For a viscoelastic material, the phase difference or angle δ between strain and stress lies between 0 (purely elastic) and 90° (purely viscous) where 45° represents the boundary between solid and liquid behavior and can indicate the onset of network formation or breakdown. The total G* consists of contributions from both elastic G' and viscous G" moduli. The phase angle is typically expressed as tan δ. In addition, the complex viscosity η* is a measure of the total resistance to flow as a function of angular frequency. The complex viscosity is equal to the ratio of complex modulus to angular frequency, or $\eta^* = G^*/\omega$. The Cox-Merz rule states that the complex viscosity as a function of frequency is equivalent to the steady shear viscosity as a function of shear rate.[233] This rule holds true for simple solutions or polymer melts, but not for more complex dispersions. A comparison of the steady shear and complex viscosities for 0.25 vol% with 0 M is shown in Figure 5.34a and overlays of 0.01 and 0.1 M are shown in Figure 5.34b. The Cox-Merz rule does not hold true for any of the dispersions. The Cox-Merz rule not being obeyed is one of the signatures for identifying liquid crystalline behavior. However, this has also been found in flocculated dispersions.[69]

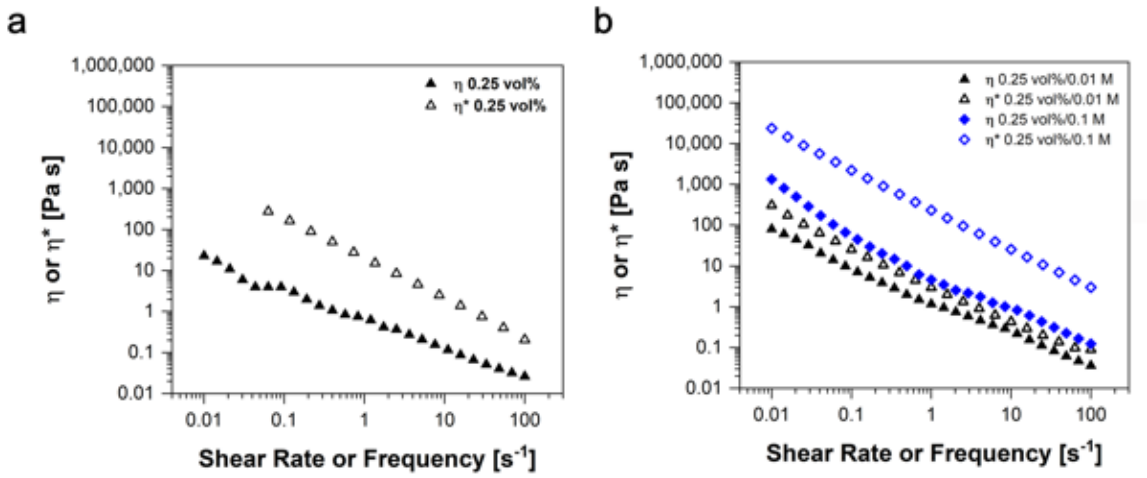

Figure 5.34. Examples of the Cox-Merz rule not obeyed for a) 0.25 vol% with 0 M (black) and b) 0.25 vol% with 0.01 M (black) and 0.1 M (blue). Solid symbols are steady shear viscosity η and open symbols are complex viscosity η*.

The oscillatory behavior can be fit to the linear viscoelastic model for frequency dependence proposed by Winter for shear modulus $G(\omega) \approx k\omega^n$, where n is the slope of the log-log plot of moduli versus angular frequency and k is the intercept which defines the degree of network connectivity.[234] The dynamic oscillatory data was fit to the power-law relationship that predicts the stress relaxation for the low frequency storage modulus G' and the results are shown in Table 4. The exponent can be used as a quantitative measure of the extent of elasticity that forms a network system. When $n \sim 0$, G' $\sim$ k and this is the case for all the dispersions studied. The very low n value indicates that G' is relatively constant supporting that the dispersions exhibit a percolated network.[235] In addition, higher values of the intercept k indicate a higher degree of network connectivity, which occurs with increasing flake concentration as well as with salt addition.

Table 4. Viscoelastic model for oscillatory data

MXene Concentration (vol%)	NaCl Concentration (M)	$G' \approx k\omega^n$		R^2
		k	n	
0.25	0	20	0.042	0.86
0.25	0.1	233	0.019	0.94
0.40	0	17	0.031	0.97
0.40	0.1	380	0.025	0.85
0.50	0	128	0.014	0.75
0.50	0.1	804	0.019	0.81
1.0	0	2600	0.080	0.97
1.0	0.1	174,000	0.026	0.96

The flake concentration dependence can also be quantitatively linked to the viscoelastic moduli as shown in Table 5. At 0 M NaCl, the power-law relationship of the elastic modulus is $G' \sim \phi^{3.9}$ and for the viscous modulus is $G'' \sim \phi^{5.2}$. However, at 0.1 M NaCl, the scaling exponent for G' is about 60% higher than that without salt and the G" exponent. This implies the very strong dependence of ϕ on the elastic modulus due to the electroviscous effect resulting in significantly higher viscosities and elasticity in the system.

Table 5. Scaling Relationships with Flake Concentration

NaCl Concentration (M)	$G' \sim \phi^c$	R^2	$G'' \sim \phi^d$	R^2
	c		d	
0	3.9	0.99	5.2	0.99
0.1	9.0	0.99	3.9	0.95

The oscillatory rheology behavior for the 0.40 vol% dispersion with 0 – 0.1 M NaCl also show an increase in viscoelastic moduli with increasing salt concentration with values

also higher than at 0.25 vol% flake concentrations (Figure 5.35). Interestingly, the 0.40 vol% alone exhibits ~2 orders of magnitude lower G' than 0.40 vol%/0.1 M, where the former still exhibits characteristic rubbery behavior. This rheological behavior resembles that of soft glassy materials or weak gels.[236, 237] The elasticity arises from the MXene flake network and is necessary for liquid crystalline nematic ordering of the flakes. For 0.40 vol%/0.05 M and 0.40 vol%/0.1 M, smaller changes in G" across the frequency range were observed compared to 0.25 vol%/0.05 M and 0.25 vol%/0.1 M, respectively. In addition, smaller changes in G" were observed with salt addition compared to the dispersions with no salt, resulting in approaching glassy or gel-like behavior at lower flake concentrations. MXene flake concentrations of 0.25 vol% and 0.40 vol% both with 0.05 and 0.1 M NaCl exhibit more closely associated particles as shown in the optical microscopy investigations. Together with the rheology results including higher yield stresses as salt concentration increases, this provides further support to the optical microscopy investigation that the addition of salt concentrations 0.05 and 0.1 M NaCl indicate a higher degree of network connectivity. However, the lower flake concentration 0.25 vol% with 0.05 and 0.1 M salt show more free space, or solvent-rich regions, than the closer packing of the flakes at 0.40 vol% with 0.05 and 0.1 M. This is caused by the high salt content having a higher concentration of ions interacting with the lower concentration of MXene flakes where the charge distribution and attractive forces resulted in the phase separation observed. The addition of NaCl to the MXene dispersions initiated particle gelation at a lower flake concentration due to the screening of electrostatic repulsions. The higher values of viscoelastic moduli, yield stresses, and viscosities with increasing salt content could be due to the bridging effect of Na^+ that is the connection of two MXene flakes from their negative

surfaces. This can also be supported with the optical microscopy investigations showing more agglomeration of particles at 0.25 vol% with salt compared to 0.40 vol% with salt.

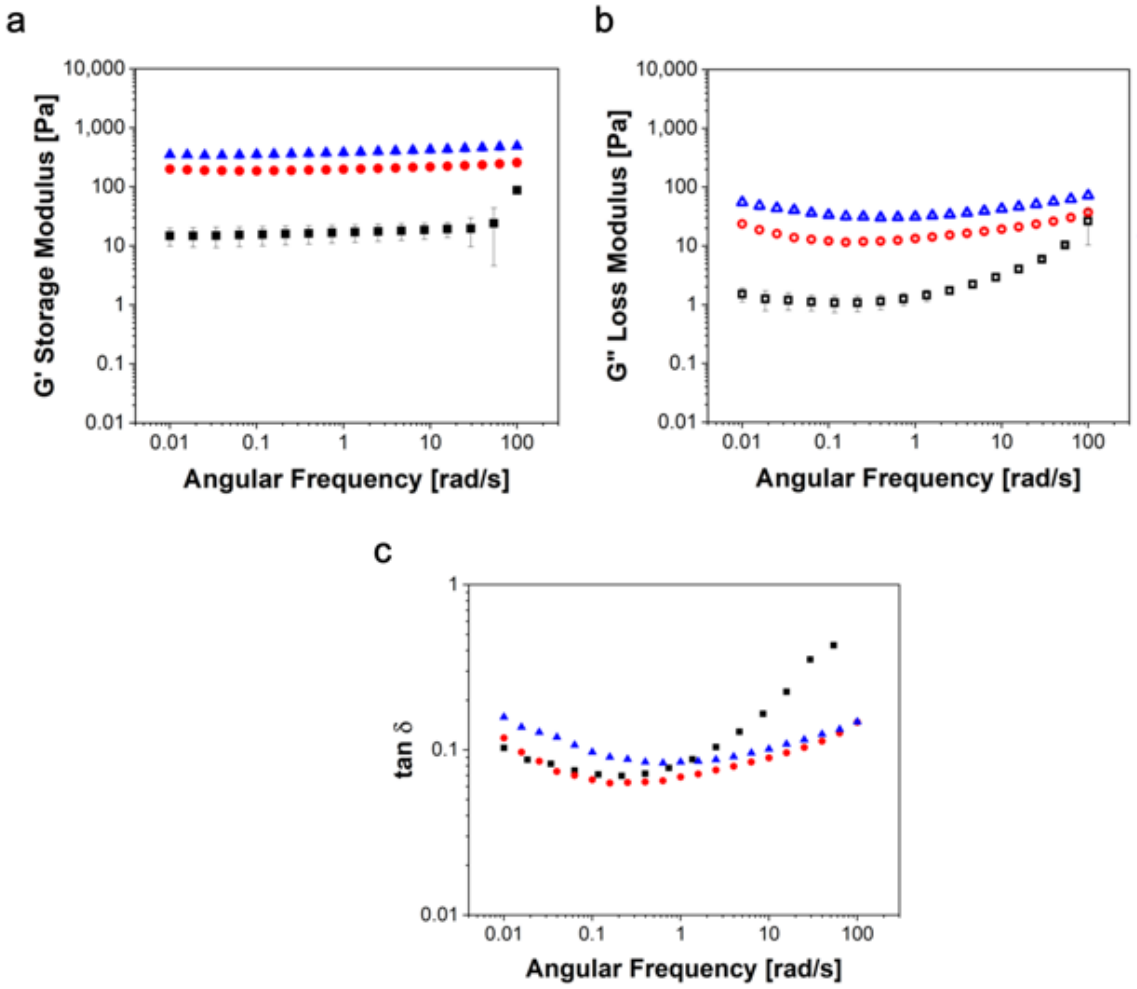

Figure 5.35. Oscillatory rheology with a) G', b) G", and c) tan δ for flake concentration of 0.40 vol% with 0 M (black squares), 0.05 M (red circles), 0.1 M (blue triangles).

The rheological properties were further investigated for 0.50 vol% with varying salt concentrations as shown in Figure 5.36. The oscillatory rheology behavior of 0.50 vol% demonstrates more elastic behavior with about one order of magnitude increase of

viscoelastic moduli from 0 to 0.1 M and two orders of magnitude increase from 0.1 to 0.5 M NaCl. The 0.50 vol%/0 M exhibits a relatively constant value of G' and gel-like behavior as observed with G" at the shorter time scales. Also, tan δ shows a decreasing trend below 0.1 rad/s at the higher frequencies with increasing salt concentration (Figure 5.37a). These results indicate a rheological percolated threshold is achieved and considered as the onset of gelation. This gel-like behavior is characteristic of elastic polymer networks that are largely immobile and has been observed with other disk-like materials.[13, 150, 238, 239] Similar behavior was previously found for nanoclays, where the dispersion stability is caused by bulk and surface properties including charges.[240] For the 0.50 vol%/0.5 M dispersion, the G' values of ~ 220,000 Pa are suggestive of jamming of the flakes forming a dense system.[230] This is also supported with the steady shear rheology results that showed the very high yield stress and viscosities as well as with the optical microscopy results indicating very dense packing of the flakes. Laponite dispersions also form gels at higher platelet concentrations and varying ionic strengths; however, the mechanism of gelation occurs due to the formation and growth of clusters as observed with the power-law behavior of frequency dependence and slow relaxation process in the gel.[241, 242]

Examples of the Cox-Merz rule not obeyed for 0.50 vol% with 0 and 0.1 M NaCl are shown in Figure 5.37b. The complex viscosities are about one order of magnitude higher than the steady shear viscosities for dispersions with and without salt, similar to what was found with lower flake concentrations. A previous study shows the rheology of concentrated GO dispersions fail to obey this rule and the network breaks down into smaller clusters with increasing shear.[243]

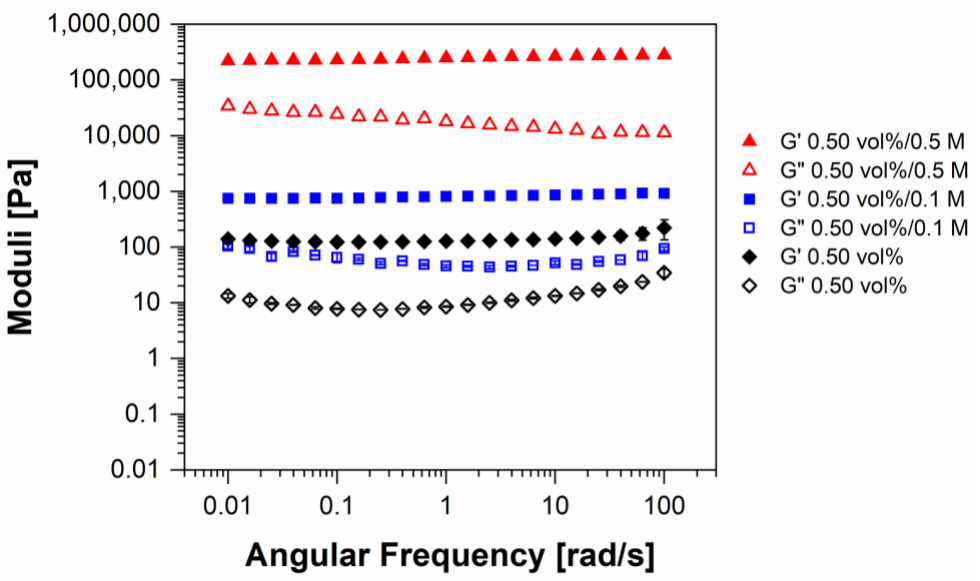

Figure 5.36. Storage G' (closed symbols) and loss G" (open symbols) moduli of 0.50 vol% with 0, 0.1, and 0.5 M NaCl.

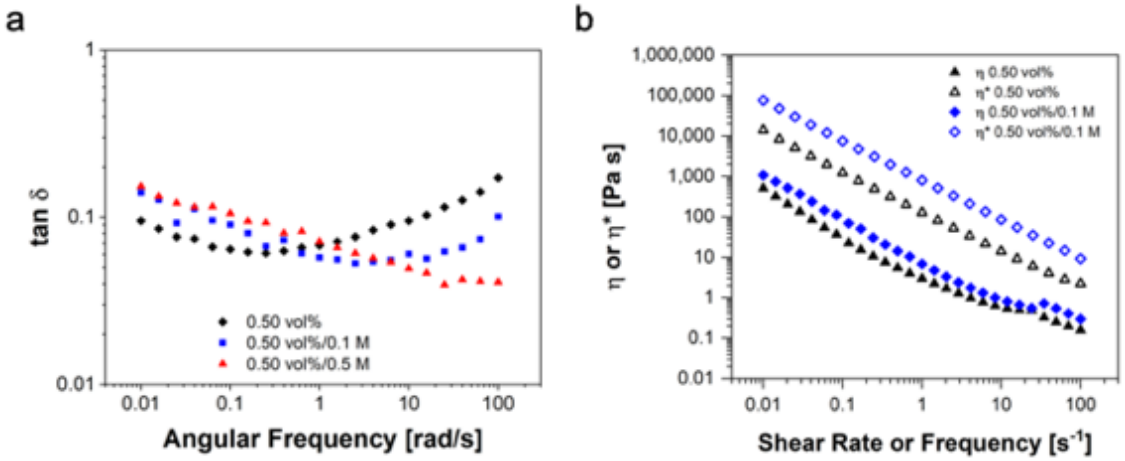

Figure 5.37. a) Oscillatory response of tan δ for 0.50 vol% with 0, 0.1, and 0.5 M NaCl. b) Comparison of steady shear η (solid symbols) and complex viscosities η* (open symbols) for 0.50 vol% with 0 and 0.1 M.

Additional MXene flake concentrations of 0.70 and 0.80 vol% both with 0.1 M NaCl were explored in between 0.50 and 1.0 vol%. As illustrated in Figure 5.38a, the

moduli increase with increasing flake concentration at the same salt concentration of 0.1 M. The 0.70 vol%/0.1 M dispersion exhibits about an order of magnitude higher moduli than 0.50 vol%/0.1 M with similar gel-like behavior. Further increasing concentration to 1.0 vol% indicates higher moduli values than lower vol% dispersions (Figure 5.38b). In addition, the 1.0 vol%/0.1 M NaCl dispersion shows about two orders of magnitude higher G' and G" than without salt. Similar to the 0.50 vol%/0.5 M dispersion, the 1.0 vol%/0.1 M dispersion only exhibits a yield stress across the shear rates studied and similar viscoelastic responses with G' ~154,000 Pa and G" ~22,000 Pa. However, performing rheology on the 1.0 vol%/0.1 M dispersion resulted in edge fracture as shown in Figure 5.39. Presence of the clumps of particles in the dispersion disrupted the uniform flow between the fixture and caused it to slide out.

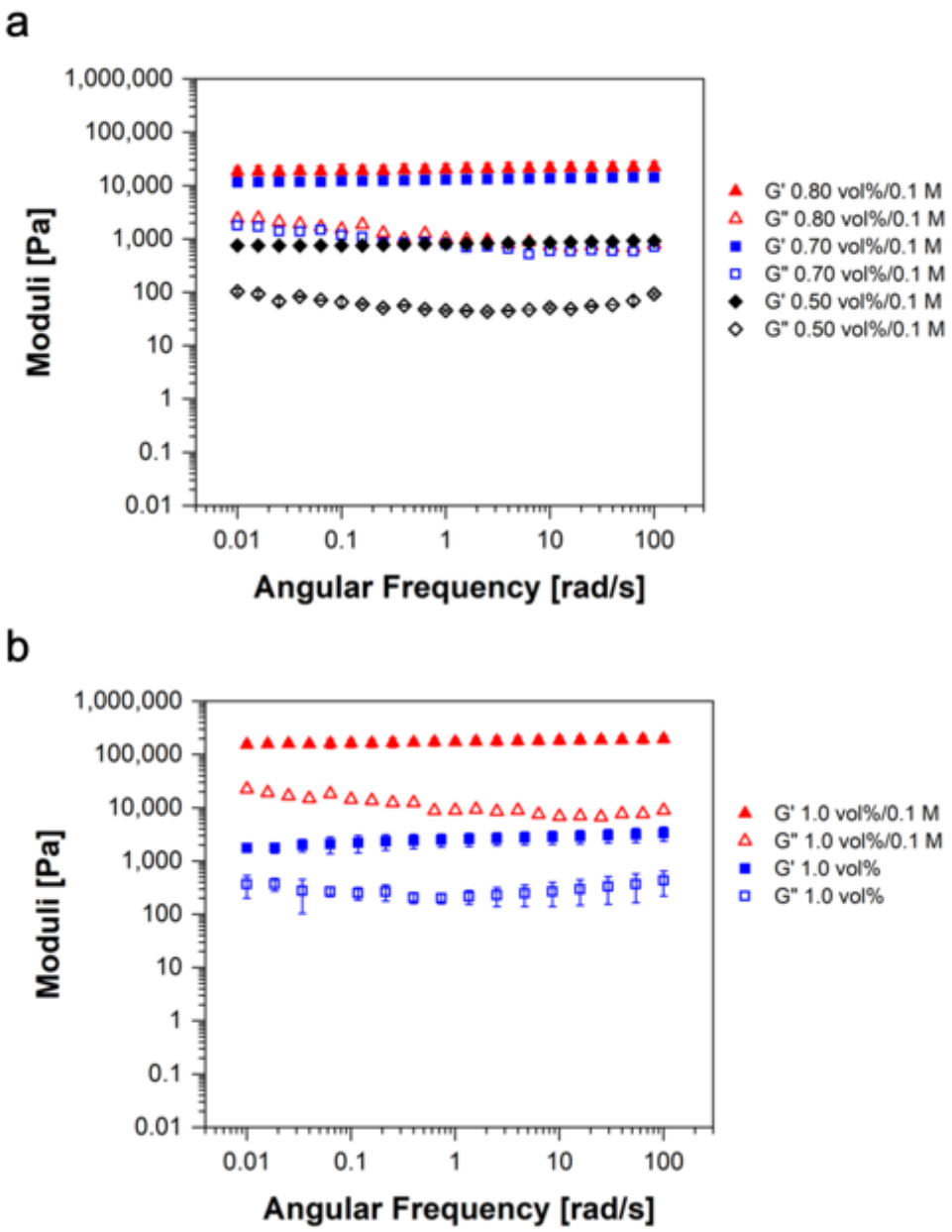

Figure 5.38. Oscillatory response showing storage and loss moduli with 0.1 M NaCl of a) 0.50, 0.70, and 0.80 vol% flake concentration. b) Comparison of 1.0 vol% with 0 and 0.1 M NaCl.

Figure 5.39. Edge fracture of a 1.0 vol%/0.1 M dispersion (left) and large-sized clumps of particles (right). Arrows indicate the MXene/NaCl dispersion.

The total interaction energy was also calculated using simple estimations based on DLVO theory (Section 2.6) for varying ionic strengths with large MXene flakes is shown in Figure 5.40. If the energy barrier is very large, primary minimum aggregation may be prevented, or disappear, while secondary minimum flocculation can still occur.[105-107] Deeper secondary minima are more likely to occur with micron-sized particles than smaller ones and the secondary minimum can lead to irreversible aggregation.[106] Nanometer sized particles typically have secondary minima of few kT, while larger particles can have values of 90 kT or more and lead to irreversible aggregation.[105] As interparticle distance increases, a strong long-range repulsion from the electrostatic double-layer dominates for all ionic strengths generating an energy barrier. To overcome the energy barrier, the kinetic energy of the particles due to thermal motion must be higher than the energy of the repulsive barrier. The values of the repulsive energy barriers are shown in Table 6. The width of the

repulsive energy barrier decreases with increasing ionic strength, which can be attributed to the stronger interplay of attractive interactions. In addition, the smallest peak was observed for 0.5 M NaCl. Beyond the energy barriers, the decay in the net repulsion results as attractive forces increase and is governed by the Debye screening length. A deep secondary minimum was found for 0.5 M NaCl where a closer approach of the particles occurs and the dispersion flocculates. The magnitude of the secondary minimum of 0.5 M is an order of magnitude larger than that of 0.1 M and two orders of magnitude larger than 0.01 M, suggesting stronger dominating attractive energy. These simple theoretical estimations provide support for the experimental results in this work; however, more complex calculations in addition to DLVO theory are necessary for predicting the effects of ionic strength on particle interactions.

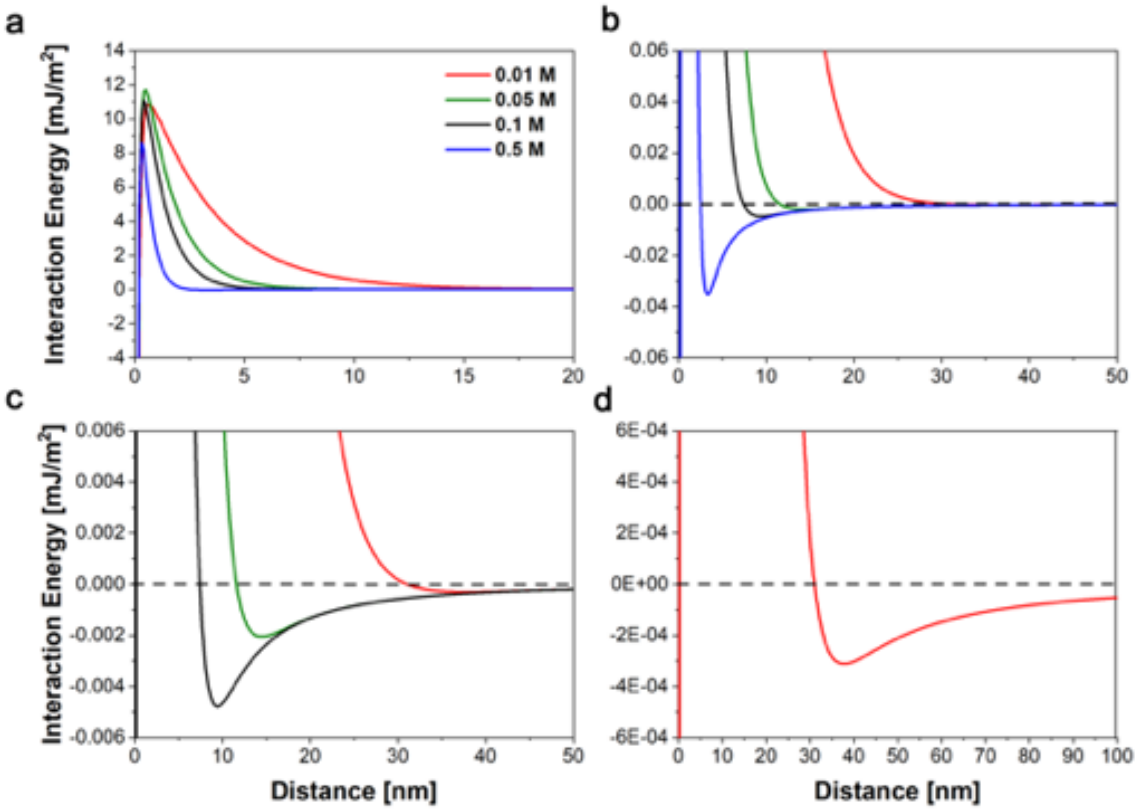

Figure 5.40. a) Total interaction energy as a function of interparticle distance for the ionic strengths 0.01, 0.05, 0.1, and 0.5 M NaCl (legend applies to entire figure). b-d) Closer look at the secondary minima. The dashed line is drawn for reference at net zero interaction energy.

Table 6. Total Interaction Energies Based on DLVO Theory for Varying Ionic Strengths

Ionic Strength	Repulsive Energy Barrier		Secondary Minimum	
[M]	W [mJ/m^2]	W/kT	W [mJ/m^2]	W/kT
0.01	10.8	4.73 x 10^7	-0.000312	-1.37 x 10^3
0.05	11.6	5.08 x 10^7	-0.00205	-8.98 x 10^3
0.1	11.1	4.86 x 10^7	-0.00477	-2.09 x 10^4
0.5	8.61	3.77 x 10^7	-0.0352	-1.54 x 10^5

Note: kT = 4.11 x 10^{-21} J

This research explored the effects of salt addition on dispersion microstructure and rheological properties. The results are summarized in Table 7 below and a phase diagram of the MXene/NaCl system is proposed in Figure 5.41. Optical microscopy, rheology, visual observations, and comparisons with phase behavior from the literature were used to understand the effects of salt addition on MXene phase behavior. MXene dispersions form entropy-driven liquid crystalline phases with salt concentrations of 0 and 0.01 M NaCl. A clear indication of change in dispersion microstructure with salt addition of 0.05, 0.1, and 0.5 M NaCl were found. At low flake concentrations, the addition of salt from 0.05 – 0.5 M NaCl resulted in flocculation with less isotropic and nematic character as salt content increased. At high flake concentrations, the dispersions with 0 and 0.1 M NaCl exhibit gel-like behavior with strong nematic character and flocculate with 0.5 M NaCl. Previous reports with similar trends in the rheological behavior for large $Ti_3C_2T_x$ and ultra-large GO dispersions have shown potential processing capabilities for wet spinning, dry spinning, extrusion printing, and spray coating,[25, 95, 117] which suggests potential processing routes for the dispersions studied in this work.

Table 7. Experimental evidence of phase assignments

Phase	Evidence
Isotropic, I	no birefringence POM, Newtonian behavior
Biphasic, I + N	some birefringence, low yield stress, increase in viscosity
Nematic, N	complete birefringence, long-range ordering with threadlike domains, G' frequency independent, G" weakly increasing with frequency, yield stress, 3-region behavior, disobey Cox-Merz rule
Gel, G	connectivity in structure, G" decreasing, G" much less than G', high yield stress and G'
Nematic and gel, N + G	Strong presence of both nematic and gel characteristics
Flocculation, F	loosely connected structure, large sized aggregates, sedimentation, weaker presence of nematic character, high viscosities, disobey Cox-Merz rule
Isotropic, nematic, and flocculation; I + N + F	Presence of isotropic and nematic regions together in a flocculated structure
Gel and flocculation, G + F	Presence of both gel and flocculated regions

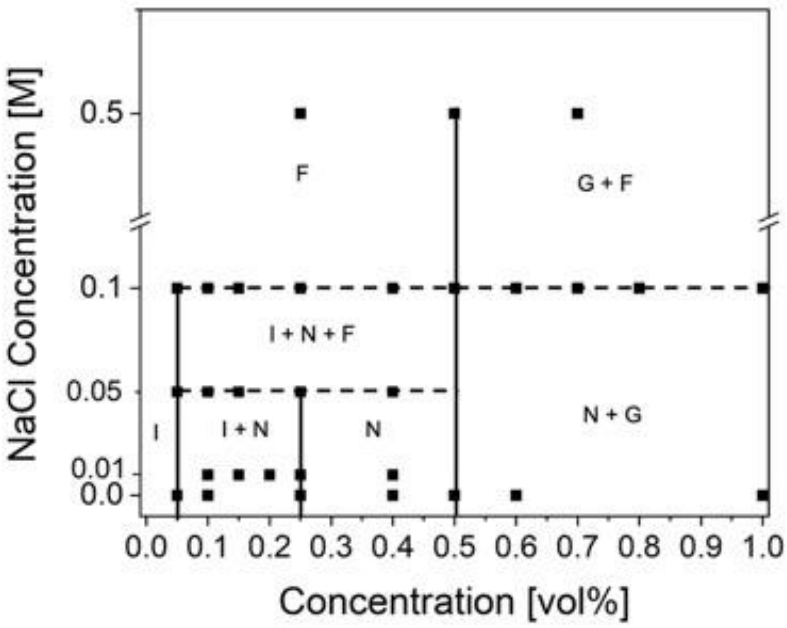

Figure 5.41. Proposed phase diagram of MXene/NaCl system. I – isotropic, N – nematic, I + N – biphasic, G – gel, F – flocculation.

5.2.3 Conclusions

In summary, this research provides insights into tuning large MXene flake dispersions with varying volume fraction of flakes and ionic strength. The negatively charged surfaces and positively charged edges of the MXene flakes coupled with NaCl salt induce electrical double layer interactions competing with van der Waals interactions. Optical microscopy and rheology studies provided an understanding of the dispersion phase behavior with the effects of salt addition. MXene dispersions in water readily form nematic liquid crystalline phases, while salt addition results in maintaining the nematic ordering at low salt content and formation of gels and flocculation at high salt content. The rheological behavior varies considerably with flake concentration and ionic strength. Rheological properties show that salt addition increases viscoelastic and steady shear properties by orders of magnitude

indicating stronger network formation, elasticity, yield stresses, and viscosities due to the electroviscous effect. Results from this work offer an interesting connection between the microstructures of MXene, GO, and nanoclay dispersions, extending the fundamental science governing the dispersion behavior of 2D materials.

Chapter 6 Conclusions

The research in this dissertation contributed to advancing understanding of two different 2D-based material systems, graphene hybrids and MXenes. Tuning the microstructure of 2D dispersions was studied by combining 2D and 1D geometries for the graphene/manganese oxide system and inclusion of salt addition for the MXene/NaCl system. The graphene work focused on understanding morphologies of ultra-large reduced graphene oxide (RGO) sheets with aspect ratio of ~40,000 and manganese oxide (MnO_2) nanowires with aspect ratio of ~50. In this work, hybrids (MnO_2/RGO) were fabricated through a versatile synthesis that occurs via electrostatic binding of the nanowires with the sheets. Two different hybrid compositions were studied that resulted in different structures and electrochemical performances: 3:1 MnO_2/RGO (75/25 wt%) designated as 3H and 10:1 MnO_2/RGO (90/10 wt%) designated as 10H. The individual materials were characterized by multiple spectroscopy, microscopy, and thermal analysis techniques to better understand the microstructure development of the hybrids. Next, electrodes were fabricated and electrochemical testing was performed to gain insights into the effects of manganese oxide content on the electrochemical response. Results from this work showed a higher specific capacitance was achieved with the 3H electrode compared to 10H. This was attributed to the more uniform distribution of nanowires along the ultra-large sheets as well as the more accessible surface area for charge transfer. Comparison of the excellent cyclability and capacitive behavior of the 3H electrode to other hybrid electrodes in the literature showed advantages of using ultra-large graphene sheets and incorporating manganese oxide.

In the second section of this dissertation, the $Ti_3C_2T_x$ MXene work focused on understanding the effects of tuning the dispersion microstructure with flake size and salt addition. This project was collaborative with synthesis of the MXenes performed by Dr. Beidaghi's group in Materials Engineering at Auburn University. Initially, rheology investigations were performed on a highly concentrated MXene dispersion composed of unfractionated flakes (~0.3 μm) to understand dispersion quality for printing hierarchical structures. The highly concentrated MXene dispersion (~7 vol%) showed desirable viscoelastic properties for extrusion printing at room temperature. Determining the rheological properties provided a link to understanding the electrochemical performances of the scalable fabrication of micro-supercapacitors (MSCs) with various architectures and electrode thicknesses on several different substrates. Next, the MXene dispersions were tuned by varying size to produce large flakes (~3 μm) and adding NaCl as a rheological modifier. Multiple flake and salt concentrations were investigated by polarized optical microscopy and rheology to understand the effects of salt addition on MXene phase behavior and rheological properties. Polarized optical microscopy provided insights into the effects of changes in flake and salt concentration on dispersion microstructure. Small amplitude oscillatory shear rheology and steady shear rheology were used to understand changes in viscoelasticity and flow behavior. The charge distribution and screening length of the dispersions resulted in very different structures and a phase diagram was proposed. Interestingly, MXene dispersions with 0 – 0.01 M NaCl exhibited nematic liquid crystalline phases, while addition of 0.05 – 0.5 M NaCl exhibited multiple phases. At lower flake concentrations, addition of 0.05 – 0.5 M NaCl showed flocculation with presence of isotropic and nematic phases. At higher flake concentrations, a gel with nematic character

formed at lower ionic strength and a gel with flocculation formed at higher ionic strengths. The phase behavior and microstructures of MXene/NaCl dispersions have similarities to those observed for graphene oxide and nanoclay dispersions in the literature.

The results from this research contributed to understanding the complex thermodynamic interactions in graphene and MXene systems for controlled anisotropic properties. In the graphene work, electrode properties of different hybrid assemblies showed enhanced electrochemical behavior compared to either individual component alone, which provides benefits to combining very different aspect ratio nanomaterials. Also, the MXene/NaCl work illustrated the effects of tuning the dispersion microstructure to form different phases with varying flake and salt concentrations. Significant changes in viscoelastic and flow behavior observed with salt addition enables tuning nanomaterial properties for potential ease of processability. Both of these research areas gave experimental and theoretical contributions to fundamental understanding of tuning 2D nanomaterial dispersion parameters on processing and final properties. The advances in graphene hybrids and MXenes from this research extends the foundation for multicomponent interactions and fabricating aligned and/or layered architectures for improving energy storage devices, fibers, catalysts, and sensors in the future.

References

1. Mensah, T. O.; Wang, B.; Bothun, G.; Winter, J.; Davis, V., *Nanotechnology commercialization: Manufacturing processes and products*. John Wiley & Sons: **2017**.
2. Davis, V. A.; Ericson, L. M.; Parra-Vasquez, A. N. G.; Fan, H.; Wang, Y.; Prieto, V.; Longoria, J. A.; Ramesh, S.; Saini, R. K.; Kittrell, C.; Billups, W. E.; Adams, W. W.; Hauge, R. H.; Smalley, R. E.; Pasquali, M., Phase Behavior and Rheology of SWNTs in Superacids. *Macromolecules* **2004,** *37* (1), 154-160.
3. Rai, P. K.; Pinnick, R. A.; Parra-Vasquez, A. N. G.; Davis, V. A.; Schmidt, H. K.; Hauge, R. H.; Smalley, R. E.; Pasquali, M., Isotropic−Nematic Phase Transition of Single-Walled Carbon Nanotubes in Strong Acids. *Journal of the American Chemical Society* **2006,** *128* (2), 591-595.
4. Kohlmeyer, R. R.; Lor, M.; Deng, J.; Liu, H.; Chen, J., Preparation of stable carbon nanotube aerogels with high electrical conductivity and porosity. *Carbon* **2011,** *49* (7), 2352-2361.
5. Chen, Z.; Zhang, H.; Wu, C.; Luo, L.; Wang, C.; Huang, S.; Xu, H., A study of the effect of carbon characteristics on capacitive deionization (CDI) performance. *Desalination* **2018,** *433*, 68-74.
6. Rodríguez-reinoso, F., The role of carbon materials in heterogeneous catalysis. *Carbon* **1998,** *36* (3), 159-175.
7. Jia, B.; Zou, L., Wettability and its influence on graphene nansoheets as electrode material for capacitive deionization. *Chemical Physics Letters* **2012,** *548*, 23-28.
8. Kim, J. E.; Oh, J. H.; Kotal, M.; Koratkar, N.; Oh, I. K., Self-assembly and morphological control of three-dimensional macroporous architectures built of two-dimensional materials. *Nano Today* **2017,** *14*, 100-123.
9. Pei, S.; Cheng, H.-M., The reduction of graphene oxide. *Carbon* **2012,** *50* (9), 3210-3228.
10. Kotal, M.; Kim, J.; Oh, J.; Oh, I.-K., Recent Progress in Multifunctional Graphene Aerogels. *Frontiers in Materials* **2016,** *3*, 29.
11. Huang, X.; Tan, C. L.; Yin, Z. Y.; Zhang, H., 25th Anniversary Article: Hybrid Nanostructures Based on Two-Dimensional Nanomaterials. *Advanced Materials* **2014,** *26* (14), 2185-2204.
12. Maleski, K.; Mochalin, V. N.; Gogotsi, Y., Dispersions of Two-Dimensional Titanium Carbide MXene in Organic Solvents. *Chemistry of Materials* **2017,** *29* (4), 1632-1640.
13. Orangi, J.; Hamade, F.; Davis, V. A.; Beidaghi, M., 3D Printing of Additive-Free 2D $Ti_3C_2T_x$ (MXene) Ink for Fabrication of Micro-Supercapacitors with Ultra-High Energy Densities. *ACS Nano* **2020,** *14* (1), 640-650.
14. Sobolciak, P.; Ali, A.; Hassan, M. K.; Helal, M. I.; Tanvir, A.; Popelka, A.; Al-Maadeed, M. A.; Krupa, I.; Mahmoud, K. A., 2D $Ti_3C_2T_x$ (MXene)-reinforced polyvinyl alcohol (PVA) nanofibers with enhanced mechanical and electrical properties. *PLoS One* **2017,** *12* (8), 18.
15. Zhao, M.-Q.; Torelli, M.; Ren, C. E.; Ghidiu, M.; Ling, Z.; Anasori, B.; Barsoum, M. W.; Gogotsi, Y., 2D titanium carbide and transition metal oxides hybrid electrodes for Li-ion storage. *Nano Energy* **2016,** *30*, 603-613.

16. Shannon, M. A.; Bohn, P. W.; Elimelech, M.; Georgiadis, J. G.; Mariñas, B. J.; Mayes, A. M., Science and technology for water purification in the coming decades. In *Nanoscience and Technology*, Co-Published with Macmillan Publishers Ltd, UK: **2009**; pp 337-346.
17. Oren, Y., Capacitive deionization (CDI) for desalination and water treatment — past, present and future (a review). *Desalination* **2008,** *228* (1), 10-29.
18. Chen, S.; Zhu, J. W.; Han, Q. F.; Zheng, Z. J.; Yang, Y.; Wang, X., Shape-Controlled Synthesis of One-Dimensional MnO_2 via a Facile Quick-Precipitation Procedure and its Electrochemical Properties. *Crystal Growth & Design* **2009,** *9* (10), 4356-4361.
19. Radich, J. G.; Kamat, P. V., Origin of Reduced Graphene Oxide Enhancements in Electrochemical Energy Storage. *ACS Catalysis* **2012,** *2* (5), 807-816.
20. Anasori, B.; Lukatskaya, M. R.; Gogotsi, Y., 2D metal carbides and nitrides (MXenes) for energy storage. *Nature Reviews Materials* **2017,** *2* (2), 16098.
21. Hope, M. A.; Forse, A. C.; Griffith, K. J.; Lukatskaya, M. R.; Ghidiu, M.; Gogotsi, Y.; Grey, C. P., NMR reveals the surface functionalisation of Ti_3C_2 MXene. *Phys. Chem. Chem. Phys.* **2016,** *18* (7), 5099-5102.
22. Alhabeb, M.; Maleski, K.; Anasori, B.; Lelyukh, P.; Clark, L.; Sin, S.; Gogotsi, Y., Guidelines for Synthesis and Processing of Two-Dimensional Titanium Carbide ($Ti_3C_2T_x$ MXene). *Chemistry of Materials* **2017,** *29* (18), 7633-7644.
23. Lukatskaya Maria, R.; Mashtalir, O.; Ren Chang, E.; Dall'Agnese, Y.; Rozier, P.; Taberna Pierre, L.; Naguib, M.; Simon, P.; Barsoum Michel, W.; Gogotsi, Y., Cation Intercalation and High Volumetric Capacitance of Two-Dimensional Titanium Carbide. *Science* **2013,** *341* (6153), 1502-1505.
24. Naguib, M.; Mochalin, V. N.; Barsoum, M. W.; Gogotsi, Y., 25th Anniversary Article: MXenes: A New Family of Two-Dimensional Materials. *Adv. Mater.* **2014,** *26* (7), 992-1005.
25. Zhang, J.; Uzun, S.; Seyedin, S.; Lynch, P. A.; Akuzum, B.; Wang, Z.; Qin, S.; Alhabeb, M.; Shuck, C. E.; Lei, W.; Kumbur, E. C.; Yang, W.; Wang, X.; Dion, G.; Razal, J. M.; Gogotsi, Y., Additive-Free MXene Liquid Crystals and Fibers. *ACS Central Science* **2020,** *6* (2), 254-265.
26. Hantanasirisakul, K.; Zhao, M.-Q.; Urbankowski, P.; Halim, J.; Anasori, B.; Kota, S.; Ren, C. E.; Barsoum, M. W.; Gogotsi, Y., Fabrication of $Ti_3C_2T_x$ MXene Transparent Thin Films with Tunable Optoelectronic Properties. *Advanced Electronic Materials* **2016,** *2* (6), 1600050.
27. Wei, T. S.; Ahn, B. Y.; Grotto, J.; Lewis, J. A., 3D printing of customized Li-ion batteries with thick electrodes. *Advanced Materials* **2018,** *30* (16), 1703027.
28. Sun, K.; Wei, T. S.; Ahn, B. Y.; Seo, J. Y.; Dillon, S. J.; Lewis, J. A., 3D printing of interdigitated Li-Ion microbattery architectures. *Advanced Materials* **2013,** *25* (33), 4539-4543.
29. Shen, K.; Ding, J.; Yang, S., 3D printing quasi-solid-state asymmetric micro-supercapacitors with ultrahigh areal energy density. *Advanced Energy Materials* **2018,** *8* (20), 1800408.

30. Gross, B. C.; Erkal, J. L.; Lockwood, S. Y.; Chen, C.; Spence, D. M., Evaluation of 3D Printing and Its Potential Impact on Biotechnology and the Chemical Sciences. *Analytical Chemistry* **2014,** *86* (7), 3240-3253.
31. Corker, A.; Ng, H. C.-H.; Poole, R. J.; García-Tuñón, E., 3D printing with 2D colloids: Designing rheology protocols to predict 'printability'of soft-materials. *Soft Matter* **2019,** *15* (6), 1444-1456.
32. Fu, K.; Wang, Y.; Yan, C.; Yao, Y.; Chen, Y.; Dai, J.; Lacey, S.; Wang, Y.; Wan, J.; Li, T.; Wang, Z.; Xu, Y.; Hu, L., Graphene Oxide-Based Electrode Inks for 3D-Printed Lithium-Ion Batteries. *Advanced Materials (Deerfield Beach, Fla.)* **2016,** *28* (13), 2587-2594.
33. Machado, F. M.; Fagan, S. B.; da Silva, I. Z.; de Andrade, M. J., Carbon Nanoadsorbents. In *Carbon Nanomaterials as Adsorbents for Environmental and Biological Applications*, Bergmann, C. P.; Machado, F. M., Eds. Springer International Publishing: Cham, **2015**; pp 11-32.
34. Mallika, K.; DeVries, R.; Komanduri, R., On the low pressure transformation of graphite to diamond in the presence of a 'catalyst-solvent'. *Thin Solid Films* **1999,** *339* (1-2), 19-33.
35. Raza, M. Synthesis of hydrogenated amorphous carbon (a-C:H) thin films by HiPIMS-based processes. **2012**.
36. Zhu, Y.; Murali, S.; Cai, W.; Li, X.; Suk, J. W.; Potts, J. R.; Ruoff, R. S., Graphene and Graphene Oxide: Synthesis, Properties, and Applications. *Advanced Materials* **2010,** *22* (35), 3906-3924.
37. Sang, M.; Shin, J.; Kim, K.; Yu, K. J., Electronic and Thermal Properties of Graphene and Recent Advances in Graphene Based Electronics Applications. *Nanomaterials (Basel)* **2019,** *9* (3), 374.
38. Kötz, R.; Carlen, M., Principles and applications of electrochemical capacitors. *Electrochimica Acta* **2000,** *45* (15), 2483-2498.
39. Mitchell, E.; Candler, J.; De Souza, F.; Gupta, R. K.; Gupta, B. K.; Dong, L. F., High performance supercapacitor based on multilayer of polyaniline and graphene oxide. *Synthetic Metals* **2015,** *199*, 214-218.
40. Bonaccorso, F.; Bartolotta, A.; Coleman, J. N.; Backes, C., 2D-crystal-based functional inks. *Advanced Materials* **2016,** *28* (29), 6136-6166.
41. Deng, S. K.; Berry, V., Wrinkled, rippled and crumpled graphene: an overview of formation mechanism, electronic properties, and applications. *Materials Today* **2016,** *19* (4), 197-212.
42. Poulin, P.; Jalili, R.; Neri, W.; Nallet, F.; Divoux, T.; Colin, A.; Aboutalebi, S. H.; Wallace, G.; Zakri, C., Superflexibility of graphene oxide. *Proc. Natl. Acad. Sci. U. S. A.* **2016,** *113* (40), 11088-11093.
43. Dreyer, D. R.; Park, S.; Bielawski, C. W.; Ruoff, R. S., The chemistry of graphene oxide. *Chemical Society Reviews* **2010,** *39* (1), 228-240.
44. Amieva, E. J. C.; Lopez-Barroso, J.; Martínez-Hernández, A. L.; Velasco-Santos, C. In *Graphene-Based Materials Functionalization with Natural Polymeric Biomolecules*, 2016.

45. Pan, Z.; Liu, N.; Fu, L.; Liu, Z., Wrinkle Engineering: A New Approach to Massive Graphene Nanoribbon Arrays. *Journal of the American Chemical Society* **2011,** *133* (44), 17578-17581.
46. Shi, W. H.; Li, H. B.; Cao, X. H.; Leong, Z. Y.; Zhang, J.; Chen, T. P.; Zhang, H.; Yang, H. Y., Ultrahigh Performance of Novel Capacitive Deionization Electrodes based on A Three-Dimensional Graphene Architecture with Nanopores. *Scientific Reports* **2016,** *6*.
47. Yin, H.; Zhao, S.; Wan, J.; Tang, H.; Chang, L.; He, L.; Zhao, H.; Gao, Y.; Tang, Z., Three-Dimensional Graphene/Metal Oxide Nanoparticle Hybrids for High-Performance Capacitive Deionization of Saline Water. *Advanced Materials* **2013,** *25* (43), 6270-6276.
48. Stankovich, S.; Dikin, D. A.; Dommett, G. H. B.; Kohlhaas, K. M.; Zimney, E. J.; Stach, E. A.; Piner, R. D.; Nguyen, S. T.; Ruoff, R. S., Graphene-based composite materials. *Nature* **2006,** *442* (7100), 282-286.
49. Chen, S.; Zhu, J. W.; Wu, X. D.; Han, Q. F.; Wang, X., Graphene Oxide-MnO_2 Nanocomposites for Supercapacitors. *ACS Nano* **2010,** *4* (5), 2822-2830.
50. Gudarzi, M. M.; Sharif, F., Characteristics of polymers that stabilize colloids for the production of graphene from graphene oxide. *Journal of Colloid and Interface Science* **2010,** *349* (1), 63-69.
51. Zhang, D.; Yan, T.; Shi, L.; Peng, Z.; Wen, X.; Zhang, J., Enhanced capacitive deionization performance of graphene/carbon nanotube composites. *Journal of Materials Chemistry* **2012,** *22* (29), 14696-14704.
52. Yang, Z. Y.; Jin, L. J.; Lu, G. Q.; Xiao, Q. Q.; Zhang, Y. X.; Jing, L.; Zhang, X. X.; Yan, Y. M.; Sun, K. N., Sponge-templated preparation of high surface area graphene with ultrahigh capacitive deionization performance. *Advanced Functional Materials* **2014,** *24* (25), 3917-3925.
53. Portehault, D.; Cassaignon, S.; Baudrin, E.; Jolivet, J.-P., Morphology Control of Cryptomelane Type MnO_2 Nanowires by Soft Chemistry. Growth Mechanisms in Aqueous Medium. *Chemistry of Materials* **2007,** *19* (22), 5410-5417.
54. Hatzell, K. B.; Fan, L.; Beidaghi, M.; Boota, M.; Pomerantseva, E.; Kumbur, E. C.; Gogotsi, Y., Composite Manganese Oxide Percolating Networks As a Suspension Electrode for an Asymmetric Flow Capacitor. *ACS Applied Materials & Interfaces* **2014,** *6* (11), 8886-8893.
55. Li, Y. G.; Wu, Y. Y., Coassembly of Graphene Oxide and Nanowires for Large-Area Nanowire Alignment. *Journal of the American Chemical Society* **2009,** *131* (16), 5851-5857.
56. Wu, Z.-S.; Ren, W.; Wang, D.-W.; Li, F.; Liu, B.; Cheng, H.-M., High-Energy MnO_2 Nanowire/Graphene and Graphene Asymmetric Electrochemical Capacitors. *ACS Nano* **2010,** *4* (10), 5835-5842.
57. Kassaee, M. Z.; Motamedi, E.; Majdi, M., Magnetic Fe_3O_4-graphene oxide/polystyrene: Fabrication and characterization of a promising nanocomposite. *Chemical Engineering Journal* **2011,** *172* (1), 540-549.
58. Yang, H.; Jiang, J.; Zhou, W.; Lai, L.; Xi, L.; Lam, Y. M.; Shen, Z.; Khezri, B.; Yu, T., Influences of graphene oxide support on the electrochemical performances of graphene oxide-MnO_2 nanocomposites. *Nanoscale Res. Lett.* **2011,** *6* (1), 531.

59. Zhang, J.; Jiang, J.; Zhao, X. S., Synthesis and Capacitive Properties of Manganese Oxide Nanosheets Dispersed on Functionalized Graphene Sheets. *The Journal of Physical Chemistry C* **2011,** *115* (14), 6448-6454.
60. Ding, J.; Li, B.; Liu, Y.; Yan, X.; Zeng, S.; Zhang, X.; Hou, L.; Cai, Q.; Zhang, J., Fabrication of Fe_3O_4@reduced graphene oxide composite via novel colloid electrostatic self-assembly process for removal of contaminants from water. *Journal of Materials Chemistry A* **2015,** *3* (2), 832-839.
61. Hao, J.; Zhong, Y.; Liao, Y.; Shu, D.; Kang, Z.; Zou, X.; He, C.; Guo, S., Face-to-face self-assembly graphene/MnO_2 nanocomposites for supercapacitor applications using electrochemically exfoliated graphene. *Electrochimica Acta* **2015,** *167*, 412-420.
62. Xu, X. T.; Pan, L. K.; Liu, Y.; Lu, T.; Sun, Z.; Chua, D. H. C., Facile synthesis of novel graphene sponge for high performance capacitive deionization. *Scientific Reports* **2015,** *5*.
63. Lagerwall, J. P. F.; Scalia, G., A new era for liquid crystal research: Applications of liquid crystals in soft matter nano-, bio- and microtechnology. *Current Applied Physics* **2012,** *12* (6), 1387-1412.
64. Donald, A. M.; Windle, A. H.; Hanna, S., *Liquid crystalline polymers*. Cambridge University Press: **2006**.
65. Dogic, Z.; Fraden, S., Smectic Phase in a Colloidal Suspension of Semiflexible Virus Particles. *Physical Review Letters* **1997,** *78* (12), 2417-2420.
66. Livolant, F.; Levelut, A. M.; Doucet, J.; Benoit, J. P., The highly concentrated liquid-crystalline phase of DNA is columnar hexagonal. *Nature* **1989,** *339* (6227), 724-726.
67. Onsager, L., THE EFFECTS OF SHAPE ON THE INTERACTION OF COLLOIDAL PARTICLES. *Annals of the New York Academy of Sciences* **1949,** *51* (1), 627-659.
68. Flory, P. J., Phase equilibria in solutions of rod-like particles. *Proceedings of the Royal Society of London. Series A. Mathematical and Physical Sciences* **1956,** *234* (1196), 73-89.
69. Larson, R. G., *The structure and rheology of complex fluids*. Oxford University Press: New York, **1999**.
70. Edwards, S. F., *The theory of polymer dynamics*. Oxford Univ. Press: **1986**.
71. Khokhlov, A. R.; Semenov, A. N., On the theory of liquid-crystalline ordering of polymer chains with limited flexibility. *Journal of Statistical Physics* **1985,** *38* (1), 161-182.
72. Green, M. J.; Parra-Vasquez, A. N. G.; Behabtu, N.; Pasquali, M., Modeling the phase behavior of polydisperse rigid rods with attractive interactions with applications to single-walled carbon nanotubes in superacids. *The Journal of Chemical Physics* **2009,** *131* (8), 084901.
73. Flory, P. J., Phase equilibria in solutions of rod-like particles. *Proceedings of the Royal Society of London. Series A. Mathematical and Physical Sciences* **1956,** *234* (1196), 73-89.
74. Flory, P. J.; Ronca, G., Theory of Systems of RodIike Particles: II. Thermotropic systems with orientation-dependent interactions. *Mol. Cryst. Liquid Cryst.* **1979,** *54* (3-4), 311-330.

75. Andrienko, D., Introduction to liquid crystals. *Journal of Molecular Liquids* **2018,** *267*, 520-541.
76. Hanson, E.; Shen, Y., Refractive indices and optical anisotropy of homologous liquid crystals. *Mol. Cryst. Liquid Cryst.* **1976,** *36* (3-4), 193-207.
77. Michel-Lévy, M.; Lacroix, A., Minéralogie sur nouveau gisemant de dumortiérite. *CR Acad Sci Paris* **1888,** *106*, 1546-1548.
78. Baek, S. G.; Magda, J. J.; Larson, R. G., Rheological differences among liquid-crystalline polymers. I. The first and second normal stress differences of PBG solutions. *Journal of Rheology* **1993,** *37* (6), 1201-1224.
79. Onogi, S.; Asada, T., Rheology and Rheo-Optics of Polymer Liquid Crystals. In *Rheology: Volume 1: Principles*, Astarita, G.; Marrucci, G.; Nicolais, L., Eds. Springer US: Boston, MA, **1980**; pp 127-147.
80. Shimamura, K.; White, J. L.; Fellers, J. F., Hydroxypropylcellulose, a thermotropic liquid crystal: characteristics and structure development in continuous extrusion and melt spinning. *Journal of Applied Polymer Science* **1981,** *26* (7), 2165-2180.
81. Kiss, G., Rheology and rheo-optics of concentrated solutions of helical polypeptides. **1979**.
82. Wissbrun, K. F., Observations on the melt rheology of thermotropic aromatic polyesters. *British Polymer Journal* **1980,** *12* (4), 163-169.
83. Fishers, J.; Fredrickson, A., Interfacial effects on the viscosity of a nematic mesophase. *Molecular Crystals* **1969,** *8* (1), 267-284.
84. Horn, R. G.; Kleman, M. In *Observations on shear-induced textures and rheology of a smectic-A phase*, Annales De Physique, EDP Sciences: **1978**; pp 229-234.
85. Nielsen, L. E., *Polymer rheology*. M. Dekker: **1977**.
86. Romo-Uribe, A.; Windle, A., "Log-rolling" alignment in main-chain thermotropic liquid crystalline polymer melts under shear: an in-situ WAXS study. *Macromolecules* **1996,** *29* (19), 6246-6255.
87. Kumar, P.; Maiti, U. N.; Lee, K. E.; Kim, S. O., Rheological properties of graphene oxide liquid crystal. *Carbon* **2014,** *80*, 453-461.
88. Ureña-Benavides, E. E.; Ao, G.; Davis, V. A.; Kitchens, C. L., Rheology and Phase Behavior of Lyotropic Cellulose Nanocrystal Suspensions. *Macromolecules* **2011,** *44* (22), 8990-8998.
89. Ciferri, A. In *Liquid crystallinity in polymers : principles and fundamental properties*, **1991**.
90. Cox, W.; Merz, E., Correlation of dynamic and steady flow viscosities. *Journal of Polymer Science* **1958,** *28* (118), 619-622.
91. Larson, R., Arrested tumbling in shearing flows of liquid-crystal polymers. *Macromolecules* **1990,** *23* (17), 3983-3992.
92. Niu, R.; Gong, J.; Xu, D. H.; Tang, T.; Sun, Z. Y., Relationship between structures and rheological properties of plate-like particle suspensions. *Colloid Surf. A-Physicochem. Eng. Asp.* **2015,** *470*, 22-30.
93. Liu, Y.; Chen, C.; Liu, L.; Zhu, G.; Kong, Q.; Hao, R.; Tan, W., Rheological Behavior of High Concentrated Dispersions of Graphite Oxide. *Soft Mater.* **2015,** *13* (3), 167-175.

94. Jalili, R.; Aboutalebi, S. H.; Esrafilzadeh, D.; Konstantinov, K.; Razal, J. M.; Moultona, S. E.; Wallace, G. G., Formation and processability of liquid crystalline dispersions of graphene oxide. *Mater. Horizons* **2014,** *1* (1), 87-91.
95. Naficy, S.; Jalili, R.; Aboutalebi, S. H.; Gorkin, R. A.; Konstantinov, K.; Innis, P. C.; Spinks, G. M.; Poulin, P.; Wallace, G. G., Graphene oxide dispersions: tuning rheology to enable fabrication. *Mater. Horizons* **2014,** *1* (3), 326-331.
96. Israelachvili, J. N., *Intermolecular and surface forces*. Academic press: **2015**.
97. Einstein, A., A new determination of molecular dimensions. *Ann. Phys.* **1906,** *19*, 289-306.
98. Hao, T., Viscosities of liquids, colloidal suspensions, and polymeric systems under zero or non-zero electric field. *Advances in Colloid and Interface Science* **2008,** *142* (1), 1-19.
99. Rubio-Hernández, F. J.; Carrique, F.; Ruiz-Reina, E., The primary electroviscous effect in colloidal suspensions. *Advances in Colloid and Interface Science* **2004,** *107* (1), 51-60.
100. Booth, F.; Mott, N. F., The electroviscous effect for suspensions of solid spherical particles. *Proceedings of the Royal Society of London. Series A. Mathematical and Physical Sciences* **1997,** *203* (1075), 533-551.
101. Watterson, I. G.; White, L. R., Primary electroviscous effect in suspensions of charged spherical particles. *Journal of the Chemical Society, Faraday Transactions 2: Molecular and Chemical Physics* **1981,** *77* (7), 1115-1128.
102. Sherwood, J., The primary electroviscous effect in a suspension of spheres. *Journal of Fluid Mechanics* **1980,** *101* (3), 609-629.
103. Hinch, E.; Sherwood, J., The primary electroviscous effect in a suspension of spheres with thin double layers. *Journal of Fluid Mechanics* **1983,** *132*, 337-347.
104. Verwey, E. J., J. Th G. Overbeek, and K. van Nes., Theory of the stability of lyophobic colloids: the interaction of sol particles having an electric double layer. **1948**.
105. Urbina-Villalba, G.; García-Sucre, M., Role of the secondary minimum on the flocculation rate of nondeformable droplets. *Langmuir* **2005,** *21* (15), 6675-6687.
106. Cortada, M.; Anta, J. A.; Molina-Bolivar, J., Secondary minimum coagulation in charged colloidal suspensions from statistical mechanics methods. *The Journal of Physical Chemistry B* **2007,** *111* (5), 1110-1118.
107. Liu, J.; Zhang, L.; Xu, Z.; Masliyah, J., Colloidal Interactions between Asphaltene Surfaces in Aqueous Solutions. *Langmuir* **2006,** *22* (4), 1485-1492.
108. Litton, G. M.; Olson, T. M., Particle size effects on colloid deposition kinetics: evidence of secondary minimum deposition. *Colloids and Surfaces A: Physicochemical and Engineering Aspects* **1996,** *107*, 273-283.
109. Jeffrey, G. C.; Ottewill, R. H., Reversible aggregation Part I. Reversible flocculation monitored by turbidity measurements. *Colloid and Polymer Science* **1988,** *266* (2), 173-179.
110. Shein, I. R.; Ivanovskii, A. L., Graphene-like nanocarbides and nanonitrides of d metals (MXenes): synthesis, properties and simulation. *Micro & Nano Letters* **2013,** *8* (2), 59-62.

111. Chaudhari, N. K.; Jin, H.; Kim, B.; San Baek, D.; Joo, S. H.; Lee, K., MXene: an emerging two-dimensional material for future energy conversion and storage applications. *Journal of Materials Chemistry A* **2017,** *5* (47), 24564-24579.
112. Mahesh, K. V.; Linsha, V.; Peer Mohamed, A.; Ananthakumar, S., Processing of 2D-MAXene nanostructures and design of high thermal conducting, rheo-controlled MAXene nanofluids as a potential nanocoolant. *Chemical Engineering Journal* **2016,** *297*, 158-169.
113. Liu, G.; Zou, J.; Tang, Q.; Yang, X.; Zhang, Y.; Zhang, Q.; Huang, W.; Chen, P.; Shao, J.; Dong, X., Surface Modified Ti_3C_2 MXene Nanosheets for Tumor Targeting Photothermal/Photodynamic/Chemo Synergistic Therapy. *ACS Applied Materials & Interfaces* **2017,** *9* (46), 40077-40086.
114. VahidMohammadi, A.; Rosen, J.; Gogotsi, Y., The world of two-dimensional carbides and nitrides (MXenes). *Science* **2021,** *372* (6547), eabf1581.
115. Paineau, E.; Michot, L. J.; Bihannic, I.; Baravian, C., Aqueous Suspensions of Natural Swelling Clay Minerals. 2. Rheological Characterization. *Langmuir* **2011,** *27* (12), 7806-7819.
116. Maleski, K.; Ren, C. E.; Zhao, M.-Q.; Anasori, B.; Gogotsi, Y., Size-Dependent Physical and Electrochemical Properties of Two-Dimensional MXene Flakes. *ACS Applied Materials & Interfaces* **2018,** *10* (29), 24491-24498.
117. Akuzum, B.; Maleski, K.; Anasori, B.; Lelyukh, P.; Alvarez, N. J.; Kumbur, E. C.; Gogotsi, Y., Rheological Characteristics of 2D Titanium Carbide (MXene) Dispersions: A Guide for Processing MXenes. *ACS Nano* **2018,** *12* (3), 2685-2694.
118. Nourizadeh, H.; Bakhshayesh, A., Nanoclay-Based Products Across Global Markets. *StatNano Applied and Industrial Series: Nanoclay-Based Products Across Global Markets: Applications and Properties* **2020**, 3-33.
119. Jabbari-Farouji, S.; Weis, J.-J.; Davidson, P.; Levitz, P.; Trizac, E., On phase behavior and dynamical signatures of charged colloidal platelets. *Scientific Reports* **2013,** *3* (1), 3559.
120. Luckham, P. F.; Rossi, S., The colloidal and rheological properties of bentonite suspensions. *Advances in Colloid and Interface Science* **1999,** *82* (1), 43-92.
121. Litchfield, D.; Baird, D., The rheology of high aspect ratio nanoparticle filled liquids. *Rheol Rev* **2006**.
122. VAN OLPHEN, H., *An Introduction to Clay Colloid Chemistry: For Clay Technologists, Geologists, and Soil Scientists*. Interscience Publ.: **1966**.
123. Kissa, E., *Dispersions: Characterization, Testing, and Measurement*. Taylor & Francis: **1999**.
124. Lin, M.; Lindsay, H. M.; Weitz, D.; Ball, R.; Klein, R.; Meakin, P., Universality in colloid aggregation. *Nature* **1989,** *339* (6223), 360-362.
125. Kroy, K.; Cates, M.; Poon, W., Cluster mode-coupling approach to weak gelation in attractive colloids. *Physical Review Letters* **2004,** *92* (14), 148302.
126. Lin, M.; Lindsay, H.; Weitz, D.; Ball, R.; Klein, R.; Meakin, P., Universal reaction-limited colloid aggregation. *Physical Review A* **1990,** *41* (4), 2005.
127. Dickinson, E., Structure and rheology of colloidal particle gels: Insight from computer simulation. *Advances in Colloid and Interface Science* **2013,** *199-200*, 114-127.

128. Wilkinson, N.; Metaxas, A.; Brichetto, E.; Wickramaratne, S.; Reineke, T. M.; Dutcher, C. S., Ionic strength dependence of aggregate size and morphology on polymer-clay flocculation. *Colloids and Surfaces A: Physicochemical and Engineering Aspects* **2017,** *529*, 1037-1046.
129. Ruzicka, B.; Zaccarelli, E., A fresh look at the Laponite phase diagram. *Soft Matter* **2011,** *7* (4), 1268-1286.
130. Liss, S. N.; Droppo, I. G.; Flannigan, D. T.; Leppard, G. G., Floc architecture in wastewater and natural riverine systems. *Environmental Science & Technology* **1996,** *30* (2), 680-686.
131. Spencer, K. L.; Wheatland, J. A. T.; Bushby, A. J.; Carr, S. J.; Droppo, I. G.; Manning, A. J., A structure–function based approach to floc hierarchy and evidence for the non-fractal nature of natural sediment flocs. *Scientific Reports* **2021,** *11* (1), 14012.
132. Inoue, M.; Yusa, S.-i.; Morishima, Y.; Nakamura, Y.; Fujii, S.; Iwasaki, Y.; Chaudhary, D., Encapsulation of water with ph-responsive polymer grafted silica gel particles. In *Chemeca 2011: Engineering a Better World: Sydney Hilton Hotel, NSW, Australia, 18-21 September 2011*, Engineers Australia Barton, ACT: **2011**; pp 2665-2673.
133. Shaikh, S. M. R.; Nasser, M. S.; Hussein, I.; Benamor, A.; Onaizi, S. A.; Qiblawey, H., Influence of polyelectrolytes and other polymer complexes on the flocculation and rheological behaviors of clay minerals: A comprehensive review. *Separation and Purification Technology* **2017,** *187*, 137-161.
134. Fettweis, M.; Baeye, M.; Lee, B. J.; Chen, P.; Yu, J. C. S., Hydro-meteorological influences and multimodal suspended particle size distributions in the Belgian nearshore area (southern North Sea). *Geo-Marine Letters* **2012,** *32* (2), 123-137.
135. Morales, V.; Anta, J. A.; Lago, S., Integral Equation Prediction of Reversible Coagulation in Charged Colloidal Suspensions. *Langmuir* **2003,** *19* (2), 475-482.
136. Kotera, A.; Furusawa, K.; Kudō, K., Colloid chemical studies of polystyrene latices polymerized without any surface-active agents. *Kolloid-Zeitschrift und Zeitschrift für Polymere* **1970,** *240* (1), 837-842.
137. Sheikhi, A.; Afewerki, S.; Oklu, R.; Gaharwar, A. K.; Khademhosseini, A., Effect of ionic strength on shear-thinning nanoclay–polymer composite hydrogels. *Biomaterials Science* **2018,** *6* (8), 2073-2083.
138. Pignon, F.; Magnin, A.; Piau, J.-M., Thixotropic Behavior of Clay Dispersions: Combinations of Scattering and Rheometric Techniques. *Journal of Rheology* **1998,** *42*, 1349-1373.
139. van der Kooij, F. M.; Lekkerkerker, H. N. W., Formation of Nematic Liquid Crystals in Suspensions of Hard Colloidal Platelets. *The Journal of Physical Chemistry B* **1998,** *102* (40), 7829-7832.
140. Rueb, C. J.; Zukoski, C. F., Viscoelastic properties of colloidal gels. *Journal of Rheology* **1997,** *41* (2), 197-218.
141. Zaccone, A.; Winter, H. H.; Siebenbürger, M.; Ballauff, M., Linking self-assembly, rheology, and gel transition in attractive colloids. *Journal of Rheology* **2014,** *58* (5), 1219-1244.
142. de Hoog, E. H.; Kegel, W. K.; van Blaaderen, A.; Lekkerkerker, H. N., Direct observation of crystallization and aggregation in a phase-separating colloid-polymer suspension. *Physical Review E* **2001,** *64* (2), 021407.

143. Gibaud, T.; Schurtenberger, P., A closer look at arrested spinodal decomposition in protein solutions. *Journal of Physics: Condensed Matter* **2009,** *21* (32), 322201.
144. Bergenholtz, J.; Poon, W. C.; Fuchs, M., Gelation in model colloid−polymer mixtures. *Langmuir* **2003,** *19* (10), 4493-4503.
145. Poon, W. C.; Haw, M., Mesoscopic structure formation in colloidal aggregation and gelation. *Advances in Colloid and Interface Science* **1997,** *73*, 71-126.
146. Trappe, V.; Prasad, V.; Cipelletti, L.; Segre, P.; Weitz, D. A., Jamming phase diagram for attractive particles. *Nature* **2001,** *411* (6839), 772-775.
147. van der Kooij, F. M.; Kassapidou, K.; Lekkerkerker, H. N. W., Liquid crystal phase transitions in suspensions of polydisperse plate-like particles. *Nature* **2000,** *406* (6798), 868-871.
148. Langmuir, I., The Role of Attractive and Repulsive Forces in the Formation of Tactoids, Thixotropic Gels, Protein Crystals and Coacervates. *The Journal of Chemical Physics* **1938,** *6* (12), 873-896.
149. Shahin, A.; Joshi, Y. M., Irreversible Aging Dynamics and Generic Phase Behavior of Aqueous Suspensions of Laponite. *Langmuir* **2010,** *26* (6), 4219-4225.
150. Mourad, M. C. D.; Byelov, D. V.; Petukhov, A. V.; Matthijs de Winter, D. A.; Verkleij, A. J.; Lekkerkerker, H. N. W., Sol−Gel Transitions and Liquid Crystal Phase Transitions in Concentrated Aqueous Suspensions of Colloidal Gibbsite Platelets. *The Journal of Physical Chemistry B* **2009,** *113* (34), 11604-11613.
151. Paineau, E.; Antonova, K.; Baravian, C.; Bihannic, I.; Davidson, P.; Dozov, I.; Impéror-Clerc, M.; Levitz, P.; Madsen, A.; Meneau, F.; Michot, L. J., Liquid-Crystalline Nematic Phase in Aqueous Suspensions of a Disk-Shaped Natural Beidellite Clay. *The Journal of Physical Chemistry B* **2009,** *113* (48), 15858-15869.
152. Wijnhoven, J. E. G. J., Seeded growth of monodisperse gibbsite platelets to adjustable sizes. *Journal of Colloid and Interface Science* **2005,** *292* (2), 403-409.
153. Abend, S.; Lagaly, G., Sol–gel transitions of sodium montmorillonite dispersions. *Applied Clay Science* **2000,** *16* (3), 201-227.
154. Michot, L. J.; Bihannic, I.; Porsch, K.; Maddi, S.; Baravian, C.; Mougel, J.; Levitz, P., Phase Diagrams of Wyoming Na-Montmorillonite Clay. Influence of Particle Anisotropy. *Langmuir* **2004,** *20* (25), 10829-10837.
155. Mourad, M. C. D.; Wijnhoven, J. E. G. J.; van 't Zand, D. D.; van der Beek, D.; Lekkerkerker, H. N. W., Gelation versus liquid crystal phase transitions in suspensions of plate-like particles. *Philosophical Transactions of the Royal Society A: Mathematical, Physical and Engineering Sciences* **2006,** *364* (1847), 2807-2816.
156. Paineau, E.; Philippe, A. M.; Antonova, K.; Bihannic, I.; Davidson, P.; Dozov, I.; Gabriel, J. C. P.; Impéror-Clerc, M.; Levitz, P.; Meneau, F.; Michot, L. J., Liquid–crystalline properties of aqueous suspensions of natural clay nanosheets. *Liquid Crystals Reviews* **2013,** *1* (2), 110-126.
157. Eppenga, R.; Frenkel, D., Monte Carlo study of the isotropic and nematic phases of infinitely thin hard platelets. *Molecular Physics* **1984,** *52* (6), 1303-1334.
158. Bates, M. A.; Frenkel, D., Influence of polydispersity on the phase behavior of colloidal liquid crystals: A Monte Carlo simulation study. *The Journal of Chemical Physics* **1998,** *109* (14), 6193-6199.

159. Becher, T. B.; Braga, C. B.; Bertuzzi, D. L.; Ramos, M. D.; Hassan, A.; Crespilho, F. N.; Ornelas, C., The structure–property relationship in LAPONITE® materials: from Wigner glasses to strong self-healing hydrogels formed by non-covalent interactions. *Soft Matter* **2019,** *15* (6), 1278-1289.
160. Murali, S.; Xu, T.; Marshall, B. D.; Kayatin, M. J.; Pizarro, K.; Radhakrishnan, V. K.; Nepal, D.; Davis, V. A., Lyotropic Liquid Crystalline Self-Assembly in Dispersions of Silver Nanowires and Nanoparticles. *Langmuir* **2010,** *26* (13), 11176-11183.
161. Ghidiu, M.; Lukatskaya, M. R.; Zhao, M.-Q.; Gogotsi, Y.; Barsoum, M. W., Conductive two-dimensional titanium carbide 'clay' with high volumetric capacitance. *Nature* **2014,** *516* (7529), 78-81.
162. Akbari, A.; Sheath, P.; Martin, S. T.; Shinde, D. B.; Shaibani, M.; Banerjee, P. C.; Tkacz, R.; Bhattacharyya, D.; Majumder, M., Large-area graphene-based nanofiltration membranes by shear alignment of discotic nematic liquid crystals of graphene oxide. *Nature Communications* **2016,** *7*, 12.
163. Naguib, M.; Mashtalir, O.; Carle, J.; Presser, V.; Lu, J.; Hultman, L.; Gogotsi, Y.; Barsoum, M. W., Two-Dimensional Transition Metal Carbides. *ACS Nano* **2012,** *6* (2), 1322-1331.
164. Iqbal, A.; Hong, J.; Ko, T. Y.; Koo, C. M., Improving oxidation stability of 2D MXenes: synthesis, storage media, and conditions. *Nano Convergence* **2021,** *8* (1), 9.
165. Subramanian, V.; Zhu, H.; Vajtai, R.; Ajayan, P. M.; Wei, B., Hydrothermal Synthesis and Pseudocapacitance Properties of MnO_2 Nanostructures. *The Journal of Physical Chemistry B* **2005,** *109* (43), 20207-20214.
166. Hamade, F.; Radich, E.; Davis, V. A., Microstructure and electrochemical properties of high performance graphene/manganese oxide hybrid electrodes. *RSC Advances* **2021,** *11* (50), 31608-31620.
167. Jalili, R.; Aboutalebi, S. H.; Esrafilzadeh, D.; Konstantinov, K.; Moulton, S. E.; Razal, J. M.; Wallace, G. G., Organic Solvent-Based Graphene Oxide Liquid Crystals: A Facile Route toward the Next Generation of Self-Assembled Layer-by-Layer Multifunctional 3D Architectures. *ACS Nano* **2013,** *7* (5), 3981-3990.
168. Aboutalebi, S. H.; Gudarzi, M. M.; Zheng, Q. B.; Kim, J. K., Spontaneous Formation of Liquid Crystals in Ultralarge Graphene Oxide Dispersions. *Advanced Functional Materials* **2011,** *21* (15), 2978-2988.
169. Gilje, S.; Han, S.; Wang, M.; Wang, K. L.; Kaner, R. B., A Chemical Route to Graphene for Device Applications. *Nano Letters* **2007,** *7* (11), 3394-3398.
170. Hamade, F.; Amit, S. K.; Woods, M. B.; Davis, V. A., The Effects of Size and Shape Dispersity on the Phase Behavior of Nanomesogen Lyotropic Liquid Crystals. *Crystals* **2020,** *10* (8).
171. Lu, H.; Zhang, J.; Luo, J.; Gong, W.; Li, C.; Li, Q.; Zhang, K.; Hu, M.; Yao, Y., Enhanced thermal conductivity of free-standing 3D hierarchical carbon nanotube-graphene hybrid paper. *Composites Part A: Applied Science and Manufacturing* **2017,** *102*, 1-8.
172. Ricciardulli, A. G.; Yang, S.; Wetzelaer, G.-J. A. H.; Feng, X.; Blom, P. W. M., Hybrid Silver Nanowire and Graphene-Based Solution-Processed Transparent Electrode for Organic Optoelectronics. *Advanced Functional Materials* **2018,** *28* (14), 1706010.

173. Jeong, H.-K.; Lee, Y. P.; Jin, M. H.; Kim, E. S.; Bae, J. J.; Lee, Y. H., Thermal stability of graphite oxide. *Chemical Physics Letters* **2009,** *470* (4), 255-258.
174. Bannov, A. G.; Timofeeva, A. A.; Shinkarev, V. V.; Dyukova, K. D.; Ukhina, A. V.; Maksimovskii, E. A.; Yusin, S. I., Synthesis and studies of properties of graphite oxide and thermally expanded graphite. *Protection of Metals and Physical Chemistry of Surfaces* **2014,** *50* (2), 183-190.
175. Gao, T.; Glerup, M.; Krumeich, F.; Nesper, R.; Fjellvåg, H.; Norby, P., Microstructures and spectroscopic properties of cryptomelane-type manganese dioxide nanofibers. *The Journal of Physical Chemistry C* **2008,** *112* (34), 13134-13140.
176. Ai, Z.; Zhang, L.; Kong, F.; Liu, H.; Xing, W.; Qiu, J., Microwave-assisted green synthesis of MnO_2 nanoplates with environmental catalytic activity. *Materials Chemistry and Physics* **2008,** *111* (1), 162-167.
177. Paredes, J. I.; Villar-Rodil, S.; Martinez-Alonso, A.; Tascon, J. M. D., Graphene oxide dispersions in organic solvents. *Langmuir* **2008,** *24* (19), 10560-10564.
178. Zhang, J.; Yang, H.; Shen, G.; Cheng, P.; Zhang, J.; Guo, S., Reduction of graphene oxide vial-ascorbic acid. *Chemical Communications* **2010,** *46* (7), 1112-1114.
179. Musil, M.; Choi, B.; Tsutsumi, A., Morphology and Electrochemical Properties of α-, β-, γ-, and δ-MnO_2 Synthesized by Redox Method. *Journal of The Electrochemical Society* **2015,** *162* (10), A2058.
180. Ferrari, A. C.; Robertson, J., Interpretation of Raman spectra of disordered and amorphous carbon. *Physical Review B* **2000,** *61* (20), 14095-14107.
181. Lucchese, M. M.; Stavale, F.; Ferreira, E. H. M.; Vilani, C.; Moutinho, M. V. O.; Capaz, R. B.; Achete, C. A.; Jorio, A., Quantifying ion-induced defects and Raman relaxation length in graphene. *Carbon* **2010,** *48* (5), 1592-1597.
182. López, V.; Sundaram, R. S.; Gómez-Navarro, C.; Olea, D.; Burghard, M.; Gómez-Herrero, J.; Zamora, F.; Kern, K., Chemical Vapor Deposition Repair of Graphene Oxide: A Route to Highly-Conductive Graphene Monolayers. *Advanced Materials* **2009,** *21* (46), 4683-4686.
183. Gómez-Navarro, C.; Meyer, J. C.; Sundaram, R. S.; Chuvilin, A.; Kurasch, S.; Burghard, M.; Kern, K.; Kaiser, U., Atomic Structure of Reduced Graphene Oxide. *Nano Letters* **2010,** *10* (4), 1144-1148.
184. Luo, D.; Zhang, G.; Liu, J.; Sun, X., Evaluation criteria for reduced graphene oxide. *The Journal of Physical Chemistry C* **2011,** *115* (23), 11327-11335.
185. Mattevi, C.; Eda, G.; Agnoli, S.; Miller, S.; Mkhoyan, K. A.; Celik, O.; Mastrogiovanni, D.; Granozzi, G.; Garfunkel, E.; Chhowalla, M., Evolution of Electrical, Chemical, and Structural Properties of Transparent and Conducting Chemically Derived Graphene Thin Films. *Advanced Functional Materials* **2009,** *19* (16), 2577-2583.
186. Yang, D.; Velamakanni, A.; Bozoklu, G.; Park, S.; Stoller, M.; Piner, R. D.; Stankovich, S.; Jung, I.; Field, D. A.; Ventrice, C. A.; Ruoff, R. S., Chemical analysis of graphene oxide films after heat and chemical treatments by X-ray photoelectron and Micro-Raman spectroscopy. *Carbon* **2009,** *47* (1), 145-152.
187. Ambrosi, A.; Bonanni, A.; Sofer, Z.; Cross, J. S.; Pumera, M., Electrochemistry at Chemically Modified Graphenes. *Chemistry – A European Journal* **2011,** *17* (38), 10763-10770.

188. Malard, L. M.; Pimenta, M. A.; Dresselhaus, G.; Dresselhaus, M. S., Raman spectroscopy in graphene. *Physics Reports* **2009,** *473* (5), 51-87.
189. Gao, T.; Fjellvåg, H.; Norby, P., A comparison study on Raman scattering properties of α-and β-MnO_2. *Analytica Chimica Acta* **2009,** *648* (2), 235-239.
190. Su, C.-Y.; Xu, Y.; Zhang, W.; Zhao, J.; Tang, X.; Tsai, C.-H.; Li, L.-J., Electrical and Spectroscopic Characterizations of Ultra-Large Reduced Graphene Oxide Monolayers. *Chemistry of Materials* **2009,** *21* (23), 5674-5680.
191. Zhao, X.; Hou, Y.; Wang, Y.; Yang, L.; Zhu, L.; Cao, R.; Sha, Z., Prepared MnO2 with different crystal forms as electrode materials for supercapacitors: experimental research from hydrothermal crystallization process to electrochemical performances. *RSC Advances* **2017,** *7* (64), 40286-40294.
192. Zhang, L.; Liu, H.; Ruan, H.; Su, Y.; Hu, R.; Tian, L.; Hu, Z.; Li, J. J. I. J. E. S., Fabrication of β-MnO_2/rGO composite and its electrochemical properties. **2016,** *11*, 10815-10826.
193. Qiu, X.; Xu, D.; Ma, L.; Wang, Y., Preparation of manganese oxide/graphene aerogel and its application as an advanced supercapacitor electrode material. *Int. J. Electrochem. Sci* **2017,** *12*, 2173-2183.
194. Zhu, X.; Zhang, P.; Xu, S.; Yan, X.; Xue, Q., Free-Standing Three-Dimensional Graphene/Manganese Oxide Hybrids As Binder-Free Electrode Materials for Energy Storage Applications. *ACS Applied Materials & Interfaces* **2014,** *6* (14), 11665-11674.
195. Lewis, J. A., Direct ink writing of 3D functional materials. *Advanced Functional Materials* **2006,** *16* (17), 2193-2204.
196. Fu, K.; Wang, Y.; Yan, C.; Yao, Y.; Chen, Y.; Dai, J.; Lacey, S.; Wang, Y.; Wan, J.; Li, T., Graphene oxide-based electrode inks for 3D-printed lithium-ion batteries. *Advanced Materials* **2016,** *28* (13), 2587-2594.
197. Compton, B. G.; Lewis, J. A., 3D-printing of lightweight cellular composites. *Advanced Materials* **2014,** *26* (34), 5930-5935.
198. Ambrosi, A.; Pumera, M., 3D-printing technologies for electrochemical applications. *Chemical Society Reviews* **2016,** *45* (10), 2740-2755.
199. Guo, Y.; Patanwala, H. S.; Bognet, B.; Ma, A. W., Inkjet and inkjet-based 3D printing: connecting fluid properties and printing performance. *Rapid Prototyping Journal* **2017,** *23* (3), 562-576.
200. Moyano, J. J.; Gómez-Gómez, A.; Pérez-Coll, D.; Belmonte, M.; Miranzo, P.; Osendi, M. I., Filament printing of graphene-based inks into self-supported 3D architectures. *Carbon* **2019,** *151*, 94-102.
201. Lipatov, A.; Alhabeb, M.; Lukatskaya, M. R.; Boson, A.; Gogotsi, Y.; Sinitskii, A., Effect of synthesis on quality, electronic properties and environmental stability of individual monolayer Ti_3C_2 MXene flakes. *Advanced Electronic Materials* **2016,** *2* (12), 1600255.
202. Zhang, C.; Kremer, M. P.; Seral-Ascaso, A.; Park, S. H.; McEvoy, N.; Anasori, B.; Gogotsi, Y.; Nicolosi, V., Stamping of flexible, coplanar micro-supercapacitors using MXene inks. *Advanced Functional Materials* **2018,** *28* (9), 1705506.
203. Zhang, C. J.; Pinilla, S.; McEvoy, N.; Cullen, C. P.; Anasori, B.; Long, E.; Park, S.-H.; Seral-Ascaso, A.; Shmeliov, A.; Krishnan, D., Oxidation stability of colloidal two-

dimensional titanium carbides (MXenes). *Chemistry of Materials* **2017,** *29* (11), 4848-4856.
204. Tian, X.; Jin, J.; Yuan, S.; Chua, C. K.; Tor, S. B.; Zhou, K., Emerging 3D-printed electrochemical energy storage devices: a critical review. *Advanced Energy Materials* **2017,** *7* (17), 1700127.
205. M'barki, A.; Bocquet, L.; Stevenson, A., Linking rheology and printability for dense and strong ceramics by direct ink writing. *Scientific Reports* **2017,** *7* (1), 1-10.
206. Naficy, S.; Jalili, R.; Aboutalebi, S. H.; Gorkin Iii, R. A.; Konstantinov, K.; Innis, P. C.; Spinks, G. M.; Poulin, P.; Wallace, G. G., Graphene oxide dispersions: tuning rheology to enable fabrication. *Mater. Horizons* **2014,** *1* (3), 326-331.
207. Russel, W. B., Review of the Role of Colloidal Forces in the Rheology of Suspensions. *Journal of Rheology* **1980,** *24* (3), 287-317.
208. Kayali, E.; VahidMohammadi, A.; Orangi, J.; Beidaghi, M., Controlling the Dimensions of 2D MXenes for Ultrahigh-Rate Pseudocapacitive Energy Storage. *ACS Applied Materials & Interfaces* **2018,** *10* (31), 25949-25954.
209. Natu, V.; Sokol, M.; Verger, L.; Barsoum, M. W., Effect of Edge Charges on Stability and Aggregation of $Ti_3C_2T_z$ MXene Colloidal Suspensions. *The Journal of Physical Chemistry C* **2018,** *122* (48), 27745-27753.
210. Forsyth, P. A.; Marčelja, S.; Mitchell, D. J.; Ninham, B. W., Onsager transition in hard plate fluid. *Journal of the Chemical Society, Faraday Transactions 2: Molecular and Chemical Physics* **1977,** *73* (1), 84-88.
211. Buining, P. A.; Lekkerkerker, H. N. W., Isotropic-nematic phase separation of a dispersion of organophilic boehmite rods. *The Journal of Physical Chemistry* **1993,** *97* (44), 11510-11516.
212. Vroege, G. J.; Lekkerkerker, H. N. W., Theory of the isotropic-nematic-nematic phase separation for a solution of bidisperse rodlike particles. *The Journal of Physical Chemistry* **1993,** *97* (14), 3601-3605.
213. Davis, V. A.; Parra-Vasquez, A. N. G.; Green, M. J.; Rai, P. K.; Behabtu, N.; Prieto, V.; Booker, R. D.; Schmidt, J.; Kesselman, E.; Zhou, W.; Fan, H.; Adams, W. W.; Hauge, R. H.; Fischer, J. E.; Cohen, Y.; Talmon, Y.; Smalley, R. E.; Pasquali, M., True solutions of single-walled carbon nanotubes for assembly into macroscopic materials. *Nature Nanotechnology* **2009,** *4* (12), 830-834.
214. Dan, B.; Behabtu, N.; Martinez, A.; Evans, J. S.; Kosynkin, D. V.; Tour, J. M.; Pasquali, M.; Smalyukh, II, Liquid crystals of aqueous, giant graphene oxide flakes. *Soft Matter* **2011,** *7* (23), 11154-11159.
215. Jalili, R.; Aboutalebi, S. H.; Esrafilzadeh, D.; Shepherd, R. L.; Chen, J.; Aminorroaya-Yamini, S.; Konstantinov, K.; Minett, A. I.; Razal, J. M.; Wallace, G. G., Scalable One-Step Wet-Spinning of Graphene Fibers and Yarns from Liquid Crystalline Dispersions of Graphene Oxide: Towards Multifunctional Textiles. *Advanced Functional Materials* **2013,** *23* (43), 5345-5354.
216. Kim, A. Y.; Hauch, K. D.; Berg, J. C.; Martin, J. E.; Anderson, R. A., Linear chains and chain-like fractals from electrostatic heteroaggregation. *Journal of Colloid and Interface Science* **2003,** *260* (1), 149-159.
217. Lu, P. J.; Conrad, J. C.; Wyss, H. M.; Schofield, A. B.; Weitz, D. A., Fluids of Clusters in Attractive Colloids. *Physical Review Letters* **2006,** *96* (2), 028306.

218. Meakin, P., Formation of fractal clusters and networks by irreversible diffusion-limited aggregation. *Physical Review Letters* **1983,** *51* (13), 1119.
219. Del Giudice, F.; Shen, A. Q., Shear rheology of graphene oxide dispersions. *Curr. Opin. Chem. Eng.* **2017,** *16*, 23-30.
220. Xu, Z.; Gao, C., Aqueous Liquid Crystals of Graphene Oxide. *ACS Nano* **2011,** *5* (4), 2908-2915.
221. Loiseau, A.; Tassin, J.-F., Model Nanocomposites Based on Laponite and Poly(ethylene oxide): Preparation and Rheology. *Macromolecules* **2006,** *39* (26), 9185-9191.
222. Nicolai, T.; Cocard, S., Structure of gels and aggregates of disk-like colloids. *Eur. Phys. J. E* **2001,** *5* (2), 221-227.
223. Guimont, A.; Beyou, E.; Martin, G.; Sonntag, P.; Cassagnau, P., Viscoelasticity of Graphite Oxide-Based Suspensions in PDMS. *Macromolecules* **2011,** *44* (10), 3893-3900.
224. Tanaka, H.; Meunier, J.; Bonn, D., Nonergodic states of charged colloidal suspensions: Repulsive and attractive glasses and gels. *Physical Review E* **2004,** *69* (3), 031404.
225. Zhao, C.; Yang, C., Electrokinetics of non-Newtonian fluids: A review. *Advances in Colloid and Interface Science* **2013,** *201-202*, 94-108.
226. Afghah, F.; Altunbek, M.; Dikyol, C.; Koc, B., Preparation and characterization of nanoclay-hydrogel composite support-bath for bioprinting of complex structures. *Scientific Reports* **2020,** *10* (1), 5257.
227. Marrucci, G., Rheology of nematic polymers. Liquid crystallinity in polymers. A. Ciferri. VCH Publishers New York: **1991**.
228. Laxton, P. B.; Berg, J. C., Relating clay yield stress to colloidal parameters. *Journal of colloid and interface science* **2006,** *296* (2), 749-755.
229. Cates, M. E.; Haw, M. D.; Holmes, C. B., Dilatancy, jamming, and the physics of granulation. *Journal of Physics: Condensed Matter* **2005,** *17* (24), S2517-S2531.
230. Ovarlez, G.; Barral, Q.; Coussot, P., Three-dimensional jamming and flows of soft glassy materials. *Nature Materials* **2010,** *9* (2), 115-119.
231. King, H. E.; Milner, S. T.; Lin, M. Y.; Singh, J. P.; Mason, T. G., Structure and rheology of organoclay suspensions. *Physical Review E* **2007,** *75* (2), 021403.
232. Ferry, J. D., *Viscoelastic properties of polymers*. John Wiley & Sons: **1980**.
233. Cox, H., The elasticity and strength of paper and other fibrous materials. *British Journal of Applied Physics* **1952,** *3* (3), 72.
234. Winter, H. H., Can the gel point of a cross-linking polymer be detected by the G′ – G″ crossover? *Polymer Engineering & Science* **1987,** *27* (22), 1698-1702.
235. Kim, C.; Yoo, B., Rheological properties of rice starch–xanthan gum mixtures. *Journal of Food Engineering* **2006,** *75* (1), 120-128.
236. Chen, D. T. N.; Wen, Q.; Janmey, P. A.; Crocker, J. C.; Yodh, A. G., Rheology of Soft Materials. *Annual Review of Condensed Matter Physics* **2010,** *1* (1), 301-322.
237. Kroon, M.; Vos, W. L.; Wegdam, G. H., Structure and formation of a gel of colloidal disks. *Physical Review E* **1998,** *57* (2), 1962-1970.
238. Sollich, P.; Lequeux, F.; Hébraud, P.; Cates, M. E., Rheology of Soft Glassy Materials. *Physical Review Letters* **1997,** *78* (10), 2020-2023.

239. Sciortino, F.; Mossa, S.; Zaccarelli, E.; Tartaglia, P., Equilibrium Cluster Phases and Low-Density Arrested Disordered States: The Role of Short-Range Attraction and Long-Range Repulsion. *Physical Review Letters* **2004,** *93* (5), 055701.
240. Sennett, P.; Olivier, J., Colloidal dispersions, electrokinetic effects, and the concept of zeta potential. *Industrial & Engineering Chemistry* **1965,** *57* (8), 32-50.
241. Cocard, S.; Tassin, J. F.; Nicolai, T., Dynamical mechanical properties of gelling colloidal disks. *Journal of Rheology* **2000,** *44* (3), 585-594.
242. Mourchid, A.; Delville, A.; Lambard, J.; LeColier, E.; Levitz, P., Phase Diagram of Colloidal Dispersions of Anisotropic Charged Particles: Equilibrium Properties, Structure, and Rheology of Laponite Suspensions. *Langmuir* **1995,** *11* (6), 1942-1950.
243. Vallés, C.; Young, R. J.; Lomax, D. J.; Kinloch, I. A., The rheological behaviour of concentrated dispersions of graphene oxide. *Journal of Materials Science* **2014,** *49* (18), 6311-6320.

Appendix

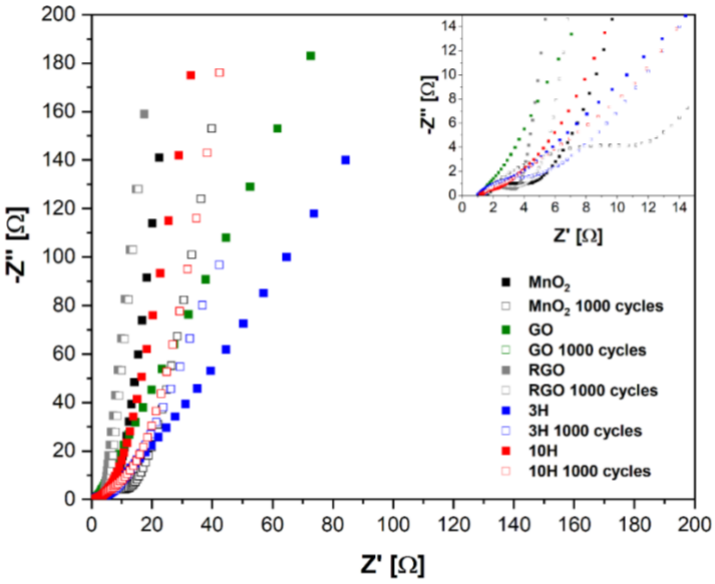

Figure A.1. EIS after 1 (closed squares) and 1000 (open squares) CV cycles performed at 20 mV/s.

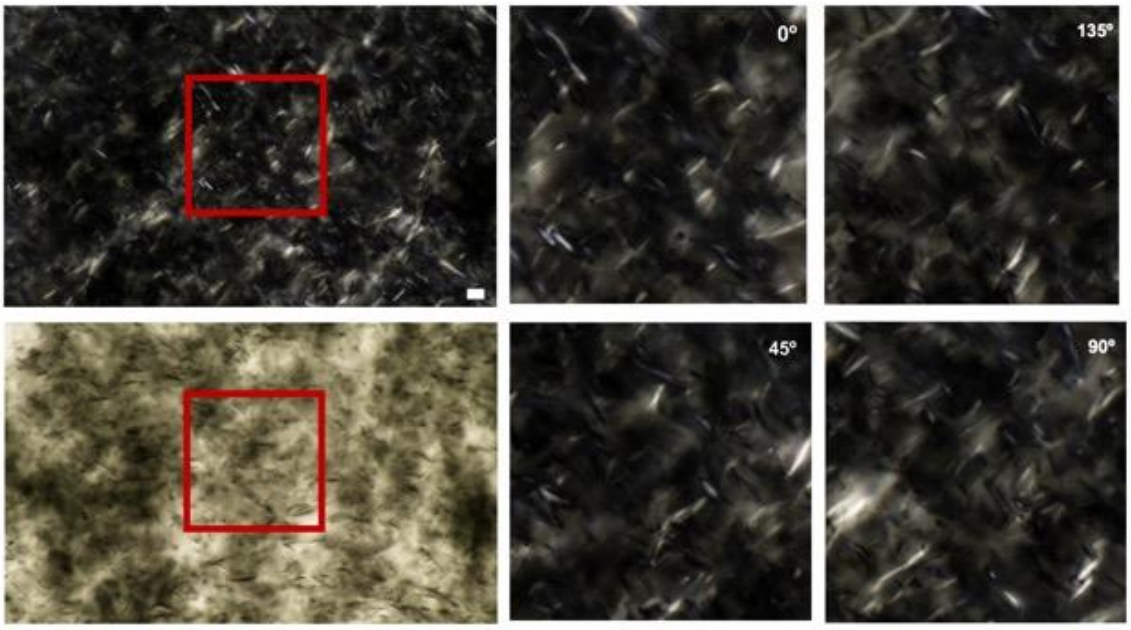

Figure A.2. Cross polarized optical microscopy of 0.15 vol%/0.1 M with stage rotations of the magnified portion of the box. The representative uncrossed image is also shown (bottom left). Scale bar is 5 μm.

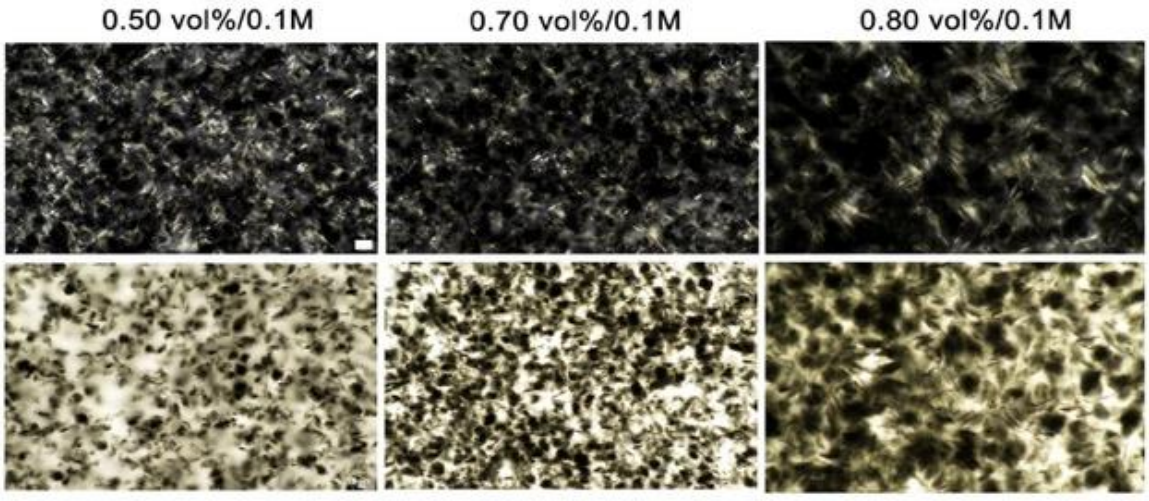

Figure A.3. MXene dispersions of crossed (top) and uncrossed (bottom) polarized optical microscopy images comparing 0.50 vol%/0.1 M, 0.70 vol%/0.1 M, and 0.80 vol%/0.1 NaCl. Scale bars represent 5 μm.

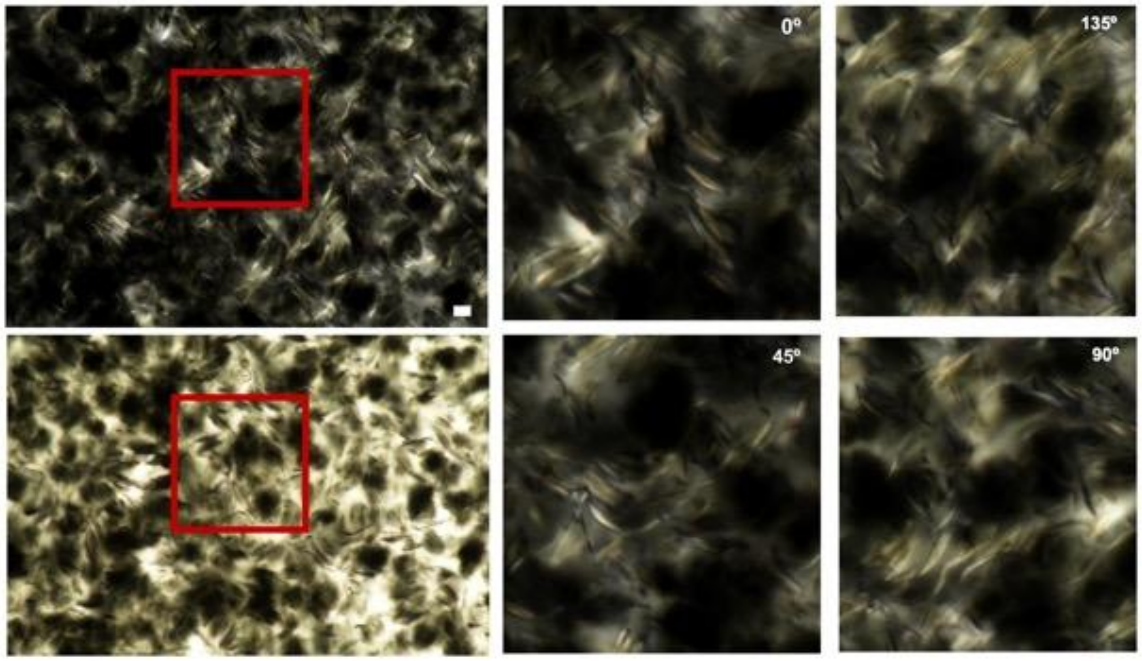

Figure A.4. Sample rotations of 0.80 vol%/0.1 M NaCl dispersion of the square region in top left. Bottom left image indicates the same area with uncrossed configuration.

Table A.1. Herschel-Bulkley Model Parameters for MXene/NaCl Dispersions for All Concentrations

MXene Concentration (vol%)	NaCl Concentration (M)	τ_0	K	n	R^2 value
0.050	0	0	0.00194	0.91	0.996
0.050	0.05	0.0078	0.0063	0.87	0.999
0.050	0.1	0.029	0.014	0.73	0.985
0.10	0	0.093	0.0047	0.88	0.904
0.10	0.05	0.019	0.010	0.97	0.999
0.10	0.1	0.11	0.0083	0.97	0.963
0.15	0.1	0.63	0.62	0.32	0.89
0.15	0.1	0	1.45	0.16	0.78
0.25	0	0.17	0.037	0	-
0.25	0	0.23	0.36	0.42	0.92
0.25	0.01	0.37	1.01	0.26	0.97
0.25	0.05	0.18	2.33	0.16	0.91
0.25	0.1	1.93	3.74	0.24	0.92
0.40	0	1.02	1.35	0.38	0.99
0.40	0.05	4.08	1.26	0.45	0.89
0.40	0.1	4.19	1.14	0.63	0.89
0.50	0	2.93	0.84	0.61	0.92
0.50	0.1	7.2	0.61	0.82	0.90
0.50	0.5	475	-	-	-
1.0	0	29.8	1.87	0.77	0.92
1.0	0.1	195	-	-	-

Table A.2. Steady Shear Viscosities at Different Shear Rates

MXene Concentration (vol%)	NaCl Concentration (M)	Viscosity at $0.01s^{-1}$ (Pa s)	Viscosity at $0.1s^{-1}$ (Pa s)	Viscosity at 100 s^{-1} (Pa s)
0.050	0	0.20	0.042	0.0013
0.050	0.05	1	0.071	0.0036
0.050	0.1	6	0.29	0.0044
0.10	0	13	0.97	0.0037
0.10	0.05	2	0.22	0.0081
0.10	0.1	21	1.15	0.0092
0.15	0.1	79	7.9	0.031
0.25	0	23	4.0	0.026
0.25	0.01	81	7.17	0.037
0.25	0.05	425	30.8	0.0052
0.25	0.1	1,346	44.8	0.12
0.25	0.3	2,190	136	0.18
0.40	0	126	23.1	0.091
0.40	0.05	570	51.7	0.14
0.40	0.1	605	39.4	0.22
0.50	0	510	36.7	0.16
0.50	0.1	1,081	112.2	0.30
0.50	0.5	49,173	6,335	4.7
1.0	0	3,607	346.1	0.88
1.0	0.1	25,154	1,877	2.0

Table A.3. Storage and Loss Moduli at Different Angular Frequencies

MXene Concentration (vol%)	NaCl Concentration (M)	G' at 0.01 rad/s	G' at 0.1 rad/s	G' at 100 rad/s	G" at 0.01 rad/s	G" at 0.1 rad/s	G" at 100 rad/s
0.15	0.1	36.0	33.5	25.3	3.75	2.09	11.6
0.25	0	*	18.9	27.9	*	2.37	3.78
0.25	0.01	3.05	2.55	10.7	0.512	0.369	5.44
0.25	0.05	53.2	46.5	63.8	4.48	3.11	14.2
0.25	0.1	237	223	296	29.5	18.1	61.7
0.25	0.3	1400	1490	1850	244	197	112
0.40	0	14.9	15.6	87.5	1.52	1.08	26.6
0.40	0.05	200	187	257	23.6	12.2	37.1
0.40	0.1	351	354	493	55.4	33.7	72.2
0.50	0	140	124	221	13.3	7.83	34.5
0.50	0.1	753	754	992	104	65.4	93.5
0.50	0.5	223,000	232,000	284,000	34,200	24,500	11,400
1.0	0	1,760	2,220	3340	366	266	433
1.0	0.1	154,000	163,000	196,000	22,400	14,500	8970

* *values out of torque range*